Nitrogen cycle-based estimates of carbon export potential in the waters adjacent to Larsen C Ice Shelf in the western Weddell Sea, Antarctica

Joshua Mirkin

Dissertation presented for the degree of Master of Science in the

Department of Oceanography

University of Cape Town

November 2022

Supervisors:
A/Prof. Sarah Fawcett
Prof. Adam West

Plagiarism declaration

I declare that the work presented in this dissertation is my own, except where indicated otherwise through citation.

Signed by candidate

Joshua Mirkin

28 November 2022

Abstract

The Southern Ocean accounts for >30% of the global ocean's sink of atmospheric CO_2, removing it through the solubility and biological pumps. To investigate the biological pump near the understudied Larsen C Ice Shelf (LCIS) in the western Weddell Sea of Antarctica, we measured the concentrations of nutrients, the nitrogen (N) and oxygen (O) isotope ratios ($\delta^{15}N$ and $\delta^{18}O$) of nitrate, and the $\delta^{15}N$ of ammonium and particulate organic N for samples collected in mid-summer 2019. From these data, we quantify carbon export potential by computing seasonal nitrate drawdown and the f-ratio (i.e., the fraction of primary production supported by new N, which is closely linked to the fraction of primary production that sinks into the ocean interior, removing CO_2). We calculate a mean f-ratio of 0.81 ± 0.18 using the N isotope data and show that of the seasonal decrease in nitrate concentration, 38 ± 15% had been exported from the mixed layer as organic N by time of sampling. Our N isotope-derived f-ratio is higher than the available incubation-based summertime f-ratio estimates measured at LCIS on the same cruise (≤0.5). This apparent discrepancy is likely due to the time scales over which the different methods integrate and the greater reliance of phytoplankton on regenerated nutrients later in the growing season. Nonetheless, our data suggest a high potential for carbon removal at LCIS, which we attribute largely to the effect of ice melt on stratification and iron supply. Carbon removal in the past can also be evaluated using the biological N cycle, with the $\delta^{15}N$ of buried organic matter representing a proxy for past biological pump strength, provided the nitrate assimilation isotope effect ($^{15}\varepsilon$) is well-constrained. We calculate a mean $^{15}\varepsilon$ near LCIS of 4.1 ± 0.7‰, which is slightly lower than previous (albeit limited) estimates from the Antarctic Zone but within the reported uncertainty. Along with showing that the present-day Weddell Sea adjacent to LCIS hosts a strong biological pump, this study provides a new estimate of $^{15}\varepsilon$ for the coastal Antarctic.

Acknowledgements

I wish to thank my supervisors, A/Prof. Sarah Fawcett and Prof. Adam West for their continual, unwavering support on the journey of my M.Sc. thesis. Sarah, I would not be the scientist I am today without your profound investment in my success and patience in the face of my idiosyncratic writing. You have been instrumental in shaping the way I engage with and present my scientific work. Adam, I deeply value your rigorous reason-based approach to being. Your advice, guidance and perspective have kept me grounded, helping me prioritize and keep focused on that which really matters throughout this journey. I would further like to extend my deepest thanks to the Mandela Rhodes Foundation for the radical impact they have had on me during this time. The community and human engagement they fostered during my time in residence will stay with me for the rest of my life and has had a profound influence on the way I engage, both with myself and my scientific work.

My deepest thanks go to the Fawcett and Altieri lab groups for collecting the samples whose data are presented in this thesis, Tahlia Henry for her work operating the CTD and cleaning its data, Raquel Flynn for coordinating the sample collection and analysing the PON concentration and $\delta^{15}N$, Raymond Roman for the nutrient concentration analysis, Shantelle Smith for the NH_4^+ $\delta^{15}N$ analysis, and Hermann Luyt for his discrete salinity sample analysis. I would additionally like to thank the captain, officers and crew of the R/V *SA Agulhas II* for their expertise in navigating and aiding in sample collection. My thanks further extend to the South African Department of Environmental Affairs (DEA) for the use of their vessel. Finally, I would like to thank the Mandela Rhodes Foundation, the Flotilla Foundation, the Weddell Sea Expedition 2019, the National Research Foundation South African National Antarctic Programme, and UCT Vice-Chancellor Future Leaders 2030 fund for their financial support.

Table of Contents

1 Introduction

The global ocean absorbs ~25% of the atmospheric CO_2 produced by humans, accounting for a removal of more than 2 PgC/yr (Friedlingstein et al., 2022; Watson et al., 2020). Through the solubility and biological pumps, this CO_2 is injected into the deep ocean where it is stored for hundreds to thousands of years (Khatiwala et al., 2012). The solubility pump operates through thermodynamics and physical mixing (Toggweiler et al., 2003), with increased solubility of CO_2 at colder temperatures. The biological pump, on the other hand, refers to the mechanism by which photosynthetically-produced organic matter sinks out of the sunlit surface layer (the "euphotic zone") to be remineralised at depth (Volk & Hoffert, 1985).

The Southern Ocean is an important region for both the solubility and biological pumps, characterised by cold surface temperatures and incomplete consumption of surface nutrients by phytoplankton. Incomplete surface nutrient consumption is driven by iron and light limitation (Coale et al., 1996; Martin et al., 1990; Martin & Fitzwater, 1988; Mitchell et al., 1991; Sunda & Huntsman, 1997), and represents a missed opportunity for CO_2 removal by the biological pump (Sarmiento & Toggweiler, 1984; Sigman & Boyle, 2000). Ice shelves can aid in reducing both light and iron limitations through their supply of meltwater. Meltwater helps stratify the water column, reducing light limitation, and supplies iron to the surface ocean, directly through the input of dissolved iron in meltwater, and indirectly by influencing the coastal circulation, which can assist in transporting iron-rich deep waters to the surface (Arrigo et al., 2015; Dinniman et al., 2020; Klunder et al., 2014; St-Laurent et al., 2017). Ice shelves can, thus, facilitate a greater degree of nutrient drawdown and a stronger biological pump in the waters adjacent to them (Hoppema et al., 2000; Jennings et al., 1984). In addition, through interactions with sea ice and ice shelves, the Southern Ocean is the source region for some of the world's densest waters, with these waters equilibrating with the atmosphere prior to subducting (Muench & Gordon, 1995; Talley et al., 2011).

Future warming, however, is threatening the stability of ice shelves, with modelling studies showing that Larsen C Ice Shelf (LCIS) is particularly vulnerable to disintegration at an atmospheric warming of 4^{o}C (Gilbert & Kittel, 2021). This warming, in conjunction with the calving of a ~6000 km^2 iceberg (A-68) from LCIS in July 2017, the collapse of the Prince Gustav and Larsen A ice shelves in 1995, and the collapse of Larsen B ice shelf in 2002, indicate the possibility of a further major collapse in the near future (Etourneau et al., 2019).

LCIS is a known formation site of the parent waters to Antarctic Bottom Water (AABW) (Kerr et al., 2018; Nicholls et al., 2004; van Caspel et al., 2015), the deepest, densest water mass found throughout much of the world's oceans. Were LCIS to disintegrate, not only would it impact the formation of AABW, but it would have wide-ranging consequences for both the solubility and biological pumps in the region. Due to the harsh ice conditions surrounding LCIS, only two direct studies have been conducted on the strength of the regional biological pump (Flynn et al., 2021; Hoppema et al., 2000), with neither making use of natural abundance isotope ratios to investigate the nitrogen and carbon cycles. In order to provide a new, independent estimate of the biological pump strength for the region, we report the concentration and nitrogen isotopes of nitrate + nitrite (NO_3^-+NO_2^-), particulate organic nitrogen (PON), and ammonium (NH_4^+), as well as the oxygen isotopes of NO_3^-+NO_2^- for samples collected throughout the water column from 16 stations adjacent to LCIS in January (i.e., austral summer) of 2019 during the Weddell Sea Expedition (WSE).

2 Literature review

2.1 Southern Ocean circulation and water masses

The Southern Ocean is found around the Antarctic continent up to approximately 30ºS, in the most inclusive definition (Chapman et al., 2020; Talley et al., 2011). This circumpolar ocean, which connects the Atlantic, Indian and Pacific Ocean basins, is dominated by the Antarctic Circumpolar Current (ACC), which encircles the globe and is formed through the changing wind fields of the Antarctic (Talley et al., 2011). The Southern Ocean can be divided into several zones. Furthest north, the Subantarctic Zone (SAZ) is found between the Subantarctic Front and Subtropical Front, between 42ºS and 52ºS (Talley et al., 2011). This is a region of Antarctic Intermediate Water and Subantarctic Mode Water (SAMW) formation. Further south, one finds the Antarctic Zone, which can be divided into the Open Antarctic Zone (OAZ), which is permanently ice-free, and the Polar Antarctic Zone (PAZ), which experiences seasonal sea-ice cover. The boundary between the OAZ and PAZ can be approximated by the northernmost extent of the winter sea ice, or the southernmost extent of Upper Circumpolar Deep Water (Orsi et al., 1994; Talley et al., 2011).

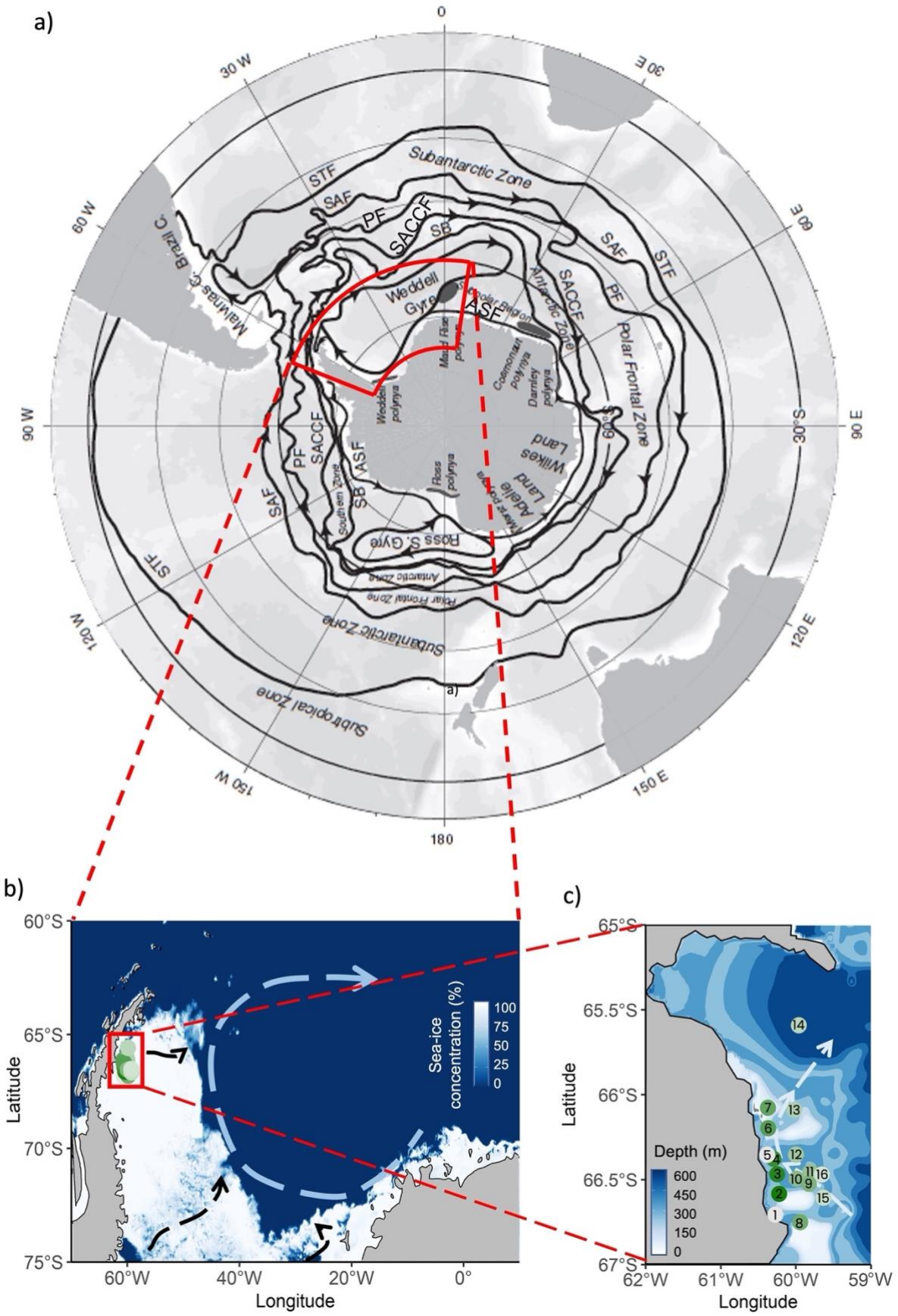

Fig. 2.1: Oceanographic circulation of (a) the Southern Ocean, (b) the Weddell Gyre, and (c) the waters adjacent to Larsen C Ice Shelf (LCIS). In (a), the thin line that follows the continental slope represents the westward-

flowing Antarctic Slope Front (ASF). The eastward-flowing Antarctic Circumpolar Current (ACC) is composed of the Southern Boundary (SB), Southern ACC Front (SACCF), Polar Front (PF) and Subantarctic Front (SAF). The northern boundary of the Southern Ocean's oceanographic region is denoted by the Subtropical Front (STF) (Orsi et al., 1994). The major recurrent polynyas are represented by the dark grey patches. Panel (a) is taken from Descriptive physical oceanography, Chapter 13, page 438 (Talley et al., 2011). Panels (b) and (c) show stations sampled during the Weddell Sea Expedition of 2019 (green and grey dots, numbered in panel (c)). The general Weddell Sea circulation is depicted in (b) with the dashed blue arrow representing the Antarctic Slope Current and dashed black arrows showing the flow of the parent water masses of Antarctic Bottom Water (Gordon et al., 1993; Schodlok et al., 2002; Schröder et al., 2002). In (b), shading represents sea ice concentration from 31 January 2020 (taken from ftp://ftp-projects.cen.uni-hamburg.de/seaice/AMSR2/3.125km) while in (c), shading shows bathymetry (ETOPO1 – NOAA National Geophysical Data Center, 2009) with the hypothesised local circulation shown by the dashed light blue arrow (Hutchinson et al., 2020; Nicholls et al., 2004).

The Weddell Sea, on the eastern side of the Antarctic Peninsula, is characterised by a large-scale clockwise circulation pattern forming the Weddell Gyre (Fig. 2.1). Regional water masses, defined by their temperature and salinity ranges, are formed and transformed through interactions with ice shelves and the atmosphere. Circumpolar Deep Water of the ACC enters the Weddell Sea at approximately 30°E and is renamed to Warm Deep Water (WDW) (Deacon, 1979; Orsi et al., 1994; Robertson et al., 2002; Weppernig et al., 1996). WDW forms a temperature and salinity maximum a few hundred meters below the surface, cooling and forming modified warm deep water (MWDW) as it progresses through the gyre by mixing with colder waters (Gordon, 1998; Robertson et al., 2002; Schröder & Fahrbach, 1999; Weppernig et al., 1996). In winter, near the LCIS and Filchner-Ronne Ice Shelf, Antarctic Surface Water (ASW) interacts with the atmosphere and ice shelves. It cools, becomes more saline, and loses buoyancy through the formation of marine ice, leading to the development of High Salinity Shelf Water (HSSW) (Hutchinson et al., 2020; Lange et al., 1990; Nicholls et al., 2009, 2012). The wind-driven offshore export of fresh water as sea ice from the ice front polynyas on the continental shelf leaves cold, saline HSSW behind (Haumann et al., 2016; Nicholls et al., 2009). The dense, cold, saline HSSW circulates beneath the ice shelf (Fig. 2.2), interacting with it and resulting in high basal melting due to the depression of the freezing point of water at high pressure (Fofonoff & Millard, 1983; Nicholls et al., 2009; Rignot et al., 2013). This interaction leads to the formation of less dense Ice Shelf Water (ISW), which has a potential temperature below the surface freezing point (Nicholls et al., 2009, 2012). Once ISW exits the ice shelf cavity and is advected down the continental slope, approximately 80% of it mixes with WDW or MWDW, forming Weddell Sea Deep Water (WSDW), which can be further mixed in the Scotia Sea to the north of the Antarctic Peninsula to form Antarctic Bottom Water (AABW) (Robertson et al., 2002; Weppernig et al., 1996). During winter, the relatively fresh ASW cools and increases its salinity due to sea-ice formation, resulting in a 100-200 m thick

surface mixed layer of Winter Water (WW) (Nicholls et al., 2009). During summer, the surface WW is diluted by meltwater, transforming it back to ASW, although WW can still be detected 50-100 m below the surface as a temperature minimum layer (Nicholls et al., 2009; Weppernig et al., 1996).

Due to the remote location of LCIS, very little is known about its regional circulation. Existing literature suggests MWDW is advected onshore towards the ice shelf along the north-facing slope of the Jason Trough (Nicholls et al., 2004), a remnant depression in the continental shelf caused by the flow of a paleo-ice stream. Here, MWDW is suggested to cool through mixing with shelf water masses such as ISW (Hutchinson et al., 2020).

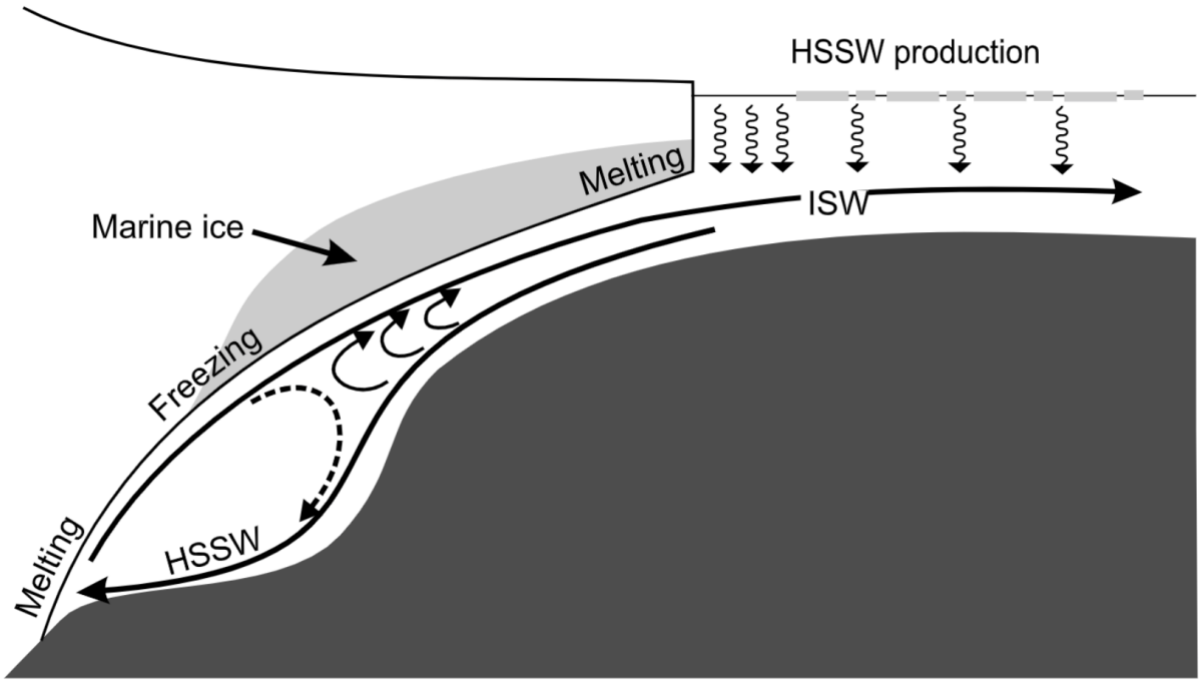

Fig. 2.2: Schematic of melting and freezing in a cold cavity ice shelf that leads to high rates of basal melting. High Salinity Shelf Water (HSSW) and Ice Shelf Water (ISW) circulation is represented on the diagram. Figure from Nicholls et al., (2009).

2.1.1 The importance of ice shelves

But let's take a step back, what are ice shelves? As land-bound ice sheets and glaciers flow into the ocean, they form ice shelves – large tongues of floating ice that have detached from the ground beneath. Antarctic ice shelves make up approximately 75% of the coastline of the continent and cover 1.5 million km^2, about 11% of the continents total area (Rignot et al., 2013). Ice shelves are fed by grounded continental ice sheets, surface accumulation due to

snowfall, and freezing of marine ice on their underside, while they are ablated through melting and the calving of icebergs (Nicholls et al., 2009; Rignot et al., 2013).

Ice shelves act to buttress the land-bound ice upstream, stabilising its discharge into the ocean (Dupont & Alley, 2005; Etourneau et al., 2019; Liu et al., 2015; Pritchard et al., 2012). Ice shelf thinning and grounding line retreat, which reduce the lateral and basal traction of the ice shelf respectively, decrease this buttressing effect, allowing for an accelerated seaward flow of land-bound ice (Shepherd et al., 2004). This accelerated flow leads to thinning of the grounded ice sheets upstream, while the increased discharge into the ocean results in global sea level rise (Dupont & Alley, 2005; Shepherd et al., 2004).

Physical ice shelf-ocean interactions are further vital for the formation of ISW (Nicholls et al., 2009, 2012), a precursor of AABW. As a result, understanding the processes that occur near the shelf break helps us understand the initial conditions of these dense water masses, and indicates that any CO_2 contained in these waters is likely to be advected down the continental slope and stored at depth. It is thus important to characterise and quantify the biological processes and determine the strength of the biological pump in ice-shelf-adjacent waters, as they will, in part, determine the chemical composition of these source waters.

2.2 Estimating the strength of the biological pump and export flux

The strength of the biological pump is directly related to net community production (NCP), the difference between net primary production (NPP) and respiration in the euphotic zone (Emerson, 2014). NCP is represented by the export flux, the fraction of NPP that escapes surface remineralisation and is exported into the deep ocean. Organic matter is exported through three main processes; the sinking of organic particles, the mixing down of dissolved organic carbon (DOC), and transport by animals (Emerson, 2014).

Annual net community production (ANCP; NCP over the annual cycle) is limited by the rate of supply of preformed nutrients (as opposed to regenerated nutrients, see section 2.2.2 below) such as nitrogen, phosphorus, and iron to the surface ocean and the efficiency with which they are taken up by phytoplankton and exported back to deeper waters (Emerson, 2014; Eppley &

Peterson, 1979). This efficiency of export is in part determined by the rate at which organic material sinks, (Armstrong et al., 2002; Francois et al., 2002; Henson et al., 2012; Klaas & Archer, 2002), as well as the mean respiration depth. Deeper respiration leads to increased drawdown of atmospheric ρCO_2 (Kwon et al., 2009), with the compensation depth – the depth where net organic matter production gives way to net respiration – depending on light penetration and nutrient availability. Below the compensation depth, the rate of respiration decreases exponentially as evidenced by both the oxygen utilization rate (Jenkins, 1998; Martz et al., 2008; Stanley et al., 2012) and direct measurements of the organic carbon flux captured in sediment traps, which collect less sinking organic matter at depth (Buesseler & Boyd, 2009; Martin et al., 1987). For ANCP, the depth of the base of the wintertime mixed layer is vital, as organic matter respired above this depth will be returned to the surface during winter mixing (Körtzinger et al., 2008). In some cases, however, the winter mixed layer is not fully ventilated (Emerson, 2014; Stanley et al., 2012), complicating the choice of the depth below which organic matter can be considered sequestered.

2.2.1 How do we measure ANCP

The strength of the biological pump has previously been estimated using global climate models, satellite products, sediment traps, and the mass balances of nitrate (NO_3^-), oxygen (O_2) and the stable carbon isotopes of dissolved inorganic carbon (Emerson, 2014 and references therein). Satellite products yield a measure of ANCP by relating ocean colour and particle backscatter to infer NPP (eg: Behrenfeld et al., 2005; Behrenfeld & Falkowski, 1997; Westberry et al., 2008), which is then multiplied by the euphotic zone respiration efficiency (NCP : NPP) derived from observations and models (Dunne et al., 2005, 2007; Emerson, 2014; Laws et al., 2000). Direct flux measurements, such as from sediment traps, can provide a measure of the sinking particle flux but fail to capture the DOC and animal transport fluxes, which can be significant in some regions, resulting in an underestimation of ANCP (Emerson, 2014). Biogeochemical proxies can help to solve this problem by inferring surface carbon export through examining dissolved chemical species, a technique that captures all modes of export flux. This technique is not perfect, however, as it often requires applying a mass balance approach to the surface ocean and assuming the ratio at which different elements occur in biological matter (Anderson, 1995; Hedges et al., 2002; Redfield et al., 1963).

Examining NO_3^- mass balance specifically, Johnson et al. (2017) estimated ANCP for the Southern Ocean using Southern Ocean Carbon and Climate Observations and Modeling (SOCCOM) float data. The authors compared the highest mixed-layer NO_3^- concentrations measured in winter with the lowest concentrations of summer and by assuming mass balance and integrating to a depth below the summertime mixed layer, estimated the amount of N removed from the surface ocean during the summer growth period. Subsequently, they converted this N export into an amount of carbon using the Redfield ratio of 106 C : 16 N, ultimately providing an ANCP estimate for the Southern ocean as a whole of between 1-4 mol C / m^2 / yr, with the highest estimates found between 40 and 50°S. This technique assumes that preformed NO_3^- is the only source of 'new' N to the euphotic zone (section 2.2.2 below), implying that there is no surface di-nitrogen (N_2) fixation which would add additional 'new' N to the surface ocean. Assuming negligible rates of N_2 fixation is fair for the Southern Ocean given the incomplete surface N drawdown and cold temperatures observed (Holl & Montoya, 2005; Knapp et al., 2012; Staal et al., 2003). Additionally, this technique assumes that very little N remains in the winter mixed layer as particulate organic nitrogen (PON), dissolved organic nitrogen (DON), ammonium (NH_4^+) or nitrite (NO_2^-). Regardless of these assumptions, the Johnson et al. (2017) estimates fall within the range of ANCP derived by other techniques, with satellite and model derived ANCP estimates falling between 0.5 and 5 mol C / m^2 / yr (Bopp et al., 2001; Dunne et al., 2007; Emerson (2014) and references therein, Laws et al., 2011; Munro et al., 2015). As mentioned earlier, this ANCP equates to the export of new or preformed (as opposed to regenerated) nutrients from the surface ocean.

2.2.2 New and regenerated production

New production is phytoplankton growth supported by nitrogen (N) sources that are 'new' to the euphotic zone (e.g., NO_3^- mixed up from the subsurface) while regenerated production refers to phytoplankton growth on recycled N forms (e.g., ammonium (NH_4^+) and urea) (Dugdale & Goering, 1967; Eppley & Peterson, 1979). On an annual basis, new production must be balanced by the export of organic matter from the euphotic zone (i.e., export production). As such, the rate of NO_3^- consumption by phytoplankton can be used as an estimate for carbon export potential, provided that euphotic zone nitrification (which yields regenerated NO_3^-) is minimal (Clark et al., 2008) and that carbon and N are incorporated into biomass in a known ratio (Johnson et al., 2017, 2022; Redfield et al., 1963).

The ratio of new to total production is often reported as the f-ratio (shorthand for "flux ratio"; Eppley & Peterson, 1979), with a higher f-ratio indicating a system primarily supported by new production with a high carbon export potential, while lower f-ratios indicate increased reliance on regenerated production with lower export potential. The f-ratio has previously been estimated using ^{15}N-tracer uptake rate experiments (e.g., Asper & Smith, 1999; Elskens et al., 2002; Mdutyana et al. 2020; Flynn et al., 2021) and stable N isotopes (e.g., Fawcett et al., 2011). Previous open Southern Ocean estimates of the f-ratio fall between 0.08 and 0.78, with the majority falling at the lower end of this range (Elskens et al., 2002; Mdutyana et al., 2020). By contrast, the highly productive ice-shelf-adjacent waters generally have a higher f-ratio, with previous estimates from incubation experiments indicating an f-ratio ranging from 0.44 to 0.89 for the Ross Sea (Asper & Smith, 1999) and 0.47 ± 0.08 for the waters adjacent to LCIS in the western Weddell Sea (Flynn et al., 2021). These estimates indicate that the ice shelf break hosts a greater degree of new production, and thus a stronger biological pump, in comparison to the open Southern Ocean. The f-ratio of the Southern Ocean has so far not been estimated using stable N isotopes.

2.3 N isotopes in the ocean

2.3.1 Kinetic isotope effect:

NO_3^- is comprised of N and O atoms, where N has two stable isotopes (^{14}N and ^{15}N), and O has three (^{16}O, ^{17}O and ^{18}O). N exists primarily as ^{14}N (99.63%), with 0.36% existing as ^{15}N, while the majority of O on Earth exists as ^{16}O (99.76%), with ^{18}O making up 0.20% and ^{17}O the remaining 0.04% (Rohling, 2013; Sigman & Fripiat, 2019). The measured ratios of these isotopes are reported in delta notation (in parts per thousand (per mille, ‰), Eq 2.1), as δ^{15}N vs atmospheric N_2 for N and δ^{18}O vs Vienna Standard Mean Ocean Water (VSMOW) for O.

$$\delta X_{sample} = \left(\frac{R_{sample} - R_{standard}}{R_{standard}}\right) \cdot 1000 \qquad \text{Eq 2.1}$$

Here, X represents the heavy isotope, while R represents the heavy/light ratio of any two isotopes (e.g., X = ^{15}N and R = ^{15}N/^{14}N for δ^{15}N, while X = ^{18}O and R = ^{18}O/^{16}O for δ^{18}O). A positive δX_{sample} indicates a sample that is enriched in the heavy isotope relative to the standard, while a negative δX_{sample} indicates a depletion in the heavy isotope. The heavy and

light isotopes of NO_3^- are discriminated by physical, chemical, and biological processes (Casciotti, 2016). In most biogeochemical reactions, the reaction rate of the substrate bearing the light isotope (^{14}N or ^{16}O) is slightly higher than that for the same substrate with the heavy isotope (^{15}N or ^{18}O) (eg., Casciotti et al., 2003; Granger et al., 2004; Knapp et al., 2018; Mariotti et al., 1981; Sigman et al., 1999; Waser et al., 1998b). This results in the lighter isotope being preferentially consumed by biogeochemical reactions, leaving the substrate pool enriched in the heavy isotope. If first-order dependence on the substrate concentration characterises the unidirectional reaction rate, the kinetic isotope effect, ε, can be defined as $\varepsilon(‰) = ({}^{light}k/{}^{heavy}k - 1) \cdot 1000‰$**,** where k represents the unidirectional reaction rate of the light (^{14}N and ^{16}O) and heavy (^{15}N and ^{18}O) isotope, and ${}^{15}\varepsilon$ and ${}^{18}\varepsilon$ represent the isotope effect associated with the N and O isotopes, respectively (Mariotti et al., 1981).

If consumption of a reactant pool occurs with a constant isotope effect and the reactant pool is constantly supplied, partially consumed, and the residual pool exported, the steady-state model is most appropriate to describe the isotope dynamics (Eq 2.2a and Eq 2.2b; Fig. 2.3, green lines) (Sigman & Fripiat, 2019). Under the steady-state model, the delta values of the reactant ($\delta X_{reactant}$, Eq 2.2a, Fig. 2.3 solid green line) and product pools ($\delta X_{product}$, Eq 2.2b, Fig. 2.3 dashed green line) can be calculated, with X representing ^{15}N and ^{18}O for changes in $\delta^{15}N$ and $\delta^{18}O$ respectively, and f the degree of consumption of the reactant pool (Sigman & Fripiat, 2019).

$$\delta X_{reactant} = \delta X_{initial} + \varepsilon \cdot (1 - f) \qquad \text{Eq 2.2a}$$

$$\delta X_{product} = \delta X_{initial} - \varepsilon \cdot f \qquad \text{Eq 2.2b}$$

If, however, consumption proceeds with no significant nutrient resupply and with a constant isotope effect, the reaction is best described by the Rayleigh model (Fripiat et al., 2019; Mariotti et al., 1981; Sigman et al., 1999).

2.3.2 Rayleigh model

The Rayleigh model can be used to calculate the δX of the reactant pool (Eq 2.3a and Eq 2.3b, Fig. 2.3 solid black line), the instantaneous product (Eq 2.3c, Fig. 2.3 dot-dashed black line)

and the accumulated product (Eq 2.3d, Fig. 2.3 dashed black line) of the reaction in the case where consumption proceeds with minimal resupply and with a constant isotope effect (Mariotti et al., 1981).

$$\ln(\delta X_{reactant} + 1) = -\varepsilon \cdot \ln([reactant]) + \ln\left(\delta X_{reactant}^{initial} + 1\right) + \varepsilon \cdot \ln([reactant]_{initial}) \quad \text{Eq 2.3a}$$

Eq 2.3a (Fripiat et al., 2019) is a modified form of the reactant equation, with X representing ^{15}N and ^{18}O for the δ^{15}N and δ^{18}O of the reactant pool, respectively, $[reactant]$ the concentration of the reactant pool, and the sub/superscript "initial" representing the initial values of the reactant pool prior to consumption. Eq 2.3a can be approximated by Eq 2.3b, where f is the fraction of reactant remaining ($\frac{[reactant]}{[reactant]_{initial}}$).

$$\delta X_{reactant} = \delta X_{reactant}^{initial} - \varepsilon \cdot \ln(f) \quad \text{Eq 2.3b}$$

The difference between the δX of the Rayleigh reactant and its instantaneous product can be approximated by ε when ε <1000‰ (Eq 2.3c) (Mariotti et al., 1981).

$$\delta X_{instantaneous} = \delta X_{reactant} - \varepsilon \quad \text{Eq 2.3c}$$

The accumulated product, which represents the cumulative total δX removed from the reactant pool since consumption began, can be represented by Eq 2.3d (Mariotti et al., 1981).

$$\delta X_{accumulated} = \delta X_{reactant}^{initial} + \varepsilon \frac{f \cdot \ln(f)}{1-(f)} \quad \text{Eq 2.3d}$$

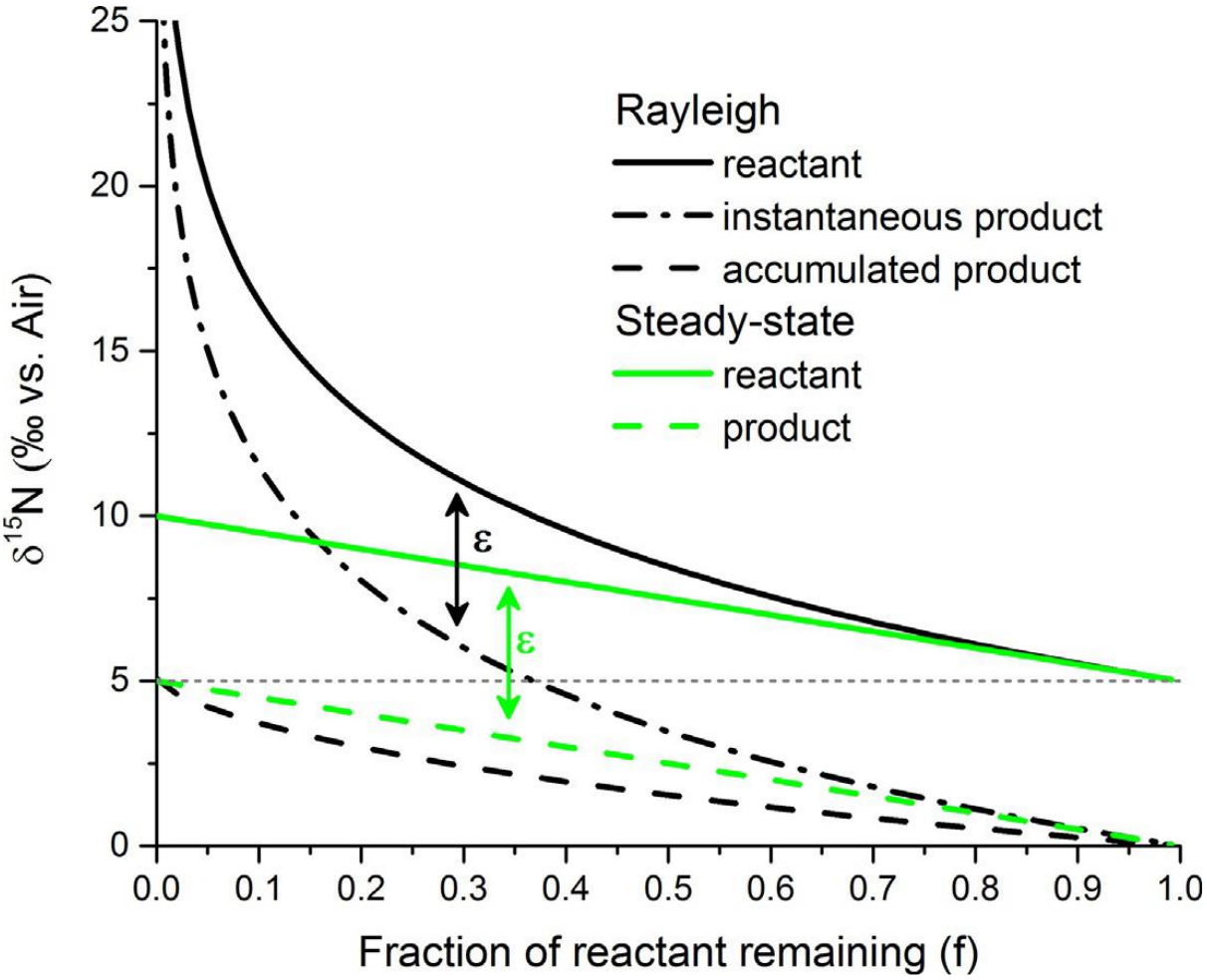

Fig. 2.3: Two theoretical models, the Rayleigh model (black) and steady-state model (green), show the changes in the N isotope ratios as a reactant pool is consumed by a single unidirectional reaction. f represents the fraction of the initial reactant concentration remaining. The Rayleigh model is appropriate for a closed pool with no nutrient resupply, while the steady-state model is appropriate in the case of continuous nutrient supply. The two models have been plotted using the same parameters, an initial $\delta^{15}N$ of 5‰ (represented by the horizontal dotted grey line) and an isotope effect ($^{15}\varepsilon$) of 5‰. The isotope effect, $^{15}\varepsilon$, approximates the difference between the initial $\delta^{15}N$ of the reactant and its product (instantaneous product for the Rayleigh model). Figure from Sigman & Fripiat, (2019).

Two key parameters in the Rayleigh model are the isotope effect (ε) and the initial δX of the reactant pool (Sigman et al., 1999).

2.3.3 Organic nitrogen sources and sinks:

2.3.3.1 Sources:

N_2 fixation, the primary process by which bioavailable N is added to the ocean system, is the process by which N_2 is converted to NH_4^+ by specialized phytoplankton called diazotrophs, which is subsequently consumed to form biomass (Burris, 1956). N_2 fixation ultimately leads

to the formation of biomass with a $\delta^{15}N$ between -2‰ and 0‰ (Carpenter et al., 1997; Delwiche et al., 1979; Hoering & Ford, 1959), which is low in comparison to the deep ocean NO_3^- $\delta^{15}N$ of ~5‰ (Fripiat et al., 2019, 2021; Sigman et al., 2000, 2009). Atmospheric N deposition and terrestrial runoff can also provide biologically available N to the surface ocean, where atmospheric deposition is associated with the input of low $\delta^{15}N$ N (-2.8‰ in the north Atlantic; Altieri et al. (2021) and references therein), while the $\delta^{15}N$ of river input is ~4‰ (Brandes & Devol, 2002 and references therein; Gaye-Haake et al., 2005), similar to that of deep ocean NO_3^-. The fluxes of atmospheric N deposition and riverine input are low (39 Tg N/year and 34 Tg N/year, respectively) compared to N_2 fixation (164 Tg N/year) and most strongly influence the coastal oceans (Jickells et al., 2017).

2.3.3.2 Sinks:

Denitrification, anammox, and burial at the seafloor are the primary processes responsible for the removal of biologically available N from the ocean. During burial, organic matter, and the $\delta^{15}N$ it has, is directly removed from the water column. Denitrification, which occurs in low oxygen environments where NO_3^- is used as an electron acceptor in lieu of O_2, preferentially consumes NO_3^- containing ^{14}N and ^{16}O with a strong isotope effect ($^{15}\varepsilon \approx {}^{18}\varepsilon$) of between 10‰ and 25‰ (Granger et al., 2008; Kritee et al., 2012). This isotope effect is likely associated with the NO_3^- reduction step within the denitrifier cell, with unconsumed high-$\delta^{15}N$ internal NO_3^- effluxing out from the cell and allowing for the expression of the enzyme-level isotope effect in the surrounding water column (refer to section 2.3.4 below). Water column denitrification in oxygen-deficient zones occurs with the (near-) full expression of the denitrification isotope effect (Altabet et al., 1999; Brandes et al., 1998; Cline & Kaplan, 1975; Liu & Kaplan, 1989; Sigman et al., 2003; Voss et al., 2001). This leaves the remaining NO_3^- in the water column enriched in ^{15}N and ^{18}O, increasing its $\delta^{15}N$ and $\delta^{18}O$. Sedimentary denitrification results in almost complete NO_3^- consumption within the sediment pore waters. This high degree of consumption, coupled with minimal escape of isotopically-enriched residual NO_3^- to the overlaying water column, yields a low apparent isotope effect, on the order of 1.5‰ (Brandes & Devol, 1997, 2002; Lehmann et al., 2007). The N isotope effects of anammox are similar to that of denitrification and are thus likely well represented by canonical denitrification (Brunner et al., 2013).

Deep ocean NO_3^-, which has a $\delta^{15}N$ of ~5‰, develops this signal through a balance between N_2 fixation and denitrification, the ultimate primary source and sink of biologically available N. N_2 fixation adds low $\delta^{15}N$ to the system, water column denitrification preferentially removes low $\delta^{15}N$ N, and sedimentary denitrification removes N with little preference expressed in the water column. As water column denitrification removes N with a $\delta^{15}N$ lower than that added by N_2 fixation, it drives up the $\delta^{15}N$ of the N remaining in the ocean. Internal N cycling is responsible for the distribution of isotopes among the different N pools but does not influence the total $\delta^{15}N$ of the ocean.

2.3.4 NO_3^- assimilation:

During the assimilation of NO_3^- by phytoplankton, ^{14}N and ^{16}O are preferentially consumed (Granger et al., 2004; Montoya & McCarthy, 1995; Sigman et al., 1999, 2000; Wada & Hattori, 1978). Laboratory studies have shown a wide range of N and O NO_3^- assimilation isotope effects ($^{15}\varepsilon$ and $^{18}\varepsilon$ respectively), ranging from 0-20‰, with most estimates converging around 5‰ (Granger et al., 2004, 2010; Karsh et al., 2012, 2013; Needoba & Harrison, 2004). This isotopic fractionation leaves the unconsumed NO_3^- enriched in ^{15}N and ^{18}O (Casciotti et al., 2002; Sigman et al., 1999). Granger et al. (2004) found a strong coupling between the relative change in the $\delta^{15}N$ and $\delta^{18}O$ of NO_3^- during assimilation, with $^{15}\varepsilon \approx {}^{18}\varepsilon$, regardless of the magnitude of the isotope effect, culture conditions or species, a finding corroborated and slightly complicated by later studies (Granger et al., 2010; Karsh et al., 2012, 2013). NO_3^- assimilation by phytoplankton, as in plants, takes place through several steps (Fig. 2.4); first, the NO_3^- is transported into the cell by cell surface active transporters. The NO_3^- is then reduced to NO_2^- by the assimilatory nitrate reductase (NR) enzyme in the cytoplasm (reviewed by Tischner, 2000). Subsequently, the NO_2^- is reduced to NH_4^+ by nitrite reductase in the chloroplasts, where this NH_4^+ is then incorporated into amino acids (reviewed by Tischner, 2000). The rate-limiting step of NO_3^- assimilation appears to be the reduction of NO_3^- to NO_2^-, catalysed by the NR enzyme (Berges & Harrison, 1995). This is supported by the fact that NO_2^- rarely accumulates within the cell, indicating that the steps following NO_3^- reduction are unlikely to limit assimilation. Millimolar concentrations of NO_3^- can accumulate in the cells of certain algal strains, reportedly to maximise the activity of the NR enzyme (Granger et al., 2004; Karsh et al., 2013; Needoba et al., 2004; Needoba & Harrison, 2004).

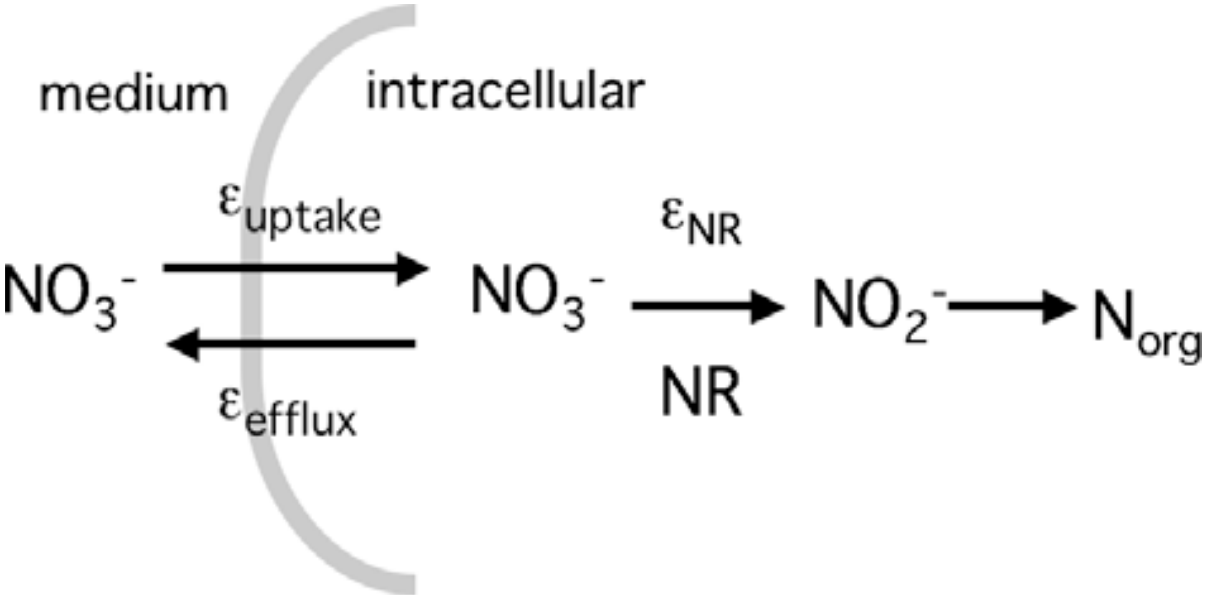

Fig. 2.4: Schematic representation of how unicellular algae fractionate NO_3^- isotopes during assimilation (Granger et al., 2004; Karsh et al., 2013). NO_3^- reduction by the nitrate reductase (NR) enzyme is the rate-limiting and first irreversible step during NO_3^- assimilation. NR involves catalytic bond breaking, which imparts an enzymatic isotope effect ($^{15}\varepsilon_{NR} = {}^{18}\varepsilon_{NR} = 26.6 \pm 0.2‰$ (Karsh et al., 2012)) that fractionates the N and O isotopes equally, leading to a $\Delta\delta^{18}O : \Delta\delta^{15}N$ of ~1. The resulting ^{15}N- and ^{18}O-enriched internal NO_3^- pool can be expressed in the surrounding medium by the efflux of NO_3^- from the cell. NO_3^- transport (uptake and efflux) imparts smaller isotope effects of $^{15}\varepsilon_{uptake} = 2.0 \pm 0.3‰$, $^{15}\varepsilon_{efflux} = 1.2 \pm 0.4‰$, and $^{18}\varepsilon_{uptake} = {}^{18}\varepsilon_{efflux} = 2.8 \pm 0.6‰$ (Karsh et al., 2013).

Intracellular NO_3^- $\delta^{15}N$ has been found to be elevated when compared to the external medium (Granger et al., 2004; Needoba et al., 2004; Needoba & Harrison, 2004). Karsh et al. (2013) showed the N and O isotope effects associated with the transport of NO_3^- into (uptake) and out of (efflux) the cell are low with $^{15}\varepsilon_{uptake} = 2.0 \pm 0.3‰$, $^{15}\varepsilon_{efflux} = 1.2 \pm 0.4‰$, and $^{18}\varepsilon_{uptake} = {}^{18}\varepsilon_{efflux} = 2.8 \pm 0.6‰$. The NR enzyme, however, appears to impart an isotope effect of $^{15}\varepsilon_{NR} = {}^{18}\varepsilon_{NR} = 26.6 \pm 0.2‰$ (Karsh et al., 2012), preferentially reducing ^{14}N and ^{16}O, lowering the $\delta^{15}N$ of the organic matter produced, and increasing the $\delta^{15}N$ of the remaining internal NO_3^- pool (Granger et al., 2004; Needoba & Harrison, 2004). The only way for the isotope effect of NR to be the primary driver of the cellular level isotope effect (i.e., that expressed in the environment), however, is for there to be significant efflux of NO_3^- from the cell (Granger et al., 2004). This efflux would allow for a portion of the internal high-$\delta^{15}N$ NO_3^- pool to be expressed in the environment. This idea seems counterintuitive given the fact that energy is spent during NO_3^- transport, making the efflux of NO_3^- appear detrimental to the cell. Further, it is unclear whether the efflux of NO_3^- is a result of passive leakage or a strictly controlled reverse flow. If passive leakage were responsible for the efflux of NO_3^- from cells, smaller cells, which have a larger cell surface area-to-volume ratio than larger cells, should efflux a larger proportion of their NO_3^- and thus be associated with a higher isotope effect (Granger et

al., 2004). However, no relationship is seen between the magnitude of the isotope effect and differences in cell volume (either within or among species) (Granger et al., 2004), indicating that cells control the balance between NO_3^- uptake, enzymatic NO_3^- reduction, and cellular efflux (Granger et al., 2010).

$$ {}^{X}\varepsilon_{organism} = {}^{X}\varepsilon_{uptake} + R\left({}^{X}\varepsilon_{NR} - {}^{X}\varepsilon_{efflux}\right) \quad \text{Eq 2.4} $$

The equation above relates the expressed organism isotope effect to the ratio of efflux : uptake (R), as well as to the uptake, enzymatic, and efflux isotope effects. X represents 15 or 18, for the changes to δ^{15}N and δ^{18}O, respectively.

Needoba et al. (2004) found that the intracellular NO_3^- pool has a higher concentration and δ^{15}N than the surrounding medium. Given that both ${}^{X}\varepsilon_{\text{uptake}}$ and ${}^{X}\varepsilon_{\text{NR}}$ have a positive isotope effect (they increase the δ^{15}N of the source pool and lower that of the product pool), the high δ^{15}N of the intracellular NO_3^- pool indicates that in a steady state case where there is no efflux (i.e., the rate of net uptake is equal to that of reduction), the isotope effect of NO_3^- reduction is greater than that associated with uptake. This further supports the idea that NO_3^- reduction is the primary fractionating step in the NO_3^- assimilation pathway, with the degree of efflux of the internal ^{15}N-enriched pool relative to the rate at which it is reduced accounting for variations observed in the cellular level isotope effect (Granger et al., 2010; Karsh et al., 2013). This explanation is also consistent with the observations that the ratio of $\Delta\delta^{15}$N : $\Delta\delta^{18}$O of the external NO_3^- pool, even over a wide range of N isotope effects, conforms to 1 : 1 (Granger et al., 2004). As different processes are likely to impart differing ratios of fractionation to N and O (i.e., different ${}^{15}\varepsilon$: ${}^{18}\varepsilon$ ratios), the consistency of the $\Delta\delta^{15}$N : $\Delta\delta^{18}$O ratio suggests that the ^{15}N and ^{18}O enrichment of the external NO_3^- is driven by a single process (Granger et al., 2004).

The rate of cellular NO_3^- efflux in the open ocean appears to be low and consistent (Granger et al., 2004), as evidenced by the relatively low organism-level isotope effects relative to the NR isotope effect (e.g., Altabet & Francois, 2001; DiFiore et al., 2006, 2009, 2010; Fripiat et al., 2019; Karsh et al., 2003; Sigman et al., 1999). In culture experiments, light limitation has been found to increase NO_3^- efflux from cells, thereby leading to a greater expression of the enzyme level isotope effect (Needoba & Harrison, 2004). Under light limitation, a decrease in the activity of the NR enzyme, and thus NO_3^- reduction rate, without a corresponding decrease in

the NO_3^- uptake rate, leads to the accumulation of a large intracellular NO_3^- pool (as has been found for some diatom species). This can ultimately lead to a greater fraction of the imported NO_3^- being effluxed back into the external pool (Needoba & Harrison, 2004). Cells are hypothesised to accumulate NO_3^- during light limitation in preparation for rapid growth should that limitation be suddenly lifted. Such rapid changes in light availability can occur in the turbulent open ocean (DiFiore et al., 2010; Needoba & Harrison, 2004). Changes in other culture conditions, such as iron limitation, mixing (which increased growth rate but not $^{15}\varepsilon$), temperature, and cell volume do not appear to have a strong or consistent impact on the rate of NO_3^- efflux from the cells and thus on the expressed isotope effect (Granger et al., 2004; Needoba & Harrison, 2004).

Granger et al. (2010) found that three cultivated cyanobacteria strains express an $^{15}\varepsilon$ and $^{18}\varepsilon$ <5‰. This is a restricted range when compared to eukaryotes, which express an $^{15}\varepsilon$ and $^{18}\varepsilon$ that ranged from 5-8‰. It is suggested that vacuoles within eukaryote cells could be used to store internal NO_3^-, thereby allowing NO_3^- uptake to continue and a large intracellular pool to accumulate during times of limited NO_3^- reduction (Needoba & Harrison, 2004). This would allow for increased efflux, and thus, a greater expression of the NR isotope effect. Prokaryotes, which lack vacuoles, may therefore need to impose a stricter balance between NO_3^- uptake and reduction, resulting in greater consistency in the efflux : uptake ratio, which could explain the narrower range of isotope effects observed in prokaryotes by Granger et al. (2010).

In the case where there is no NO_3^- efflux from the cell (R=0 in Eq 2.4), the first irreversible step in NO_3^- assimilation would be NO_3^- uptake, which would then be the only step that could impart an isotope effect on the surrounding medium (Granger et al., 2010). NO_3^- transport is associated with a small isotope effect, with $^{15}\varepsilon_{\text{uptake}} < {}^{18}\varepsilon_{\text{uptake}}$ (Karsh et al., 2013), meaning the O atoms of NO_3^- experience greater fractionation than the N atoms during transport. This means as the proportional influence of NO_3^- uptake increases ($R \ll 1$ in Eq 2.4), we expect a decoupling in the 1 : 1 ratio of O versus N isotope effects (Granger et al., 2010; Karsh et al., 2013). This mechanism was invoked by Granger et al. (2010) to explain their observed $\Delta\delta^{18}O : \Delta\delta^{15}N$ of ~2 in heterotrophic prokaryotes, which expressed an organism N isotope effect as low as 0.4‰. The authors suggested that this low value indicates minimal expression of the nitrate reductase isotope effect caused by minimal NO_3^- efflux. The isotope effect associated with transport (into the cell) was thus proposed to be the primary contributor to the isotope

effect expressed at the organism level (Granger et al., 2010). As transport has a very small isotope effect in comparison to NO_3^- reduction, it will only be observed when cellular efflux is minimal (i.e., the organism-level isotope effect is low). Thus, if assimilation is the only process acting on the NO_3^- pool, deviations from the $\Delta\delta^{18}O : \Delta\delta^{15}N$ of 1 are only detectable when the organism-level isotope effect is very low ($^{15}\varepsilon \approx 2‰$, (Karsh et al., 2013)). The isotope effect associated with the entire phytoplankton community likely reflects the weighted average of the isotope effects of all NO_3^--using species. Thus, at the isotope effects generally measured in the surface ocean (~5‰, DiFiore et al., 2009; Fripiat et al., 2019; Sigman et al., 1999), the transport isotope effects are too low to detectibly alter the observed $\Delta\delta^{18}O : \Delta\delta^{15}N$ (Granger et al., 2010).

Denitrification fractionates the ^{15}N and ^{18}O of NO_3^- equally with an isotope effect expressed in the environment of between 10 and 25‰ (Granger et al., 2008; Kritee et al., 2012). This suggests that the $\Delta\delta^{18}O : \Delta\delta^{15}N$ ratio of 1 : 1 observed during NO_3^- assimilation may be intrinsic to the reduction of NO_3^-. The higher organism-level isotope effect of denitrifiers may be explained if they permit NO_3^- to rapidly efflux from their cells ($R \approx 1$, Eq 2.4), thereby allowing for the isotope effect associated with the NR enzyme to be nearly fully expressed (Granger et al., 2004). Marine denitrifiers may exhibit this more open system behaviour because ambient NO_3^- concentrations are generally high in regions where denitrification is favoured, thereby decreasing the competitive advantage of NO_3^- storage (Granger et al., 2004, 2008)

2.3.4.1 Degree of NO_3^- consumption

Partial consumption of the water column NO_3^- pool by phytoplankton, as observed in the Southern Ocean, occurs where growth is limited by light (Mitchell et al., 1991) and/or iron (Martin et al., 1990). As phytoplankton preferentially consume ^{14}N and ^{16}O, the remaining unconsumed NO_3^- pool is enriched in ^{15}N and ^{18}O, increasing the $\delta^{15}N$ and $\delta^{18}O$ of water column NO_3^-. Within the framework of the Rayleigh model (Fig. 2.3, black lines), under partial NO_3^- consumption ($0<f<1$), the accumulated particulate organic nitrogen (PON) biomass will have a $\delta^{15}N$ that is lower than that of the NO_3^- originally supplied to the mixed layer. The $\delta^{15}N$ of the PON varies as a function of the degree of NO_3^- consumption, for as the supplied NO_3^- is consumed, the remaining pool becomes progressively more enriched in ^{15}N, increasing the $\delta^{15}N$ of newly formed (instantaneous) PON biomass (Sigman et al., 1999). As the NO_3^- pool

tends towards being completely consumed (f ≈ 0), the accumulated PON biomass $\delta^{15}N$ converges on the initial $\delta^{15}N$ of the NO_3^- supply (Sigman et al., 1999).

2.3.5 PON $\delta^{15}N$ set by source N consumed by phytoplankton

The $\delta^{15}N$ of PON is set by the $\delta^{15}N$ of the N consumed during biomass formation (Altabet, 1988, 1989; Fawcett et al., 2011, 2014; Lourey et al., 2003; Treibergs et al., 2014; van Oostende et al., 2017). Where NO_3^- is consumed to form PON, the $\delta^{15}N$ of the PON produced depends on the $\delta^{15}N$ of the NO_3^- supplied, the degree of NO_3^- consumption, and the $^{15}\varepsilon$ at which NO_3^- consumption occurs Mariotti et al., 1981; Sigman et al., 1999). Partial NO_3^- consumption is associated with the production of PON with a $\delta^{15}N$ lower than the NO_3^- supplied, while complete NO_3^- consumption leads to the formation of PON with a bulk $\delta^{15}N$ that is equal to the NO_3^- $\delta^{15}N$ supplied to the surface ocean. PON can also be formed through the consumption of recycled nutrients in the surface ocean, such as NH_4^+, which have a low $\delta^{15}N$ compared to the NO_3^- supplied to the surface ocean (<0‰; Checkley & Miller, 1989; Macko et al., 1986). The low $\delta^{15}N$ of recycled nutrients develops as a result of the ε associated with the degradation of PON, as well as the preferential export of high $\delta^{15}N$ from the surface ocean (see section 2.3.7 below (Altabet, 1988, 1989; Lehmann et al., 2002)). The knowledge that the $\delta^{15}N$ of the N source consumed determines the $\delta^{15}N$ of the PON produced has previously been used to study the sources of N to different size classes of phytoplankton (Fawcett et al., 2011, 2014; Treibergs et al., 2014). In the Sargasso Sea, a region that experiences complete surface NO_3^- consumption, prokaryotes have been shown to have a low $\delta^{15}N$, indicative of their reliance on recycled N forms, while eukaryotes have a higher $\delta^{15}N$, indicating a greater affinity for NO_3^- assimilation, though upon the depletion of NO_3^-, their $\delta^{15}N$ decreases as they become more reliant on recycled N forms (Fawcett et al., 2011, 2014; Treibergs et al., 2014). The $\delta^{15}N$ of PON in the Southern Ocean, which experiences incomplete surface NO_3^- consumption, can similarly be used to determine the N sources consumed by phytoplankton. In the early to midsummer Southern Ocean, PON $\delta^{15}N$ is primarily controlled by NO_3^- consumption, while late summer and winter PON $\delta^{15}N$ indicates a greater reliance on recycled N (Lourey et al., 2003; Smart et al., 2020).

2.3.6 Remineralisation

When phytoplankton die and decompose, their PON biomass is largely broken down into NH_4^+, which is then oxidised to NO_2^- and NO_3^- by nitrifying microorganisms. During this process, the N atoms that eventually form NO_3^- are sourced directly from the PON. Thus, the $\delta^{15}N$ of the newly-formed NO_3^- is dependent on the $\delta^{15}N$ of the PON being remineralised.

2.3.6.1 N isotope remineralisation signals

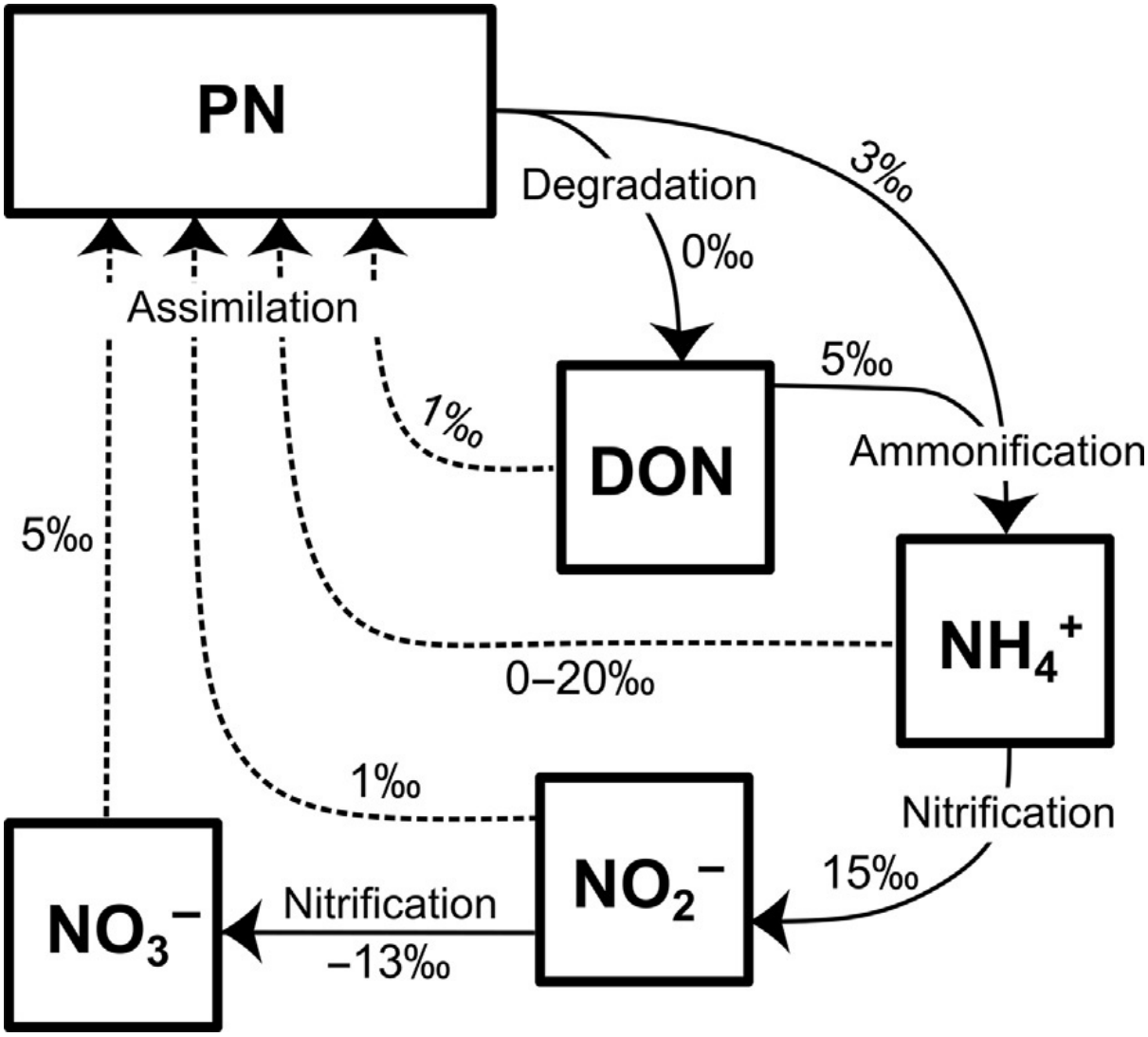

Fig. 2.5: Isotope effects ($^{15}\varepsilon$) associated with internal N cycling in the ocean. Dashed arrows represent assimilation into PON, while solid arrows represent the remineralisation process. For the NH_4^+ pool, complete consumption during nitrification in the ocean interior or assimilation in the surface leads to the associated isotope effects having little impact on the N isotope distributions. When NH_4^+ assimilation and nitrification co-occur, however, the $\delta^{15}N$ of the respective products, PON and NO_2^-, will be affected by the isotope effects. During nitrification, ammonia (NH_3) not ammonium (NH_4^+) is oxidised, yet NH_4^+ is the dominant form in the ocean. There is an isotope effect associated with NH_4^+ - NH_3 equilibrium, with the values presented here calculated for the consumption of NH_4^+ and thus taking this equilibrium into account. (Casciotti, 2009; Casciotti et al., 2003; Knapp et al., 2018; Möbius, 2012; Sigman & Fripiat, 2019; Vo et al., 2013; Waser et al., 1998). Figure from Sigman & Fripiat (2019).

In the case where the PON is completely remineralised and nitrified, as occurs below the euphotic zone, the $\delta^{15}N$ of the newly nitrified NO_3^- is equal to the $\delta^{15}N$ of the PON, regardless of the isotope effects imparted by the steps involved in remineralisation (Rafter et al., 2013). As such, the low-$\delta^{15}N$ NO_3^- that was removed from the NO_3^- pool and incorporated into PON during assimilation is returned to the water column, effectively reversing the NO_3^- $\delta^{15}N$ increase and NO_3^- concentration decrease associated with NO_3^- assimilation (DiFiore et al., 2009). Traditionally, nitrification was thought to only occur in the sub-euphotic zone, as nitrifying microorganisms are impeded by light (Guerrero & Jones, 1996a, 1996b; Hooper & Terry, 1974) and out-competed by NH_4^+ assimilating phytoplankton (Smith et al., 2014). This meant that one could assume that growth supported by the assimilation of NO_3^- (or N2 fixation) could be termed new production, growth supported from an N source that is external to the euphotic zone. If one were to then assume that the biomass in the euphotic zone is in a steady state, this biomass produced through externally sourced N (new production) would be available for export (Casciotti, 2016; Eppley & Peterson, 1979).

It, however, has been shown that nitrification can occur in the euphotic zone, particularly near its base or under conditions of deep mixing (e.g., Clark et al., 2008; Dore & Karl, 1996; Ward, 2005; Ward et al., 1989; Mdutyana et al. 2020; Wallschuss et al. 2022). This allows for the assimilation of regenerated NO_3^- in the euphotic zone, which would complicate the new production paradigm, as NO_3^- assimilation could no longer be equated to new production (Smart et al., 2015; Mdutyana et al. 2020; Yool et al., 2007). This calls for the use of a tracer that can identify remineralisation and reveal an assimilation signal that has been subsequently overprinted.

2.3.6.2 O isotope remineralisation signal

During remineralisation, the O atoms of the newly formed NO_3^- are sourced from both ambient seawater (H_2O) and dissolved oxygen (O_2). During nitrification of NH_4^+ to NO_2^-, one of the O atoms is sourced from the ambient H_2O, while the other is sourced from dissolved O_2 (Andersson & Hooper, 1983). The oxidation of NO_2^- to NO_3^- adds an O atom that is sourced from the ambient H_2O (Kumar et al., 1983). The addition of these O atoms occurs with an associated isotope effect, such that the $\delta^{18}O$ of the O atoms added depends not only on the $\delta^{18}O$ of the ambient H_2O and O_2, but also the isotope effect associated with their incorporation

(Boshers et al., 2019; Buchwald et al., 2012; Buchwald & Casciotti, 2010; Casciotti et al., 2010). In addition, it has been shown that the intermediate, NO_2^-, undergoes equilibrium exchange with H_2O at an associated isotope effect (Buchwald & Casciotti, 2013; Casciotti et al., 2002, 2007) and that there is an isotope effect associated with the oxidation of NO_2^- to NO_3^- (Boshers et al., 2019; Buchwald & Casciotti, 2010).

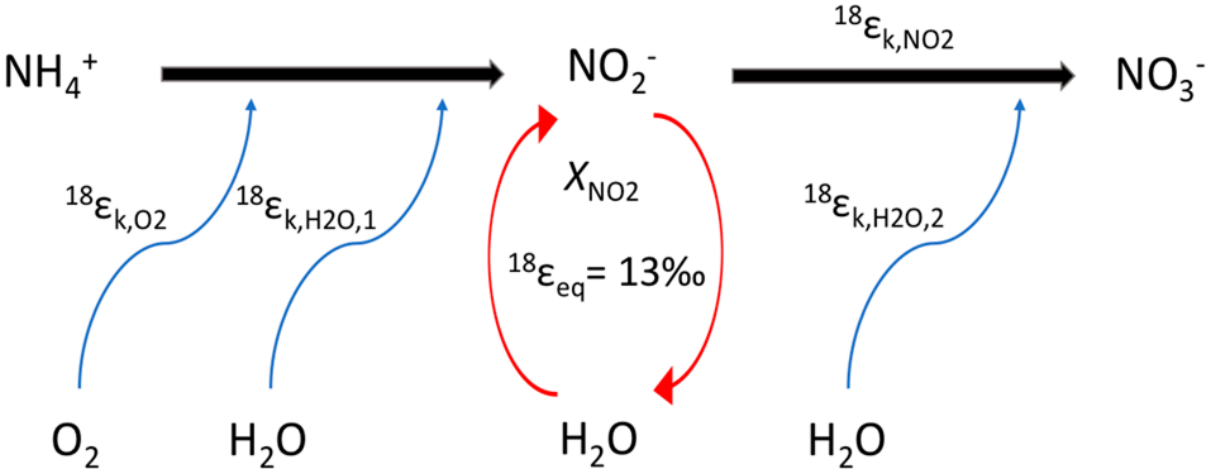

Fig. 2.6: A schematic of nitrification, showing the fractionations associated with the incorporation of O atoms. For NH_4^+ to NO_2^- oxidation, the O atoms are sourced from both O_2 and H_2O with potential isotope effects of $^{18}\varepsilon_{k,O2}$ and $^{18}\varepsilon_{k,H2O,1}$, respectively. NO_2^- can undergo equilibrium exchange of O atoms with the ambient water associated with an isotope effect of $^{18}\varepsilon_{eq}$ and with X_{NO2} representing the fraction of NO_2^- O atoms that have equilibrated with H_2O. NO_2^- oxidation to NO_3^- occurs with a potential O isotope effect of $^{18}\varepsilon_{k,NO2}$, while the additional O atom is sourced from ambient H_2O with a potential incorporation isotope effect of $^{18}\varepsilon_{k,H2O,2}$ (Boshers et al., 2019; Buchwald et al., 2012; Buchwald & Casciotti, 2010, 2013; Casciotti et al., 2007, 2010). Figure from Boshers et al. (2019).

Estimates of $^{18}\varepsilon_{k,O2}$, $^{18}\varepsilon_{k,H2O,1}$ and $^{18}\varepsilon_{k,H2O,2}$ range between 0 and 40‰ (Boshers et al., 2019; Buchwald et al., 2012; Buchwald & Casciotti, 2010; Casciotti et al., 2010). This means that ^{16}O is preferentially incorporated from the ambient O_2 and H_2O pools. NO_2^- oxidation to NO_3^- is thought to be associated with a slightly negative kinetic isotope effect, meaning that ^{18}O-bearing NO_2^- is preferentially oxidised to NO_3^- (Boshers et al., 2019; Buchwald & Casciotti, 2010). In the case where oxidation is the only process acting on the NO_2^- pool and all the NO_2^- is oxidised to NO_3^-, however, the impact of this isotope effect can be neglected.

NO_2^- undergoes both abiotic and biologically-facilitated exchange of O atoms with H_2O (Casciotti et al., 2002, 2007; Garber & Hollocher, 1982; Ye et al., 1991). The isotope effect ($^{18}\varepsilon_{eq}$) associated with this equilibrium exchange is temperature dependent, with $^{18}\varepsilon_{eq} = -0.12 \cdot T + 48.79$ for T between 277-306K (Buchwald & Casciotti, 2013), which yield a value of $^{18}\varepsilon_{eq}$ of ~13‰ at room temperature (Boshers et al., 2019; Casciotti et al., 2007). This

means that as the fraction of NO_2^- O atoms that have undergone equilibrium exchange with H_2O increases (as X_{NO2} approaches 1 in Fig. 2.6), $\delta^{18}O_{NO2} = \delta^{18}O_{H2O} + 13‰$ (Buchwald & Casciotti, 2013; Casciotti et al., 2010). The degree of abiotic exchange depends on both the rate of equilibration between NO_2^- and H_2O, and the residence time of the NO_2^-, with longer residence times allowing for a higher degree of exchange (Buchwald & Casciotti, 2013). The rate at which abiotic equilibrium exchange occurs appears to be a function of both temperature and pH, with complete equilibration taking on the order of weeks to months under neutral pH conditions, but hours to days under acidic conditions (Buchwald & Casciotti, 2013). Biologically mediated O exchange occurs at four times the rate of abiotic exchange and has been linked to the rate of NH_3 oxidation. This increased biologically mediated rate may stem from the acidic conditions found in the periplasm of the cell (Boshers et al., 2019).

Within the ocean, a balance between the O isotope effects associated with the incorporation of O atoms from H_2O and O_2, equilibrium exchange between NO_2^- and H_2O and the oxidation of NO_2^- to NO_3^- leads to the newly nitrified NO_3^- having a $\delta^{18}O$ that is ~1.1‰ higher than the $\delta^{18}O$ of the H_2O it was remineralised in (i.e., $\delta^{18}O_{NO3} = \delta^{18}O_{H2O} + 1.1‰$; Boshers et al., 2019; Buchwald et al., 2012; Casciotti et al., 2008; Sigman et al., 2009). This means that during nitrification, the $\delta^{18}O$ of the NO_3^- is 'reset' and its value, unlike the $\delta^{15}N$ of NO_3^-, does not depend on the isotopic composition of the PON/NH_4^+ that is being nitrified.

2.3.6.3 Coupled N and O isotope remineralisation signals

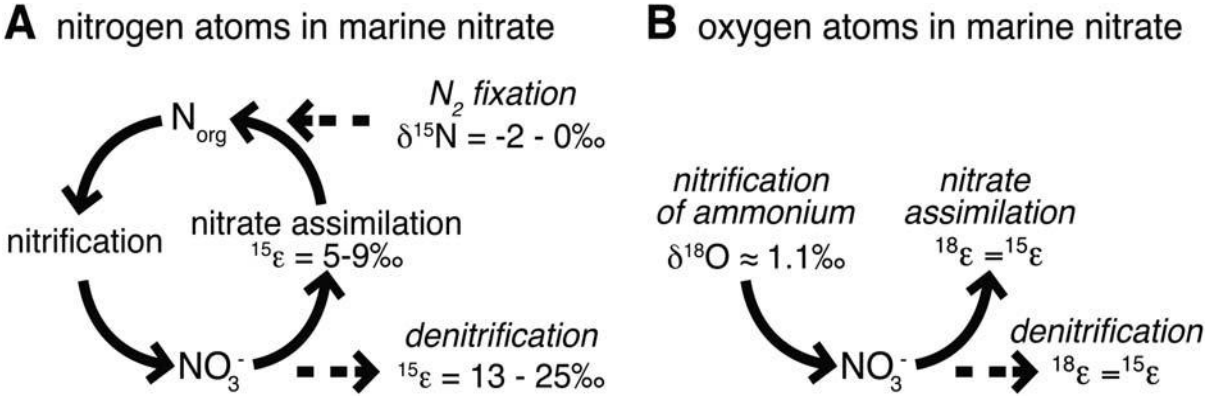

Fig. 2.7: Nitrogen (a) and oxygen (b) isotope dynamics associated with the cycling of marine NO_3^-. (a) $\delta^{15}N$ and N isotope effects ($^{15}\varepsilon$), reported relative to atmospheric N_2, for N_2 fixation (Carpenter et al., 1997; Delwiche et al., 1979; Hoering & Ford, 1959), NO_3^- assimilation (DiFiore et al., 2010; Fripiat et al., 2019), and denitrification (Granger et al., 2008; Kritee et al., 2012). In most of the ocean, the NH_4^+ released from PON is completely oxidised to NO_3^-, negating the uncertain and potentially large isotope effects associated with nitrification. (b) $\delta^{18}O$ and O isotope effects ($^{18}\varepsilon$), reported relative to VSMOW (Boshers et al., 2019; Casciotti et al., 2002; Granger et al.,

2004, 2008, 2010). The $\delta^{15}N$ of deep ocean NO_3^- is determined by a balance between N_2 fixation and denitrification, the ultimate source and sink of oceanic N, while the $\delta^{18}O$ of deep ocean NO_3^- is determined by the balance between nitrification, assimilation, and denitrification. Figure from Rafter et al. (2013).

From the perspective of the NO_3^- N atom (Fig. 2.7A), N_2 fixation and denitrification are the ultimate sources and sinks, while NO_3^- assimilation and nitrification are part of the internal cycling of fixed N. From the perspective of the O atom of NO_3^- (Fig. 2.7B), however, nitrification is the absolute source, while NO_3^- assimilation and denitrification are the absolute sinks (Fawcett et al., 2015; Sigman et al., 2005, 2009). Because the $\delta^{18}O$ of NO_3^- is reset during nitrification and, unlike the $\delta^{15}N$ of the newly nitrified NO_3^-, does not depend on the NH_4^+ that is being nitrified, co-occurring NO_3^- consumption and nitrification decouple the $\delta^{15}N$ and $\delta^{18}O$ of NO_3^- (Fawcett et al., 2015; Sigman et al., 2005, 2009). As NO_3^- assimilation and denitrification are associated with ${}^{15}\varepsilon = {}^{18}\varepsilon$, (Granger et al., 2004, 2008; 2010), the remaining unassimilated NO_3^- moves up a 1 : 1 line in $\delta^{18}O$ vs $\delta^{15}N$ space. Where NO_3^- regeneration is coincidentally significant, however, the $\delta^{18}O$ of NO_3^- may deviate from this 1 : 1 line (Casciotti, 2016; Rafter et al., 2013; Sigman et al., 2005, 2009).

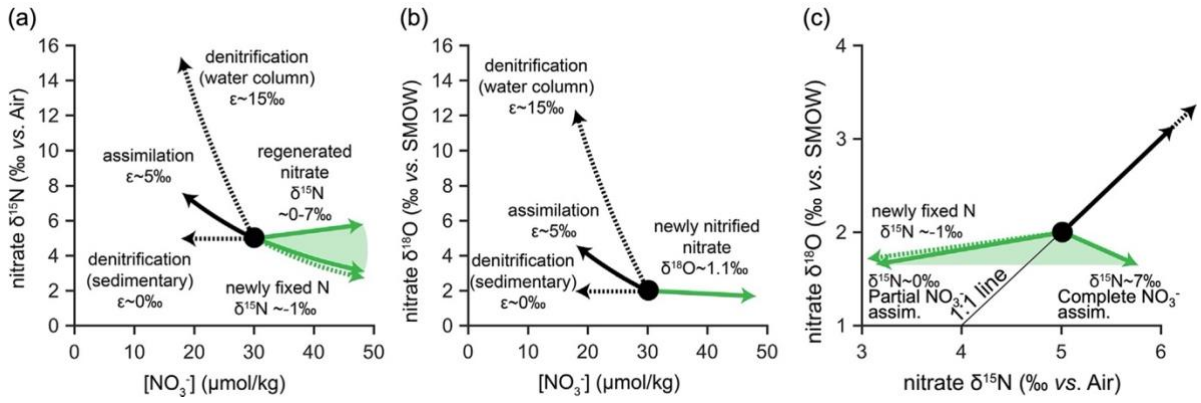

Fig. 2.8: (a) NO_3^- $\delta^{15}N$ and concentration ($[NO_3^-]$), (b) NO_3^- $\delta^{18}O$ and $[NO_3^-]$, and (c) NO_3^- $\delta^{18}O$ vs $\delta^{15}N$, illustrating the impact of marine processes on the NO_3^- pool. Each process (represented by the arrow trajectories) is plotted using the ε estimate represented on the figure, an initial NO_3^- concentration, $\delta^{15}N$, and $\delta^{18}O$ of 30 μmol/kg, 5‰, and 2‰, respectively, and by assuming a 30% change in NO_3^- concentration. Solid arrows denote processes that are responsible for the internal cycling of fixed N (assimilation and nitrification), while dashed arrows represent processes that add or remove biologically available N from the ocean (N_2 fixation and denitrification). The $\delta^{15}N$ of regenerated NO_3^- (solid green arrows) varies (green shading) as it is dependent on the $\delta^{15}N$ of the organic matter being remineralised, which can range in $\delta^{15}N$. The $\delta^{18}O$ of regenerated NO_3^- is primarily controlled by the $\delta^{18}O$ of ambient seawater. In (c), a 1 : 1 relationship between $\delta^{18}O$ and $\delta^{15}N$ during NO_3^- assimilation and denitrification can be seen. Deviations from the 1 : 1 relationship develop as a result of N_2 fixation (which adds low $\delta^{15}N$ N to the system) and through the remineralisation of organic matter. Remineralising organic matter formed through partial NO_3^- assimilation adds NO_3^- with a $\delta^{18}O$ that is higher than the $\delta^{18}O$ removed during assimilation, while the remineralisation of organic matter formed through complete NO_3^- assimilation produces NO_3^- with a $\delta^{18}O$ lower than that removed during assimilation, resulting in deviations from the 1 : 1 relationship in NO_3^- $\delta^{18}O$ vs $\delta^{15}N$ space. Figure adapted from Sigman & Fripiat, (2019).

Nitrification of PON formed through NO_3^- assimilation results in a deviation from the 1 : 1 line in $\delta^{18}O$ vs $\delta^{15}N$ space, as the $\delta^{18}O$ of the newly nitrified NO_3^- is reset. The $\delta^{15}N$ of the newly nitrified NO_3^- is equal to the $\delta^{15}N$ of the PON that is being remineralised, therefore, should this PON have formed locally through NO_3^- assimilation, its remineralisation would return the $\delta^{15}N$ consumed from the NO_3^- pool (~0‰ in the case of partial consumption, and 5-7‰ in the case of complete consumption). The addition of this low $\delta^{15}N$ newly nitrified NO_3^- to the ^{15}N enriched NO_3^- pool acts to erase the NO_3^- assimilation $\delta^{15}N$ signal. In the case of remineralisation following partial NO_3^- consumption, the $\delta^{18}O$ of the newly nitrified NO_3^- is higher than the $\delta^{18}O$ that was removed during NO_3^- assimilation (~1‰ versus -3 to 0‰, respectively) (Fawcett et al., 2015). The remineralisation of PON formed through partial NO_3^- assimilation results, therefore, in the addition of NO_3^- with a higher than expected $\delta^{18}O$, driving the NO_3^- above the 1 : 1 line in $\delta^{18}O$ vs $\delta^{15}N$ space (DiFiore et al., 2009; Fawcett et al., 2015; Wankel et al., 2007). The overall effect of nitrification would still be to lower the $\delta^{15}N$ and $\delta^{18}O$ of the NO_3^-, however, meaning that mixed layer nitrification would partially overprint the assimilation signal in both the N and O isotope profiles (Smart et al., 2015). In the case of remineralisation following complete NO_3^- consumption, the $\delta^{18}O$ of the newly nitrified NO_3^- is lower than the $\delta^{18}O$ removed during NO_3^- assimilation (~1‰ versus ~2‰, respectively), driving the NO_3^- below the 1 : 1 line in $\delta^{18}O$ vs $\delta^{15}N$ space. Deviations from the 1 : 1 line in NO_3^- $\delta^{18}O$ vs $\delta^{15}N$ space can, therefore, be used to identify nitrification in the water column.

N_2 fixation adds new N with a $\delta^{15}N$ of ~-1‰ to the N cycle (Carpenter et al., 1997; Delwiche et al., 1979; Hoering & Ford, 1959). The nitrification of PON formed from newly fixed N, therefore, adds NO_3^- with a lower than expected $\delta^{15}N$, driving the NO_3^- left of the 1 : 1 line in NO_3^- $\delta^{18}O$ vs $\delta^{15}N$ space.

In the case, however, where there is a significant difference in the $\delta^{15}N$ of the PON that is being remineralised and the NO_3^- that is formed, the NO_3^- $\delta^{15}N$ vs $\delta^{18}O$ signal could become significantly more complex (DiFiore et al., 2009). This could occur in the case where there is incomplete remineralisation of the PON, or where assimilation, nitrification and other processes are acting simultaneously on the same N pool. If multiple processes with different ε act on an N pool, the process with the largest ε will dominate the resulting isotopic distribution.

2.3.7 Degradation of organic matter

Bacterial degradation of PON to NH_4^+ occurs with a net isotope effect of ~3‰, leading to NH_4^+ having a comparatively low $\delta^{15}N$ (Lehmann et al., 2002). In the case where not all the PON is remineralised within the euphotic zone, isotopic fractionation occurs, with lower $\delta^{15}N$ N being preferentially remineralised and retained within the euphotic zone while the higher $\delta^{15}N$ organic matter is exported from surface waters (Möbius, 2012). This effect is compounded by zooplankton, which release low $\delta^{15}N$ NH_4^+, making their solid waste and tissue from higher $\delta^{15}N$ N (Altabet & Small, 1990; Checkley & Miller, 1989). This leads to the higher $\delta^{15}N$ N being preferentially exported from the surface as sinking particles, while low $\delta^{15}N$ N is retained as NH_4^+ in the surface ocean. The subsequent consumption of the NH_4^+ by phytoplankton results in the formation of similarly low-$\delta^{15}N$ PON (Altabet, 1988, 1989). Continued assimilation of this low $\delta^{15}N$ NH_4^+ by phytoplankton, followed by partial remineralisation of the PON produced could act to compound this effect, producing suspended PON with a $\delta^{15}N$ as low as -5‰ (Lourey et al., 2003; Smart et al., 2015).

2.3.8 Concurrent NH_4^+ assimilation and oxidation

In the case where NH_4^+ is both assimilated and oxidised simultaneously, one can no longer assume that the $\delta^{15}N$ of the newly nitrified NO_3^- is equal to that of the NH_4^+ being nitrified. Nitrifiers, which are impeded by light (Guerrero & Jones, 1996a, 1996b; Hooper & Terry, 1974; Vanzella et al., 1989), greatly reduce, although do not completely halt their activity when exposed to elevated light (Clark et al., 2008; Dore & Karl, 1996; Smith et al., 2014; Ward, 2005; Ward et al., 1989). Additionally, nitrifiers are out-competed for NH_4^+ by NH_4^+ assimilating phytoplankton (Smith et al., 2014). These factors combine to give phytoplankton a competitive advantage over nitrifiers in the euphotic zone, leading to the surface system being dominated by photoautotrophic NH_4^+ assimilation (Smith et al., 2014; Ward, 1985). In the case of deep mixed layers or at/near the base of the euphotic zone, however, the mean light experienced by phytoplankton decreases, reducing their activity and leading to the potential for simultaneous NH_4^+ assimilation and nitrification (Smith et al., 2014; Ward, 1985).

Ammonium assimilation (AmA) by phytoplankton has an associated enzymatic isotope effect of between 0 and 27‰, (Hoch et al., 1992; Liu et al., 2013; Pennock et al., 1996; Vo et al., 2013; Waser et al., 1998a). At the low NH_4^+ concentrations that are typical of the ocean, we expect minimal cellular efflux of NH_4^+, leading to a negligible expressed cellular isotope effect

(ε_{AmA}) (Hoch et al., 1992; Liu et al., 2013). Ammonium oxidation (AmOx), on the other hand, generally expresses a cellular isotope effect (ε_{AmOx}) of between 14 and 19‰ (for saltwater cultures; Casciotti et al., 2003, in reality, ammonia (NH_3), not ammonium (NH_4^+) is oxidised, with there existing an NH_4^+ - NH_3 equilibrium isotope effect, the values presented here are calculated for the consumption of NH_4^+, thus taking this equilibrium into account). As $\varepsilon_{AmOx} > \varepsilon_{AmA}$, the simultaneous nitrification and assimilation of NH_4^+ leads to low $\delta^{15}N$ being directed into the NO_2^- pool, while the $\delta^{15}N$ of the organic matter would increase (DiFiore et al., 2009).

The final distribution of the isotopes depends on the relative rates of AmA and AmOx (DiFiore et al., 2009; Kemeny et al., 2016; Smart et al., 2015). Near the base of the euphotic zone, it is expected that AmOx is the dominant process, with AmA only accounting for a small fraction of NH_4^+ consumption (Smith et al., 2014; Ward, 1985). The $\delta^{15}N$ of the NO_2^- produced under these conditions will be approximately equal to the $\delta^{15}N$ of the NH_4^+ supplied (DiFiore et al., 2009). This is because even though $\delta^{15}N_{NO2\ instantaneous} \approx \delta^{15}N_{NH4} - \varepsilon_{AmOx}$, which leads to an initially low $\delta^{15}N$ for the instantaneously produced NO_2^-, the progressive oxidation of ^{14}N-NH_4^+ drives up the $\delta^{15}N$ of the remaining NH_4^+ pool. While AmA, which operates with a negligible isotope effect at concentrations relevant to the ocean, consumes NH_4^+ at the $\delta^{15}N$ it exists, which results in AmA consuming some of the higher $\delta^{15}N$ NH_4^+. This means that as the NH_4^+ pool approaches complete consumption, its $\delta^{15}N$ increases strongly. At the same time, the $\delta^{15}N$ of the accumulated NO_2^- pool approaches the original $\delta^{15}N$ of the NH_4^+ substrate, while the PON produced by AmA will have a $\delta^{15}N$ that is considerably higher than the initially supplied NH_4^+.

In contrast to the base of the euphotic zone, AmA is expected to be the dominant process in well-lit surface waters, with AmOx only accounting for a small fraction of NH_4^+ consumption (Smith et al., 2014; Ward, 1985). Under these conditions, the NO_2^- that is produced will have a $\delta^{15}N$ that is 14-19‰ lower than the source NH_4^+ (Kemeny et al., 2016). This is because, assuming no resupply to the NH_4^+ pool, as the NH_4^+ is consumed, AmOx forms NO_2^- with a $\delta^{15}N_{NO2\ instantaneous} \approx \delta^{15}N_{NH4} - \varepsilon_{AmOx}$. As ε_{AmOx} = 14 - 19‰, low $\delta^{15}N$ N is preferentially removed from the NH_4^+ pool by AmOx, slightly increasing the $\delta^{15}N$ of the remaining NH_4^+. As AmA is the dominant process and has a negligible isotope effect, it will consume N with the same $\delta^{15}N$ as that of the NH_4^+ pool. As such, the $\delta^{15}N$ of the NH_4^+ pool will remain

relatively stable as it is consumed. The resulting accumulated NO_2^- pool will, therefore, have a $\delta^{15}N$ that is much lower than the initial $\delta^{15}N$ of the NH_4^+ pool, while the PON produced through AmA will have a $\delta^{15}N$ that is approximately equal to, if not slightly higher than, the initial NH_4^+ $\delta^{15}N$ (DiFiore et al., 2009).

2.3.9 NO_2^- - NO_3^- interconversion

When light-impeded marine nitrifiers are mixed up or added to the well-lit surface waters, the activity of the nitrite oxidoreductase enzyme (NXR), used by some nitrifiers, decreases, thereby decreasing the rate at which NO_2^- is oxidised to NO_3^- (Smith et al., 2014; Vanzella et al., 1989; Ward, 1985). It has been suggested that under these stressed conditions, in addition to oxidising NO_2^- to NO_3^-, the NXR enzyme can also catalyse the reduction of NO_3^- to NO_2^- (Buchwald & Wankel, 2022; Kemeny et al., 2016). The reversibility of the NXR enzyme can, at times, allow for the full expression of a NO_2^- - NO_3^- interconversion N isotope effect of between ~51 and 90‰ (Buchwald & Wankel, 2022; Casciotti, 2009; Kemeny et al., 2016; Wunderlich et al., 2013). The expression of this equilibrium N isotope effect does not require net oxidation or reduction at either the organism or enzyme level (Brunner et al., 2013) but nonetheless causes ^{15}N to accumulate in the NO_3^- pool, which increases its $\delta^{15}N$, while the NO_2^- pool becomes depleted in ^{15}N (Casciotti, 2009), which can lead to it having a $\delta^{15}N$ as low as -90‰ (Fripiat et al., 2019; Kemeny et al., 2016). Throughout this process, the $\delta^{15}N$ of the NO_2^- + NO_3^- pool remains unchanged (Fripiat et al., 2019; Kemeny et al., 2016).

The impact of interconversion on the $\delta^{18}O$ of NO_2^-+NO_3^- is complex, but appears to result in a net decrease in NO_2^-+NO_3^- $\delta^{18}O$ (Buchwald & Wankel, 2022). This decrease is driven by the open system incorporation and loss of O atoms as well as abiotic exchange between seawater and NO_2^- (Boshers et al., 2019; Buchwald & Casciotti, 2013; Buchwald & Wankel, 2022).

The isotopic differences between NO_3^- and NO_2^-, whether due to NO_2^- - NO_3^- interconversion or simply a balance between NH_4^+ assimilation and oxidation, have led previous studies to wonder whether it is most appropriate to examine the NO_3^-+NO_2^- pool, or NO_3^--only pool when investigating surface NO_3^- cycling. In the subtropics (e.g., at BATS; Fawcett et al. (2015)) NO_2^- removal was necessary to return the $\delta^{15}N$ and $\delta^{18}O$ data to a 1 : 1 line, while in the Southern Ocean, Fripiat et al. (2019) and Kemeny et al. (2016) recommend considering the NO_3^-+NO_2^- pool.

The isotopes of N and O across the dissolved N pools in the ocean can thus provide insights into and constraints on the overlapping N cycle processes occurring in a region. In this thesis, I report concentration and isotope data for the ammonium (NH_4^+), particulate organic nitrogen (PON), and nitrite + nitrate (NO_2^-+NO_3^-) pools adjacent to Larsen C Ice Shelf in the Western Weddell Sea for summer 2019. To evaluate the processes occurring in this region, an overview of the isotopic landscape of the Southern Ocean is required.

2.4 Previous Southern Ocean NO_3^- assimilation isotope effect estimates

During summer in the Southern Ocean, macronutrients such as NO_3^- and phosphate in the surface mixed layer are not completely consumed. This is thought to be the result of combined iron and light limitation of phytoplankton, where iron is a vital micronutrient required for phytoplankton growth (Coale et al., 1996; Martin et al., 1990; Martin & Fitzwater, 1988; Mitchell et al., 1991; Sunda & Huntsman, 1997). The main sources of iron to the ocean are sediment resuspension, atmospheric deposition of continental dust, hydrothermal, and river inputs (Sedwick et al., 2000; Tagliabue et al., 2009). As the Antarctic is far removed from large continental dust sources, the supply of dust is minimal. The well-stratified shallow summer mixed layer further inhibits the upwelling of resuspended iron, leading to the region being iron limited. As a result, the degree of phytoplankton productivity in the Southern Ocean depends on the availability of micronutrients, rather than on macronutrient availability, as is the case in much of the lower latitude ocean (Moore et al., 2013). Sea ice can act as a store of iron, with summer melting supplying it to the surface ocean, alleviating some of the micronutrient limitation at the sea ice margins (Janssens et al., 2016; Lannuzel et al., 2008, 2016; Sedwick & DiTullio, 1997). This results in these areas being more productive than the open Southern Ocean, allowing for a greater degree of macronutrient consumption (Sedwick & DiTullio, 1997) and thus a stronger biological pump (Johnson et al., 2017).

The partial consumption of NO_3^- by phytoplankton, as occurs in the Southern Ocean, results in the expression of the NO_3^- assimilation isotope effect. As phytoplankton preferentially remove NO_3^- containing ^{14}N, this leaves the unconsumed NO_3^- pool high in $\delta^{15}N$. The $^{15}\varepsilon$ associated with NO_3^- assimilation has been shown to be variable across the Southern Ocean, ranging from

1.6‰ to 9‰, with generally higher values in Subantarctic than Antarctic waters, and the lowest values estimated in winter (Altabet & Francois, 2001; DiFiore et al., 2006, 2009, 2010; Fripiat et al., 2019; Karsh et al., 2003; Sigman et al., 1999; Smart et al., 2015). The $^{18}\varepsilon$ of NO_3^- assimilation across the Southern Ocean shows a more restricted range of 3‰ to 7‰, with a less pronounced latitudinal and seasonal variation (DiFiore et al., 2009; Fripiat et al., 2019; Smart et al., 2015). For the Antarctic, a recent metanalysis showed that the $^{15}\varepsilon$ associated with the consumption of NO_3^-+NO_2^- in the summer is relatively constant at 5.5 ± 0.6‰ (Fripiat et al., 2019). The authors attribute this consistency in their $^{15}\varepsilon$ estimate to it being derived from the NO_3^-+NO_2^- as opposed to the NO_3^-only pool, with them positing that the NO_3^-+NO_2^- pool more accurately represents the N available for consumption (producing PON) and is independent of NO_3^--NO_2^- interconversion or any other process that differentially alters the isotopic compositions of NO_3^- and NO_2^- (Fripiat et al., 2019; Kemeny et al., 2016).

In the Southern Ocean, PON δ^{15}N tends to track the δ^{15}N of NO_3^-+NO_2^-, with a higher δ^{15}N indicating a stronger degree of NO_3^-+NO_2^- consumption (Altabet & Francois, 2001; Altabet & McCarthy, 1985, 1986; Sigman et al., 1999). This relationship arises as NO_3^-+NO_2^- is assimilated with an associated $^{15}\varepsilon$, leading to the accumulated PON produced through NO_3^-+NO_2^- assimilation having a δ^{15}N lower than the source NO_3^-+NO_2^-, with the PON δ^{15}N rising as NO_3^-+NO_2^- assimilation progresses. As a result, if the δ^{15}N of the source NO_3^-+NO_2^- is known, the mean δ^{15}N of buried PON can be used to reconstruct the degree of NO_3^-+NO_2^- drawdown, and thus the strength of the biological pump, in the past ocean (Altabet & Francois, 1994, 2001; Francois et al., 1992, 1997; Martínez-García et al., 2014; Studer et al., 2015). Of vital importance in this past reconstruction, however, is a reliable estimate of the NO_3^-+NO_2^- assimilation $^{15}\varepsilon$, as well as an understanding of the internal N cycling (especially nitrification), which may act to disconnect NO_3^-+NO_2^- assimilation from N export.

Nitrification, which decouples NO_3^-+NO_2^- δ^{15}N and δ^{18}O, has been shown to be minimal in the surface summer Southern Ocean, accounting for a maximum of 6% of the NO_3^- assimilation rate (DiFiore et al., 2009). DiFiore et al. (2009) observed a strong coupling between the δ^{15}N and δ^{18}O of NO_3^-, with the data falling along a 1 : 1 line in NO_3^- δ^{18}O vs δ^{15}N space as is expected if assimilation is the primary process acting on the NO_3^- pool (Granger et al., 2004, 2010). In addition, when considering interconversion, Fripiat et al. (2019) found no deviation in NO_3^-+NO_2^- δ^{18}O vs δ^{15}N space from the 1 : 1 line, once again indicating minimal surface

nitrification across the summer Southern Ocean. The winter Southern Ocean, however, shows clear evidence of surface nitrification, with the data deviating from the 1 : 1 line in NO_3^-+NO_2^- $\delta^{18}O$ vs $\delta^{15}N$ space (Smart et al., 2015). As a result of the nitrification of low $\delta^{15}N$ PON, low $\delta^{15}N$ NO_3^-+NO_2^- is produced, leading to a lower than expected $^{15}\varepsilon$ of between 1.6‰ and 3.3‰ being calculated from the winter data (Smart et al., 2015). The $^{18}\varepsilon$ derived from winter data falls in line with summer estimates of between 3‰ and 7‰ (DiFiore et al., 2009; Fripiat et al., 2019; Smart et al., 2015). Nitrification in the surface Southern Ocean, therefore, appears to only be a primary process during winter, with the summertime surface ocean showing evidence of minimal surface nitrification.

Kemeny et al. (2016) suggested that NO_3^--NO_2^- interconversion occurs in the Southern Ocean during periods of mixed layer deepening, at the end of summer (late March to early April) during the deepening of the summer mixed layer. They proposed that this mixed-layer deepening allows for the entrainment of nitrifiers into the euphotic zone, where they experience light stress. Fripiat et al. (2019) subsequently suggested that short-term variability in the Southern Ocean mixed layer depth could entrain sub-mixed layer nitrifiers into the euphotic zone at any point during the summer. This would allow for NO_3^--NO_2^- interconversion to occur throughout summer and autumn in the Southern Ocean, raising the $\delta^{15}N$ and likely lowering the $\delta^{18}O$ of NO_3^--only, while not changing the $\delta^{15}N$ and possibly lowering the $\delta^{18}O$ of the NO_2^- +NO_3^- pool. Isotope effects derived for the assimilation by phytoplankton from these pools will display a similar pattern, with interconversion acting to increase the $^{15}\varepsilon$ derived from NO_3^--only and lower the $^{18}\varepsilon$ of both NO_3^--only and NO_2^-+NO_3^-, while leaving the $^{15}\varepsilon$ of NO_2^-+NO_3^- unchanged (Fripiat et al., 2019). For this reason, we have chosen to focus on the $\delta^{15}N$ and $\delta^{18}O$ of the NO_2^-+NO_3^- pool (rather than NO_3^--only) in this thesis.

3 Thesis scope

The hostile, inaccessible, and seasonal nature of the Antarctic environment makes it a very challenging place in which to conduct research. The harsh sea ice conditions surrounding LCIS make it even more challenging to study, with only two direct studies having been conducted on the strength of the regional biological pump (Flynn et al., 2021; Hoppema et al., 2000). In this study, we provide a new, independent estimate of the biological pump strength by reporting the measured concentration and $\delta^{15}N$ of the nitrate + nitrite ($NO_3^-+NO_2^-$), particulate organic nitrogen (PON), and ammonium (NH_4^+) pools as well as the $\delta^{18}O$ of $NO_3^-+NO_2^-$ collected from 16 stations adjacent LCIS in January of 2019. The central goal of the work detailed in this thesis is to provide a new characterisation of biological pump strength for the waters adjacent to LCIS in the western Weddell Sea. Using the isotopes of the N pools allows for a somewhat time-integrated (at least on a near seasonal cycle scale) view of the biological pump, and allows for potentially overlapping N cycle processes (such as $NO_3^-+NO_2^-$ assimilation and nitrification) to be identified. In addition, the $NO_3^-+NO_2^-$ isotope data detailed herein allow for a new estimation of the N and O isotope effect ($^{15}\varepsilon$ and $^{18}\varepsilon$, respectively) associated with $NO_3^-+NO_2^-$ assimilation in the coastal Antarctic. Such values are important because in order to reconstruct the degree of $NO_3^-+NO_2^-$ drawdown, and thus biological pump strength in the past from buried organic matter, a reliable estimate of the $NO_3^-+NO_2^-$ assimilation $^{15}\varepsilon$ is required. The following section in which these results are presented is structured as a single chapter, as it is intended to be submitted to a scientific journal.

4 Nitrogen cycle-based estimates of carbon export potential in the waters adjacent to Larsen C Ice Shelf in the western Weddell Sea, Antarctica

4.1. Introduction

Atmospheric CO_2 is transferred to the deep ocean via the biological pump, the mechanism by which photosynthetically-produced organic matter sinks out of the sunlit surface layer (euphotic zone) to be remineralised at depth (Volk & Hoffert, 1985). Biological pump strength can be assessed by the fraction of new to regenerated production, where new production is phytoplankton growth supported by nitrogen (N) sources that are "new" to the euphotic zone (e.g., nitrate (NO_3^-) mixed up from the subsurface) while regenerated production refers to phytoplankton growth on recycled N forms (e.g., ammonium (NH_4^+) and urea) (Dugdale & Goering, 1967; Eppley & Peterson, 1979). On an annual basis, new production must be balanced by the export of organic matter from the euphotic zone (i.e., "export production"). As such, the extent of phytoplankton NO_3^- consumption can be used to estimate carbon export potential, provided that euphotic zone nitrification (i.e., the oxidation of recycled NH_4^+ to nitrite (NO_2^-) and then NO_3^-, which yields regenerated NO_3^-) is minimal (Dugdale & Goering, 1967; Mdutyana et al., 2020; Yool et al., 2007) and that carbon and N are incorporated into biomass in a known ratio (Redfield et al., 1963).

Across much of the Southern Ocean, the biological pump is weaker than expected based on the upward supply of NO_3^- (Sarmiento & Toggweiler, 1984). This weakness, which is largely due to iron and light limitation of phytoplankton (Martin et al., 1990; Strzepek et al., 2019; Sunda & Huntsman, 1997), manifests in high concentrations of the macronutrients NO_3^- (and phosphate) left unconsumed in surface waters. In coastal Antarctic waters, seasonal ice melt, sediment resuspension, and coastal runoff can, at least partly, alleviate phytoplankton iron limitation (e.g., Dinniman et al., 2020; Janssens et al., 2016; Lannuzel et al., 2008, 2016). A flux of low-density meltwater into the euphotic zone also increases surface stratification, shoaling the mixed layer and thus helping to alleviate the light limitation of phytoplankton (Arrigo et al., 1999; Sedwick & DiTullio, 1997). As such, Southern Ocean waters near Antarctica are often highly productive in spring and summer and characterized by significantly greater NO_3^- drawdown than the offshore waters to the north (Flynn et al., 2021; Li et al., 2016). Stratified, iron-rich waters and their associated elevated rates of primary productivity have been

observed at Antarctic ice shelf breaks, including adjacent to Larsen C Ice Shelf (LCIS) in the western Weddell Sea, which is the focus of this study (Flynn et al., 2021; Hoppema et al., 2000).

LCIS is, in addition, a formation site of Ice Shelf Water, a water mass with a potential temperature below the surface freezing point (Nicholls et al., 2009, 2012), that is advected down the continental slope and is a parent water mass to Antarctic Bottom Water (Nicholls et al., 2009; Robertson et al., 2002; Weppernig et al., 1996). The offshore advection and descent of this cold, dense water transports the CO_2 it contains into the deep ocean, storing it in some of the world's densest water masses. Organic matter that has remineralised and released its CO_2 into this dense water prior to its advection offshore will, therefore, be acting to directly inject CO_2 into the deep ocean. It is, thus, important to characterize the amount of organic matter that sinks from the mixed layer adjacent to LCIS, as it has the potential to be transported into some of the world's densest water masses.

Export production and biological pump strength can be approximated by measurements of net community production (NCP), which quantifies the net export of biomass from the surface ocean through particle sinking, downward mixing of dissolved organic matter, and transport by animals (Emerson, 2014). NCP has previously been estimated from sediment traps, global climate models, satellite-based products, oxygen mass balance, surface NO_3^- drawdown, and carbon isotope mass balance (Emerson, 2014 and references therein; Johnson et al., 2017). NCP in the Southern Ocean has previously been calculated using NO_3^- mass balance by subtracting the lowest summer mixed layer NO_3^- concentration from the highest winter mixed layer NO_3^- concentration and integrating the quantity of nitrogen (N) removed to a depth below the base of the summertime mixed layer (Johnson et al., 2017). This quantity of N, which equates to the amount of organic N exported during the spring and summer growth period, can subsequently be converted to carbon export using the molar C : N ratio of marine biomass, which is typically on the order of 106 C : 16 N (Anderson, 1995; Hedges et al., 2002; Johnson et al., 2022; Redfield et al., 1963). For the Southern Ocean, this approach yields an estimate of NCP of 1 to 4 mol C / m^2 / yr (Johnson et al., 2017), similar to satellite- and model-based estimates of NCP for the same region (Bopp et al., 2001; Dunne et al., 2007; Emerson, 2014 and references therein; Laws et al., 2011; Munro et al., 2015).

The strength of the biological pump can also be evaluated through measurements of N isotopes. In the environment, N exists primarily as ^{14}N (99.63%), with 0.37% existing as ^{15}N. Measured ratios of these isotopes are reported in delta notation as $\delta^{15}N$, in ‰ versus N_2 in air, = $(^{15}N/^{14}N_{sample})/ (^{15}N/^{14}N_{air}) - 1) \cdot 1000$. During most biological reactions, ^{14}N reacts faster than ^{15}N, such that the product pool is lower in $\delta^{15}N$ than the reactant pool. The extent to which a particular reaction discriminates against ^{15}N is quantified by the isotope effect ($^{15}\varepsilon$), which, in ‰ versus N_2 in air, = $(1 - {}^{15}k/{}^{14}k) \cdot 1000$, where ^{15}k and ^{14}k are the rate constants for the ^{15}N- and ^{14}N-bearing reactions, respectively (Mariotti et al., 1981; Sigman & Fripiat, 2019). As the reaction proceeds, this isotopic fractionation causes the $\delta^{15}N$ of both the reactant and product to rise until, upon exhaustion of the reactant, the $\delta^{15}N$ of the product converges upon its initial $\delta^{15}N$ (Mariotti et al., 1981).

The isotope effect associated with NO_3^- assimilation by phytoplankton ($^{15}\varepsilon_{assim}$) has been shown to be variable across the Southern Ocean, ranging from 1.6‰ to 9‰, with generally higher values in Subantarctic than Antarctic waters (Altabet & Francois, 2001; DiFiore et al., 2006, 2009, 2010; Fripiat et al., 2019; Karsh et al., 2003; Sigman et al., 1999; Smart et al., 2015). For the Antarctic, a recent metanalysis showed that the $^{15}\varepsilon_{assim}$ associated with the consumption of nitrate + nitrite ($NO_3^-+NO_2^-$) is relatively constant at 5.5 ± 0.6‰ (Fripiat et al., 2019), although this average includes very few data from coastal waters. Coastal values of $^{15}\varepsilon_{assim}$ have been challenging to estimate due to the low degree of NO_3^- consumption observed in these waters in previous studies, leading to a very small increase in $\delta^{15}N$ from the source waters into the surface, which is close to the analytical precision (Fripiat et al., 2019).

Using $^{15}\varepsilon_{assim}$ and the $\delta^{15}N$ of $NO_3^-+NO_2^-$, one can calculate the $\delta^{15}N$ of particulate organic nitrogen (PON) that will be generated from $NO_3^-+NO_2^-$ consumption using the Rayleigh model, provided assimilation is the only process acting on the $NO_3^-+NO_2^-$ pool (i.e., a closed system with no in situ nitrification or mixing) and that assimilation proceeds with a constant $^{15}\varepsilon_{assim}$. NH_4^+ can also be consumed to form PON, the $\delta^{15}N$ of which will equal that of the NH_4^+ since the $^{15}\varepsilon$ associated with NH_4^+ assimilation appears to be negligible at the NH_4^+ concentrations typical of the ocean (i.e., <5 μM) (Hoch et al., 1992; Liu et al., 2013; Pennock et al., 1996; Vo et al., 2013; Waser et al., 1998b). The $\delta^{15}N$ of NH_4^+ in the euphotic zone should be lower than that of $NO_3^-+NO_2^-$ mixed up from depth because of isotope fractionation associated with NH_4^+ production (Altabet, 1988; Lehmann et al., 2002; Möbius, 2012). As such, one can use the $\delta^{15}N$

of PON, $NO_3^-+NO_2^-$, and NH_4^+ to quantify the relative contributions of new and regenerated N to PON formation, and by extension, derive an estimate of the strength of the biological pump.

Here we use new measurements of $NO_3^-+NO_2^-$, PON, and NH_4^+ concentration and $\delta^{15}N$ to estimate the relative importance of new (versus total) production (Fawcett et al., 2011) in the waters adjacent to LCIS in the Weddell Sea during the summer of 2019. Our results indicate that LCIS waters host a strong biological pump with the potential to sequester a large quantity of atmospheric CO_2. Moreover, it appears that new production is highest in the early summer and declines as the growing season progresses, with phytoplankton shifting to relatively higher dependence on recycled NH_4^+. We also use our $NO_3^-+NO_2^-$ isotope data to estimate ${}^{15}\varepsilon_{assim}$ for coastal Weddell Sea Waters, which we find to be consistent with previous estimates from the Antarctic Zone of the Southern Ocean.

4.2. Methods:

4.2.1 Field sampling

The data presented in this thesis were collected in the vicinity of Larsen C Ice Shelf (LCIS) between the 10th and 24th of January 2019 during the Weddell Sea Expedition (WSE) onboard the R/V *SA Agulhas II* (Fig. 4.1). Hydrographic data from 16 stations were collected using a SeaBird conductivity-temperature-depth (CTD) profiler (SeaBird SBE 9/11 plus). The CTD was equipped with an oxygen sensor in addition to sensors to measure pressure, conductivity, and temperature, which were used to derive depth (m), absolute salinity (g/kg), conservative temperature (°C), and potential density anomaly (kg/m^3; = potential density – 1000 kg/m^3, reported as sigma theta (σ_θ)). Derivations were made using Ocean Data View (Schlitzer, 2018), which relies on the TEOS–10 equations of state.

Seawater samples were collected during each CTD cast from between 13 and 19 discrete depths per station with a vertical resolution of 3-25 m in the surface (0-60 m) and 10-123 m at depths >60 m using 12L Niskin bottles attached to the CTD rosette. Samples for direct measurement of salinity and dissolved oxygen were collected at 3-5 depths from each cast and analyzed shipboard using a Portasal 8410A salinometer and Ocean Scientific International Ltd (OSIL) standards (salinity) and Winkler titration (oxygen; Strickland & Parsons, (1972)) to calibrate and verify the accuracy of the CTD sensors (Hutchinson et al., 2020). Samples for the

concentrations of nitrate + nitrite ($NO_3^-+NO_2^-$), nitrite (NO_2^-), and urea-N were collected at each Niskin depth in 50 ml centrifuge tubes that were rinsed with sample prior to filling. The $NO_3^-+NO_2^-$ and urea-N samples were immediately frozen, while the NO_2^- samples were measured shipboard. Ammonium (NH_4^+) samples were collected in duplicate in "aged" high-density polyethylene (HDPE) bottles and frozen prior to analysis, which occurred within 24 hours.

Samples were collected at each Niskin depth for $NO_3^-+NO_2^-$ $\delta^{15}N$ and $\delta^{18}O$ in acid-washed HDPE bottles that were copiously rinsed with sample water prior to filling, then stored frozen at -20ºC. Seawater samples for NH_4^+ $\delta^{15}N$ analysis were collected in sample rinsed 250 ml low-density polyethylene (LDPE) bottles and fixed with 0.1 ml of 2 mol/l HCl to achieve a final pH of ~4 prior to freezing at -20ºC until analysis on land. Particulate organic nitrogen (PON) was collected from 3 to 5 depths in the upper 100 m of the water column by filtering 200-4000 ml of seawater onto pre-combusted (450ºC for 5 hours) 0.3 μm glass fibre (GF-75; Sterlitech) filters. The filters were wrapped in combusted (450ºC for 5 hours) foil and stored at -80ºC until later analysis on land.

4.2.2 Nutrient concentrations

Seawater $NO_3^-+NO_2^-$ concentrations were measured using a Lachat QuickChem flow injection analysis platform following published protocols (Grasshoff, 1976) in the Marine Biogeochemistry Lab at the University of Cape Town (UCT-MBL). The detection limit for this configuration was 0.5 μmol/l, with duplicate measurements of the same sample on different days yielding a precision of <0.5μmol/l (Flynn et al., 2021). The NO_2^- concentrations were measured manually onboard using a standard benchtop colourimetric method (Bendschneider & Robinson, 1952; Strickland & Parsons, 1972) and a Thermo Scientific Genesys 30 Visible spectrophotometer. The detection limit was <0.05 μmol/l, with a precision for duplicate samples of ≤0.05 μmol/l. Aliquots of a certified reference material (CRM; JAMSTEC, lot CG) were run during the autoanalyzer and manual batch runs to ensure measurement accuracy.

The NH_4^+ concentrations were measured onboard using the fluorometric method of Holmes et al. (1999) and a Turner Designs Trilogy fluorometer equipped with a UV detection module (see Smith et al. (2022) for more details). The detection limit was <0.05 μmol/l with a precision for duplicate samples of <0.05 μmol/l. The matrix effect resulting from the use of Milli-Q

standards to calibrate seawater samples was calculated via the standard addition method (Saxberg & Kowalski, 1979). All samples were corrected for the matrix effect (Taylor et al., 2007), which was always <10% and typically ≤5%.

Urea-N concentrations were measured in the UCT-MBL via the colourimetric method (Revilla et al., 2005) using a Thermo Scientific Genesys 30 Visible spectrophotometer equipped with either a 1 cm or 5 cm pathlength cell. The detection limit was 0.05 μmol/l and the precision for duplicate samples was ≤0.05 μmol/l. Hereafter, we use "urea" when referring to urea-N.

4.2.3 Bulk PON concentration and $\delta^{15}N$

At the UCT-MBL, filters containing PON were dried for 24h at 40^{o}C and a subsample was cored and packaged into a tin cup for analysis. Samples were measured using a Delta V Plus isotope ratio mass spectrometer (IRMS) coupled to a Flash 1112 Series Elemental Analyzer with a detection limit of 0.07 μmoles N. Unused pre-combusted filter blanks were included in each run. The PON concentrations were derived from daily standard curves of IRMS voltages versus known N masses, which yields N content that was subsequently normalized to filtration volume. The PON $\delta^{15}N$ measurements were referenced to N_2 in air using internal laboratory standards that had been calibrated against International Atomic Energy Agency (IAEA) reference materials and that were measured after every five to seven samples. The pooled standard deviation for the internal standards was 0.05‰ for Choc and 0.34‰ for Valine.

4.2.4 NO_3^-+NO_2^- $\delta^{15}N$ and $\delta^{18}O$

To prepare the samples for analysis, they were defrosted, shaken to homogenise the contents, and filtered to remove organic matter. During filtration, a 50 ml syringe with a detachable 0.2 μm filter was rinsed three times with Type 1 Milli Q water, rinsed twice with a small volume of sample, and then used to filter the sample. Aliquots of the filtered samples were stored in acid-washed HDPE bottles at -20^{o}C and sent to the UC Davis Stable Isotope Facility for isotope analysis using the "denitrifier method" (Sigman et al., 2001).

Briefly, the denitrifier method is used to measure the $\delta^{15}N$ and $\delta^{18}O$ of NO_3^-+NO_2^- using a strain of denitrifying bacteria that lacks an active nitrous oxide (N_2O) reductase enzyme (*Pseudomonas chlororaphis* f. sp. *Aureofaciens*). Under anoxic conditions, *P. aureofaciens*

quantitatively converts seawater NO_3^-+NO_2^- to N_2O gas, which is then extracted and purified using a ThermoFinnigan GasBench plus PreCon trace gas concentration system interfaced with a ThermoScientific Delta V Plus IRMS (Casciotti et al., 2002; Sigman et al., 2001; McIlvin and Casciotti 2007). The samples were calibrated against certified reference materials (CRMs) IAEA NO3 ($\delta^{15}N$ = +4.7 ± 0.2‰ versus N_2 in air and $\delta^{18}O$ = +25.6 ± 0.4 versus Vienna Standard Mean Ocean Water (VSMOW)) and United States Geological Survey (USGS) 34 ($\delta^{15}N$ = -1.8 ± 0.2‰ versus N_2 in air and $\delta^{18}O$ = -27.9 ± 0.6 versus VSMOW) (Böhlke et al., 2003; Gonfiantini et al., 1995). As such the sample $\delta^{15}N$ and $\delta^{18}O$ are reported versus N_2 in air and VSMOW, respectively.

The NO_3^-+NO_2^- isotope data undergo two methodological corrections. The first is related to the bacterial blank, with the data corrected for any N_2O produced by the bacteria in the absence of sample seawater; these bacterial blanks were assessed in every IRMS batch run. The second correction is applied to the $\delta^{18}O$ data only and is required when the seawater sample contains a measurable concentration of NO_2^-. The NO_2^- correction is necessary because during bacterial conversion of sample NO_3^-+NO_2^- to N_2O, NO_3^- loses a larger proportion of its O atoms than NO_2^- ($2NO_3^- \rightarrow N_2O + 5O$ versus $2NO_2^- \rightarrow N_2O + 3O$; 5/6 O atoms are lost from NO_3^- compared to 3/4 from NO_2^-). The O isotope effects associated with the loss of these O atoms are accounted for in the case of NO_3^- by the fact the data are standardised using NO_3^- reference materials (i.e., IAEA NO3 and USGS 34). For NO_2^-, however, the $\delta^{18}O$ of the N_2O produced by the denitrifier method is ~25‰ lower than that produced from NO_3^- with the same starting $\delta^{18}O$ (Casciotti et al., 2007). To counteract this methodological bias, the measured $\delta^{18}O$ of the NO_3^-+NO_2^- pool must be increased in proportion to the fraction of NO_2^- in each sample (i.e., $\delta^{18}O_{corrected} = \delta^{18}O_{measured} + 25‰ \cdot [NO_2^-]/[NO_3^-+NO_2^-]$) (Fawcett et al., 2015; Kemeny et al., 2016). All the NO_3^-+NO_2^- $\delta^{18}O$ data reported hereafter have undergone this correction. The precision for duplicate measurements of NO_3^-+NO_2^- $\delta^{15}N$ was 0.08‰ with a pooled CRM standard deviation of 0.15‰, while NO_3^-+NO_2^- $\delta^{18}O$ samples had a precision for duplicate measurements of 0.15‰ and pooled CRM standard deviation of 0.32‰.

4.2.5 NH_4^+ $\delta^{15}N$ analysis

NH_4^+ $\delta^{15}N$ was measured in the Department of Marine Science at the University of Connecticut for samples with NH_4^+ concentrations ≥0.8 μmol/l. The NH_4^+ was quantitatively oxidized to NO_2^- using hypobromite (Zhang et al., 2007), with the NO_2^- subsequently reduced to N_2O using

a 1 : 1 sodium azide and acetic acid buffer solution (McIlvin & Altabet, 2005). Samples were then transferred to combusted glass vials with the volumes adjusted to ensure a quantity of 12.5 nmoles of sample N in each vial. The N_2O $\delta^{15}N$ was measured using a modified GasBench II in-line with a Thermo Delta V Advantage IRMS (Sigman et al., 2001; McIlvin and Casciotti 2007). Individual N_2O isotope ratios were referenced against N_2O from a pure gas cylinder and then standardised by comparison with three international CRMs. The CRMs used were IAEA-N1 ($\delta^{15}N$ = +0.4 ± 0.2‰ versus N_2 in air), IAEA-N2 ($\delta^{15}N$ = +20.3 ± 0.2‰ versus N_2 in air), and USGS-25 ($\delta^{15}N$ = -30.4 ± 0.4‰ versus N_2 in air) (Böhlke et al., 1993), which were diluted with low NH_4^+ deep Atlantic (~4000 m) seawater and run at regular intervals throughout the run. The full NH_4^+ to N_2O reaction blank (prepared in deep Atlantic seawater) was 6.00 ± 0.21 nmol N. All samples were run in duplicate batch runs with a pooled precision of 0.2‰. The pooled averages and standard deviations for all measurements of IAEA-N1, IAEA-N2, and USGS-25 (n=35, n=36, and n=10) were +0.4±0.1, +20.3±0.2, and -30.3±0.2‰, respectively.

4.3 Results:

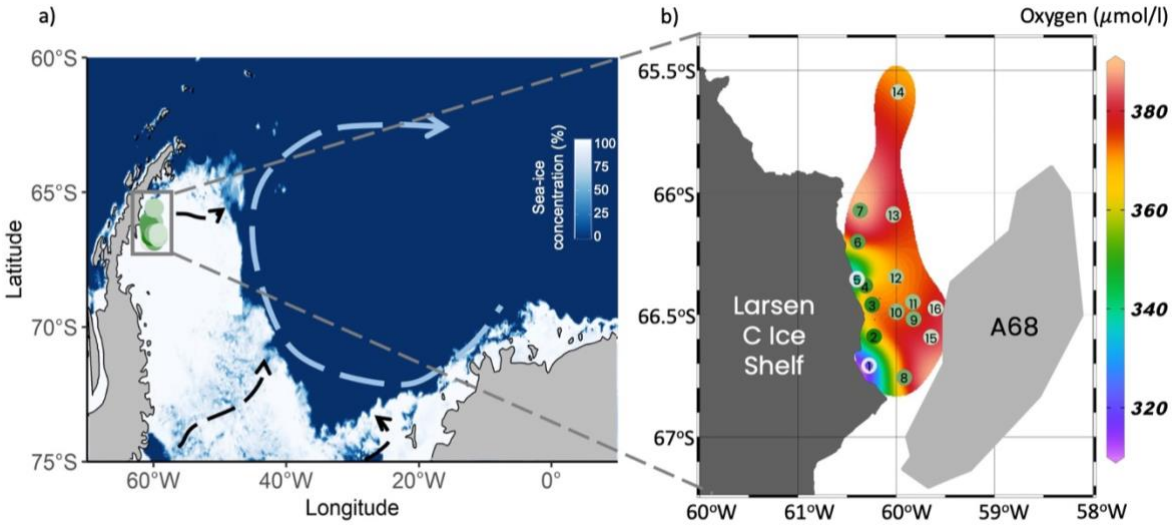

Fig. 4.1: Maps of (a) the Weddell Gyre and (b) the study site showing the locations of CTD stations adjacent to the Larsen C Ice Shelf (LCIS) (green circles) that were occupied during the Weddell Sea Expedition of 2019. The general Weddell Sea circulation is depicted in (a), with the dashed blue arrow representing the Antarctic Slope Current. The input of modified water masses from the Filchner-Ronne Ice Shelf and LCIS are indicated by the dashed black arrows (Gordon et al., 1993; Schodlok et al., 2002; Schröder et al., 2002). Shading shows the sea ice concentration for 31 January 2020 (ftp://ftp-projects.cen.uni-hamburg.de/seaice/AMSR2/3.125km). In panel b, the green station markers indicate non-upwelling stations L2-L4 and L6-L16 while the grey markers indicate upwelling stations L1 and L5 (see text for details); the numbers refer to the stations (i.e., 1 is station L1). The surface colour shows the oxygen concentrations, measured by the CTD oxygen sensor which was calibrated to direct measurements via Winkler titration (Hutchinson et al., 2020). Also shown is the position at the time of our sampling of iceberg A68 (6000 km^2) that calved off LCIS in July 2017.

4.3.1 Hydrographic context

At the stations adjacent to LCIS, we observed strong gradients in density (0.14 kg.m^{-3}<$\Delta\sigma_\theta$<0.22 kg.m^{-3}) between the surface mixed layer and the underlying source waters (Fig. 4.2a). Two notable exceptions were shelf-break stations L1 and L5 (open grey symbols in Fig. 4.1b) where weaker density gradients ($\Delta\sigma_\theta$ <0.11 kg.m^{-3}) were evident. Here, we define the surface mixed layer as the depth interval over which a NO_3^-+NO_2^- assimilation signal is apparent (i.e., NO_3^-+NO_2^- δ^{15}N rises as its concentration declines; Fig. 4.3 green symbols, Table 4.1). The source water is Winter Water (WW), the remnant wintertime mixed layer that is found directly beneath the summer mixed layer. WW has a temperature of between -1.85ºC and -1.6ºC and salinity between 34.65 g/kg and 34.70 g/kg (Hutchinson et al., 2020; Nicholls et al., 2004; Robertson et al., 2002; Weppernig et al., 1996) and is found between 48 m and 297 m at LCIS (Fig. 4.2, purple shading). The depth of the surface mixed layer ranged from 50 m to 161 m and averaged 99 ± 34 m for stations L2 to L4 and L6 to L16, while at stations L1 and L5, the mixed layer depth was 125 m and 151 m, respectively (Table 4.1).

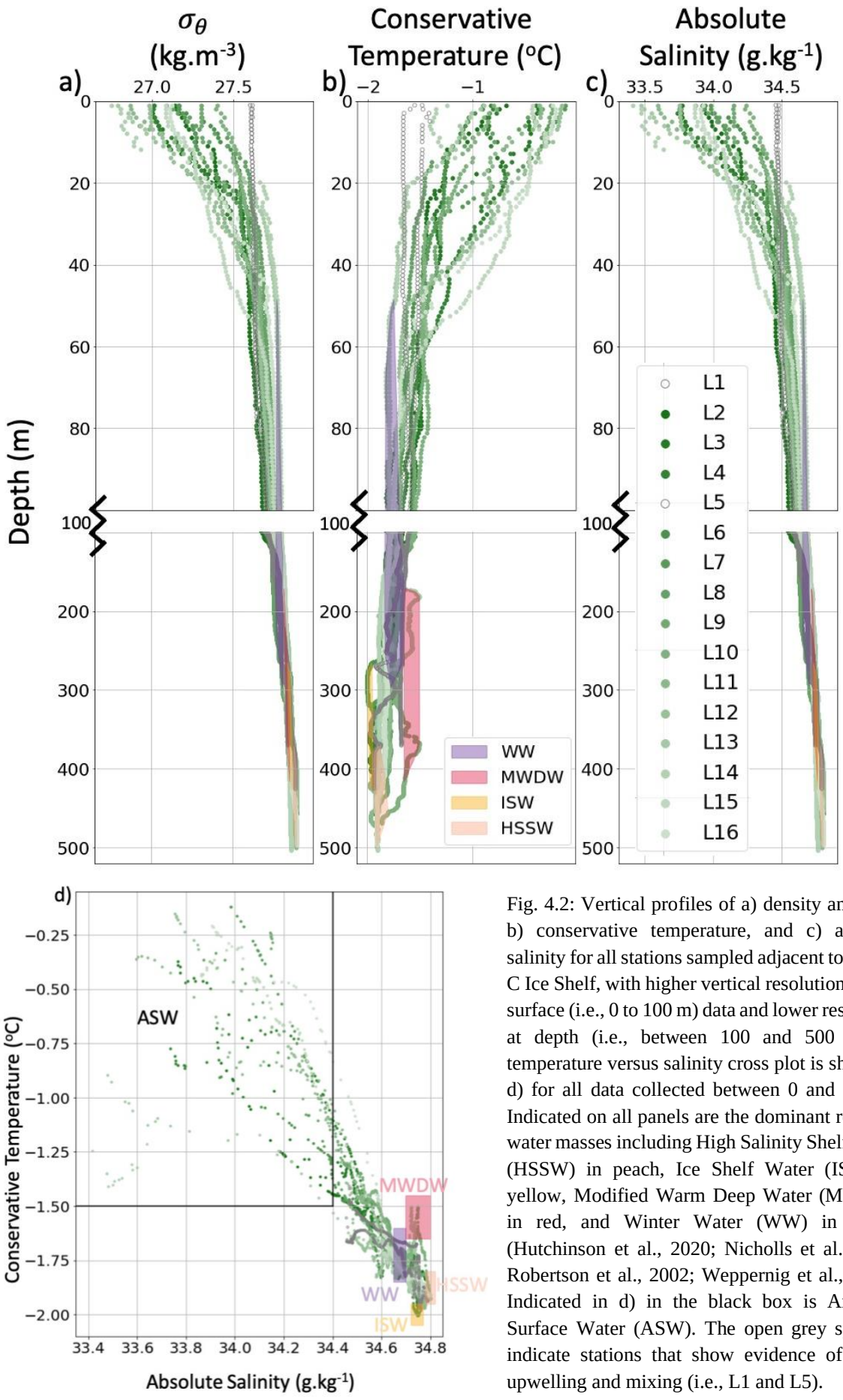

Fig. 4.2: Vertical profiles of a) density anomaly, b) conservative temperature, and c) absolute salinity for all stations sampled adjacent to Larsen C Ice Shelf, with higher vertical resolution for the surface (i.e., 0 to 100 m) data and lower resolution at depth (i.e., between 100 and 500 m). A temperature versus salinity cross plot is shown in d) for all data collected between 0 and 500 m. Indicated on all panels are the dominant regional water masses including High Salinity Shelf Water (HSSW) in peach, Ice Shelf Water (ISW) in yellow, Modified Warm Deep Water (MWDW) in red, and Winter Water (WW) in purple (Hutchinson et al., 2020; Nicholls et al., 2004; Robertson et al., 2002; Weppernig et al., 1996). Indicated in d) in the black box is Antarctic Surface Water (ASW). The open grey symbols indicate stations that show evidence of recent upwelling and mixing (i.e., L1 and L5).

The shallowest measured oxygen concentrations (~1 m) ranged from 364 μmol/l to 389 μmol/l (98% to 107% saturation) at all but the two shelf break stations (L1 and L5) where lower surface oxygen concentrations were measured (315 μmol/l and 316 μmol/l, respectively, 84% saturation in both cases; Fig. 4.1b). Since oxygen equilibrates rapidly with the atmosphere, undersaturated surface concentrations indicate recent (possibly ongoing) upwelling of lower-oxygen subsurface waters, which is consistent with the weak density gradients observed at stations L1 and L5 (Fig. 4.2a). By contrast, the other 14 stations were characterized by a strongly stratified upper water column and no evidence in the oxygen data of upwelling at the time of our sampling.

4.3.2 Nutrient concentrations and isotopes

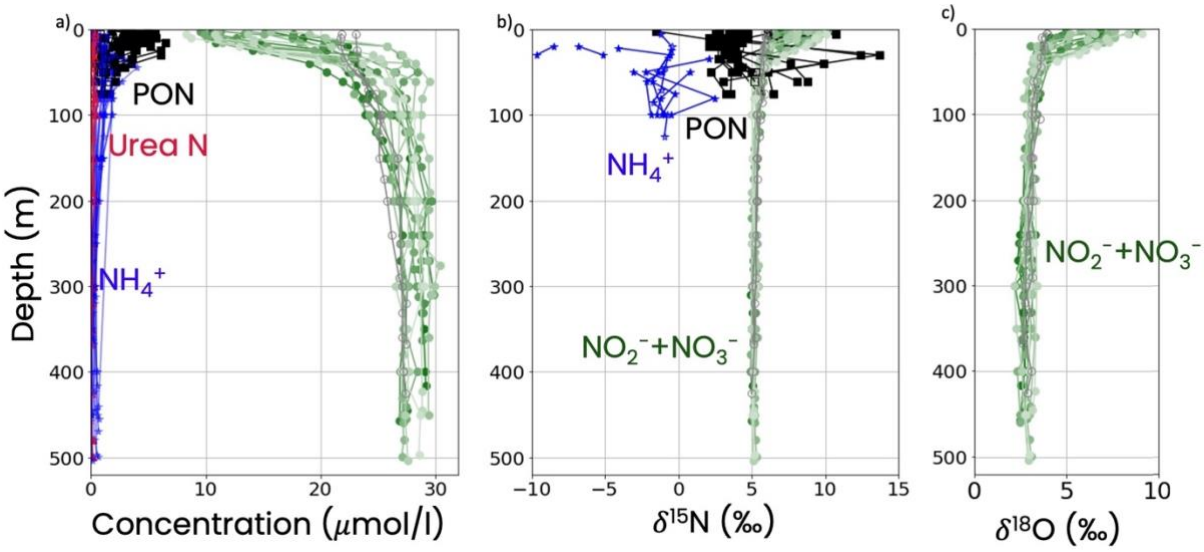

Fig. 4.3: Vertical profiles of the measured a) concentration and b) $\delta^{15}N$ of PON (black), urea N (red), NH_4^+ (blue), and NO_3^-+NO_2^- (green) at all stations sampled adjacent to Larsen C Ice Shelf. Also shown is c) the $\delta^{18}O$ of NO_3^-+NO_2^-. We do not distinguish among stations here as we observe no coherent trend between station hydrography or biogeochemistry and distance from the shelf or latitude. In the text, we instead report the regional average parameters, taking the different stations to represent varying degrees of consumption of the same NO_3^-+NO_2^- source. The exception to this is upwelling stations L1 and L5, which are shown by the open grey symbols; these stations are not included in the regional averages.

The nutrient concentrations presented here were first reported by Flynn et al. (2021). At stations L2 to L4 and L6 to L16, the mixed layer NO_3^-+NO_2^- concentrations ranged from 16.4 μmol/l to 23.7 μmol/l (averaging 20.3 ± 2.3 μmol/l; n = 14 stations), which amounts to a decrease of 3.7 μmol/l to 11.1 μmol/l (average of 7.1 ± 2.6 μmol/l; n = 14 stations) relative to the concentrations measured in the underlying WW (average NO_3^-+NO_2^- concentration of 27.4 ±

1.1 μmol/l across the sampling region; Fig. 4.3a green symbols, Table 4.1). Coincident with the subsurface-to-mixed layer decline in the NO_3^-+NO_2^- concentrations, NO_3^-+NO_2^- $\delta^{15}N$ increased between 0.60‰ and 2.23‰ (1.10 ± 0.45‰ on average; n = 14) and $\delta^{18}O$ increased between 0.31‰ and 2.51‰ (1.09 ± 0.57‰ on average; n = 14) relative to the source WW where NO_3^-+NO_2^- $\delta^{15}N$ and $\delta^{18}O$ averaged 5.21 ± 0.12‰ and 3.01 ± 0.20‰, respectively (Fig. 4.3b and c, green symbols). Stations L1 and L5 showed weaker gradients, with an average source-to-mixed-layer decrease in the NO_3^-+NO_2^- concentration of 3.6 ± 1.4 μmol/l and increase in the $\delta^{15}N$ and $\delta^{18}O$ of 0.47 ± 0.13‰ and 0.28 ± 0.35‰, respectively (n = 2). At all stations, NO_3^-+NO_2^- $\delta^{15}N$ and $\delta^{18}O$ increased approximately in unison from the WW to the surface, with a $\Delta\delta^{18}O$: $\Delta\delta^{15}N$ ratio of approximately 1.17:1 (Fig. 4.4).

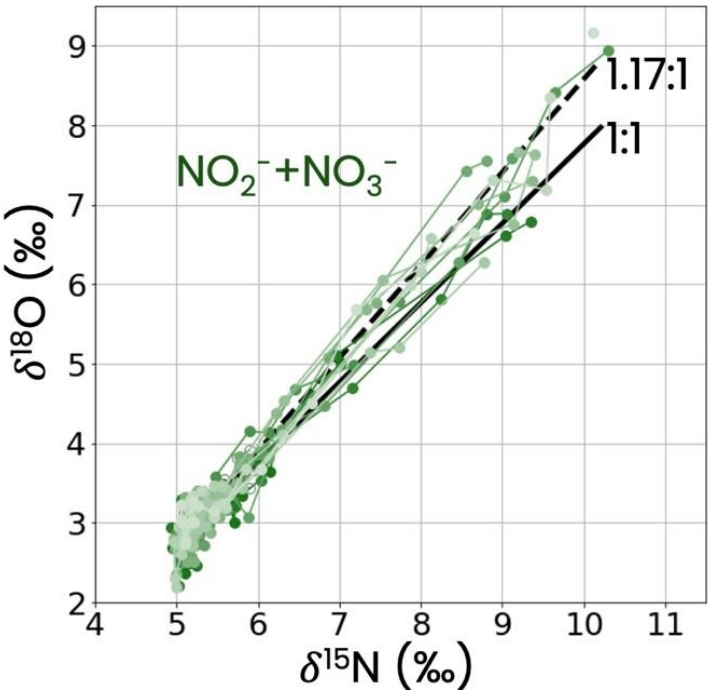

Fig. 4.4: NO_3^-+NO_2^- $\delta^{18}O$ versus $\delta^{15}N$ with the 1:1 (solid line) and 1.17:1 (dashed line) relationships plotted. The data largely fall on the 1.17:1 line, a relationship that can be explained by NO_3^-+NO_2^- assimilation by phytoplankton. This relationship further indicates that the NO_3^-+NO_2^- $\delta^{18}O$ versus $\delta^{15}N$ data show no evidence of surface-layer nitrification.

The NO_2^- concentrations were low throughout the mixed layer across the study region (average of 0.04 ± 0.02 μmol/l, reaching a maximum of 0.16 ± 0.13 μmol/l at station L6 (5 m); data not shown). Since the mixed-layer NO_3^-+NO_2^- concentrations averaged 20.3 ± 2.3 μmol/l, reaching a minimum of 8.3 ± 0.1 μmol/l at station L16 (5 m), NO_2^- accounted for an average of 0.2 ± 0.1% (maximum of 1.0 ± 0.2%) of the NO_3^-+NO_2^- pool. This result indicates that for NO_2^- to have a noticeable impact on the isotopic composition of the NO_3^-+NO_2^- pool, it would have to be extremely low in $\delta^{15}N$ and/or $\delta^{18}O$. Since the $\delta^{15}N$ of NO_2^- in the Antarctic Zone of the Southern Ocean has been estimated to range from -80‰ to -20‰ (Fripiat et al., 2019; Kemeny et al., 2016; Smart et al., 2015), we cannot rule out an influence of the low measured NO_2^- concentrations on the $\delta^{15}N$ of NO_3^-+NO_2^-. Extremely low NO_2^- $\delta^{15}N$ is hypothesized to result from an equilibrium N isotope effect between NO_3^-+NO_2^- that is expressed during enzymatic

NO_3^- – NO_2^- interconversion (Buchwald & Wankel, 2022; Kemeny et al., 2016). This process concentrates ^{15}N in the NO_3^- pool, strongly decreasing the $\delta^{15}N$ of the NO_2^- pool but leaving the $\delta^{15}N$ of the NO_3^-+NO_2^- pool unchanged (Kemeny et al., 2016). The impact of interconversion on the $\delta^{18}O$ of NO_2^-+NO_3^- is complex, but appears to result in a net decrease in NO_2^-+NO_3^- $\delta^{18}O$ (Buchwald & Wankel, 2022) driven by the open system incorporation and loss of O atoms as well as abiotic exchange between seawater and NO_2^- (Boshers et al., 2019; Buchwald & Casciotti, 2013; Buchwald & Wankel, 2022). Building on the work of Kemeny et al. (2016), in a recent analysis of data from all sectors of the Antarctic Zone of the Southern Ocean, Fripiat et al. (2019) concluded that isotopic changes to the NO_3^-+NO_2^- pool better record phytoplankton nitrate assimilation than do the isotopes of NO_3^- only. As such, we focus here on the combined NO_3^-+NO_2^- pool.

The mixed-layer NH_4^+ concentrations ranged from 0.1 to 4.0 μmol/l, averaging 0.91 ± 0.29 μmol/l (Fig. 4.3a blue symbols and Table 4.1; n = 14 stations). In all profiles, the NH_4^+ concentration typically reached a maximum near the base of the mixed layer before declining to values <0.35 μmol/l by 250 m. Surface mixed-layer concentrations of urea were lower than NH_4^+, averaging 0.20 ± 0.06 μmol/l, with a maximum of 0.48 μmol/l measured at 5 m and 10 m at stations L1 and L15, respectively (Fig. 4.3a). The urea concentrations showed no distinctive pattern with depth in or below the mixed layer, remaining consistently low and averaging 0.25 μmol/l by 250 m. Where measurable, NH_4^+ $\delta^{15}N$ ranged between -4.0‰ and 2.5‰, averaging -0.9‰ ± 0.3‰ (std error) with a median of -1.1 ± 0.1‰ when the four measurements of NH_4^+ $\delta^{15}N$ <-5‰ are excluded (Fig. 4.3b, blue symbols; see section 4.4.2.2 below). There was no clear pattern in NH_4^+ $\delta^{15}N$ with depth, with fairly homogenous values observed throughout the mixed layer. Stations L1 and L5 showed a less significant NH_4^+ concentration decrease into the surface than the other LCIS stations, while their urea distributions were similar to the other stations. Additionally, the NH_4^+ $\delta^{15}N$ at L1 appeared marginally less variable than at the non-upwelling LCIS stations (NH_4^+ $\delta^{15}N$ was not measured for station L5; Appendix Fig. A1 to Fig. A16).

The PON concentrations at stations L2-L4 and L6-L16 increased from an average of 0.35 ± 0.05 μmol/l in the WW to a mixed-layer average of 3.05 ± 0.83 μmol/l (range of 0.3 to 6.5 μmol/l, median of 3.2 μmol/l; Fig. 4.3a, black symbols). By contrast, the $\delta^{15}N$ of PON decreased towards the surface, from an average of 8.5 ± 0.3‰ in the source WW to 3.8 ± 1.3‰

in the mixed layer. Stations L1 and L5 had a much lower mixed-layer PON concentration, of 1.29 ± 0.64 μmol/l, and a higher average PON δ^{15}N, of 4.2 ± 0.2‰.

The physical and biogeochemical properties of stations L1 and L5 clearly differ from the rest of the stations, with the upper water column characterized by weak WW-to-mixed-layer density gradients, unsaturated surface oxygen concentrations, minimal NO_3^-+NO_2^- drawdown, high mixed-layer NH_4^+ concentrations, and low mixed-layer PON concentrations. These traits are consistent with stations L1 and L5 having undergone recent upwelling and/or mixing along the shelf front (as was also concluded by Flynn et al. (2021)), possibly as a result of wind-driven Ekman suction. By contrast, we see no evidence of upwelling or vigorous mixing at stations L2-L4 and L6-L16 where the surface oxygen concentrations were fully saturated and the mixed layer was strongly stratified. Additionally, we observe no coherent trend between the properties of stations and their distance from the ice shelf or latitude. We have, therefore, chosen to treat stations L2-L4 and L6-L16 as representing varying degrees of consumption of the same NO_3^- +NO_2^- source (i.e., WW), supplied prior to our sampling and subsequently isolated below the mixed layer by the strong pycnocline. As such, unless otherwise stated, all averages reported in the Discussion refer to stations L2-L4 and L6-L16.

4.4 Discussion:

At the 14 stratified stations occupied in the waters adjacent to LCIS in mid-summer 2019, we observed clear evidence of photosynthetic NO_3^-+NO_2^- drawdown in the strong decrease in NO_3^- +NO_2^- concentration and increase in NO_3^-+NO_2^- δ^{15}N and δ^{18}O between the source WW and the surface (Fig. 4.3, green symbols). On average, mixed-layer NO_3^-+NO_2^- concentrations declined by 7.1 μmol/l relative to the concentration that would have been supplied by convective mixing in winter. This decrease is far larger than that observed during the same cruise in the offshore Weddell Sea (0.4 ± 0.3 μmol/l; Flynn et al. (2021)) and on the higher end of previous Polar Antarctic Zone (PAZ) observations (2 – 9 μmol/l; DiFiore et al., 2009; Fripiat et al., 2019). In addition, the mixed layer PON concentrations (which averaged >3 μmol/l across the region) were high relative to summertime measurements from the open Weddell Sea (0.7 ± 0.3 μmol/l; Flynn et al. (2021)) and the PAZ north of the Coastal and Continental Shelf Zone (2.2 ± 0.2 μmol/l; DiFiore et al. (2009)). Our data thus indicate that the sunlit surface waters adjacent to LCIS support high rates of summertime phytoplankton productivity, and

relatedly, a strong biological pump. Below, we use our data to quantify the strength of the LCIS biological pump.

4.4.1 The seasonal cycle of NO_3^-+NO_2^- supply and consumption near LCIS

The seasonal cycle of perpetually sunlit summers and dark winters heavily impacts the Southern Ocean upper water column structure. In winter, the upper water column of the western Weddell Sea is covered by sea ice (Vernet et al., 2019) and characterized by deep mixed layers and low productivity due to light limitation of phytoplankton (Mitchell et al., 1991; Nicholls et al., 2009). During this season, deep on-shelf convection introduces high subsurface NO_3^-+NO_2^- concentrations into the mixed layer (Hoppema et al., 2007). In spring and summer, with surface warming and the influx of relatively warm and fresh meltwater, a shallow mixed layer stratifies out of the winter mixed layer (Nicholls et al., 2009; Weppernig et al., 1996). As such, a remnant winter mixed layer is preserved directly beneath the summer mixed layer (i.e., the so-called WW layer), which archives the physical and biogeochemical conditions present at the beginning of the spring growing season following wintertime NO_3^-+NO_2^- recharge.

The N sources consumed by phytoplankton also shift with the changing seasons. In the winter Southern Ocean, iron and extreme light limitation result in the near cessation of photosynthetic NO_3^-+NO_2^- uptake (Mdutyana et al., 2020), with the primary biological processes instead being ammonification and nitrification of PON and regenerated N forms (i.e., NH_4^+) that remain from the previous autumn, along with slow assimilation of regenerated N (Mdutyana et al., 2020, 2022a,b; Philibert et al., 2015; Smart et al., 2015; Smith et al., 2022). Ultimately, NH_4^+ assimilation and oxidation during winter and early spring lead to very limited availability of regenerated N in spring and early summer (Smith et al., 2022). Coupled with enhanced iron availability following winter mixing, this condition renders NO_3^-+NO_2^- the primary N source to phytoplankton at the start of the growing season. As light returns in spring, phytoplankton begin to assimilate NO_3^-+NO_2^- to produce biomass, a process that likely began for our sampling region with the opening of a polynya at LCIS on the 30th of November 2018, roughly two months prior to sampling (Flynn et al., 2021). The removal of sea ice through the opening of the polynya would have increased the light available to phytoplankton (by reducing shading, combined with a melt water-driven shoaling of the mixed layer), causing biological production to ramp up. As the growing season continues, biomass (i.e., PON) concentrations increase, with

some organic matter sinking into the subsurface and some accumulating in the mixed layer. In both cases, the biomass is consumed by heterotrophic organisms (e.g., bacteria and zooplankton), resulting in the production of NH_4^+ and dissolved organic N forms that fuel nitrification at depth and support further phytoplankton growth in the surface. As such, we expect the proportion of primary production fueled by regenerated N to rise as the growing season progresses, particularly as NH_4^+ concentrations increase and iron is depleted (Goeyens et al., 1995). With such a transition to proportionally more regenerated production, the phytoplankton community will likely change from one dominated by large, ballasted diatoms that are strong vectors for carbon export, to one dominated by smaller and/or less dense phytoplankton, including mixotrophs, that contribute significantly less to carbon export (Deppeler & Davidson, 2017; Goeyens et al., 1995; Karsh et al., 2003; Koike et al., 1986; Lomas & Glibert, 1999; Petrou et al., 2016; Probyn & Painting, 1985; Wright et al., 2010).

4.4.2 Quantifying carbon export potential using N isotopes

Biological pump strength can be assessed by quantifying the amount of organic matter exported out of the mixed layer. Assuming that the surface ocean is in a steady-state over an annual cycle, the strength of the biological pump can be approximated by the f-ratio (shorthand for "flux ratio"; Eppley & Peterson, 1979):

$$f-ratio = \frac{new\ production}{new+regenerated\ production} \quad \text{Eq 4.1}$$

As per the original formulation of the new production paradigm (Dugdale & Goering, 1967), new production is the phytoplankton growth supported by subsurface NO_3^-+NO_2^- mixed up into the surface layer, and regenerated production is the phytoplankton growth supported by recycled N, which we take to be well represented by NH_4^+ (see section 4.4.2.2 below). Together, these N forms are used to build biomass (PON) with a δ^{15}N that is set by the fraction of NO_3^-+NO_2^- ($f\mathrm{NO_3^-}$) versus NH_4^+ ($f\mathrm{NH_4^+}$) consumed by the phytoplankton, along with their respective δ^{15}N values ($\delta^{15}N_{NO3\ consumed}$ and $\delta^{15}N_{NH4\ consumed}$, respectively).

$$\delta^{15}N_{PON} = fNO_3^-(\delta^{15}N_{NO3\ consumed}) + fNH_4^+(\delta^{15}N_{NH4\ consumed}) \quad \text{Eq 4.2a}$$

where

$$fNO_3^- + fNH_4^+ = 1 \quad \text{Eq 4.2b}$$

such that

$$\delta^{15}N_{PON} = fNO_3^-(\delta^{15}N_{NO3\ consumed}) + (1 - fNO_3^-)(\delta^{15}N_{NH4\ consumed}) \quad \text{Eq 4.2c}$$

Provided mixed-layer nitrification is negligible (see section 4.4.2.3.1 below), NO_3^-+NO_2^- consumption in the mixed-layer near LCIS should approximate new production because other potential sources of new N (i.e., atmospheric N deposition, riverine N inputs, and N_2 fixation (which is reduced at cold temperatures or if ambient NO_3^- is present (Holl & Montoya, 2005; Knapp et al., 2012; Staal et al., 2003))) are negligible in the Antarctic Zone (Jickells et al., 2017 and references therein). As such, $f\mathrm{NO_3^-}$ in Eq 4.2c is equivalent to the f-ratio and can be computed following Fawcett et al. (2011) as:

$$f - ratio = \frac{\delta^{15}N_{PON} - \delta^{15}N_{NH4\ consumed}}{\delta^{15}N_{NO3\ consumed} - \delta^{15}N_{NH4\ consumed}} \quad \text{Eq 4.3}$$

Below, we discuss each of the terms in Eq 4.3 and then solve for the f-ratio at LCIS.

4.4.2.1 $\delta^{15}\mathrm{N_{PON}}$

The concentration and δ^{15}N of the particles measured in the mixed layer ($\mathrm{PON_{measured}}$) represent the sum of a dominant growing PON component ($\mathrm{PON_{growing}}$) and a minor recalcitrant ("background") component ($\mathrm{PON_{background}}$). The $\mathrm{PON_{background}}$ is highly decomposed material that was present in the surface waters at the beginning of the growing season, remaining following in situ wintertime ammonification and/or mixed-up during winter convection from the subsurface (along with NO_3^-+NO_2^-) where it would have been strongly decomposed by heterotrophic bacteria. We suggest that $\mathrm{PON_{background}}$ can be approximated by the PON measured in the source WW, which has a concentration and δ^{15}N of 0.35 ± 0.05 μmol/l and 8.50 ± 0.35‰, respectively. These values are consistent with previous wintertime surface PON concentrations of 0.2 to 0.5 μmol/l in the PAZ (Smith et al., 2022). Additionally, Smart et al. (2020) showed for the Polar Frontal Zone of the Southern Ocean that PON δ^{15}N can rise by as much as 8‰ (mean of ~5‰) between summer and late winter as its concentration declines, which the authors attributed to net heterotrophic degradation in winter. Finally, our measured WW PON δ^{15}N is similar to the theoretical value of 6.45 ± 1.60‰ that we calculate by

degrading the average mixed layer $PON_{measured}$ (concentration = 3.05 ± 0.83 μmol/l and $\delta^{15}N$ = 3.8 ± 1.3‰) to the deep concentration of 0.35 μmol/l using the steady state equation (i.e., $\delta^{15}N_{PON\ degraded} = \delta^{15}N_{PON\ measured} + {}^{15}\varepsilon_{ammonification} \cdot (1 - f)$, where f is the degree of consumption of $PON_{measured}$; Sigman & Fripiat (2019)) and a ${}^{15}\varepsilon_{ammonification}$ of 3.0 ± 0.1‰ (Lehmann et al., 2002; Möbius, 2012).

$PON_{growing}$ can be calculated by removing $PON_{background}$ from $PON_{measured}$, which yields an average mixed layer $PON_{growing}$ concentration and $\delta^{15}N$ of 2.70 ± 0.83 μmol/l and 3.2 ± 2.3‰, respectively (versus 3.05 ± 0.83 μmol/l and 3.8 ± 1.3‰ for $PON_{measured}$). Mixed layer $PON_{measured}$ is thus clearly dominated by $PON_{growing}$, with the low concentration and high $\delta^{15}N$ of $PON_{background}$ only making up a small fraction (on average 0.11 ± 0.04) of the mixed layer $PON_{measured}$. Supporting this notion is the biomass C : N ratio measured at LCIS at the time of our sampling (average of 7.4 ± 1.9; Flynn et al. (2021)), which is indistinguishable from that expected for non-limited phytoplankton (6.63; Redfield et al. (1963)), indicating that the measured PON pool is largely the result of active and balanced phytoplankton growth (Hupe & Karstensen, 2000; Körtzinger et al., 2001; Osterroht & Thomas, 2000; Thomas et al., 1999). Additionally, data collected coincident with our sampling show that the rates of primary productivity at LCIS were extremely high, and that the upper-ocean ecosystem was dominated by rapidly growing phytoplankton taxa such as *Phaeocystis antarctica* and the centric diatom, *Thalassiosira sp*. (Flynn et al., 2021). Since $PON_{growing}$, despite being similar to $PON_{measured}$ in the mixed layer, more accurately represents the concentration and $\delta^{15}N$ of the biomass formed through N consumption during the growing season, all use of mixed-layer PON hereafter refers to $PON_{growing}$, unless otherwise noted.

4.4.2.2 $\delta^{15}N_{NH4\ consumed}$

At the concentrations of NH_4^+ measured in our study, the available data suggest that its consumption by phytoplankton will occur with negligible isotopic fractionation (Hoch et al., 1992; Liu et al., 2013); thus, the PON produced through NH_4^+ assimilation will have a $\delta^{15}N$ that is the same as the $\delta^{15}N$ of the NH_4^+ pool present at the time of sampling. Here, we directly measured the $\delta^{15}N$ of NH_4^+, which is unusual for open ocean studies given the detection limit of the available method.

The method used to measure the $\delta^{15}N$ of NH_4^+ is tricky and can produce strongly negative values if NH_4^+ conversion to NO_2^- is incomplete (Zhang et al., 2007). We observe four anomalously low NH_4^+ $\delta^{15}N$ values, between -9.5‰ and -5.1‰, at stations L13 and L14. Before discounting these values as methodological artefacts, we must first consider whether there exists an in-situ mechanism (or combination of mechanisms) that could generate such low-$\delta^{15}N$ NH_4^+. NH_4^+ assimilation appears to occur without significant isotopic fractionation at NH_4^+ concentrations <5 μmol/l (Hoch et al., 1992; Liu et al., 2013; Pennock et al., 1996), and so should not change the $\delta^{15}N$ of NH_4^+ in the water column. By contrast, marine ammonia oxidation occurs with a strongly positive isotope effect ranging from 14-19‰ (Casciotti et al., 2003) which would act to increase, rather than decrease, the $\delta^{15}N$ of the NH_4^+ pool being oxidized. The only process that lowers the $\delta^{15}N$ of NH_4^+ is the ammonification of organic N, which occurs with a small isotope effect of ~3‰ (i.e., producing NH_4^+ that is ~3‰ lower in $\delta^{15}N$ than the PON being ammonified; Lehmann et al. (2002); Möbius, (2012)). This mechanism has previously been invoked to explain the production of low-$\delta^{15}N$ NH_4^+ in the late summer/autumn Southern Ocean, where partial remineralisation of euphotic zone PON followed by export of high-$\delta^{15}N$ PON results in low $\delta^{15}N$ NH_4^+ being retained in the surface layer (Möbius, 2012; Smart et al., 2015). Repeated cycles of these processes can significantly lower surface NH_4^+ $\delta^{15}N$ (Lourey et al., 2003; Smart et al., 2015). However, for this mechanism to yield $\delta^{15}N$ NH_4^+ values of -9.5‰ to -5.1‰ would require the PON being remineralised to have a $\delta^{15}N$ of -6.5‰ to -2.1‰ (i.e., $\delta^{15}N$ NH_4^+ plus an isotope effect of 3‰), which we do not observe in our mixed-layer measured PON $\delta^{15}N$ data that average 3.8 ± 1.3‰ (minimum measured value of -1.5‰ at 2 m at station L3, with the next lowest measured PON $\delta^{15}N$ being 2.1‰ at 10 m at station L13). Thus, a far more likely explanation of the four very low NH_4^+ $\delta^{15}N$ values is that they derive from the incomplete conversion of NH_4^+ to NO_2^- during analysis (Zhang et al., 2007). Removing these methodological outliers yields a regional average NH_4^+ $\delta^{15}N$ of -0.9 ± 0.3‰ (n = 7 stations).

We apply the regional average NH_4^+ $\delta^{15}N$ to all stations in our analysis as only samples with an NH_4^+ concentration >0.8 μmol/l could be analyzed for $\delta^{15}N$ (i.e., we do not have NH_4^+ $\delta^{15}N$ data from all stations and depths). Nonetheless, all our measured values of NH_4^+ $\delta^{15}N$ are similar, which suggests that applying the regional average to all stations is reasonable. NH_4^+ is not the only recycled N form available to phytoplankton, however, with growth supported by urea also constituting regenerated production. Urea was unlikely a primary N source to

phytoplankton at the time of our sampling as the urea concentrations were low, averaging 0.20 ± 0.06 μmol/l, and showed no clear pattern with depth, either within or below the mixed layer (Fig. 4.3a). While low urea concentrations do not necessarily indicate a low urea flux, the lack of a clear pattern with depth to 200 m indicates that in net, urea assimilation was not significantly depleting the surface urea pool. This notion is supported by direct rate measurements of urea and NH_4^+ uptake made at 10 of the LCIS stations at the same time as our sampling (Flynn et al., 2021). The regionally averaged, euphotic zone-integrated rates of NH_4^+ uptake (2.6 ± 1.3 mmol/m^2/d) were far higher than those of urea uptake (0.6 ± 0.3 mmol/m^2/d), demonstrating that NH_4^+ was the primary regenerated N source to phytoplankton, at least at the time of our sampling. In any case, even if urea did support significant regenerated production at LCIS (e.g., prior to our sampling), we expect it to be similarly low in δ^{15}N to NH_4^+ because of the similar isotope effects associated with its production (Macko et al., 1986; Silfer et al., 1992). Additionally, as urea assimilation appears to occur with no isotope effect (Waser et al., 1998b), urea-fueled PON would have a low δ^{15}N, similar to that resulting from the assimilation of NH_4^+. Within our analytical framework, this low-δ^{15}N PON would be characterized as regenerated production, regardless of whether it was fueled by urea or NH_4^+. We thus conclude that regenerated production is reasonably represented by $\delta^{15}N_{NH4\ consumed}$ (i.e., the mean NH_4^+ δ^{15}N of -0.9 ± 0.3‰).

4.4.2.3 $\delta^{15}N_{NO3\ consumed}$

The δ^{15}N of new production is significantly more complicated to calculate than the $\delta^{15}N_{NH4\ consumed}$ as we must account for isotopic fractionation during NO_3^-+NO_2^- assimilation given that the mixed layer NO_3^-+NO_2^- concentrations were non-zero across the study region. Since the upper water column was well stratified at the time of our sampling, we can use the Rayleigh model to estimate both $^{15}\varepsilon_{assim}$ and the δ^{15}N of the PON that would be produced from the consumption of NO_3^-+NO_2^- (i.e., new production; $\delta^{15}N_{NO3\ consumed}$).

4.4.2.3.1 The N and O isotope effects of NO_3^-+NO_2^- assimilation

The Rayleigh model (Mariotti et al., 1981) describes a unidirectional transformation (in this case, NO_3^-+NO_2^- assimilation into PON) that proceeds with a constant isotope effect ($^{15}\varepsilon_{assim}$) under conditions where the reactant (NO_3^-+NO_2^-) is neither resupplied (e.g., by mixing) nor lost (e.g., via sinking) by any mechanism other than the unidirectional transformation

(assimilation into PON). The Rayleigh model-derived relationship between the δ^{15}N and concentration of the reactant pool, as well as the isotope effect associated with its consumption, is represented by Eq 4.4 (Fripiat et al., 2019; Mariotti et al., 1981)

$$\delta^{15}N_{NO_3^-+NO_2^-} = \delta^{15}N^{o}_{NO_3^-+NO_2^-} - {}^{15}\varepsilon_{assim} \cdot ln\left(\frac{[NO_3^-+NO_2^-]}{[NO_3^-+NO_2^-]_o}\right) \quad \text{Eq 4.4}$$

Where $[NO_3^- + NO_2^-]$ is the $NO_3^-+NO_2^-$ concentration and the sub/superscript "o" denotes the source water values. Eq 4.4 can be rearranged to allow for the calculation of the isotope effect ($^{15}\varepsilon_{assim}$):

$$-{}^{15}\varepsilon_{assim} = \frac{\delta^{15}N_{NO_3^-+NO_2^-} - \delta^{15}N^{o}_{NO_3^-+NO_2^-}}{\ln([NO_3^-+NO_2^-]) - \ln([NO_3^-+NO_2^-]_o)} \quad \text{Eq 4.5}$$

The isotope effect can thus be determined from the negative slope of the relationship between the δ^{15}N of $NO_3^-+NO_2^-$ and ln($[NO_3^-+NO_2^-]$) (Fig. 4.5). Applying the Rayleigh model to the data available over the depth of the $NO_3^-+NO_2^-$ assimilation signal at all our non-upwelling stations (L2-L4 and L6-L16), we calculate a mean $^{15}\varepsilon_{assim}$ of 4.1 ± 0.7‰ (Fig. 4.5a; n = 14 stations; estimates of $^{15}\varepsilon_{assim}$ for each station in Appendix Fig. A1.1 to Fig. A1.16). Upwelling stations L1 and L5 show a much lower degree of $NO_3^-+NO_2^-$ drawdown (Fig. A1.1 and Fig. A1.5), with a $^{15}\varepsilon_{assim}$ of 3.6 ± 0.6‰ and 2.4 ± 1.4‰ calculated for stations L1 and L5, respectively (Fig. 4.5c).

The O isotope ratio of $NO_3^-+NO_2^-$ ($^{18}O/^{16}O$, reported as δ^{18}O versus VSMOW) can also be used to calculate the $NO_3^-+NO_2^-$ assimilation isotope effect ($^{18}\varepsilon_{assim}$), by substituting $\delta^{18}O_{NO_3^-+NO_2^-}$ for $\delta^{15}N_{NO_3^-+NO_2^-}$ in Eq 4.5. Using the measured δ^{18}O of $NO_3^-+NO_2^-$, we calculate a mean $^{18}\varepsilon_{assim}$ of 4.7 ± 0.8‰ for stations L2-L4 and L6-L16 (Fig. 4.5b; n = 14 stations; estimates of $^{18}\varepsilon_{assim}$ for each station in Fig. A1.1 to Fig. A1.16) and 4.7 ± 0.6‰ and 5.0 ± 0.6‰ for stations L1 and L5.

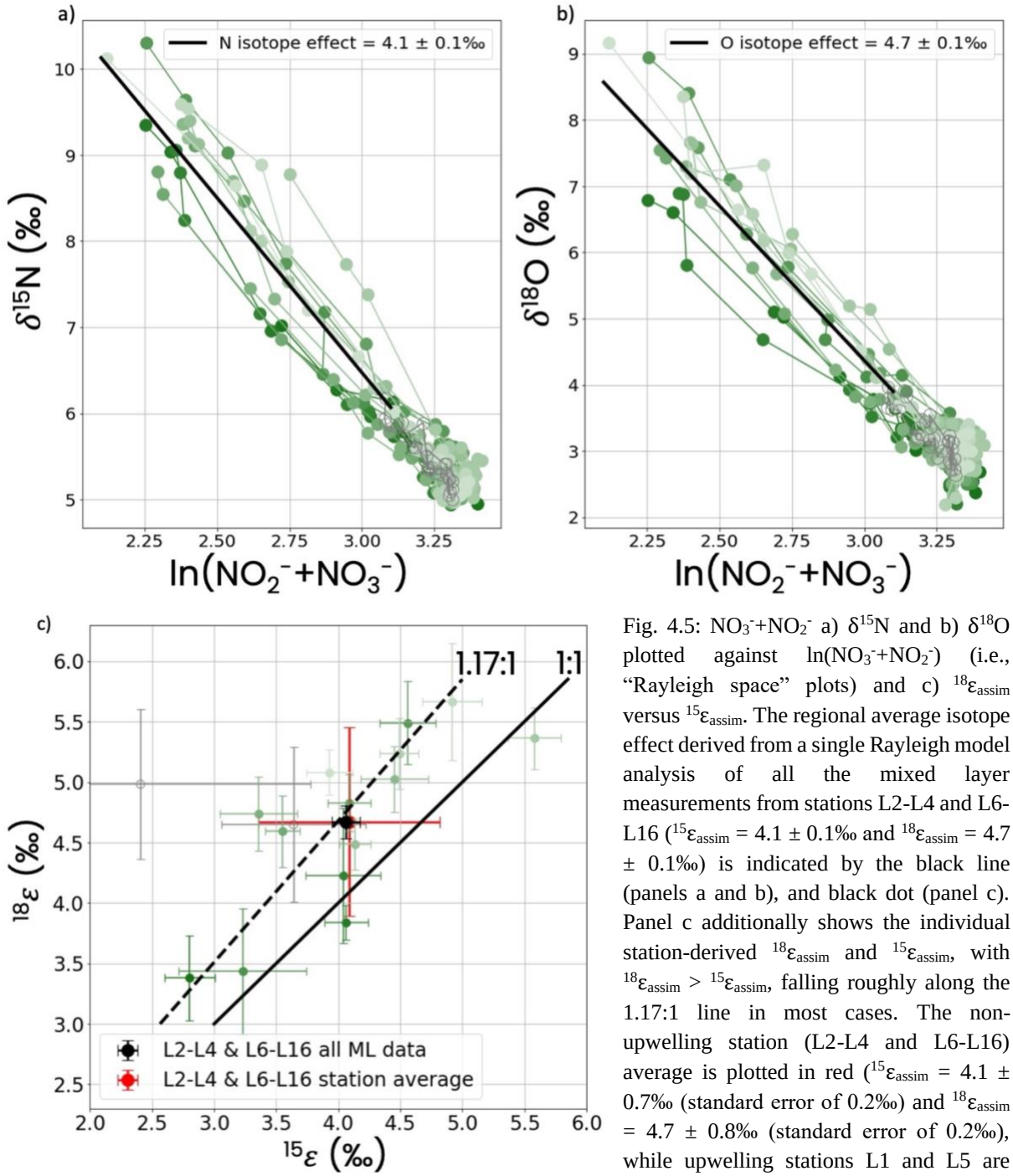

Fig. 4.5: $NO_3^-+NO_2^-$ a) $\delta^{15}N$ and b) $\delta^{18}O$ plotted against $\ln(NO_3^-+NO_2^-)$ (i.e., "Rayleigh space" plots) and c) $^{18}\varepsilon_{assim}$ versus $^{15}\varepsilon_{assim}$. The regional average isotope effect derived from a single Rayleigh model analysis of all the mixed layer measurements from stations L2-L4 and L6-L16 ($^{15}\varepsilon_{assim}$ = 4.1 ± 0.1‰ and $^{18}\varepsilon_{assim}$ = 4.7 ± 0.1‰) is indicated by the black line (panels a and b), and black dot (panel c). Panel c additionally shows the individual station-derived $^{18}\varepsilon_{assim}$ and $^{15}\varepsilon_{assim}$, with $^{18}\varepsilon_{assim}$ > $^{15}\varepsilon_{assim}$, falling roughly along the 1.17:1 line in most cases. The non-upwelling station (L2-L4 and L6-L16) average is plotted in red ($^{15}\varepsilon_{assim}$ = 4.1 ± 0.7‰ (standard error of 0.2‰) and $^{18}\varepsilon_{assim}$ = 4.7 ± 0.8‰ (standard error of 0.2‰), while upwelling stations L1 and L5 are shown in grey. Error bars represent ± 1 standard deviation. The introduction of $NO_3^-+NO_2^-$ to the mixed layer via upwelling or mixing violates the conditions of the Rayleigh model, artificially lowering the calculated $^{15}\varepsilon_{assim}$ and $^{18}\varepsilon_{assim}$ (Sigman et al., 1999); L1 appears to fall in line with the mean regional estimate and only $^{15}\varepsilon_{assim}$ is lower than expected at L5.

At all stations, the derived $^{18}\varepsilon_{assim}$ is either statistically indistinguishable from, or slightly higher than, the coincident estimate of $^{15}\varepsilon_{assim}$ (Fig. 4.5c). Stations L2 and L6 are characterized by an unexpectedly low $^{15}\varepsilon_{assim}$ of 2.8 ± 0.2‰ and 3.2 ± 0.5‰, respectively, and $^{18}\varepsilon_{assim}$ of 3.4 ± 0.4‰ and 3.4 ± 0.5‰ (Fig. 4.5c). These lower values of $^{15}\varepsilon_{assim}$ and $^{18}\varepsilon_{assim}$ may result from water

column mixing, which would violate the closed system Rayleigh model through the addition of deep, high-concentration low-δ^{15}N and δ^{18}O NO_3^-+NO_2^- to surface waters (Sigman et al., 1999). The addition of this deeper NO_3^-+NO_2^- lowers the shallow NO_3^-+NO_2^- δ^{15}N and δ^{18}O to a greater degree than it increases its concentration, in net lowering the calculated $^{15}\varepsilon_{assim}$ and $^{18}\varepsilon_{assim}$ (Appendix Fig. A2.1.1). However, there is no hydrographic evidence for upwelling or mixing at stations L2 and L6, which both have strong density gradients of $\Delta\sigma_\theta$ > 0.16 kg/m^3 between the mixed layer and the waters beneath (Fig. 4.2). That said, mixing may have occurred prior to our sampling, with the surface layer subsequently stratifying following its cessation even as the δ^{15}N (and δ^{18}O) of NO_3^-+NO_2^- versus ln([NO_3^-+NO_2^-]) relationship was altered. Stations L1 and L5 *do* show hydrographic evidence for upwelling and mixing (Fig. 4.1 and 4.2), with L5 having a low $^{15}\varepsilon_{assim}$ and L1 a comparable $^{15}\varepsilon_{assim}$ to the mean value derived for stations L2-L4 and L6-L16. Were mixing responsible for the low $^{15}\varepsilon_{assim}$ at L5, we would expect $^{18}\varepsilon_{assim}$ to be similarly low (Fig. A2.1.1). However, the $^{18}\varepsilon_{assim}$ at station L5 is high (5.0 ± 0.6‰) and indistinguishable from that estimated for the non-upwelling stations, suggesting that a process other than mixing may be responsible for decoupling the δ^{15}N and δ^{18}O of NO_3^-+NO_2^- (and thus $^{15}\varepsilon_{assim}$ and $^{18}\varepsilon_{assim}$) at station L5.

Mixed-layer nitrification, which represents a source of regenerated NO_3^-+NO_2^- to phytoplankton, violates the closed-system Rayleigh model and, if it occurred coincident with NO_3^-+NO_2^- assimilation, would decouple NO_3^-+NO_2^- δ^{15}N and δ^{18}O (and thus $^{15}\varepsilon_{assim}$ and $^{18}\varepsilon_{assim}$). This decoupling results from ammonification+nitrification returning low-δ^{15}N N to the NO_3^-+NO_2^- pool, thereby (partly) erasing the signal of assimilation in NO_3^-+NO_2^- δ^{15}N. At the same time, the δ^{18}O of newly nitrified NO_3^-+NO_2^- is higher than the δ^{18}O removed during assimilation (~1‰ versus -3.1 to 0.2‰, respectively), such that the co-occurrence of NO_3^-+NO_2^- assimilation and nitrification raises the δ^{18}O but not the δ^{15}N of the combined (i.e., partially assimilated plus newly-nitrified) NO_3^-+NO_2^- pool (Appendix Fig. A2.2.1; Fawcett et al., 2015; Sigman et al., 2009; Smart et al., 2015; Wankel et al., 2007). Plotting NO_3^-+NO_2^- δ^{18}O versus δ^{15}N for the LCIS stations reveals no evidence of mixed-layer nitrification as all the data fall roughly along a 1.17:1 line (Fig. 4.4), which is the relationship expected for NO_3^-+NO_2^- assimilation alone (see below).

During assimilation of NO_3^- by phytoplankton, as in plants, NO_3^- is transported into the cell and reduced to NO_2^-, which is then transported into the chloroplast and further reduced to NH_4^+

that is subsequently incorporated into amino acids (reviewed by Tischner, (2000). The rate-limiting step in this sequence is intracellular NO_3^- reduction to NO_2^-, with millimolar concentrations of NO_3^- frequently accumulating inside the cell (Berges & Harrison, 1995; Granger et al., 2004; Needoba & Harrison, 2004). The NO_3^- reductase enzyme (NR) responsible for reducing NO_3^- to NO_2^- has a large isotope effect of ${}^{15}\varepsilon_{NR} = {}^{18}\varepsilon_{NR} = 26.6 \pm 0.2‰$ (Granger et al., 2004; Karsh et al., 2012), such that NO_3^- reduction leaves the cell's internal NO_3^- pool strongly enriched in $\delta^{15}N$ and $\delta^{18}O$. Apparently regardless of the surrounding environmental NO_3^- concentration, a portion of this high-concentration, high-$\delta^{15}N$ and $\delta^{18}O$ NO_3^- is effluxed from the cell during NO_3^- assimilation, causing partial expression of the NR isotope effect in the surrounding water column (Granger et al., 2004, 2010). The ratio of NO_3^- efflux to NO_3^- uptake largely determines the expression of ${}^{15}\varepsilon_{NR}$ (and ${}^{18}\varepsilon_{NR}$) in the environment (i.e., at the whole organism level). This organism level isotope effect (defined here as ${}^{15}\varepsilon_{assim}$ and ${}^{18}\varepsilon_{assim}$) can be calculated as the sum of the isotope effects associated with NO_3^- transport (uptake and efflux) and NO_3^- reduction, weighted (in the case of reduction and efflux) by the efflux to uptake ratio (Granger et al., 2010; Karsh et al., 2012):

$$ {}^{X}\varepsilon_{assim} = {}^{X}\varepsilon_{uptake} + R\left({}^{X}\varepsilon_{NR} - {}^{X}\varepsilon_{efflux}\right) \qquad \text{Eq 4.6} $$

where X represents 15 or 18 and R is the NO_3^- efflux to uptake ratio. According to the literature, ${}^{15}\varepsilon_{uptake} = 2.0 \pm 0.3‰$ (Karsh et al., 2013), ${}^{15}\varepsilon_{efflux} = 1.2 \pm 0.4‰$ (Karsh et al., 2013), ${}^{18}\varepsilon_{uptake} = {}^{18}\varepsilon_{efflux} = 2.8 \pm 0.6‰$ (Karsh et al., 2013), and ${}^{15}\varepsilon_{NR} = {}^{18}\varepsilon_{NR} = 26.6 \pm 0.2‰$ (Granger et al., 2004; Karsh et al., 2012). From our derived organism-level ${}^{15}\varepsilon_{assim}$ of 4.1 ± 0.7%, we use Eq 4.6 to calculate R = 0.08 ± 0.03 (i.e., NO_3^- efflux is 8 ± 3% of uptake), which we can then use to compute a theoretical organism-level ${}^{18}\varepsilon_{assim}$ of 4.8 ± 1.0‰ and an ${}^{18}\varepsilon/{}^{15}\varepsilon$ of 1.17 ± 0.36. This theoretical ${}^{18}\varepsilon_{assim}$ is statistically indistinguishable from our data-derived ${}^{18}\varepsilon_{assim}$ of 4.7 ± 0.8‰, and the theoretically derived ${}^{18}\varepsilon/{}^{15}\varepsilon$ ratio is also in line with our observations (Fig. 4.5). Thus, the N and O isotopes of NO_3^-+NO_2^- indicate that mixed-layer nitrification was negligible at LCIS in mid-summer and that photosynthetic assimilation was the dominant process acting on the NO_3^-+NO_2^- pool.

Further evidence in support of negligible mixed-layer nitrification is the lack of an observed rise in NH_4^+ $\delta^{15}N$ at the base of the euphotic zone. Nitrifiers greatly reduce, although do not completely halt, their activity when exposed to elevated light levels (Guerrero & Jones, 1996a,

1996b; Hooper & Terry, 1974; Vanzella et al., 1989) such as those that characterize the summertime euphotic zone at LCIS (Clark et al., 2008; Dore & Karl, 1996; Smith et al., 2014; Ward, 2005; Ward et al., 1989). Additionally, nitrifiers are strongly outcompeted by phytoplankton for NH_4^+ in the euphotic zone (Smith et al., 2014; Ward, 1985), leading to well-lit surface waters being dominated by NH_4^+ assimilation, with nitrification becoming potentially more important at the base of the euphotic zone. Provided the available NH_4^+ is not completely oxidized to NO_2^-, nitrification considerably increases NH_4^+ $\delta^{15}N$ as it occurs with an isotope effect of 14-19‰ (Casciotti et al., 2003) By contrast, NH_4^+ assimilation occurring at the base of the euphotic zone would have little effect on the NH_4^+ $\delta^{15}N$ because of its negligible isotope effect (DiFiore et al., 2009; Hoch et al., 1992; Liu et al., 2013). As such, the coincidence of NH_4^+ oxidation and NH_4^+ assimilation would yield a strong increase in NH_4^+ $\delta^{15}N$ at the base of the euphotic zone (Appendix Fig. A2.2.3), which we do not observe.

Finally, direct nitrification rate measurements made at the same time as our sampling show that mixed-layer nitrification was extremely low (averaging 1.3 ± 1.0 nmol/day and always below 3.8 nmol/day; Flynn et al. (2021)). The absence of mixed-layer nitrification during the growing season at LCIS means that NO_3^-+NO_2^- assimilation can be directly equated to new production. It also means, however, that another process is likely responsible for the decoupling of ${}^{15}\varepsilon_{assim}$ and ${}^{18}\varepsilon_{assim}$ observed at station L5.

Surface meltwater input could influence the apparent (i.e., calculated) values of ${}^{15}\varepsilon_{assim}$ and ${}^{18}\varepsilon_{assim}$ as both sea-ice- and ice-shelf-melt are characterized by low- to near-zero concentrations of NO_3^-+NO_2^- (Fripiat et al., 2017; Vincent & Howard-Williams, 1994). The influence of ice melt can be determined at each depth in the mixed layer by comparing its salinity to the salinity of the underlying WW (i.e., the source water). WW has a salinity of 34.68 ± 0.01 g/kg (S_{WW}), while LCIS mixed-layer salinity ranges from 34.21 to 34.54 g/kg ($S_{measured}$), and ice melt will have a salinity ranging from ~0 g/kg for ice-shelf melt and precipitation to ~6 g/kg for sea ice (S_{melt}), albeit with a considerable range (Eicken, 1992; Potter et al., 1984). Using a linear mixing model (Eq 4.7a), we can solve for f_{melt}, the fraction of meltwater present at every depth in the mixed layer:

$$S_{measured} = f_{melt} \cdot S_{melt} + (1 - f_{melt}) \cdot S_{WW} \qquad \text{Eq 4.7a}$$

Varying S_{melt} from 0 to 6 g/kg and solving for f_{melt} indicates that ice melt contributes an average of 1.1 ± 1.0% (maximum of 4.1%) of the water in the mixed layer adjacent to LCIS (Appendix Fig. A2.3.1). Removing the effect of ice melt on the measured $NO_3^-+NO_2^-$ concentrations can be achieved through another linear mixing model (Eq 4.7b), solving for $[NO_3^-+NO_2^-]_{melt\ removed}$:

$$[NO_3^-+NO_2^-]_{measured} = f_{melt} \cdot [NO_3^-+NO_2^-]_{melt} + (1 - f_{melt}) \cdot [NO_3^-+NO_2^-]_{melt\ removed} \quad \text{Eq 4.7b}$$

Similarly, the effect of ice melt on the $\delta^{15}N$ and $\delta^{18}O$ of water column $NO_3^-+NO_2^-$ can be removed using Eq 4.7c, solving for $\delta X_{melt\ removed}$, where X represents ^{15}N or ^{18}O:

$$[NO_3^-+NO_2^-]_{measured} \cdot \delta X_{measured} = f_{melt} \cdot [NO_3^-+NO_2^-]_{melt} \cdot \delta X_{melt} + (1 - f_{melt}) \cdot [NO_3^-+NO_2^-]_{melt\ removed} \cdot \delta X_{melt\ removed} \quad \text{Eq 4.7c}$$

Varying the ice-melt salinity from 0 to 10 g/kg, $[NO_3^-+NO_2^-]_{melt}$ from 0 to 10 μmol/l, and $\delta^{15}N_{ice\ melt}$ and $\delta^{18}O_{ice\ melt}$ from 0 to 10‰ yields a minimum and maximum $^{15}\varepsilon_{melt\ removed}$ of 4.1 ± 0.7‰ and 4.4 ± 0.7‰, respectively, and minimum and maximum $^{18}\varepsilon_{melt\ removed}$ of 4.6 ± 0.8‰ and 4.9 ± 0.8‰, respectively (Appendix Fig. A2.3.2a and b). These values fall within the uncertainty of our original derived $^{15}\varepsilon_{assim}$ of 4.1 ± 0.7‰ and $^{18}\varepsilon_{assim}$ of 4.7 ± 0.8‰, indicating that ice melt has very little power to alter the apparent $NO_3^-+NO_2^-$ assimilation isotope effects. We can thus be confident in our data-derived estimates of $^{15}\varepsilon_{assim}$ and $^{18}\varepsilon_{assim}$ for the coastal Antarctic, which fall within the 4 to 9‰ range (albeit at the low end) of previous summertime estimates for the pelagic Antarctic Zone of the Southern Ocean (Altabet & Francois, 2001; DiFiore et al., 2006, 2009, 2010; Fripiat et al., 2019; Karsh et al., 2003; Sigman et al., 1999).

Our derived $^{15}\varepsilon_{assim}$ of 4.1 ± 0.7‰ is slightly lower, but within the uncertainty of the $^{18}\varepsilon_{assim}$ of 4.7 ± 0.8‰ computed for the L2-L4 and L6-L16 station average, driven by the greater isotopic fractionation experienced by O atoms compared to N atoms during transport of NO_3^- into and out of the cell (Granger et al., 2010; Karsh et al., 2013). The difference between $^{15}\varepsilon_{assim}$ and $^{18}\varepsilon_{assim}$ at station L5 cannot be explained by mixing, nitrification, or meltwater input, making the most likely explanation the fact that this station is characterized by less $NO_3^-+NO_2^-$ drawdown than the other LCIS stations (2.9 ± 1.7 μmol/l versus 7.1 ± 2.6 μmol/l). The apparent WW-to-mixed-layer changes in $\delta^{15}N$ and $\delta^{18}O$ were thus near the analytical limit, making them

more uncertain. This issue has been invoked previously during attempts to estimate $^{15}\varepsilon_{assim}$ and $^{18}\varepsilon_{assim}$ in regions of the coastal Antarctic characterized by a very low degree of $NO_3^-+NO_2^-$ drawdown (Fripiat et al., 2019). In contrast to L1 and L5, our measurements from stations L2-L4 and L6-L16 do not suffer from this issue as the mixed layer was strongly stratified at these stations and a high degree of $NO_3^-+NO_2^-$ consumption was observed.

4.4.2.3.2 $\delta^{15}N_{NO3\ consumed}$ is best approximated by the integrated-instantaneous product of $NO_3^-+NO_2^-$ assimilation

Using the Rayleigh model, with the derived value of $^{15}\varepsilon_{assim}$, the $\delta^{15}N$ of the PON produced from the assimilation of $NO_3^-+NO_2^-$ (i.e., $\delta^{15}N_{NO3\ consumed}$) can be calculated. The Rayleigh model yields two different estimates of PON $\delta^{15}N$, and thus of $\delta^{15}N_{NO3\ consumed}$ (Fig. 4.6a): 1) the instantaneous product and 2) the accumulated product. The instantaneous product of $NO_3^-+NO_2^-$ assimilation ($\delta^{15}N_{NO3\ consumed\ instantaneous}$) represents the $\delta^{15}N$ of the N removed from the $NO_3^-+NO_2^-$ pool at each moment of consumption and can be approximated by the $\delta^{15}N$ of the $NO_3^-+NO_2^-$ pool at that degree of consumption minus $^{15}\varepsilon_{assim}$ (for $^{15}\varepsilon_{assim}$ <<1000‰) (Mariotti et al., 1981) (Eq 4.8a). Writing this in terms of the source $NO_3^-+NO_2^-$ (sub/superscript "o") by substituting Eq 4.4 into Eq 4.8a, yields Eq 4.8b, which represents a more general solution for $\delta^{15}N_{NO3\ consumed\ instantaneous}$. The accumulated product of $NO_3^-+NO_2^-$ assimilation ($\delta^{15}N_{NO3\ consumed\ accumulated}$) represents the $\delta^{15}N$ of all the N removed from the $NO_3^-+NO_2^-$ pool since consumption of the source $NO_3^-+NO_2^-$ began (Eq 4.9) (Mariotti et al., 1981).

$$\delta^{15}N_{NO3\ consumed\ instantaneous} = \delta^{15}N_{NO_3^-+NO_2^-} - {}^{15}\varepsilon_{assim} \quad \text{Eq 4.8a}$$

$$\delta^{15}N_{NO3\ consumed\ instantaneous} = \delta^{15}N^0_{NO_3^-+NO_2^-} - {}^{15}\varepsilon_{assim} \cdot ln\,(f) - {}^{15}\varepsilon_{assim} \quad \text{Eq 4.8b}$$

$$\delta^{15}N_{NO3\ consumed\ accumulated} = \delta^{15}N^0_{NO_3^-+NO_2^-} + {}^{15}\varepsilon_{assim}\frac{f \cdot ln\,(f)}{1-(f)} \quad \text{Eq 4.9}$$

where $f = \frac{[NO_3^-+NO_2^-]}{[NO_3^-+NO_2^-]_o}$

To determine whether the instantaneous or accumulated product best represents the $\delta^{15}N_{NO3\ consumed}$ at LCIS (Eq 4.2c), we consider the extent to which newly produced PON has been

exported from the mixed layer. If a significant quantity of PON produced from the assimilation of the NO_3^-+NO_2^- supplied during winter was exported by the time of our sampling, then the $\delta^{15}N$ of the PON remaining in the mixed layer cannot be approximated by the accumulated product equation (Eq 4.9).

At LCIS, the concentration of mixed-layer PON was significantly lower than the total amount of N consumed since the beginning of the growing season, indicating that the measured PON $\delta^{15}N$ cannot be approximated by the $\delta^{15}N$ of the accumulated product (Table 4.1). As outlined previously, the summertime mixed layer shoals out of the winter mixed layer, leaving the remnant WW layer as a record of the conditions present at the beginning of the growing season (Flynn et al., 2021; Goeyens et al., 1995; Hoppema et al., 2007; Jennings et al., 1984). At LCIS, WW has a mean NO_3^-+NO_2^- concentration of 27.4 ± 1.1 μmol/l, while the surface mixed layer at stations L2-L4 and L6-L16 has an average NO_3^-+NO_2^- concentration of 20.3 ± 2.3 μmol/l, amounting to an average NO_3^-+NO_2^- decrease (i.e., due to consumption) of 7.1 ± 2.6 μmol/l (Table 4.1). The mixed-layer PON pool at these stations has an average concentration of 3.1 ± 0.8 μmol/l, which accounts for less than half of the NO_3^-+NO_2^- consumed.

However, PON is not the only N pool present in the mixed layer that ultimately derives from NO_3^-+NO_2^- supplied by winter mixing (i.e., $[NO_3^- + NO_2^-]_o$). The mean concentration of the non-NO_3^-+NO_2^- N pools (i.e., PON + NH_4^+ + urea) in the mixed layer is 4.2 ± 1.0 μmol/l, which is also insufficient to account for all the NO_3^-+NO_2^- drawdown since the beginning of the growing season. Assuming mass balance (Eq 10), we calculate that an average of 3.0 ± 1.9 μmol/l of N was exported from the mixed layer during the growing season prior to our sampling.

$$[NO_3^- + NO_2^-]_o = [NO_3^- + NO_2^-] + [PON] + [NH_4^+] + [urea] + N\ export$$

Eq 4.10

While the $\delta^{15}N_{NO3\ consumed}$ cannot be estimated from the accumulated product equation, it also cannot be derived from the instantaneous product equation. This is because there has clearly been some accumulation of PON in the mixed layer, even as a significant quantity has been exported. The instantaneous product, by definition, provides the $\delta^{15}N_{NO3\ consumed}$ at the moment of consumption (Eq 4.8b). Consider an example case of the sample from 25 m at station L15:

here, the NO_3^-+NO_2^- concentration and δ^{15}N were 15.5 ± 0.1 μmol/l and 7.9 ± 0.2‰, respectively. Using the $[NO_3^- + NO_2^-]_o$ and $\delta^{15}N^0_{NO_3^-+NO_2^-}$ of WW (27.4 ± 1.1 μmol/l and 5.21 ± 0.12‰), $^{15}\varepsilon_{assim}$ of 4.1 ± 0.7‰, and f (= 15.5 ± 0.1 μmol/l / 27.4 ± 1.1 μmol/l) of 0.57 ± 0.02, we calculate an instantaneous $\delta^{15}N_{NO3\ consumed}$ of 3.4 ± 0.3‰. This δ^{15}N value applies to the PON produced instantaneously at the time of sampling. However, the concentration of the PON pool at 25 m at station L15 was 6.1 μmol/l, which means (assuming all the PON is derived, directly or indirectly (i.e., through regenerated N) from the assimilation of NO_3^-+NO_2^-) that it would have begun to accumulate when the NO_3^-+NO_2^- concentration was 15.5 ± 0.1 μmol/l + 6.1 ± 0.1 μmol/l = 21.6 ± 0.1 μmol/l. Using Eq 4.8b we calculate that this PON would have had a δ^{15}N of 2.1 ± 0.3‰ as it began to accumulate, a value that is significantly lower than the δ^{15}N predicted for the instantaneous product at the time of our sampling. Additionally, even at the highest rate of NO_3^- uptake of 0.27 μmol/l/day measured directly at LCIS at the time of our sampling (Flynn et al., 2021), it would take ~24 days to produce 6.1 μmol/l PON, an amount of time that cannot be described as "instantaneous". This exercise confirms that the instantaneous product is not an appropriate estimation of the $\delta^{15}N_{NO3\ consumed}$.

Instead, we propose that the $\delta^{15}N_{NO3\ consumed}$ can be estimated by integrating the instantaneous product over the concentration of PON + NH_4^+ + urea remaining in the mixed layer at the time of sampling. Even though some of that PON would have been produced from the assimilation of recycled N, the recycled N would have ultimately derived from the NO_3^-+NO_2^- supplied during winter mixing (i.e., neither NH_4^+ nor urea is mixed up into surface waters from below). As such, by mass balance, the concentration of mixed-layer PON + NH_4^+ + urea represents the product of NO_3^-+NO_2^- consumption that has not been exported. Calculating the $\delta^{15}N_{NO3\ consumed}$ by integrating over this quantity of N yields a theoretical δ^{15}N for PON produced exclusively from the assimilation of NO_3^-+NO_2^-. The calculation is as follows:

From Eq 4.4:

$$\delta^{15}N_{NO_3^-+NO_2^-\ start\ integrating} = \delta^{15}N^0_{NO_3^-+NO_2^-} - {}^{15}\varepsilon_{assim} \cdot \ln\left(\frac{[NO_3^-+NO_2^-]+[PON]+[NH_4^+]+[urea]}{[NO_3^-+NO_2^-]_o}\right) \quad \text{Eq 4.11}$$

Where $\delta^{15}N_{NO_3^-+NO_2^-\ start\ integrating}$ is the theoretical δ^{15}N of the $NO_3^-+NO_2^-$ pool at the concentration of total N (i.e., $NO_3^-+NO_2^-$ + PON + NH_4^+ + urea) present in the mixed layer at a particular station;

From Eq 4.9:

$$\delta^{15}N_{NO3\ consumed} = \delta^{15}N_{NO_3^-+NO_2^-\ start\ integrating} + {}^{15}\varepsilon_{assim}\frac{f \cdot ln\,(f)}{1-(f)} \qquad \text{Eq 4.12}$$

where $f = \frac{[NO_3^-+NO_2^-]}{[NO_3^-+NO_2^-]+[PON]+[NH_4^+]+[urea]}$

Substituting Eq 4.11 into Eq 4.12 and simplifying (see Appendix A3.1) yields:

$$\delta^{15}N_{NO3\ consumed} = \delta^{15}N^0_{NO_3^-+NO_2^-} + {}^{15}\varepsilon_{assim}\left(\ln\left(\frac{[NO_3^-+NO_2^-]_o}{[NO_3^-+NO_2^-]+[PON]+[NH_4^+]+[urea]}\right) + \frac{[NO_3^-+NO_2^-]}{[PON]+[NH_4^+]+[urea]} \cdot \ln\left(\frac{[NO_3^-+NO_2^-]}{[NO_3^-+NO_2^-]+[PON]+[NH_4^+]+[urea]}\right)\right) \qquad \text{Eq 4.13}$$

4.4.2.4 Calculating the f-ratio

Using Eq 4.3, with the $\delta^{15}N_{PON}$, $\delta^{15}N_{NH4\ consumed}$, and $\delta^{15}N_{NO3\ consumed}$ represented by $\delta^{15}N_{PON\ growing}$, the regionally-averaged measured NH_4^+ δ^{15}N, and the integrated instantaneous product of $NO_3^-+NO_2^-$ assimilation (Eq 4.13), respectively, we calculate a regionally averaged N isotope-derived f-ratio of 0.81 ± 0.18 (Fig. 4.6b and 4.8). This value indicates that $NO_3^-+NO_2^-$ is the dominant N source to phytoplankton at LCIS, accounting for ~80% of the N consumed over the past 0.5 – 1.5 months (at the average NO_3^- uptake rate of 0.11 ± 0.07 μmol/l/d measured adjacent to LCIS (Flynn et al., 2021), the average PON concentration of 2.70 ± 0.83 μmol/l would take 1 ± 0.5 months to accumulate).

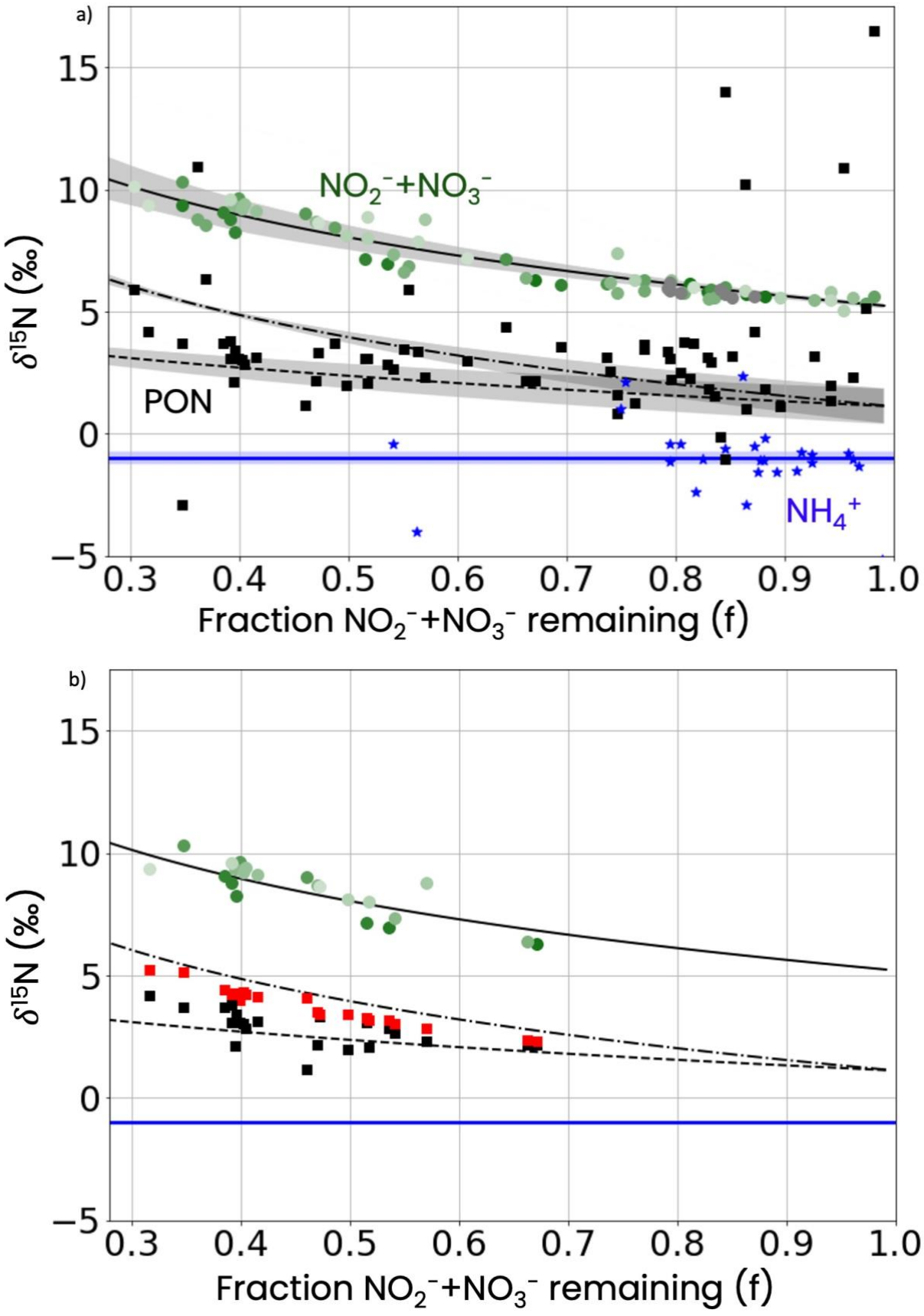

Fig. 4.6: Rayleigh model plots showing $\delta^{15}N$ versus the fraction of the $NO_3^-+NO_2^-$ pool remaining (i.e., the measured $NO_3^-+NO_2^-$ concentration divided by the source (i.e., winter water; WW) $NO_3^-+NO_2^-$ concentration). The black lines show the output of the Rayleigh model run with $^{15}\varepsilon_{assim}$ = 4.1 ± 0.7‰ and initial $NO_3^-+NO_2^-$ $\delta^{15}N$

= 5.21 ± 0.12‰ (i.e., the mean value calculated for the WW), with the theoretical $NO_3^-+NO_2^-$ $\delta^{15}N$ (i.e., substrate) shown by the solid black line, the instantaneous product by the dot-dashed black line, and accumulated product by the dashed line. In all cases, the grey shading indicates ± 1 standard deviation. Also shown are our measured NH_4^+ (blue; with the blue horizontal line showing the regional average ± 1 standard error (blue shading)), $PON_{growing}$ (black), and $NO_3^-+NO_2^-$ (green) data. Panel b) additionally shows the $\delta^{15}N_{NO3\ consumed}$ end member (red), calculated using the instantaneous product integrated over the PON + NH_4^+ + urea concentration measured at each depth/station (Eq 4.13). Panel a) shows all mixed layer PON data while panel b) shows only the data used to calculate the f-ratio (i.e., where $\delta^{15}N_{NH4\ consumed}<\delta^{15}N_{PON}<\delta^{15}N_{NO3\ consumed}$ and the derived f-ratio has a standard deviation <0.25).

The regional f-ratio is derived by averaging individual f-ratios calculated at each station and depth where $\delta^{15}N_{NH4\ consumed}\leq\delta^{15}N_{PON}\leq\delta^{15}N_{NO3\ consumed}$ and the individual f-ratio is associated with a standard deviation <0.25. These criteria ensure that the f-ratio falls between 0 and 1 and is robust (see Appendix A3.2). We have confidence in the derived regional f-ratio, although it is still important to characterize the sensitivity of this value to the various terms in Eq 4.3. As such, we performed a sensitivity analysis by varying $\delta^{15}N_{NH4\ consumed}$, $\delta^{15}N_{NO3\ consumed}$ (through varying the source water $NO_3^-+NO_2^-$ concentration and $\delta^{15}N$, ${}^{15}\varepsilon_{assim}$, and the PON + NH_4^+ + urea concentration that is integrated to yield $\delta^{15}N_{NO3\ consumed}$), and $\delta^{15}N_{PON}$ (by varying the $PON_{background}$ concentration and $\delta^{15}N$). Varying each of these parameters over a realistic range (vertical dashed grey lines in Fig. 4.7) shows that their respective uncertainties are more than accounted for in the reported uncertainty associated with our mean f-ratio.

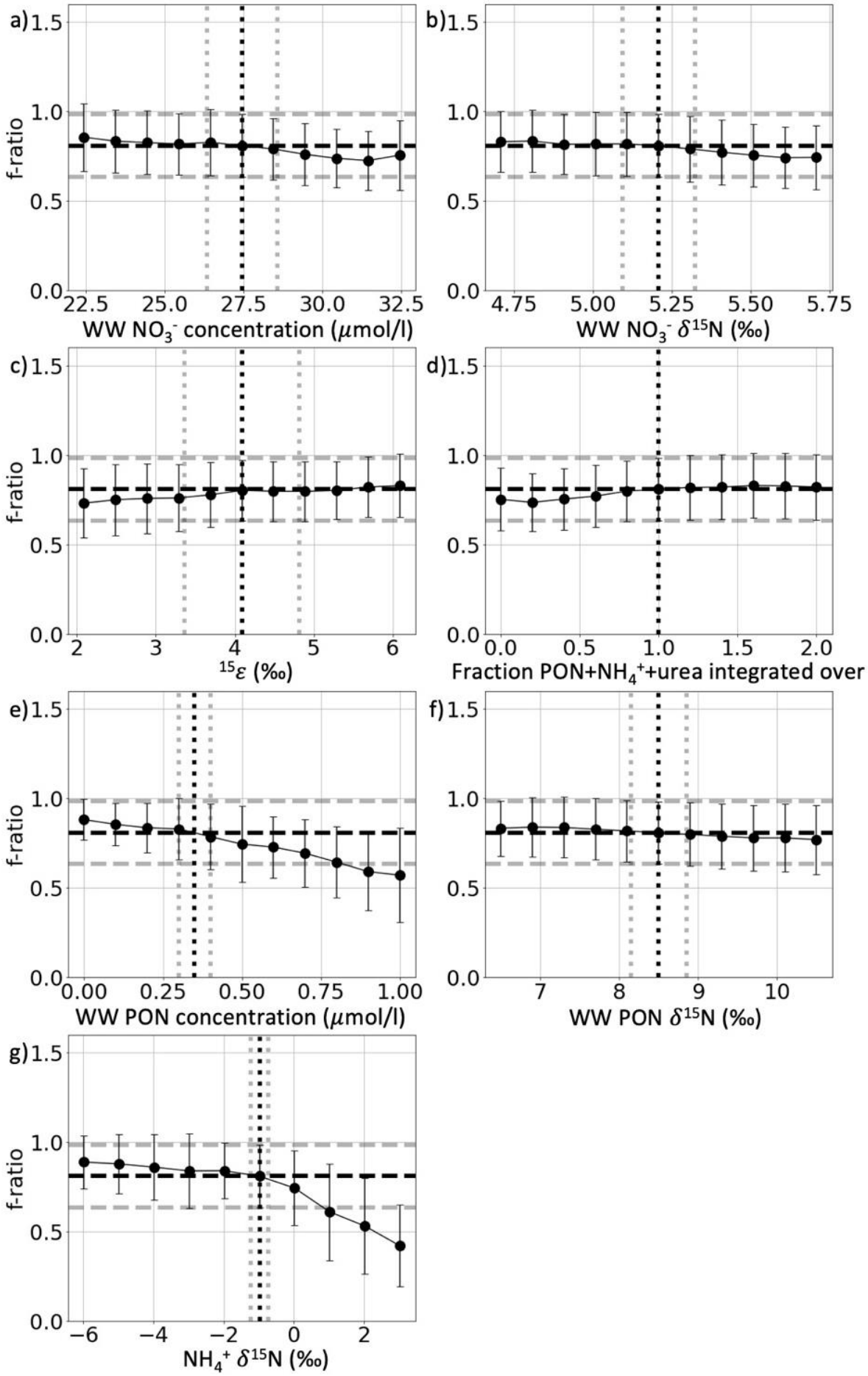
a)
b)
c)
d)
e)
f)
g)
f-ratio
WW NO_3^- concentration (μmol/l)
WW NO_3^- δ^{15}N (‰)
$^{15}\varepsilon$ (‰)
Fraction PON+NH_4^++urea integrated over
WW PON concentration (μmol/l)
WW PON δ^{15}N (‰)
NH_4^+ δ^{15}N (‰)

Fig. 4.7: Exploring the sensitivity of the derived f-ratios to variations in a) the source WW $NO_3^-+NO_2^-$ concentration, b) the source WW $NO_3^-+NO_2^-$ $\delta^{15}N$, c) the $NO_3^-+NO_2^-$ N assimilation isotope effect ($^{15}\varepsilon_{assim}$), d) the fraction of the PON + NH_4^+ + urea concentration that is integrated over to derive $\delta^{15}N_{NO3\ consumed}$, e) the source WW PON concentration, f) the source WW PON $\delta^{15}N$, and g) the NH_4^+ $\delta^{15}N$. The horizontal dashed lines represent the average regional f-ratio (black dashed line) ± 1 standard deviation (grey dashed lines) of 0.81 ± 0.18. The vertical dotted lines represent the regional average value of each parameter (black) ± 1 standard deviation (grey). The f-ratios plotted in this figure are the regional averages, calculated for individual points that meet the criteria of $\delta^{15}N_{NH4\ consumed} \leq \delta^{15}N_{PON} \leq \delta^{15}N_{NO3\ consumed}$, with the individual f-ratio characterized by a standard deviation <0.25. We performed a second test (Appendix Fig. A4.1) of the sensitivity of the derived f-ratio using the original 22 points only (i.e., the selection criteria are not applied because the 22 data points are already selected). For both sensitivity tests, varying each parameter within a reasonable range (vertical dotted grey lines) yields respective uncertainties in the f-ratio that are more than accounted for in the uncertainty of our reported f-ratio.

The sensitivity analysis further shows that the lowest possible f-ratio that can be derived from our isotope data is 0.75 ± 0.17 if the Rayleigh instantaneous product is used to represent the $\delta^{15}N_{NO3\ consumed}$ end member. However, as outlined in section 4.4.2.3.2, it is inappropriate to use the instantaneous product to represent $\delta^{15}N_{NO3\ consumed}$ since a considerable portion of the PON produced from the consumption of $NO_3^-+NO_2^-$ remains in the mixed layer adjacent to LCIS. Varying $\delta^{15}N_{NH4\ consumed}$ within a realistic range has the largest impact on the calculated f-ratio, driven primarily by the uncertainty associated with the measurements of NH_4^+ $\delta^{15}N$; however, even the effect of varying the NH_4^+ $\delta^{15}N$ by ± 1.5‰ is more than accounted for by our reported f-ratio standard deviation. The results of the sensitivity analysis increase our confidence in the regional average f-ratio of 0.81 ± 0.18 that we derive for the waters adjacent to LCIS. This f-ratio indicates that phytoplankton growth was fueled primarily by the consumption of $NO_3^-+NO_2^-$, as opposed to NH_4^+ or urea. Moreover, since mixed-layer nitrification was negligible, the $NO_3^-+NO_2^-$ consumption was the consumption of preformed nutrients, indicating that new production accounts for 81 ± 18% of total production and that the potential for carbon export from the surface waters adjacent to LCIS was high.

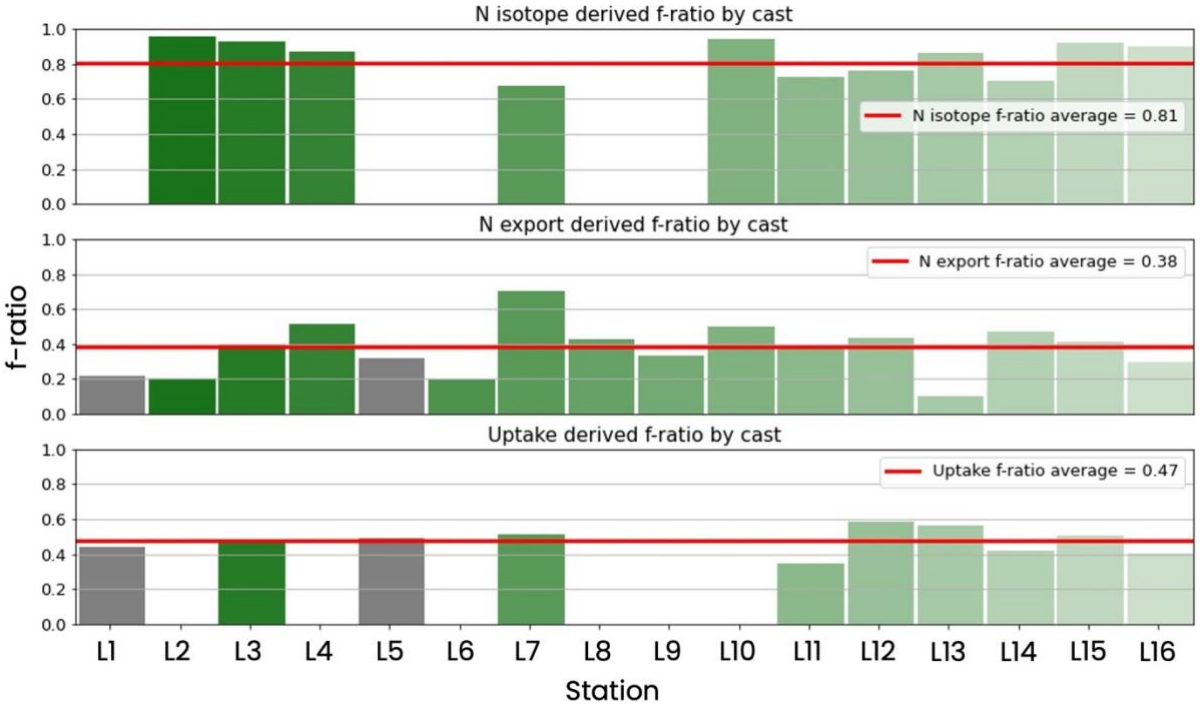

Fig. 4.8: Estimates of the f-ratio at each station, derived from a) measurements of the N isotopes, (b) the fraction of NO_3^-+NO_2^- consumed that had already been exported from the mixed layer (Table 4.1), and (c) direct uptake rate experiments (Flynn et al., 2021). The station L2-L4 and L6-L16 regional average is plotted as the horizontal red line. Upwelling stations L1 and L5 (grey) are excluded from the regional average.

While we are confident that our isotope-derived f-ratio is robust, it is very high compared to other estimates from the region. For example, on the same cruise as our sampling, Flynn et al. (2021) estimated an f-ratio of 0.47 ± 0.08 (Fig. 4.8) from direct (i.e., instantaneous, ^{15}N-tracer based) measurements of NO_3^-+NO_2^- and regenerated N uptake. So why do these two different methods yield such divergent estimates of the f-ratio? The most likely explanation is that the isotope-derived f-ratio integrates over a considerable portion of the growing season while the Flynn et al. (2021) estimate quantifies the behaviour of the phytoplankton community at the moment of sampling (i.e., the experiments conducted to quantify N uptake last less than six hours) and can be taken as representative of a few days at most. Moreover, one would expect the f-ratio estimated from direct rate measurements made in mid- to late-summer to be lower than that estimated from the N isotope changes occurring over all of the growing season prior to this date. This is because, as mentioned above, the concentrations of organic matter and regenerated N are very low in spring when the growing season commences, so NO_3^-+NO_2^- consumption (i.e., new production) supports almost all phytoplankton growth. As summer approaches, however, more and more of the phytoplankton biomass is consumed and/or decomposed, releasing NH_4^+. Thus, as the growing season progresses, we expect more NH_4^+ to become available to phytoplankton, increasing the relative importance of regenerated

production. At the same time, the surface-layer iron concentrations decline, rendering NO_3^- reduction less favourable (Einsle & Kroneck, 2004; Morel & Price, 2003; Timmermans et al., 2004) and further enhancing phytoplankton reliance on regenerated N. This explanation is consistent with our findings, with our partially time-integrated isotope-derived f-ratio of 0.81 ± 0.18 indicating NO_3^-+NO_2^- as the primary source of N to phytoplankton for the 0.5 – 1.5 months prior to sampling, with near-exclusive NO_3^-+NO_2^- consumption likely occurring earlier in this period. By contrast, the increased availability of regenerated N and decreased availability of iron by the time of our sampling explains the lower f-ratio of 0.47 ± 0.08 estimated by Flynn et al. (2021). We expect that in the weeks following our sampling, the f-ratio would have continued to decline as regenerated production increased and new production declined.

4.4.3 NO_3^- drawdown-based estimates of net community production

While the f-ratios discussed above provide a normalized measure of carbon export potential, they do not yield an estimate of NCP, which is a measure of the amount of carbon exported from the surface ocean (i.e., the rate of export production). One way of estimating NCP involves measuring net NO_3^-+NO_2^- drawdown over the entire growing season and converting that to carbon using an appropriate C : N ratio (Johnson et al., 2017, 2022; Redfield et al., 1963). To estimate the amount of NO_3^-+NO_2^- exported from the mixed layer by the time of our sampling, we use the L2-L4 and L6-L16 average mixed-layer N export estimate of 3.0 ± 1.9 μmol/l (Eq 4.10; Table 4.1). Integrating this concentration over the depth of the mixed layer and multiplying by the C : N ratio derived for the Antarctic Zone of the Southern Ocean from float data (6.3 ± 0.5 for 65 to 70^{o}S (Johnson et al., 2022), which is indistinguishable from 6.63 (Redfield et al., 1963)) yields an estimate of carbon export of 1.7 ± 0.9 mol C/m^2. In addition, we calculate that of the quantity of NO_3^-+NO_2^- consumed prior to the time of sampling, an average of 38 ± 15% had already been exported from the surface ocean adjacent to LCIS (Fig. 4.8).

Cast	Depth of base assim. signal (m)	ML ave. $NO_3^- + NO_2^-$ (μM)	ML ave. NH_4^+ (μM)	ML ave. urea (μM)	ML ave. PON (μM)	Regen N (μM)	Total N (μM)	ML ave. $NO_3^- + NO_2^-$ consumed (μM)	ML N exported (μM)	Fraction $NO_3^- + NO_2^-$ consumed that has been exported	C exported from ML (assume C:N=6.3±0.5) (mol/m²)
Winter Water (WW)		27.44 ± 1.12	0.63 ± 0.27	0.19 ± 0.09	0.35 ± 0.05	1.18 ± 0.29	28.61 ± 1.15				
L1	125	23.26 ± 1.34	1.21 ± 0.12	0.32 ± 0.1	1.74 ± 0.29	3.27 ± 0.33	26.53 ± 1.38	4.18 ± 1.74	0.91 ± 1.78	0.22 ± 0.43	0.72 ± 1.4
L2	120	22.78 ± 3.42	0.92 ± 0.23	0.2 ± 0.06	2.6 ± 0.73	3.72 ± 0.77	26.5 ± 3.51	4.66 ± 3.6	0.94 ± 3.68	0.2 ± 0.81	0.71 ± 2.79
L3	161	20.05 ± 5.6	0.79 ± 0.42	0.19 ± 0.13	3.45 ± 0.55	4.43 ± 0.71	24.48 ± 5.64	7.39 ± 5.71	2.96 ± 5.75	0.4 ± 0.84	3 ± 5.84
L4	81	16.49 ± 5.19	0.97 ± 0.7	0.2 ± 0.06	4.14 ± 0.68	5.31 ± 0.98	21.8 ± 5.28	10.95 ± 5.31	5.64 ± 5.39	0.52 ± 0.55	2.88 ± 2.76
L5	151	24.51 ± 1.26	0.93 ± 0.16	0.22 ± 0.09	0.83 ± 0.05	1.99 ± 0.19	26.5 ± 1.27	2.93 ± 1.68	0.94 ± 1.69	0.32 ± 0.61	0.9 ± 1.61
L6	120	23.16 ± 3.98	0.93 ± 0.29	0.2 ± 0.06	2.33 ± 0.94	3.45 ± 0.98	26.61 ± 4.1	4.28 ± 4.14	0.83 ± 4.25	0.19 ± 1.01	0.63 ± 3.21
L7	50	16.38 ± 6.34	0.74 ± 0.54	0.07 ± 0.05	2.45 ± 1.84	3.26 ± 1.91	19.64 ± 6.62	11.06 ± 6.44	7.8 ± 6.71	0.71 ± 0.73	2.46 ± 2.12
L8	100	23.24 ± 5.71	0.49 ± 0.14	0.2 ± 0.06	1.72 ± 0.99	2.4 ± 1	25.64 ± 5.8	4.2 ± 5.82	1.8 ± 5.91	0.43 ± 1.53	1.13 ± 3.72
L9	100	19.22 ± 5.77	1.18 ± 0.74	0.2 ± 0.06	4.08 ± 0.94	5.46 ± 1.2	24.68 ± 5.9	8.22 ± 5.88	2.76 ± 6	0.34 ± 0.77	1.74 ± 3.78
L10	120	20.29 ± 3.97	0.95 ± 0.65	0.2 ± 0.06	2.42 ± 1.38	3.56 ± 1.52	23.86 ± 4.25	7.15 ± 4.13	3.58 ± 4.4	0.5 ± 0.68	2.71 ± 3.33
L11	151	20.06 ± 5.92	1.37 ± 0.85	0.22 ± 0.1	2.98 ± 1.38	4.57 ± 1.63	24.63 ± 6.14	7.38 ± 6.02	2.81 ± 6.24	0.38 ± 0.9	2.67 ± 5.94
L12	100	20.13 ± 7.36	0.97 ± 0.67	0.2 ± 0.04	2.98 ± 0.85	4.15 ± 1.08	24.28 ± 7.44	7.31 ± 7.45	3.16 ± 7.53	0.43 ± 1.12	1.99 ± 4.74
L13	61	23.7 ± 4.9	0.63 ± 0.38	0.22 ± 0.06	2.52 ± 2.06	3.37 ± 2.09	27.07 ± 5.33	3.74 ± 5.03	0.37 ± 5.45	0.1 ± 1.46	0.14 ± 2.09
L14	61	20.83 ± 5.16	0.66 ± 0.27	0.24 ± 0.09	2.6 ± 1.74	3.5 ± 1.76	24.32 ± 5.45	6.61 ± 5.28	3.12 ± 5.56	0.47 ± 0.92	1.2 ± 2.14
L15	61	18.79 ± 6.14	0.6 ± 0.45	0.24 ± 0.2	4.22 ± 1.91	5.06 ± 1.97	23.85 ± 6.44	8.65 ± 6.24	3.59 ± 6.54	0.42 ± 0.81	1.38 ± 2.52
L16	100	18.95 ± 7.3	1.48 ± 1.25	0.2 ± 0.06	4.28 ± 1.37	5.95 ± 1.85	24.9 ± 7.53	8.49 ± 7.38	2.54 ± 7.61	0.3 ± 0.93	1.6 ± 4.8
All station mean		20.74 ± 2.5	0.93 ± 0.28	0.21 ± 0.06	2.83 ± 1	3.97 ± 1.1	24.7 ± 1.93	6.7 ± 2.5	2.73 ± 1.93	0.37 ± 0.15	1.62 ± 0.91
L2-L4 & L6-L16 mean		20.29 ± 2.32	0.91 ± 0.29	0.2 ± 0.06	3.05 ± 0.83	4.16 ± 1.01	24.45 ± 1.93	7.15 ± 2.32	2.99 ± 1.93	0.38 ± 0.15	1.73 ± 0.92
L1 & L5 mean		23.89 ± 0.88	1.07 ± 0.2	0.27 ± 0.07	1.29 ± 0.64	2.63 ± 0.91	26.51 ± 0.02	3.55 ± 0.88	0.93 ± 0.02	0.27 ± 0.07	0.81 ± 0.13

Table 4.1: Mixed layer (ML) average (± 1 standard deviation) values of $NO_3^-+NO_2^-$, NH_4^+, urea, and PON concentrations for stations L1-L16 adjacent to Larsen C Ice Shelf. Blue highlighted cells indicate that no urea measurements are available, in which case the L2-L4 and L6-L16 ML average is used. The ML average concentrations of regenerated N (NH_4^+ + urea + PON) and total N ($NO_3^-+NO_2^-$ + NH_4^+ + urea + PON) are listed for each station. The ML $NO_3^-+NO_2^-$ consumed is calculated by subtracting the ML $NO_3^-+NO_2^-$ concentration from that of the source WW ($NO_3^-+NO_2^-$ concentration = 27.44 ± 1.12 μmol/l), while the N exported from the ML is calculated by subtracting the ML regenerated N from the ML $NO_3^-+NO_2^-$ consumed. The fraction of the $NO_3^-+NO_2^-$ consumed that was exported by the time of our sampling is calculated by dividing the ML N exported by the ML NO_3^- + NO_2^- consumed. Finally, carbon (C) export from the ML is calculated by multiplying the ML N export by the depth of the ML (i.e., to yield a ML integrated value) and then by a C : N ratio of 6.3 ± 0.5. The ML average across all stations, L2-L4 & L6-L16, and L1 & L5, are reported at the bottom of the Table, with stations L1 and L5 (grey highlight) singled out due to the evidence for recent upwelling and/or mixing, which violate the Rayleigh model. Using the concentrations of the various N pools, we can determine the fraction of $NO_3^-+NO_2^-$ consumed at the non-upwelling stations since the beginning of the growing season that had been exported (i.e., NCP) prior to our sampling (0.38 ± 0.15), which, when integrated over the ML depth, equates to 1.7 ± 0.9 mol C / m^2.

Our calculation above indicates that the minimum annual NCP for the waters adjacent to LCIS is 1.7 ± 0.9 mol C/m^2 since as the growing season continues, carbon exported will increase, as is required by mass balance. Indeed, additional NO_3^-+NO_2^- consumption had already occurred but the produced PON (and C) had not yet been exported from the mixed layer. Additional NO_3^-+NO_2^- would likely also have been consumed following sampling, although we hypothesize that the rate of NO_3^-+NO_2^- consumption would have slowed given the transition of the upper ocean ecosystem towards regenerated production. Previous estimates of annual NCP for the open Southern Ocean range from 0.5 to 5 mol C/m^2 (Bopp et al., 2001; Dunne et al., 2007; Emerson, 2014 (and references therein); Johnson et al., 2017 (and references therein); Laws et al., 2011; Munro et al., 2015), with NCP for the Antarctic shelf falling between 1 and ~6 mol C/m^2 (Li et al., 2016). Our results are in line with these earlier open ocean estimates, but at the low end of existing shelf estimates, presumably due to our measurements capturing only the first part of the growing season. By the time of our sampling, the total amount of NO_3^-+NO_2^- consumed following winter recharge was 7.2 ± 2.3 μmol/l. Integrating this value over the depth of the mixed layer and multiplying by the Johnson et al. (2022) float-derived C : N ratio yields an estimate of NCP of 4.3 ± 1.7 mol C/m^2. This value, while more consistent with the higher NCP previously reported for the Antarctic shelf, is likely also an underestimation of annual NCP at LCIS, however, as NO_3^-+NO_2^- consumption would have continued, albeit at a decreasing rate, for some time following our sampling. One consequence of an absolute and relative decline in NO_3^-+NO_2^- consumption is that the f-ratio would have decreased even as NCP increased (i.e., the two parameters are decoupled on the timescale of the growing season although not over the annual cycle).

4.5 Conclusion

In this study, we estimate the strength of the biological pump in the waters adjacent to LCIS by calculating the f-ratio from the N isotope ratios of the NO_3^-+NO_2^-, NH_4^+, and PON pools present in the mixed layer in mid-summer. This partially time-integrated f-ratio of 0.81 ± 0.18 indicates that most of the productivity near LCIS was as new production, which by mass balance, leads to carbon export (Dugdale & Goering 1967; Eppley & Peterson, 1979). Of the amount of NO_3^-+NO_2^- consumed by the January / February time of sampling, we estimate that 38 ± 15% had already been exported from the surface mixed layer, equating to 1.7 ± 0.9 mol C.m^{-2} (Table 4.1). At the same stations, Flynn et al. (2021) derived an f-ratio of 0.47 ± 0.08

using direct rate measurements, indicating that at time of sampling, the ecosystem had shifted towards a greater reliance on regenerated production than implied by our isotope-derived f-ratio. From the net amount of NO_3^-+NO_2^- consumption that occurred after winter mixing and before our sampling (7.2 ± 2.3 μmol/l), we calculate that NCP for the region adjacent to LCIS would have been at least 4.3 ± 1.7 mol C/m^2. Annually, this value is likely higher given that as the growing season continued beyond our sampling, phytoplankton would have continued to consume NO_3^-+NO_2^- even as regenerated production became progressively and proportionally more dominant. In summary, we show that the waters adjacent to the LCIS in the western Weddell Sea of Antarctica are highly productive, hosting a strong biological pump with a large carbon export potential.

While the focus of our study was on the biological pump adjacent to LCIS, we were also able to use our new measurements of the δ^{15}N and δ^{18}O of the NO_3^-+NO_2^- pool to derive NO_3^-+NO_2^- assimilation N and O isotope effects ($^{15}\varepsilon_{assim}$ and $^{18}\varepsilon_{assim}$) of 4.1 ± 0.7‰ and 4.7 ± 0.8‰, respectively. These values represent some of the only robust $^{15}\varepsilon_{assim}$ and $^{18}\varepsilon_{assim}$ available for the coastal Antarctic. We further showed no evidence of mixed-layer nitrification in summertime LCIS waters, with the $\Delta\delta^{18}$O : $\Delta\delta^{15}$N of the NO_3^-+NO_2^- pool increasing in the ratio of 1.17:1 expected for NO_3^-+NO_2^- assimilation as the NO_3^-+NO_2^- concentration declined. As such, NO_3^-+NO_2^- consumption over the growing season at LCIS (at least until the time of our sampling) can reliably be used to estimate regional carbon export and the f-ratio.

References

Altabet, M. A. (1988). Variations in nitrogen isotopic composition between sinking and suspended particles: implications for nitrogen cycling and particle transformation in the open ocean. *Deep Sea Research Part A. Oceanographic Research Papers*, *35*(4), 535–554. https://doi.org/10.1016/0198-0149(88)90130-6

Altabet, M. A. (1989). A time-series study of the vertical structure of nitrogen and particle dynamics in the Sargasso Sea. *Limnology and Oceanography*, *34*(7), 1185–1201. https://doi.org/10.4319/LO.1989.34.7.1185

Altabet, M. A., & Francois, R. (1994). Sedimentary nitrogen isotopic ratio as a recorder for surface ocean nitrate utilization. *Global Biogeochemical Cycles*, *8*(1), 103–116. https://doi.org/10.1029/93GB03396

Altabet, M. A., & Francois, R. (2001). Nitrogen isotope biogeochemistry of the Antarctic polar frontal zone at 170°W. *Deep-Sea Research Part II: Topical Studies in Oceanography*, *48*(19–20), 4247–4273. https://doi.org/10.1016/S0967-0645(01)00088-1

Altabet, M. A., & McCarthy, J. J. (1985). Temporal and spatial variations in the natural abundance of ^{15}N in PON from a warm-core ring. *Deep Sea Research Part A. Oceanographic Research Papers*, *32*(7), 755–772. https://doi.org/10.1016/0198-0149(85)90113-X

Altabet, M. A., & McCarthy, J. J. (1986). Vertical patterns in ^{15}N natural abundance in PON from the surface waters of warm-core rings. *Journal of Marine Research*, *44*(1), 185–201. https://doi.org/10.1357/002224086788460148

Altabet, M. A., Pilskaln, C., Thunell, R., Pride, C., Sigman, D., Chavez, F., & Francois, R. (1999). The nitrogen isotope biogeochemistry of sinking particles from the margin of the Eastern North Pacific. *Deep Sea Research Part I: Oceanographic Research Papers*, *46*(4), 655–679. https://doi.org/10.1016/S0967-0637(98)00084-3

Altabet, M. A., & Small, L. F. (1990). Nitrogen isotopic ratios in fecal pellets produced by marine Zooplankton. *Geochimica et Cosmochimica Acta*, *54*(1), 155–163. https://doi.org/10.1016/0016-7037(90)90203-W

Altieri, K. E., Fawcett, S. E., & Hastings, M. G. (2021). Reactive Nitrogen Cycling in the Atmosphere and Ocean. *Annual Review of Earth and Planetary Sciences*, *49*(1), 523–550. https://doi.org/10.1146/annurev-earth-083120-052147

Anderson, L. A. (1995). On the hydrogen and oxygen content of marine phytoplankton. *Deep Sea Research Part I: Oceanographic Research Papers*, *42*(9), 1675–1680. https://doi.org/10.1016/0967-0637(95)00072-E

Andersson, K. K., & Hooper, A. B. (1983). O_2 and H_2O are each the source of one O in NO_2^- produced from NH_3 by Nitrosomonus: ^{15}N-NMR evidence. *FEBS Letters*, *164*(2), 236–240. https://doi.org/10.1016/0014-5793(83)80292-0

Armstrong, R. A., Lee, C., Hedges, J. I., Honjo, S., & Wakeham, S. G. (2002). A new, mechanistic model for organic carbon fluxes in the ocean based on the quantitative association of POC with ballast minerals. *Deep-Sea Research II*, *49*(1–3), 219–236. https://doi.org/10.1016/S0967-0645(01)00101-1

Arrigo, K. R., Robinson, D. H., Worthen, D. L., Dunbar, R. B., DiTullio, G. R., VanWoert, M., & Lizotte, M. P. (1999). Phytoplankton community structure and the drawdown of nutrients and CO_2 in the Southern Ocean. *Science*, *283*(5400), 365–367. https://doi.org/10.1126/science.283.5400.365

Arrigo, K. R., van Dijken, G. L., & Strong, A. L. (2015). Environmental controls of marine productivity hot spots around Antarctica. *Journal of Geophysical Research: Oceans*, *120*(8), 5545–5565. https://doi.org/10.1002/2015JC010888

Asper, V. L., & Smith, W. O. (1999). Particle fluxes during austral spring and summer in the southern Ross Sea, Antarctica. *Journal of Geophysical Research: Oceans*, *104*(C3), 5345–5359. https://doi.org/10.1029/1998JC900067

Behrenfeld, M. J., Boss, E., Siegel, D. A., Shea, D. M., Behrenfeld, M. J., Boss, E., Siegel, D. A., & Shea, D. M. (2005). Carbon-based ocean productivity and phytoplankton physiology from space. *Global Biogeochemical Cycles*, *19*(1), 1–14. https://doi.org/10.1029/2004GB002299

Behrenfeld, M. J., & Falkowski, P. G. (1997). Photosynthetic rates derived from satellite-based chlorophyll concentration. *Limnology and Oceanography*, *42*(1), 1–20. https://doi.org/10.4319/LO.1997.42.1.0001

Bendschneider, K., & Robinson, R. J. (1952). A new spectrophotometric method for the determination of nitrite in sea water. *University of Washington Oceanographic Laboratories*.

Berges, J. A., & Harrison, P. J. (1995). Nitrate reductase activity quantitatively predicts the rate of nitrate incorporation under steady state light limitation: A revised assay and characterization of the enzyme in three species of marine phytoplankton. *Limnology and Oceanography*, *40*(1), 82–93. https://doi.org/10.4319/lo.1995.40.1.0082

Böhlke, J. K., Gwinn, C. J., & Coplen, T. B. (1993). New reference materials for nitrogen-isotope-ratio measurements. *Geostandards Newsletter*, *17*(1), 159–164. https://doi.org/10.1111/J.1751-908X.1993.TB00131.X

Böhlke, J. K., Mroczkowski, S. J., & Coplen, T. B. (2003). Oxygen isotopes in nitrate: new reference materials for ^{18}O:^{17}O:^{16}O measurements and observations on nitrate-water equilibration. *Rapid Communications in Mass Spectrometry*, *17*(16), 1835–1846. https://doi.org/10.1002/RCM.1123

Bopp, L., Monfray, P., Aumont, O., Dufresne, J. L., le Treut, H., Madec, G., Terray, L., & Orr, J. C. (2001). Potential impact of climate change on marine export production. *Global Biogeochemical Cycles*, *15*(1), 81–99. https://doi.org/10.1029/1999GB001256

Boshers, D. S., Granger, J., Tobias, C. R., Böhlke, J. K., & Smith, R. L. (2019). Constraining the Oxygen Isotopic Composition of Nitrate Produced by Nitrification. *Environmental Science and Technology*, *53*(3), 1206–1216. https://doi.org/10.1021/acs.est.8b03386

Brandes, J. A., & Devol, A. H. (1997). Isotopic fractionation of oxygen and nitrogen in coastal marine sediments. *Geochimica et Cosmochimica Acta*, *61*(9), 1793–1801. https://doi.org/10.1016/S0016-7037(97)00041-0

Brandes, J. A., & Devol, A. H. (2002). A global marine-fixed nitrogen isotopic budget: Implications for Holocene nitrogen cycling. *Global Biogeochemical Cycles*, *16*(4), 67–1. https://doi.org/10.1029/2001GB001856

Brandes, J. A., Devol, A. H., Yoshinari, T., Jayakumar, D. A., & Naqvi, S. W. A. (1998). Isotopic composition of nitrate in the central Arabian Sea and eastern tropical North Pacific: A tracer for mixing and nitrogen cycles. *Limnology and Oceanography*, *43*(7), 1680–1689. https://doi.org/10.4319/LO.1998.43.7.1680

Brunner, B., Contreras, S., Lehmann, M. F., Matantseva, O., Rollog, M., Kalvelage, T., Klockgether, G., Lavik, G., Jetten, M. S. M., Kartal, B., & Kuypers, M. M. M. (2013). Nitrogen isotope effects induced by anammox bacteria. *Proceedings of the National Academy of Sciences of the United States of America*, *110*(47), 18994–18999. https://doi.org/10.1073/pnas.1310488110

Buchwald, C., & Casciotti, K. L. (2010). Oxygen isotopic fractionation and exchange during bacterial nitrite oxidation. *Limnology and Oceanography*, *55*(3), 1064–1074. https://doi.org/10.4319/LO.2010.55.3.1064

Buchwald, C., & Casciotti, K. L. (2013). Isotopic ratios of nitrite as tracers of the sources and age of oceanic nitrite. *Nature Geoscience*, *6*(4), 308–313. https://doi.org/10.1038/ngeo1745

Buchwald, C., Santoro, A. E., McIlvin, M. R., & Casciotti, K. L. (2012). Oxygen isotopic composition of nitrate and nitrite produced by nitrifying cocultures and natural marine assemblages. *Limnology and Oceanography*, *57*(5), 1361–1375. https://doi.org/10.4319/lo.2012.57.5.1361

Buchwald, C., & Wankel, S. D. (2022). Enzyme-catalyzed isotope equilibrium: A hypothesis to explain apparent N cycling phenomena in low oxygen environments. *Marine Chemistry*, *244*, 104140. https://doi.org/10.1016/j.marchem.2022.104140

Buesseler, K. O., & Boyd, P. W. (2009). Shedding light on processes that control particle export and flux attenuation in the twilight zone of the open ocean. *Limnology and Oceanography*, *54*(4), 1210–1232. https://doi.org/10.4319/LO.2009.54.4.1210

Burris, R. H. (1956). Studies on the mechanism of biological nitrogen fixation. *Inorganic Nitrogen Metabolism*, 316–343.

Carpenter, E. J., Harvey, H. R., Fry, B., & Capone, D. G. (1997). Biogeochemical tracers of the marine cyanobacterium *Trichodesmium*. *Deep Sea Research Part I: Oceanographic Research Papers*, *44*(1), 27–38. https://doi.org/10.1016/S0967-0637(96)00091-X

Casciotti, K. L. (2009). Inverse kinetic isotope fractionation during bacterial nitrite oxidation. *Geochimica et Cosmochimica Acta*, *73*(7), 2061–2076. https://doi.org/10.1016/j.gca.2008.12.022

Casciotti, K. L. (2016). Nitrogen and Oxygen Isotopic Studies of the Marine Nitrogen Cycle. *Annual Review of Marine Science*, *8*(1), 379–407. https://doi.org/10.1146/annurev-marine-010213-135052

Casciotti, K. L., Böhlke, J. K., McIlvin, M. R., Mroczkowski, S. J., & Hannon, J. E. (2007). Oxygen isotopes in nitrite: Analysis, calibration, and equilibration. *Analytical Chemistry*, *79*(6), 2427–2436. https://doi.org/10.1021/ac061598h

Casciotti, K. L., McIlvin, M., & Buchwald, C. (2010). Oxygen isotopic exchange and fractionation during bacterial ammonia oxidation. *Limnology and Oceanography*, *55*(2), 753–762. https://doi.org/10.4319/lo.2010.55.2.0753

Casciotti, K. L., Sigman, D. M., Hastings, M. G., Böhlke, J. K., & Hilkert, A. (2002). Measurement of the oxygen isotopic composition of nitrate in seawater and freshwater using the denitrifier method. *Analytical Chemistry*, *74*(19), 4905–4912. https://doi.org/10.1021/ac020113w

Casciotti, K. L., Sigman, D. M., & Ward, B. B. (2003). Linking diversity and stable isotope fractionation in ammonia-oxidizing bacteria. *Geomicrobiology Journal*, *20*(4), 335–353. https://doi.org/10.1080/01490450303895

Casciotti, K. L., Trull, T. W., Glover, D. M., & Davies, D. (2008). Constraints on nitrogen cycling at the subtropical North Pacific Station ALOHA from isotopic measurements of nitrate and particulate nitrogen. *Deep-Sea Research Part II: Topical Studies in Oceanography*, *55*(14–15), 1661–1672. https://doi.org/10.1016/j.dsr2.2008.04.017

Chapman, C. C., Lea, M. A., Meyer, A., Sallée, J. B., & Hindell, M. (2020). Defining Southern Ocean fronts and their influence on biological and physical processes in a changing climate. In *Nature Climate Change* (Vol. 10, Issue 3, pp. 209–219). Nature Research. https://doi.org/10.1038/s41558-020-0705-4

Checkley, D. M., & Miller, C. A. (1989). Nitrogen isotope fractionation by oceanic zooplankton. *Deep Sea Research Part A. Oceanographic Research Papers*, *36*(10), 1449–1456. https://doi.org/10.1016/0198-0149(89)90050-2

Clark, D. R., Rees, A. P., & Joint, I. (2008). Ammonium regeneration and nitrification rates in the oligotrophic Atlantic Ocean: Implications for new production estimates. *Limnology and Oceanography*, *53*(1), 52–62. https://doi.org/10.4319/lo.2008.53.1.0052

Cline, J. D., & Kaplan, I. R. (1975). Isotopic fractionation of dissolved nitrate during denitrification in the eastern tropical north Pacific Ocean. *Marine Chemistry*, *3*(4), 271–299. https://doi.org/10.1016/0304-4203(75)90009-2

Coale, K. H., Johnson, K. S., Fitzwater, S. E., Gordon, R. M., Tanner, S., Chavez, F. P., Ferioli, L., Sakamoto, C., Rogers, P., Millero, F., Steinberg, P., Nightingale, P., Cooper, D., Cochlan, W. P., Landry, M. R., Constantinou, J., Rollwagen, G., Trasvina, A., & Kudela, R. (1996). A massive phytoplankton bloom induced by an ecosystem-scale iron fertilization experiment in the equatorial Pacific Ocean. *Nature*, *383*(6600), 495. https://doi.org/10.1038/383495a0

Deacon, G. E. R. (1979). The Weddell gyre. *Deep Sea Research Part A. Oceanographic Research Papers*, *26*(9), 981–995. https://doi.org/10.1016/0198-0149(79)90044-X

Delwiche, C. C., Zinke, P. J., Johnson, C. M., & Virginia, R. A. (1979). Nitrogen Isotope Distribution as a Presumptive Indicator of Nitrogen Fixation. *Botanical Gazette*, *140*, S65–S69. https://doi.org/10.1086/337037

Deppeler, S. L., & Davidson, A. T. (2017). Southern Ocean phytoplankton in a changing climate. *Frontiers in Marine Science*, *4*(FEB), 40. https://doi.org/10.3389/FMARS.2017.00040/BIBTEX

DiFiore, P. J., Sigman, D. M., & Dunbar, R. B. (2009). Upper ocean nitrogen fluxes in the Polar Antarctic Zone: Constraints from the nitrogen and oxygen isotopes of nitrate. *Geochemistry, Geophysics, Geosystems*, *10*(11). https://doi.org/10.1029/2009GC002468

DiFiore, P. J., Sigman, D. M., Karsh, K. L., Trull, T. W., Dunbar, R. B., & Robinson, R. S. (2010). Poleward decrease in the isotope effect of nitrate assimilation across the Southern Ocean. *Geophysical Research Letters*, *37*(17), 1–5. https://doi.org/10.1029/2010GL044090

DiFiore, P. J., Sigman, D. M., Trull, T. W., Lourey, M. J., Karsh, K., Cane, G., & Ho, R. (2006). Nitrogen isotope constraints on subantarctic biogeochemistry. *Journal of Geophysical Research: Oceans*, *111*(8), 1–19. https://doi.org/10.1029/2005JC003216

Dinniman, M. S., St-Laurent, P., Arrigo, K. R., Hofmann, E. E., & van Dijken, G. L. (2020). Analysis of Iron Sources in Antarctic Continental Shelf Waters. *Journal of Geophysical Research: Oceans*, *125*(5). https://doi.org/10.1029/2019JC015736

Dore, J. E., & Karl, D. M. (1996). Nitrification in the euphotic zone as a source for nitrite, nitrate, and nitrous oxide at Station ALOHA. *Limnology and Oceanography*, *41*(8), 1619–1628. https://doi.org/10.4319/lo.1996.41.8.1619

Dugdale, R. C., & Goering, J. J. (1967). Uptake of new and regenerated forms of nitrogen in primary productivity. *Limnology and Oceanography*, *12*(2). https://doi.org/10.4319/lo.1967.12.2.0196

Dunne, J. P., Armstrong, R. A., Gnnadesikan, A., & Sarmiento, J. L. (2005). Empirical and mechanistic models for the particle export ratio. *Global Biogeochemical Cycles*, *19*(4), 4026. https://doi.org/10.1029/2004GB002390

Dunne, J. P., Sarmiento, J. L., & Gnanadesikan, A. (2007). A synthesis of global particle export from the surface ocean and cycling through the ocean interior and on the seafloor. *Global Biogeochemical Cycles*, *21*(4). https://doi.org/10.1029/2006GB002907

Dupont, T. K., & Alley, R. B. (2005). Assessment of the importance of ice-shelf buttressing to ice-sheet flow. *Geophysical Research Letters*, *32*(4), 1–4. https://doi.org/10.1029/2004GL022024

Eicken, H. (1992). Salinity profiles of Antarctic sea ice: Field data and model results. *Journal of Geophysical Research*, *97*(C10), 15545–15557. https://doi.org/10.1029/92JC01588

Einsle, O., & Kroneck, P. M. H. (2004). Structural basis of denitrification. *Biological Chemistry*, *385*(10), 875–883. https://doi.org/10.1515/BC.2004.115

Elskens, M., Baeyens, W., Cattaldo, T., Dehairs, F., & Griffiths, B. (2002). N uptake conditions during summer in the Subantarctic and Polar Frontal Zones of the Australian sector of the Southern Ocean. *J. Geophys. Res*, *107*(C11), 3182. https://doi.org/10.1029/2001JC000897

Emerson, S. (2014). Annual net community production and the biological carbon flux in the ocean. *Global Biogeochemical Cycles*, *28*(1). https://doi.org/10.1002/2013GB004680

Eppley, R. W., & Peterson, B. J. (1979). Particulate organic matter flux and planktonic new production in the deep ocean. *Nature*, *282*(5740). https://doi.org/10.1038/282677a0

Etourneau, J., Sgubin, G., Crosta, X., Swingedouw, D., Willmott, V., Barbara, L., Houssais, M., Schouten, S., Damsté, J. S. S., Goosse, H., Escutia, C., Crespin, J., Massé, G., & Kim, J. (2019). Ocean temperature impact on ice shelf extent in the eastern Antarctic Peninsula. *Nature Communications*, *10*(1), 8–15. https://doi.org/10.1038/s41467-018-08195-6

Fawcett, S. E., Lomas, M. W., Casey, J. R., Ward, B. B., & Sigman, D. M. (2011). Assimilation of upwelled nitrate by small eukaryotes in the Sargasso Sea. *Nature Geoscience*, *4*(10), 717–722. https://doi.org/10.1038/ngeo1265

Fawcett, S. E., Lomas, M. W., Ward, B. B., & Sigman, D. M. (2014). The counterintuitive effect of summer-to-fall mixed layer deepening on eukaryotic new production in the Sargasso Sea. *Global Biogeochemical Cycles*, *28*(2), 86–102. https://doi.org/10.1002/2013GB004579

Fawcett, S. E., Ward, B. B., Lomas, M. W., & Sigman, D. M. (2015). Vertical decoupling of nitrate assimilation and nitrification in the Sargasso Sea. *Deep-Sea Research Part I: Oceanographic Research Papers*, *103*, 64–72. https://doi.org/10.1016/j.dsr.2015.05.004

Flynn, R. F., Bornman, T. G., Burger, J. M., Smith, S., Spence, K. A. M., & Fawcett, S. E. (2021). Summertime productivity and carbon export potential in the Weddell Sea, with a focus on the waters adjacent to Larsen C Ice Shelf. *Biogeosciences*, *18*(22), 6031–6059. https://doi.org/10.5194/bg-18-6031-2021

Fofonoff, N. P., & Millard, R. C. (1983). Algorithms for the computation of fundamental properties of seawater. *UNESCO Technical Papers in Marine Sciences*. https://doi.org/https://doi.org/10.25607/OBP-1450

Francois, R., Altabet, M. A., & Burckle, L. H. (1992). Glacial to interglacial changes in surface nitrate utilization in the Indian Sector of the Southern Ocean as recorded by sediment $\delta^{15}N$. *Paleoceanography*, *7*(5), 589–606. https://doi.org/10.1029/92PA01573

Francois, R., Altabett, M. A., Yu, E. F., Sigman, D. M., Bacon, M. P., Frank, M., Bohrmann, G., Bareille, G., & Labeyrie, L. D. (1997). Contribution of Southern Ocean surface-water stratification to low atmospheric CO_2 concentrations during the last glacial period. *Nature 1997 389:6654*, *389*(6654), 929–935. https://doi.org/10.1038/40073

Francois, R., Honjo, S., Krishfield, R., & Manganini, S. (2002). Factors controlling the flux of organic carbon to the bathypelagic zone of the ocean. *Global Biogeochemical Cycles*, *16*(4). https://doi.org/10.1029/2001GB001722

Friedlingstein, P., Jones, M. W., O'Sullivan, M., Andrew, R. M., Bakker, D. C. E., Hauck, J., le Quéré, C., Peters, G. P., Peters, W., Pongratz, J., Sitch, S., Canadell, J. G., Ciais, P., Jackson, R. B., Alin, S. R., Anthoni, P., Bates, N. R., Becker, M., Bellouin, N., … Zeng, J. (2022). Global Carbon Budget 2021. *Earth System Science Data*, *14*(4), 1917–2005. https://doi.org/10.5194/ESSD-14-1917-2022

Fripiat, F., Martínez-García, A., Fawcett, S. E., Kemeny, P. C., Studer, A. S., Smart, S. M., Rubach, F., Oleynik, S., Sigman, D. M., & Haug, G. H. (2019). The isotope effect of nitrate assimilation in the Antarctic Zone: Improved estimates and paleoceanographic implications. *Geochimica et Cosmochimica Acta*, *247*, 261–279. https://doi.org/10.1016/j.gca.2018.12.003

Fripiat, F., Martínez-García, A., Marconi, D., Fawcett, S. E., Kopf, S. H., Luu, V. H., Rafter, P. A., Zhang, R., Sigman, D. M., & Haug, G. H. (2021). Nitrogen isotopic constraints on nutrient transport to the upper ocean. *Nature Geoscience*, *14*(11), 855–861. https://doi.org/10.1038/s41561-021-00836-8

Fripiat, F., Meiners, K. M., Vancoppenolle, M., Papadimitriou, S., Thomas, D. N., Ackley, S. F., Arrigo, K. R., Carnat, G., Cozzi, S., Delille, B., Dieckmann, G. S., Dunbar, R. B., Fransson, A., Kattner, G., Kennedy, H., Lannuzel, D., Munro, D. R., Nomura, D., Rintala, J.-M., … Tison, J.-L. (2017). Macro-nutrient concentrations in Antarctic pack ice: Overall patterns and overlooked processes. *Elementa: Science of the Anthropocene*, *5*(13). https://doi.org/10.1525/elementa.217

Garber, E. A., & Hollocher, T. C. (1982). ^{15}N,^{18}O tracer studies on the activation of nitrite by denitrifying bacteria. Nitrite/water-oxygen exchange and nitrosation reactions as indicators of electrophilic catalysis. *Journal of Biological Chemistry*, *257*(14). https://doi.org/10.1016/s0021-9258(18)34301-1

Gaye-Haake, B., Lahajnar, N., Emeis, K. C., Unger, D., Rixen, T., Suthhof, A., Ramaswamy, V., Schulz, H., Paropkari, A. L., Guptha, M. V. S., & Ittekkot, V. (2005). Stable nitrogen isotopic ratios of sinking particles and sediments from the northern Indian Ocean. *Marine Chemistry*, *96*(3–4), 243–255. https://doi.org/10.1016/J.MARCHEM.2005.02.001

Gilbert, E., & Kittel, C. (2021). Surface Melt and Runoff on Antarctic Ice Shelves at 1.5°C, 2°C, and 4°C of Future Warming. *Geophysical Research Letters*, *48*(8). https://doi.org/10.1029/2020GL091733

Goeyens, L., Tréguer, P., Baumann, M. E. M., Baeyens, W., & Dehairs, F. (1995). The leading role of ammonium in the nitrogen uptake regime of Southern Ocean marginal ice zones. *Journal of Marine Systems*, *6*(4), 345–361. https://doi.org/10.1016/0924-7963(94)00033-8

Gonfiantini, R., Stichler, W., & Rozanski, K. (1995). Standards and intercomparison materials distributed by the International Atomic Energy Agency for stable isotope measurements. *International Atomic Energy Agency*, *IAEA-TECDOC-825*. http://inis.iaea.org/Search/search.aspx?orig_q=RN:27021328

Gordon, A. L. (1998). Western Weddell sea thermohaline stratification. *Ocean, Ice and Atmosphere: Interactions at the Antarctic Continental Margin, Antarctic Research Series*, *75*, 215–240.
Gordon, A. L., Huber, B. A., Hellmer, H. H., & Ffield, A. (1993). Deep and Bottom Water of the Weddell Sea's Western Rim. *Science*, *262*(55), 95–97. https://doi.org/10.1126/SCIENCE.262.5130.95
Granger, J., Sigman, D. M., Lehmann, M. F., & Tortell, P. D. (2008). Nitrogen and oxygen isotope fractionation during dissimilatory nitrate reduction by denitrifying bacteria. *Limnology and Oceanography*, *53*(6), 2533–2545. https://doi.org/10.4319/lo.2008.53.6.2533
Granger, J., Sigman, D. M., Needoba, J. A., & Harrison, P. J. (2004). Coupled nitrogen and oxygen isotope fractionation of nitrate during assimilation by cultures of marine phytoplankton. *Limnology and Oceanography*, *49*(5), 1763–1773. https://doi.org/10.4319/lo.2004.49.5.1763
Granger, J., Sigman, D. M., Rohde, M. M., Maldonado, M. T., & Tortell, P. D. (2010). N and O isotope effects during nitrate assimilation by unicellular prokaryotic and eukaryotic plankton cultures. *Geochimica et Cosmochimica Acta*, *74*(3), 1030–1040. https://doi.org/10.1016/j.gca.2009.10.044
Grasshoff, K. (1976). *Methods of Seawater Analysis* (K. Grasshoff, K. Kremling, & M. Ehrhardt, Eds.). Wiley. https://doi.org/10.1002/9783527613984
Guerrero, M. A., & Jones, R. D. (1996a). Photoinhibition of marine nitrifying bacteria. I. Wavelength-dependent response. *Marine Ecology Progress Series*, *141*(1–3), 183–192. https://doi.org/10.3354/meps141183
Guerrero, M. A., & Jones, R. D. (1996b). Photoinhibition of marine nitrifying bacteria. II. Dark recovery after monochromatic or polychromatic irradiation. *Marine Ecology Progress Series*, *141*(1–3), 193–198. https://doi.org/10.3354/meps141193
Haumann, A. F., Gruber, N., Münnich, M., Frenger, I., & Kern, S. (2016). Sea-ice transport driving Southern Ocean salinity and its recent trends. *Nature*, *537*(7618), 89–92. https://doi.org/10.1038/nature19101
Hedges, J. I., Baldock, J. A., Gélinas, Y., Lee, C., Peterson, M. L., & Wakeham, S. G. (2002). The biochemical and elemental compositions of marine plankton: A NMR perspective. *Marine Chemistry*, *78*(1), 47–63. https://doi.org/10.1016/S0304-4203(02)00009-9
Henson, S. A., Sanders, R., & Madsen, E. (2012). Global patterns in efficiency of particulate organic carbon export and transfer to the deep ocean. *Global Biogeochemical Cycles*, *26*(1). https://doi.org/10.1029/2011GB004099
Hoch, M. P., Fogel, M. L., & Kirchman, D. L. (1992). Isotope fractionation associated with ammonium uptake by a marine bacterium. *Limnology and Oceanography*, *37*(7), 1447–1459. https://doi.org/10.4319/lo.1992.37.7.1447
Hoering, T. C., & Ford, H. T. (1959). The Isotope Effect in the Fixation of Nitrogen by Azotobacter. *Journal of the American Chemical Society*, *82*(2), 376–378. https://pubs.acs.org/sharingguidelines
Holl, C. M., & Montoya, J. P. (2005). Interactions between nitrate uptake and nitrogen fixation in continuous cultures of the marine diazotroph *Trichodesmium* (cyanobacteria). *Journal of Phycology*, *41*(6), 1178–1183. https://doi.org/10.1111/J.1529-8817.2005.00146.X
Holmes, R. M., Aminot, A., Kérouel, R., Hooker, B. A., & Peterson, B. J. (1999). A simple and precise method for measuring ammonium in marine and freshwater ecosystems. *Canadian Journal of Fisheries and Aquatic Sciences*, *56*(10), 1801–1808. https://doi.org/10.1139/f99-128
Hooper, A. B., & Terry, K. R. (1974). Photoinactivation of ammonia oxidation in Nitrosomonas. *Journal of Bacteriology*, *119*(3), 899–906. https://doi.org/10.1128/jb.119.3.899-906.1974
Hoppema, M., Goeyens, L., & Fahrbach, E. (2000). Intense nutrient removal in the remote area off Larsen Ice Shelf (Weddell Sea). *Polar Biology*, *23*(2), 85–94. https://doi.org/10.1007/s003000050012
Hoppema, M., Middag, R., de Baar, H. J. W., Fahrbach, E., van Weerlee, E. M., & Thomas, H. (2007). Whole season net community production in the Weddell Sea. *Polar Biology*, *31*(1), 101–111. https://doi.org/10.1007/S00300-007-0336-5/FIGURES/5
Hupe, A., & Karstensen, J. (2000). Redfield stoichiometry in Arabian Sea subsurface waters. *Global Biogeochemical Cycles*, *14*(1), 357–372. https://doi.org/10.1029/1999GB900077
Hutchinson, K., Deshayes, J., Sallee, J. B., Dowdeswell, J. A., de Lavergne, C., Ansorge, I., Luyt, H., Henry, T., & Fawcett, S. E. (2020). Water Mass Characteristics and Distribution Adjacent to Larsen C Ice Shelf, Antarctica. *Journal of Geophysical Research: Oceans*, *125*(4), 1–11. https://doi.org/10.1029/2019JC015855
Janssens, J., Meiners, K. M., Tison, J.-L., Dieckmann, G., Delille, B., & Lannuzel, D. (2016). Incorporation of iron and organic matter into young Antarctic sea ice during its initial growth stages. *Elementa: Science of the Anthropocene*, *4*. https://doi.org/10.12952/journal.elementa.000123
Jenkins, W. J. (1998). Studying subtropical thermocline ventilation and circulation using tritium and ^{3}He. *Journal of Geophysical Research: Oceans*, *103*(C8), 15817–15831. https://doi.org/10.1029/98JC00141
Jennings, J. C., Gordon, L. I., & Nelson, D. M. (1984). Nutrient depletion indicates high primary productivity in the Weddell Sea. *Nature*, *309*(5963), 51–54. https://doi.org/10.1038/309051a0

Jickells, T. D., Buitenhuis, E., Altieri, K., Baker, A. R., Capone, D., Duce, R. A., Dentener, F., Fennel, K., Kanakidou, M., LaRoche, J., Lee, K., Liss, P., Middelburg, J. J., Moore, J. K., Okin, G., Oschlies, A., Sarin, M., Seitzinger, S., Sharples, J., … Zamora, L. M. (2017). A reevaluation of the magnitude and impacts of anthropogenic atmospheric nitrogen inputs on the ocean. *Global Biogeochemical Cycles*, *31*(2), 289–305. https://doi.org/10.1002/2016GB005586

Johnson, K. S., Mazloff, M. R., Bif, M. B., Takeshita, Y., Jannasch, H. W., Maurer, T. L., Plant, J. N., Verdy, A., Walz, P. M., Riser, S. C., & Talley, L. D. (2022). Carbon to Nitrogen Uptake Ratios Observed Across the Southern Ocean by the SOCCOM Profiling Float Array. *Journal of Geophysical Research: Oceans*, *127*(9). https://doi.org/10.1029/2022JC018859

Johnson, K. S., Plant, J. N., Dunne, J. P., Talley, L. D., & Sarmiento, J. L. (2017). Annual nitrate drawdown observed by SOCCOM profiling floats and the relationship to annual net community production. *Journal of Geophysical Research: Oceans*, *122*(8). https://doi.org/10.1002/2017JC012839

Karsh, K. L., Granger, J., Kritee, K., & Sigman, D. M. (2012). Eukaryotic assimilatory nitrate reductase fractionates N and O isotopes with a ratio near unity. *Environmental Science and Technology*, *46*(11), 5727–5735. https://doi.org/10.1021/es204593q

Karsh, K. L., Trull, T. W., Lourey, M. J., & Sigman, D. M. (2003). Relationship of nitrogen isotope fractionation to phytoplankton size and iron availability during the Southern Ocean Iron RElease Experiment (SOIREE). *Limnology and Oceanography*, *48*(3), 1058–1068. https://doi.org/10.4319/LO.2003.48.3.1058

Karsh, K. L., Trull, T. W., Sigman, D. M., Thompson, P. A., & Granger, J. (2013). The contributions of nitrate uptake and efflux to isotope fractionation during algal nitrate assimilation. *Geochimica et Cosmochimica Acta*, *132*, 391–412. https://doi.org/10.1016/j.gca.2013.09.030

Kemeny, P. C., Weigand, M. A., Zhang, R., Carter, B. R., Karsh, K. L., Fawcett, S. E., & Sigman, D. M. (2016). Enzyme-level interconversion of nitrate and nitrite in the fall mixed layer of the Antarctic Ocean. *Global Biogeochemical Cycles*, *30*(7), 1069–1085. https://doi.org/10.1002/2015GB005350

Kerr, R., Dotto, T. S., Mata, M. M., & Hellmer, H. H. (2018). Three decades of deep water mass investigation in the Weddell Sea (1984–2014): Temporal variability and changes. *Deep Sea Research Part II: Topical Studies in Oceanography*, *149*, 70–83. https://doi.org/10.1016/j.dsr2.2017.12.002

Khatiwala, S., Primeau, F., & Holzer, M. (2012). Ventilation of the deep ocean constrained with tracer observations and implications for radiocarbon estimates of ideal mean age. *Earth and Planetary Science Letters*, *325–326*, 116–125. https://doi.org/10.1016/J.EPSL.2012.01.038

Klaas, C., & Archer, D. E. (2002). Association of sinking organic matter with various types of mineral ballast in the deep sea: Implications for the rain ratio. *Global Biogeochemical Cycles*, *16*(4), 63–1. https://doi.org/10.1029/2001GB001765

Klunder, M. B., Laan, P., de Baar, H. J. W., Middag, R., Neven, I., & van Ooijen, J. (2014). Dissolved Fe across the Weddell Sea and Drake Passage: Impact of DFe on nutrient uptake. *Biogeosciences*, *11*(3), 651–669. https://doi.org/10.5194/BG-11-651-2014

Knapp, A. N., Casciotti, K. L., & Prokopenko, M. G. (2018). Dissolved Organic Nitrogen Production and Consumption in Eastern Tropical South Pacific Surface Waters. *Global Biogeochemical Cycles*, *32*(5), 769–783. https://doi.org/10.1029/2017GB005875

Knapp, A. N., Dekaezemacker, J., Bonnet, S., Sohm, J. A., & Capone, D. G. (2012). Sensitivity of *Trichodesmium erythraeum* and *Crocosphaera watsonii* abundance and N_2 fixation rates to varying NO_3^- and PO_4^{3-} concentrations in batch cultures. *Aquatic Microbial Ecology*, *66*(3), 223–236. https://doi.org/10.3354/AME01577

Koike, I., Holm-Hansen, O., & Biggs, D. C. (1986). Inorganic nitrogen metabolism by Antarctic phytoplankton with special reference to ammonium cycling. *Marine Ecology - Progress Series*, *30*, 105–116.

Körtzinger, A., Koeve, W., Kähler, P., & Mintrop, L. (2001). C : N ratios in the mixed layer during the productive season in the northeast Atlantic Ocean. *Deep Sea Research Part I: Oceanographic Research Papers*, *48*(3), 661–688. https://doi.org/10.1016/S0967-0637(00)00051-0

Körtzinger, A., Send, U., Lampitt, R. S., Hartman, S., Wallace, D. W. R., Karstensen, J., Villagarcia, M. G., Llinás, O., & DeGrandpre, M. D. (2008). The seasonal pCO_2 cycle at 49°N/16.5°W in the northeastern Atlantic Ocean and what it tells us about biological productivity. *Journal of Geophysical Research: Oceans*, *113*(C4). https://doi.org/10.1029/2007JC004347

Kritee, K., Sigman, D. M., Granger, J., Ward, B. B., Jayakumar, A., & Deutsch, C. (2012). Reduced isotope fractionation by denitrification under conditions relevant to the ocean. *Geochimica et Cosmochimica Acta*, *92*, 243–259. https://doi.org/10.1016/j.gca.2012.05.020

Kumar, S., Nicholas, D. J. D., & Williams, E. H. (1983). Definitive ^{15}N NMR evidence that water serves as a source of "O" during nitrite oxidation by *Nitrobacter agilis*. *FEBS Letters*, *152*(1), 71–74. https://doi.org/10.1016/0014-5793(83)80484-0

Kwon, E. Y., Primeau, F., & Sarmiento, J. L. (2009). The impact of remineralization depth on the air–sea carbon balance. *Nature Geoscience*, *2*(9), 630–635. https://doi.org/10.1038/ngeo612

Lange, M. A., Schlosser, P., Ackley, S. F., Wadhams, P., & Dieckmann, G. S. (1990). ^{18}O Concentrations in Sea Ice of the Weddell Sea, Antarctica. *Journal of Glaciology*, *36*(124), 315–323. https://doi.org/10.3189/002214390793701291

Lannuzel, D., Schoemann, V., de Jong, J., Chou, L., Delille, B., Becquevort, S., & Tison, J. L. (2008). Iron study during a time series in the western Weddell pack ice. *Marine Chemistry*, *108*(1–2), 85–95. https://doi.org/10.1016/J.MARCHEM.2007.10.006

Lannuzel, D., Vancoppenolle, M., van der Merwe, P., de Jong, J., Meiners, K. M., Grotti, M., Nishioka, J., & Schoemann, V. (2016). Iron in sea ice: Review & new insights. In J. W. Deming & L. A. Miller (Eds.), *Elementa* (Vol. 4). https://doi.org/10.12952/journal.elementa.000130

Laws, E. A., D'Sa, E., & Naik, P. (2011). Simple equations to estimate ratios of new or export production to total production from satellite-derived estimates of sea surface temperature and primary production. *Limnology and Oceanography: Methods*, *9*(12), 593–601. https://doi.org/10.4319/LOM.2011.9.593

Laws, E. A., Falkowski, P. G., Smith, W. O., Ducklow, H., & McCarthy, J. J. (2000). Temperature effects on export production in the open ocean. *Global Biogeochemical Cycles*, *14*(4), 1231–1246. https://doi.org/10.1029/1999GB001229

Lehmann, M. F., Bernasconi, S. M., Barbieri, A., & McKenzie, J. A. (2002). Preservation of organic matter and alteration of its carbon and nitrogen isotope composition during simulated and in situ early sedimentary diagenesis. *Geochimica et Cosmochimica Acta*, *66*(20), 3573–3584. https://doi.org/10.1016/S0016-7037(02)00968-7

Lehmann, M. F., Sigman, D. M., McCorkle, D. C., Granger, J., Hoffmann, S., Cane, G., & Brunelle, B. G. (2007). The distribution of nitrate $^{15}N/^{14}N$ in marine sediments and the impact of benthic nitrogen loss on the isotopic composition of oceanic nitrate. *Geochimica et Cosmochimica Acta*, *71*(22), 5384–5404. https://doi.org/10.1016/J.GCA.2007.07.025

Li, Z., Cassar, N., Huang, K., Ducklow, H., & Schofield, O. (2016). Interannual variability in net community production at the Western Antarctic Peninsula region (1997–2014). *Journal of Geophysical Research: Oceans*, *121*(7), 4748–4762. https://doi.org/10.1002/2015JC011378

Liu, K. K., Kao, S. J., Chiang, K. P., Gong, G. C., Chang, J., Cheng, J. S., & Lan, C. Y. (2013). Concentration dependent nitrogen isotope fractionation during ammonium uptake by phytoplankton under an algal bloom condition in the Danshuei estuary, northern Taiwan. *Marine Chemistry*, *157*, 242–252. https://doi.org/10.1016/J.MARCHEM.2013.10.005

Liu, K. K., & Kaplan, I. R. (1989). The eastern tropical Pacific as a source of ^{15}N-enriched nitrate in seawater off southern California. *Limnology and Oceanography*, *34*(5), 820–830. https://doi.org/10.4319/LO.1989.34.5.0820

Liu, Y., Moore, J. C., Cheng, X., Gladstone, R. M., Bassis, J. N., Liu, H., Wen, J., & Hui, F. (2015). Ocean-driven thinning enhances iceberg calving and retreat of Antarctic ice shelves. *Proceedings of the National Academy of Sciences of the United States of America*, *112*(11), 3263–3268. https://doi.org/10.1073/pnas.1415137112

Lomas, M. W., & Glibert, P. M. (1999). Interactions between NH_4^+ and NO_3^- uptake and assimilation: comparison of diatoms and dinoflagellates at several growth temperatures. *Marine Biology*, *133*(3), 541–551. https://doi.org/10.1007/s002270050494

Lourey, M. J., Trull, T. W., & Sigman, D. M. (2003). Sensitivity of $\delta^{15}N$ of nitrate, surface suspended and deep sinking particulate nitrogen to seasonal nitrate depletion in the Southern Ocean. *Global Biogeochemical Cycles*, *17*(3). https://doi.org/10.1029/2002gb001973

Macko, S. A., Estep, M. L. F., Engel, M. H., & Hare, P. E. (1986). Kinetic fractionation of stable nitrogen isotopes during amino acid transamination. *Geochimica et Cosmochimica Acta*, *50*(10), 2143–2146. https://doi.org/10.1016/0016-7037(86)90068-2

Mariotti, A., Germon, J. C., Hubert, P., Kaiser, P., Letolle, R., Tardieux, A., & Tardieux, P. (1981). Experimental determination of nitrogen kinetic isotope fractionation: Some principles; illustration for the denitrification and nitrification processes. *Plant and Soil*, *62*(3), 413–430. https://doi.org/10.1007/BF02374138

Martin, J. H., & Fitzwater, S. E. (1988). Iron deficiency limits phytoplankton growth in the north-east Pacific subarctic. *Nature*, *331*, 341–343. https://doi.org/10.1038/331341a0

Martin, J. H., Fitzwater, S. E., & Gordon, R. M. (1990). Iron deficiency limits phytoplankton growth in Antarctic waters. *Global Biogeochemical Cycles*, *4*(1), 5–12. https://doi.org/10.1029/GB004i001p00005

Martin, J. H., Knauer, G. A., Karl, D. M., & Broenkow, W. W. (1987). VERTEX: carbon cycling in the northeast Pacific. *Deep Sea Research Part A. Oceanographic Research Papers*, *34*(2), 267–285. https://doi.org/10.1016/0198-0149(87)90086-0

Martínez-García, A., Sigman, D. M., Ren, H., Anderson, R. F., Straub, M., Hodell, D. A., Jaccard, S. L., Eglinton, T. I., & Haug, G. H. (2014). Iron Fertilization of the Subantarctic Ocean During the Last Ice Age. *Science*, *343*(6177), 1347–1350. https://doi.org/10.1126/science.1246848

Martz, T. R., Johnson, K. S., & Riser, S. C. (2008). Ocean metabolism observed with oxygen sensors on profiling floats in the South Pacific. *Limnology and Oceanography*, *53*(5, part 2), 2094–2111. https://doi.org/10.4319/lo.2008.53.5_part_2.2094

McIlvin, M. R., & Altabet, M. A. (2005). Chemical Conversion of Nitrate and Nitrite to Nitrous Oxide for Nitrogen and Oxygen Isotopic Analysis in Freshwater and Seawater. *Analytical Chemistry*, *77*(17), 5589–5595. https://doi.org/10.1021/ac050528s

Mdutyana, M., Marshall, T., Sun, X., Burger, J. M., Thomalla, S. J., Ward, B. B., & Fawcett, S. E. (2022a). Controls on nitrite oxidation in the upper Southern Ocean: insights from winter kinetics experiments in the Indian sector. *Biogeosciences*, *19*(14), 3425–3444. https://doi.org/10.5194/BG-19-3425-2022

Mdutyana, M., Sun, X., Burger, J. M., Flynn, R. F., Smith, S., van Horsten, N. R., Roychoudhury, A. N., Planquette, H., Bucciarelli, E., Thomalla, S. J., Ward, B. B., & Fawcett, S. E. (2022b). The kinetics of ammonium uptake and oxidation across the Southern Ocean. *Limnology and Oceanography*, *67*(4), 973–991. https://doi.org/10.1002/LNO.12050

Mdutyana, M., Thomalla, S. J., Philibert, R., Ward, B. B., & Fawcett, S. E. (2020). The Seasonal Cycle of Nitrogen Uptake and Nitrification in the Atlantic Sector of the Southern Ocean. *Global Biogeochemical Cycles*, *34*(7). https://doi.org/10.1029/2019GB006363

Mitchell, B. G., Brody, E. A., Holm-Hansen, O., McClain, C., & Bishop, J. (1991). Light limitation of phytoplankton biomass and macronutrient utilization in the Southern Ocean. *Limnology and Oceanography*, *36*(8), 1662–1677. https://doi.org/10.4319/lo.1991.36.8.1662

Möbius, J. (2012). Isotope fractionation during nitrogen remineralization (ammonification): Implications for nitrogen isotope biogeochemistry. *Geochimica et Cosmochimica Acta*, *105*, 422–432. https://doi.org/10.1016/j.gca.2012.11.048

Montoya, J. P., & McCarthy, J. J. (1995). Isotopic fractionation during nitrate uptake by phytoplankton grown in continuous culture. *Journal of Plankton Research*, *17*(3), 439–464. https://doi.org/10.1093/plankt/17.3.439

Moore, C. M., Mills, M. M., Arrigo, K. R., Berman-Frank, I., Bopp, L., Boyd, P. W., Galbraith, E. D., Geider, R. J., Guieu, C., Jaccard, S. L., Jickells, T. D., la Roche, J., Lenton, T. M., Mahowald, N. M., Marañón, E., Marinov, I., Moore, J. K., Nakatsuka, T., Oschlies, A., … Ulloa, O. (2013). Processes and patterns of oceanic nutrient limitation. In *Nature Geoscience* (Vol. 6, Issue 9, pp. 701–710). Nature Publishing Group. https://doi.org/10.1038/ngeo1765

Morel, F. M. M., & Price, N. M. (2003). The Biogeochemical Cycles of Trace Metals in the Oceans. *Science*, *300*(5621), 944–947. https://doi.org/10.1126/science.1083545

Muench, R. D., & Gordon, A. L. (1995). Circulation and transport of water along the western Weddell Sea margin. *Journal of Geophysical Research*, *100*(C9). https://doi.org/10.1029/95jc00965

Munro, D. R., Lovenduski, N. S., Stephens, B. B., Newberger, T., Arrigo, K. R., Takahashi, T., Quay, P. D., Sprintall, J., Freeman, N. M., & Sweeney, C. (2015). Estimates of net community production in the Southern Ocean determined from time series observations (2002–2011) of nutrients, dissolved inorganic carbon, and surface ocean pCO_2 in Drake Passage. *Deep Sea Research Part II: Topical Studies in Oceanography*, *114*, 49–63. https://doi.org/10.1016/J.DSR2.2014.12.014

Needoba, J. A., & Harrison, P. J. (2004). Influence of low light and a light: Dark cycle on NO_3^- uptake, intracellular NO_3^-, and nitrogen isotope fractionation by marine phytoplankton. *Journal of Phycology*, *40*(3), 505–516. https://doi.org/10.1111/j.1529-8817.2004.03171.x

Needoba, J. A., Sigman, D. M., & Harrison, P. J. (2004). The mechanism of isotope fractionation during algal nitrate assimilation as illuminated by the $^{15}N/^{14}N$ of intracellular nitrate. *Journal of Phycology*, *40*(3), 517–522. https://doi.org/10.1111/J.1529-8817.2004.03172.X

Nicholls, K. W., Makinson, K., & Venables, E. J. (2012). Ocean circulation beneath Larsen C Ice Shelf, Antarctica from in situ observations. *Geophysical Research Letters*, *39*(19), 1–6. https://doi.org/10.1029/2012GL053187

Nicholls, K. W., Østerhus, S., Makinson, K., Gammelsrød, T., & Fahrbach, E. (2009). Ice-ocean processes over the continental shelf of the southern Weddell Sea, Antarctica: A review. *Reviews of Geophysics*, *47*(3), 1–23. https://doi.org/10.1029/2007RG000250

Nicholls, K. W., Pudsey, C. J., & Morris, P. (2004). Summertime water masses off the northern Larsen C Ice Shelf, Antarctica. *Geophysical Research Letters*, *31*(9). https://doi.org/10.1029/2004GL019924

Orsi, A. H., Whitworth, T., & Nowlin, W. D. (1994). On the meridional extent and fronts of the Antarctic Circumpolar Current. *Deep-Sea Research Part I*, *42*(5), 641–673. https://doi.org/10.1016/0967-0637(95)00021-W

Osterroht, C., & Thomas, H. (2000). New production enhanced by nutrient supply from non-Redfield remineralisation of freshly produced organic material. *Journal of Marine Systems*, *25*(1), 33–46. https://doi.org/10.1016/S0924-7963(00)00007-5

Pennock, J. R., Velinsky, D. J., Ludlam, J. M., Sharp, J. H., & Fogel, M. L. (1996). Isotopic fractionation of ammonium and nitrate during uptake by *Skeletonema costatum*: Implications for $\delta^{15}N$ dynamics under bloom conditions. *Limnology and Oceanography*, *41*(3), 451–459. https://doi.org/10.4319/lo.1996.41.3.0451

Petrou, K., Kranz, S. A., Trimborn, S., Hassler, C. S., Ameijeiras, S. B., Sackett, O., Ralph, P. J., & Davidson, A. T. (2016). Southern Ocean phytoplankton physiology in a changing climate. *Journal of Plant Physiology*, *203*, 135–150. https://doi.org/10.1016/J.JPLPH.2016.05.004

Philibert, R., Waldron, H., & Clark, D. (2015). A geographical and seasonal comparison of nitrogen uptake by phytoplankton in the Southern Ocean. *Ocean Science*, *11*(2), 251–267. https://doi.org/10.5194/OS-11-251-2015

Potter, J. R., Paren, J. G., & Loynes, J. (1984). Glaciological and oceanographic calculations of the mass balance and oxygen isotope ratio of a melting ice shelf. *Journal of Glaciology*, *30*(105), 161–170. https://doi.org/10.1017/S002214300000589X

Pritchard, H. D., Ligtenberg, S. R. M., Fricker, H. A., Vaughan, D. G., van den Broeke, M. R., & Padman, L. (2012). Antarctic ice-sheet loss driven by basal melting of ice shelves. *Nature*, *484*(7395), 502–505. https://doi.org/10.1038/nature10968

Probyn, T. A., & Painting, S. J. (1985). Nitrogen uptake by size-fractionated phytoplankton populations in Antarctic surface waters. *Limnology and Oceanography*, *30*(6), 1327–1332. https://doi.org/10.4319/LO.1985.30.6.1327

Rafter, P. A., DiFiore, P. J., & Sigman, D. M. (2013). Coupled nitrate nitrogen and oxygen isotopes and organic matter remineralization in the Southern and Pacific Oceans. *Journal of Geophysical Research: Oceans*, *118*(10), 4781–4794. https://doi.org/10.1002/jgrc.20316

Redfield, A. C., Ketchum, B. H., & Richards, F. A. (1963). The influence of organisms on the composition of seawater. *The Sea*, *2*, 26–77.

Revilla, M., Alexander, J., & Glibert, P. M. (2005). Urea analysis in coastal waters: comparison of enzymatic and direct methods. *Limnology and Oceanography: Methods*, *3*(7), 290–299. https://doi.org/10.4319/LOM.2005.3.290

Rignot, E., Jacobs, S., Mouginot, J., & Scheuchl, B. (2013). Ice-shelf Melting Around Antarctica. *Science*, *341*(6143), 266–270. https://doi.org/10.1126/science.1235798

Robertson, R., Visbeck, M., Gordon, A. L., & Fahrbach, E. (2002). Long-term temperature trends in the deep waters of the Weddell Sea. *Deep-Sea Research Part II: Topical Studies in Oceanography*, *49*(21), 4791–4806. https://doi.org/10.1016/S0967-0645(02)00159-5

Rohling, E. J. (2013). Oxygen Isotope Composition of Seawater. *The Encyclopedia of Quaternary Science*, *2*, 915–922.

Sarmiento, J. L., & Toggweiler, J. R. (1984). A new model for the role of the oceans in determining atmospheric PCO_2. *Nature*, *308*(5960), 621–624. https://doi.org/10.1038/308621a0

Saxberg, B. E. H., & Kowalski, B. R. (1979). Generalized Standard Addition Method. *Analytical Chemistry*, *51*(7), 1031–1036. https://pubs.acs.org/sharingguidelines

Schlitzer, R. (2018). Ocean Data View. https://odv.awi.de/

Schodlok, M. P., Hellmer, H. H., & Beckmann, A. (2002). On the transport, variability and origin of dense water masses crossing the South Scotia Ridge. *Deep Sea Research Part II: Topical Studies in Oceanography*, *49*(21), 4807–4825. https://doi.org/10.1016/S0967-0645(02)00160-1

Schröder, M., & Fahrbach, E. (1999). On the structure and the transport of the eastern Weddell Gyre. *Deep-Sea Research Part II: Topical Studies in Oceanography*, *46*(1–2). https://doi.org/10.1016/S0967-0645(98)00112-X

Schröder, M., Hellmer, H. H., & Absy, J. M. (2002). On the near-bottom variability in the northwestern Weddell Sea. *Deep Sea Research Part II: Topical Studies in Oceanography*, *49*(21), 4767–4790. https://doi.org/10.1016/S0967-0645(02)00158-3

Sedwick, P. N., Di Tullio, G. R., & Mackey, D. J. (2000). Iron and manganese in the Ross Sea, Seasonal iron limitation in Antarctic. *Journal of Geophysical Research: Oceans*, *105*(C5), 11321–11336. https://doi.org/10.1029/2000JC000256

Sedwick, P. N., & DiTullio, G. R. (1997). Regulation of algal blooms by the release of iron from in Antarctic shelf melting sea ice. *October*, *24*(20), 2515–2518.

Shepherd, A., Wingham, D., & Rignot, E. (2004). Warm ocean is eroding West Antarctic Ice Sheet. *Geophysical Research Letters*, *31*(23), 1–4. https://doi.org/10.1029/2004GL021106

Sigman, D. M., Altabet, M. A., McCorkle, D. C., Francois, R., & Fischer, G. (1999). The $\delta^{15}N$ of nitrate in the Southern Ocean: Consumption of nitrate in surface waters. *Global Biogeochemical Cycles*, *13*(4), 1149–1166. https://doi.org/10.1029/1999GB900038

Sigman, D. M., Altabet, M. A., McCorkle, D. C., Francois, R., & Fischer, G. (2000). The $\delta^{15}N$ of nitrate in the Southern Ocean: Nitrogen cycling and circulation in the ocean interior. *Journal of Geophysical Research: Oceans*, *105*(C8), 19599–19614. https://doi.org/10.1029/2000jc000265

Sigman, D. M., & Boyle, E. A. (2000). Glacial/interglacial variations in atmospheric carbon dioxide. *Nature 2000 407:6806*, *407*(6806), 859–869. https://doi.org/10.1038/35038000

Sigman, D. M., Casciotti, K. L., Andreani, M., Barford, C., Galanter, M., & Böhlke, J. K. (2001). A bacterial method for the nitrogen isotopic analysis of nitrate in seawater and freshwater. *Analytical Chemistry*, *73*(17), 4145–4153. https://doi.org/10.1021/ac010088e

Sigman, D. M., DiFiore, P. J., Hain, M. P., Deutsch, C., Wang, Y., Karl, D. M., Knapp, A. N., Lehmann, M. F., & Pantoja, S. (2009). The dual isotopes of deep nitrate as a constraint on the cycle and budget of oceanic fixed nitrogen. *Deep-Sea Research Part I: Oceanographic Research Papers*, *56*(9), 1419–1439. https://doi.org/10.1016/j.dsr.2009.04.007

Sigman, D. M., & Fripiat, F. (2019). Nitrogen isotopes in the ocean. In *Encyclopedia of Ocean Sciences* (Issue September 2018, pp. 263–278). Elsevier Ltd. https://doi.org/10.1016/B978-0-12-409548-9.11605-7

Sigman, D. M., Granger, J., DiFiore, P. J., Lehmann, M. M., Ho, R., Cane, G., & van Geen, A. (2005). Coupled nitrogen and oxygen isotope measurements of nitrate along the eastern North Pacific margin. *Global Biogeochemical Cycles*, *19*(4), 1–14. https://doi.org/10.1029/2005GB002458

Sigman, D. M., Robinson, R., Knapp, A. N., van Geen, A., McCorkle, D. C., Brandes, J. A., & Thunell, R. C. (2003). Distinguishing between water column and sedimentary denitrification in the Santa Barbara Basin using the stable isotopes of nitrate. *Geochemistry, Geophysics, Geosystems*, *4*(5). https://doi.org/10.1029/2002GC000384

Silfer, J. A., Engel, M. H., & Macko, S. A. (1992). Kinetic fractionation of stable carbon and nitrogen isotopes during peptide bond hydrolysis: Experimental evidence and geochemical implications. *Chemical Geology: Isotope Geoscience Section*, *101*(3–4), 211–221. https://doi.org/10.1016/0009-2541(92)90003-N

Smart, S. M., Fawcett, S. E., Ren, H., Schiebel, R., Tompkins, E. M., Martínez-García, A., Stirnimann, L., Roychoudhury, A., Haug, G. H., & Sigman, D. M. (2020). The Nitrogen Isotopic Composition of Tissue and Shell-Bound Organic Matter of Planktic Foraminifera in Southern Ocean Surface Waters. *Geochemistry, Geophysics, Geosystems*, *21*(2). https://doi.org/10.1029/2019GC008440

Smart, S. M., Fawcett, S. E., Thomalla, S. J., Weigand, M. A., Reason, C. J. C., & Sigman, D. M. (2015). Isotopic evidence for nitrification in the Antarctic winter mixed layer. *Global Biogeochemical Cycles*, *29*(4), 427–445. https://doi.org/10.1002/2014GB005013

Smith, J. M., Chavez, F. P., & Francis, C. A. (2014). Ammonium uptake by phytoplankton regulates nitrification in the sunlit ocean. *PLoS ONE*, *9*(9). https://doi.org/10.1371/journal.pone.0108173

Smith, S., Altieri, K. E., Mdutyana, M., Walker, D. R., Parrott, R. G., Gallie, S., Spence, K. A. M., Burger, J. M., & Fawcett, S. E. (2022). Biogeochemical controls on ammonium accumulation in the surface layer of the Southern Ocean. *Biogeosciences*, *19*(3), 715–741. https://doi.org/10.5194/BG-19-715-2022

Staal, M., Meysman, F. J. R., & Stal, L. J. (2003). Temperature excludes N_2-fixing heterocystous cyanobacteria in the tropical oceans. *Nature 2003 425:6957*, *425*(6957), 504–507. https://doi.org/10.1038/nature01999

Stanley, R. H. R., Doney, S. C., Jenkins, W. J., & Lott, D. E. (2012). Apparent oxygen utilization rates calculated from tritium and helium-3 profiles at the Bermuda Atlantic Time-series Study site. *Biogeosciences*, *9*(6), 1969–1983. https://doi.org/10.5194/BG-9-1969-2012

St-Laurent, P., Yager, P. L., Sherrell, R. M., Stammerjohn, S. E., & Dinniman, M. S. (2017). Pathways and supply of dissolved iron in the Amundsen Sea (Antarctica). *Journal of Geophysical Research: Oceans*, *122*(9), 7135–7162. https://doi.org/10.1002/2017JC013162

Strickland, J. D. H., & Parsons, T. R. (1972). *A Practical Handbook of Seawater Analysis, 2nd edition.* Fisheries Research Board of Canada. https://doi.org/10.25607/OBP-1791

Strzepek, R. F., Boyd, P. W., & Sunda, W. G. (2019). Photosynthetic adaptation to low iron, light, and temperature in Southern Ocean phytoplankton. *Proceedings of the National Academy of Sciences of the United States of America*, *116*(10). https://doi.org/10.1073/pnas.1810886116

Studer, A. S., Sigman, D. M., Martínez-García, A., Benz, V., Winckler, G., Kuhn, G., Esper, O., Lamy, F., Jaccard, S. L., Wacker, L., Oleynik, S., Gersonde, R., & Haug, G. H. (2015). Antarctic Zone nutrient conditions during the last two glacial cycles. *Paleoceanography*, *30*(7), 845–862. https://doi.org/10.1002/2014PA002745

Sunda, W. G., & Huntsman, S. A. (1997). Interrelated influence of iron, light and cell size on marine phytoplankton growth. *Nature*, *390*(6658), 389–392. https://doi.org/10.1038/37093

Tagliabue, A., Bopp, L., & Aumont, O. (2009). Evaluating the importance of atmospheric and sedimentary iron sources to Southern Ocean biogeochemistry. *Geophysical Research Letters*, *36*(13), 1–5. https://doi.org/10.1029/2009GL038914

Talley, L. D., Pickard, G. L., Emery, W. J., & Swift, J. H. (2011). Southern Ocean. *Descriptive Physical Oceanography*, 437–471. https://doi.org/10.1016/b978-0-7506-4552-2.10013-7

Taylor, B. W., Keep, C. F., Hall, R. O., Koch, B. J., Tronstad, L. M., Flecker, A. S., & Ulseth, A. J. (2007). Improving the fluorometric ammonium method: matrix effects, background fluorescence, and standard additions. *The North American Benthological Society*, *26*(2), 167–177. https://doi.org/10.1899/0887-3593

Thomas, H., Ittekkot, V., Osterroht, C., & Schneider, B. (1999). Preferential recycling of nutrients-the ocean's way to increase new production and to pass nutrient limitation? *Limnology and Oceanography*, *44*(8), 1999–2004. https://doi.org/10.4319/LO.1999.44.8.1999

Timmermans, K. R., van der Wagt, B., & de Baar, H. J. W. (2004). Growth rates, half-saturation constants, and silicate, nitrate, and phosphate depletion in relation to iron availability of four large, open-ocean diatoms from the Southern Ocean. *Limnology and Oceanography*, *49*(6), 2141–2151. https://doi.org/10.4319/LO.2004.49.6.2141

Tischner, R. (2000). Nitrate uptake and reduction in higher and lower plants. *Plant, Cell & Environment*, *23*(10), 1005–1024. https://doi.org/10.1046/J.1365-3040.2000.00595.X

Toggweiler, J. R., Gnanadesikan, A., Carson, S., Murnane, R., & Sarmiento, J. L. (2003). Representation of the carbon cycle in box models and GCMs: 1. Solubility pump. *Global Biogeochemical Cycles*, *17*(1). https://doi.org/10.1029/2001GB001401

Treibergs, L. A., Fawcett, S. E., Lomas, M. W., & Sigman, D. M. (2014). Nitrogen isotopic response of prokaryotic and eukaryotic phytoplankton to nitrate availability in Sargasso Sea surface waters. *Limnology and Oceanography*, *59*(3), 972–985. https://doi.org/10.4319/LO.2014.59.3.0972

van Caspel, M., Schröder, M., Huhn, O., & Hellmer, H. H. (2015). Precursors of Antarctic Bottom Water formed on the continental shelf off Larsen Ice Shelf. *Deep-Sea Research Part I: Oceanographic Research Papers*, *99*, 1–9. https://doi.org/10.1016/j.dsr.2015.01.004

van Oostende, N., Fawcett, S. E., Marconi, D., Lueders-Dumont, J., Sabadel, A. J. M., Woodward, E. M. S., Jönsson, B. F., Sigman, D. M., & Ward, B. B. (2017). Variation of summer phytoplankton community composition and its relationship to nitrate and regenerated nitrogen assimilation across the North Atlantic Ocean. *Deep Sea Research Part I: Oceanographic Research Papers*, *121*, 79–94. https://doi.org/10.1016/J.DSR.2016.12.012

Vanzella, A., Guerrero, M., & Jones, R. (1989). Effect of CO and light on ammonium and nitrite oxidation by chemolithotrophic bacteria. *Marine Ecology Progress Series*, *57*, 69–76. https://doi.org/10.3354/meps057069

Vernet, M., Geibert, W., Hoppema, M., Brown, P. J., Haas, C., Hellmer, H. H., Jokat, W., Jullion, L., Mazloff, M., Bakker, D. C. E., Brearley, J. A., Croot, P., Hattermann, T., Hauck, J., Hillenbrand, C. D., Hoppe, C. J. M., Huhn, O., Koch, B. P., Lechtenfeld, O. J., … Verdy, A. (2019). The Weddell Gyre, Southern Ocean: Present Knowledge and Future Challenges. *Reviews of Geophysics*, *57*(3), 623–708. https://doi.org/10.1029/2018RG000604

Vincent, W. F., & Howard-Williams, C. (1994). Nitrate-rich inland waters of the Ross Ice Shelf region, Antarctica. *Antarctic Science*, *6*(3), 339–346. https://doi.org/10.1017/S0954102094000519

Vo, J., Inwood, W., Hayes, J. M., & Kustu, S. (2013). Mechanism for nitrogen isotope fractionation during ammonium assimilation by *Escherichia coli* K12. *Proceedings of the National Academy of Sciences of the United States of America*, *110*(21), 8696–8701. https://doi.org/10.1073/pnas.1216683110

Volk, T., & Hoffert, M. I. (1985). Ocean Carbon Pumps: Analysis of Relative Strengths and Efficiencies in Ocean-Driven Atmospheric CO_2 Changes. In *The carbon cycle and atmospheric CO_2: natural variations Archean to present* (Vol. 32, pp. 99–110). American Geophysical Union. https://doi.org/10.1029/GM032p0099

Voss, M., Dippner, J. W., & Montoya, J. P. (2001). Nitrogen isotope patterns in the oxygen-deficient waters of the Eastern Tropical North Pacific Ocean. *Deep Sea Research Part I: Oceanographic Research Papers*, *48*(8), 1905–1921. https://doi.org/10.1016/S0967-0637(00)00110-2

Wada, E., & Hattori, A. (1978). Nitrogen isotope effects in the assimilation of inorganic nitrogenous compounds by marine diatoms. *Geomicrobiology Journal*, *1*(1), 85–101. https://doi.org/10.1080/01490457809377725

Wankel, S. D., Kendall, C., Pennington, J. T., Chavez, F. P., & Paytan, A. (2007). Nitrification in the euphotic zone as evidenced by nitrate dual isotopic composition: Observations from Monterey Bay, California. *Global Biogeochemical Cycles*, *21*(2), 1–13. https://doi.org/10.1029/2006GB002723

Ward, B. B. (1985). Light and substrate concentration relationships with marine ammonium assimilation and oxidation rates. *Marine Chemistry*, *16*(4), 301–316. https://doi.org/10.1016/0304-4203(85)90052-0

Ward, B. B. (2005). Temporal variability in nitrification rates and related biogeochemical factors in Monterey Bay, California, USA. *Marine Ecology Progress Series*, *292*, 97–109. https://doi.org/10.3354/meps292097

Ward, B. B., Kilpatrick, K. A., Renger, E. H., & Eppley, R. W. (1989). Biological nitrogen cycling in the nitracline. *Limnology and Oceanography*, *34*(3), 493–513. https://doi.org/10.4319/lo.1989.34.3.0493

Waser, N. A. D., Harrison, P. J., Nielsen, B., Calvert, S. E., & Turpin, D. H. (1998b). Nitrogen isotope fractionation during the uptake and assimilation of nitrate, nitrite, ammonium, and urea by a marine diatom. *Limnology and Oceanography*, *43*(2), 215–224. https://doi.org/10.4319/lo.1998.43.2.0215

Waser, N. A. D., Yin, K., Yu, Z., Tada, K., Harrison, P. J., Turpin, D. H., & Calvert, S. E. (1998a). Nitrogen isotope fractionation during nitrate, ammonium and urea uptake by marine diatoms and coccolithophores under various conditions of N availability. *Marine Ecology Progress Series*, *169*, 29–41. https://doi.org/10.3354/meps169029

Watson, A. J., Schuster, U., Shutler, J. D., Holding, T., Ashton, I. G. C., Landschützer, P., Woolf, D. K., & Goddijn-Murphy, L. (2020). Revised estimates of ocean-atmosphere CO_2 flux are consistent with ocean carbon inventory. *Nature Communications*, *11*(1), 4422. https://doi.org/10.1038/s41467-020-18203-3

Weigand, M. A., Foriel, J., Barnett, B., Oleynik, S., & Sigman, D. M. (2016). Updates to instrumentation and protocols for isotopic analysis of nitrate by the denitrifier method. *Rapid Communications in Mass Spectrometry*, *30*(12), 1365–1383. https://doi.org/10.1002/rcm.7570

Weppernig, R., Schlosser, P., Khatiwala, S., & Fairbanks, R. G. (1996). Isotope data from Ice Station Weddell: Implications for deep water formation in the Weddell Sea. *Journal of Geophysical Research: Oceans*, *101*(C11), 25723–25739. https://doi.org/10.1029/96JC01895

Westberry, T., Behrenfeld, M. J., Siegel, D. A., & Boss, E. (2008). Carbon-based primary productivity modeling with vertically resolved photoacclimation. *Global Biogeochemical Cycles*, *22*(2). https://doi.org/10.1029/2007GB003078

Wright, S. W., van den Enden, R. L., Pearce, I., Davidson, A. T., Scott, F. J., & Westwood, K. J. (2010). Phytoplankton community structure and stocks in the Southern Ocean (30–80°E) determined by CHEMTAX analysis of HPLC pigment signatures. *Deep Sea Research Part II: Topical Studies in Oceanography*, *57*(9–10), 758–778. https://doi.org/10.1016/J.DSR2.2009.06.015

Wunderlich, A., Meckenstock, R. U., & Einsiedl, F. (2013). A mixture of nitrite-oxidizing and denitrifying microorganisms affects the $\delta^{18}O$ of dissolved nitrate during anaerobic microbial denitrification depending on the $\delta^{18}O$ of ambient water. *Geochimica et Cosmochimica Acta*, *119*, 31–45. https://doi.org/10.1016/j.gca.2013.05.028

Ye, R. W., Toro-Suarez, I., Tiedje, J. M., & Averill, B. A. (1991). $H_2{}^{18}O$ isotope exchange studies on the mechanism of reduction of nitric oxide and nitrite to nitrous oxide by denitrifying bacteria: Evidence for an electrophilic nitrosyl during reduction of nitric oxide. *Journal of Biological Chemistry*, *266*(20). https://doi.org/10.1016/s0021-9258(18)98771-5

Yool, A., Martin, A. P., Fernández, C., & Clark, D. R. (2007). The significance of nitrification for oceanic new production. *Nature*, *447*(7147), 999–1002. https://doi.org/10.1038/nature05885

Zhang, L., Altabet, M. A., Wu, T., & Hadas, O. (2007). Sensitive Measurement of $NH_4{}^+$ $^{15}N/^{14}N$ ($\delta^{15}NH_4{}^+$) at Natural Abundance Levels in Fresh and Saltwaters. *Analytical Chemistry*, *79*(14), 5297–5303. https://doi.org/10.1021/ac070106d

Appendix

The supporting information presented here provides additional details relating to the (A1) isotope effect and f-ratio derived for each station, (A2) impact of mixing, remineralisation, and meltwater on the isotope effect, (A3) data selection criteria for calculation of the f-ratio, (A4) f-ratio sensitivity analysis, and (A5) theoretical nitrogen (N) isotope fractionation model.

A1: Station data

Fig. A1.1 – A1.16 (a-c) Physical and chemical depth profiles, (d) $NO_2^-+NO_3^-$ $\delta^{18}O$ versus $\delta^{15}N$, (e) N and O isotope effects, and (f) f-ratios for each station L1 (Fig. A1.1), L2 (Fig. A1.2), L3 (Fig. A1.3), …, L16 (Fig. A1.16). For Fig. A1.1 to A1.16, (a) shows depth profiles of conservative temperature (°C; blue), absolute salinity (g/kg; red), and oxygen (µmol/kg; green), (b) shows depth profiles of the concentrations (µmol/l) of $NO_2^-+NO_3^-$ (green), PON (black), NH_4^+ (blue), and urea-N (red), and (c) shows depth profiles of the $\delta^{15}N$ of $NO_2^-+NO_3^-$ (green), PON (black), and NH_4^+ (blue) and the $\delta^{18}O$ of $NO_2^-+NO_3^-$ (orange). The depth of the mixed layer is represented by the horizontal dashed black line in plots (a-c). (d) $NO_2^-+NO_3^-$ $\delta^{18}O$ versus $\delta^{15}N$ with the 1:1 (solid black line) and 1.17:1 (dashed black line) relationships plotted. (e) $\delta^{15}N$ and $\delta^{18}O$ vs $\ln([NO_2^-+NO_3^-])$ (i.e., "Rayleigh space"), with station-specific isotope effects calculated over the mixed layer samples (blue dots), while deeper samples are shown in grey. The N and O isotope effects are represented by the negative gradient of the regression line over the mixed layer $\delta^{15}N$ ($^{15}\varepsilon_{assim}$, green dotted line) and $\delta^{18}O$ ($^{18}\varepsilon_{assim}$, orange dotted line) vs $\ln([NO_2^-+NO_3^-])$ samples, respectively. Represented on the plot are the equations for the regression line and their r^2, in green for $^{15}\varepsilon_{assim}$ and orange for $^{18}\varepsilon_{assim}$. (f) $\delta^{15}N$ versus the fraction of the $NO_2^-+NO_3^-$ pool remaining (i.e., the measured $NO_2^-+NO_3^-$ concentration divided by the source $NO_2^-+NO_3^-$ concentration). The black lines show the output of the Rayleigh model run with $^{15}\varepsilon_{assim}$ = 4.1‰ and initial $NO_2^-+NO_3^-$ $\delta^{15}N$ = 5.21‰ (i.e., the mean value calculated for winter water; WW). The theoretical $NO_2^-+NO_3^-$ $\delta^{15}N$ (i.e., substrate) is shown by the solid black line, the instantaneous product by the dot-dashed black line, and the accumulated product by the dashed line. Also shown are the measured NH_4^+ (blue; with the blue horizontal line showing the regional average ± 1 standard error (blue shading)), $PON_{growing}$ (black squares), $NO_2^-+NO_3^-$ (green), and $\delta^{15}N_{NO3\ consumed}$ end member (red), calculated using the instantaneous product integrated over the PON + NH_4^+ + urea concentration (Eq 4.13). For $PON_{growing}$, open black squares indicate that the selection criteria (i.e., $\delta^{15}N_{NH4\ consumed}<\delta^{15}N_{PON}<\delta^{15}N_{NO3\ consumed}$ and the derived f-ratio has a standard deviation <0.25; see A3.2) are not met for that sample, while filled black squares meet the criteria and are included in the regional f-ratio estimate.

L1

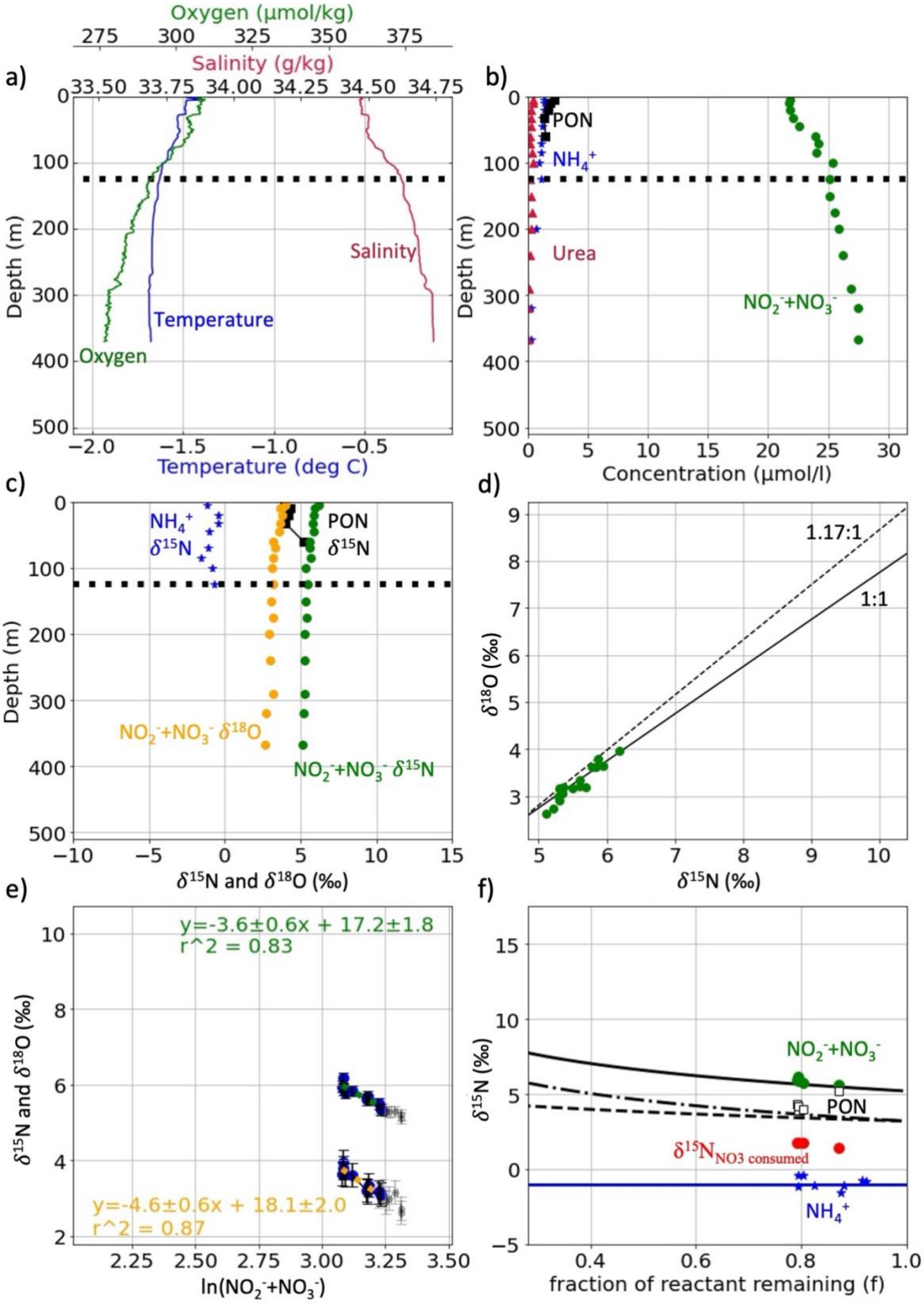
a)
Oxygen (µmol/kg)
Salinity (g/kg)
Depth (m)
Temperature (deg C)
Oxygen
Temperature
Salinity
b)
PON
NH_4^+
Urea
NO_2^-+NO_3^-
Concentration (µmol/l)
c)
NH_4^+ $\delta^{15}N$
PON $\delta^{15}N$
NO_2^-+NO_3^- $\delta^{18}O$
NO_2^-+NO_3^- $\delta^{15}N$
$\delta^{15}N$ and $\delta^{18}O$ (‰)
d)
1.17:1
1:1
$\delta^{18}O$ (‰)
$\delta^{15}N$ (‰)
e)
y=-3.6±0.6x + 17.2±1.8
r^2 = 0.83
y=-4.6±0.6x + 18.1±2.0
r^2 = 0.87
$\delta^{15}N$ and $\delta^{18}O$ (‰)
ln(NO_2^-+NO_3^-)
f)
NO_2^-+NO_3^-
PON
$\delta^{15}N_{NO3\ consumed}$
NH_4^+
$\delta^{15}N$ (‰)
fraction of reactant remaining (f)

L2

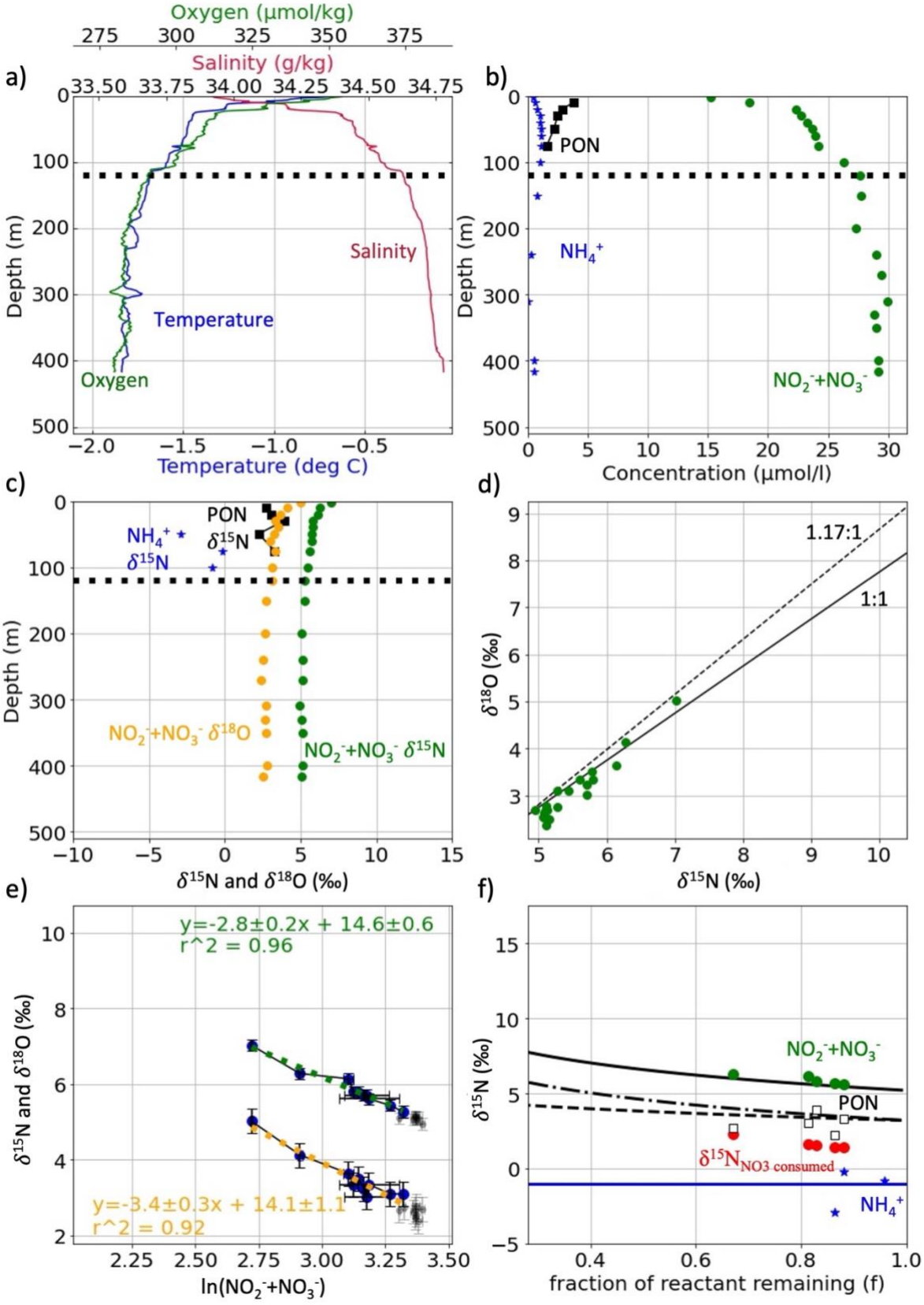
a)
Oxygen (µmol/kg)
275 300 325 350 375
Salinity (g/kg)
33.50 33.75 34.00 34.25 34.50 34.75
Depth (m)
Salinity
Temperature
Oxygen
−2.0 −1.5 −1.0 −0.5
Temperature (deg C)
b)
PON
NH_4^+
NO_2^-+NO_3^-
Depth (m)
0 5 10 15 20 25 30
Concentration (µmol/l)
c)
PON
NH_4^+ $\delta^{15}N$
$\delta^{15}N$
NO_2^-+NO_3^- $\delta^{18}O$
NO_2^-+NO_3^- $\delta^{15}N$
Depth (m)
−10 −5 0 5 10 15
$\delta^{15}N$ and $\delta^{18}O$ (‰)
d)
1.17:1
1:1
$\delta^{18}O$ (‰)
5 6 7 8 9 10
$\delta^{15}N$ (‰)
e)
y=-2.8±0.2x + 14.6±0.6
r^2 = 0.96
y=-3.4±0.3x + 14.1±1.1
r^2 = 0.92
$\delta^{15}N$ and $\delta^{18}O$ (‰)
2.25 2.50 2.75 3.00 3.25 3.50
ln(NO_2^-+NO_3^-)
f)
NO_2^-+NO_3^-
PON
$\delta^{15}N_{NO3\ consumed}$
NH_4^+
$\delta^{15}N$ (‰)
0.4 0.6 0.8 1.0
fraction of reactant remaining (f)

L3

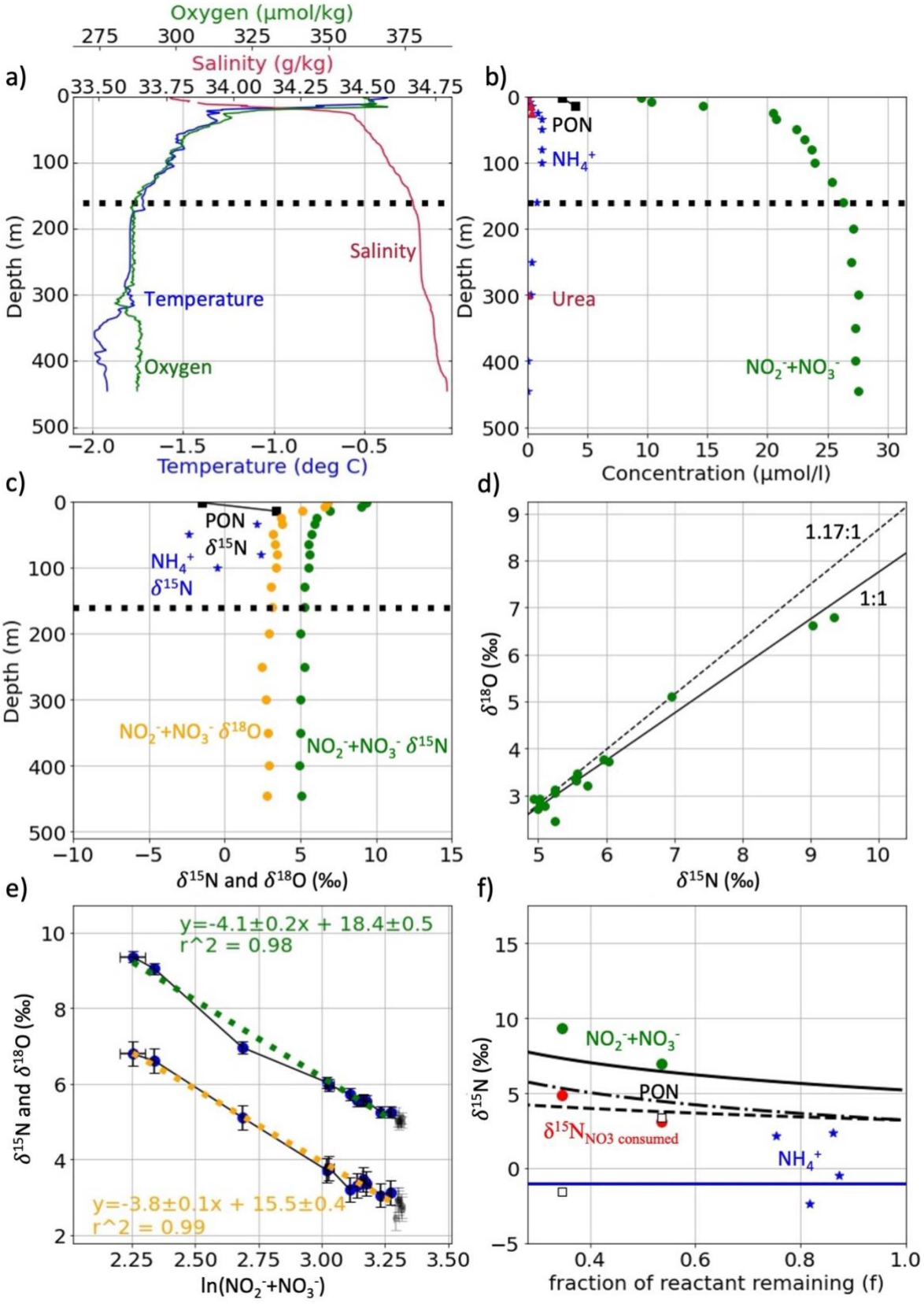
a)
Oxygen (µmol/kg)
Salinity (g/kg)
Depth (m)
Temperature
Salinity
Oxygen
Temperature (deg C)
b)
PON
NH_4^+
Urea
NO_2^-+NO_3^-
Depth (m)
Concentration (µmol/l)
c)
PON
$\delta^{15}N$
NH_4^+
$\delta^{15}N$
NO_2^-+NO_3^- $\delta^{18}O$
NO_2^-+NO_3^- $\delta^{15}N$
Depth (m)
$\delta^{15}N$ and $\delta^{18}O$ (‰)
d)
1.17:1
1:1
$\delta^{18}O$ (‰)
$\delta^{15}N$ (‰)
e)
y=-4.1±0.2x + 18.4±0.5
r^2 = 0.98
y=-3.8±0.1x + 15.5±0.4
r^2 = 0.99
$\delta^{15}N$ and $\delta^{18}O$ (‰)
ln(NO_2^-+NO_3^-)
f)
NO_2^-+NO_3^-
PON
$\delta^{15}N_{NO3\ consumed}$
NH_4^+
$\delta^{15}N$ (‰)
fraction of reactant remaining (f)

L4

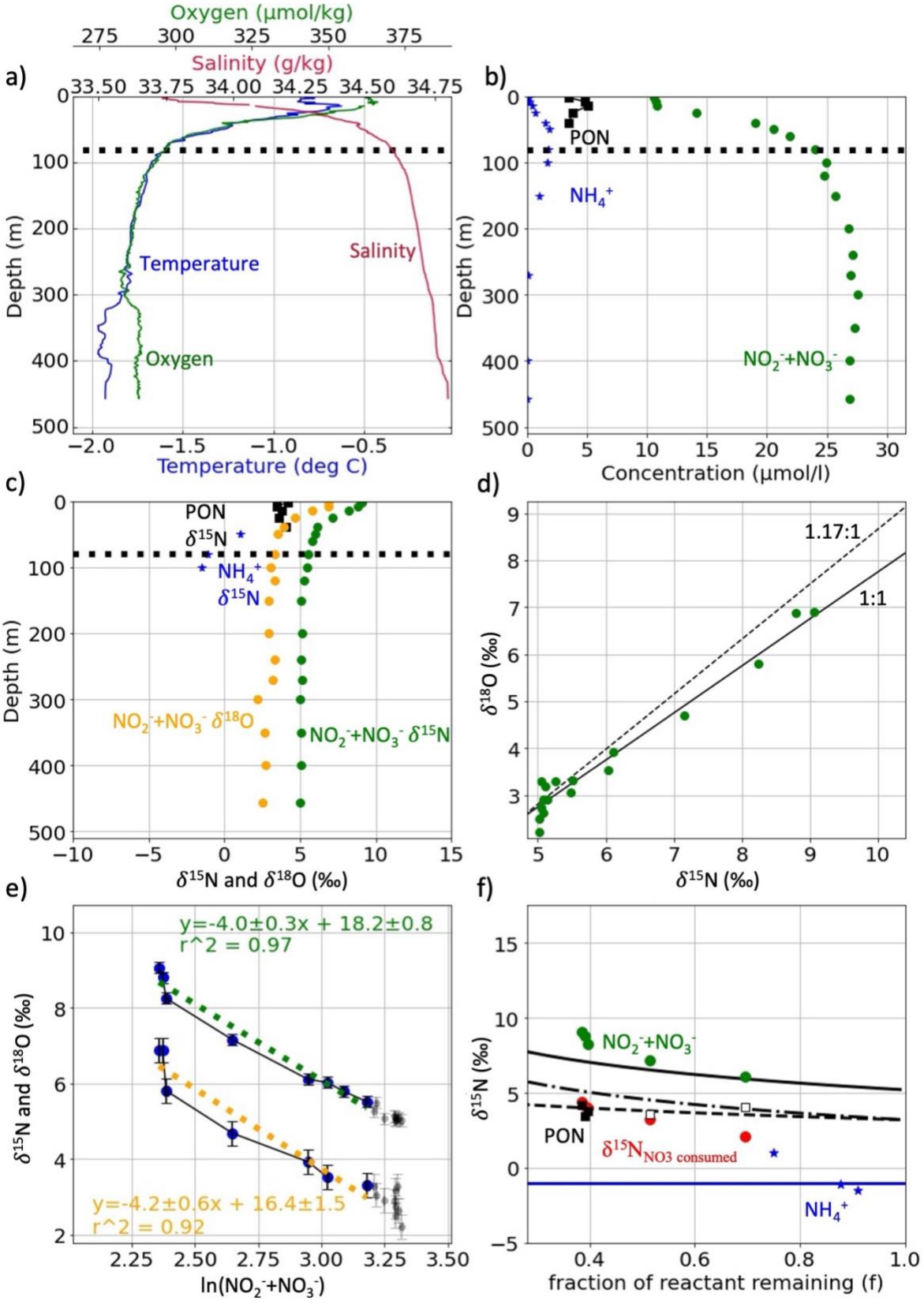
a)
Oxygen (µmol/kg)
275 300 325 350 375
Salinity (g/kg)
33.50 33.75 34.00 34.25 34.50 34.75
Depth (m)
Temperature
Salinity
Oxygen
Temperature (deg C)
b)
PON
NH4+
NO2-+NO3-
Concentration (µmol/l)
c)
PON
δ15N
NH4+
δ15N
NO2-+NO3- δ18O
NO2-+NO3- δ15N
δ15N and δ18O (‰)
d)
1.17:1
1:1
δ18O (‰)
δ15N (‰)
e)
y=-4.0±0.3x + 18.2±0.8
r^2 = 0.97
y=-4.2±0.6x + 16.4±1.5
r^2 = 0.92
δ15N and δ18O (‰)
ln(NO2-+NO3-)
f)
NO2-+NO3-
PON
δ15NNO3 consumed
NH4+
δ15N (‰)
fraction of reactant remaining (f)

L5

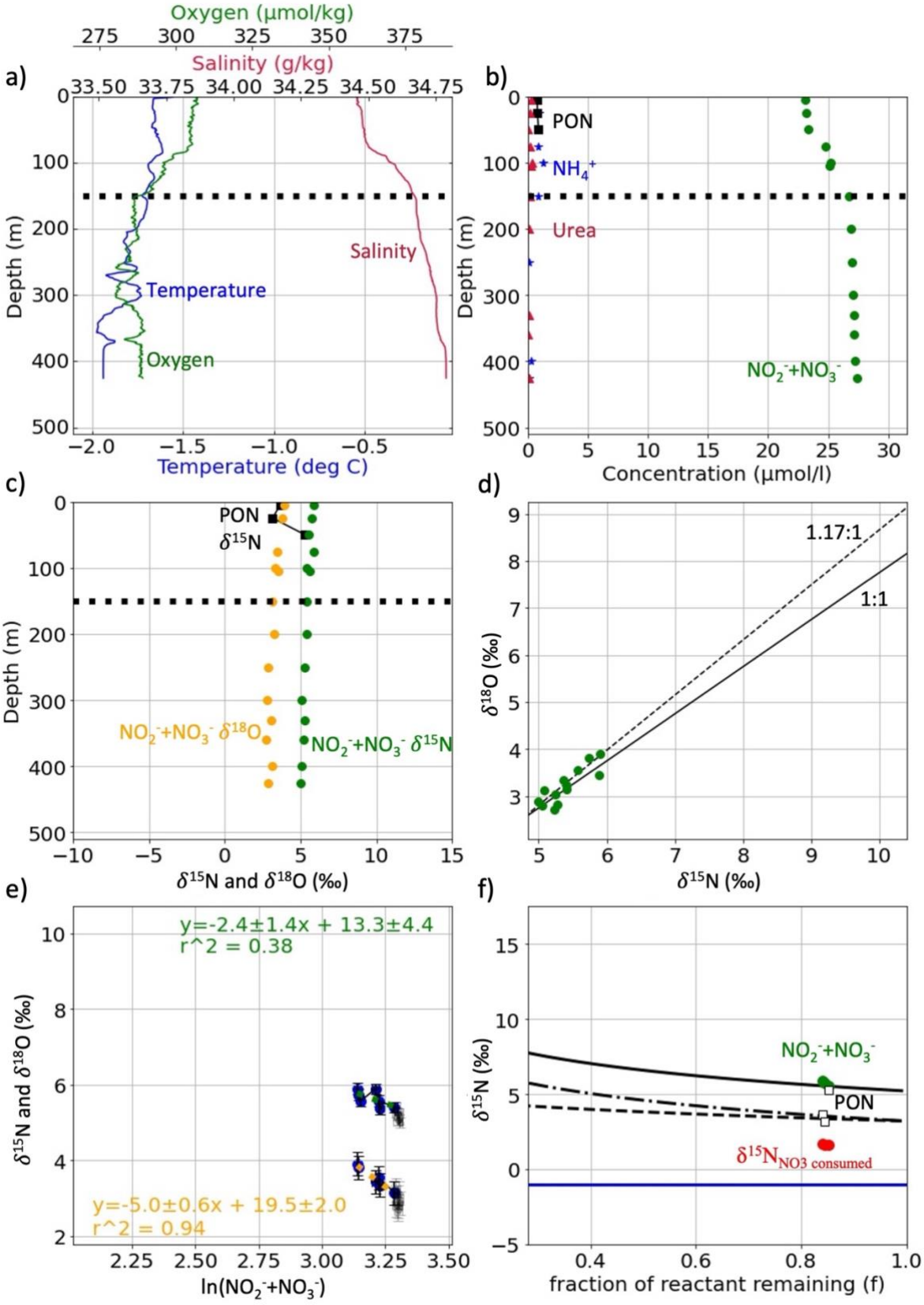
a)
Oxygen (µmol/kg)
275 300 325 350 375
Salinity (g/kg)
33.50 33.75 34.00 34.25 34.50 34.75
Depth (m)
Temperature
Salinity
Oxygen
Temperature (deg C)
b)
PON
NH_4^+
Urea
NO_2^-+NO_3^-
Concentration (µmol/l)
c)
PON
$\delta^{15}N$
NO_2^-+NO_3^- $\delta^{18}O$
NO_2^-+NO_3^- $\delta^{15}N$
$\delta^{15}N$ and $\delta^{18}O$ (‰)
d)
1.17:1
1:1
$\delta^{18}O$ (‰)
$\delta^{15}N$ (‰)
e)
y=-2.4±1.4x + 13.3±4.4
r^2 = 0.38
y=-5.0±0.6x + 19.5±2.0
r^2 = 0.94
$\delta^{15}N$ and $\delta^{18}O$ (‰)
ln(NO_2^-+NO_3^-)
f)
NO_2^-+NO_3^-
PON
$\delta^{15}N_{NO3\ consumed}$
$\delta^{15}N$ (‰)
fraction of reactant remaining (f)

L6

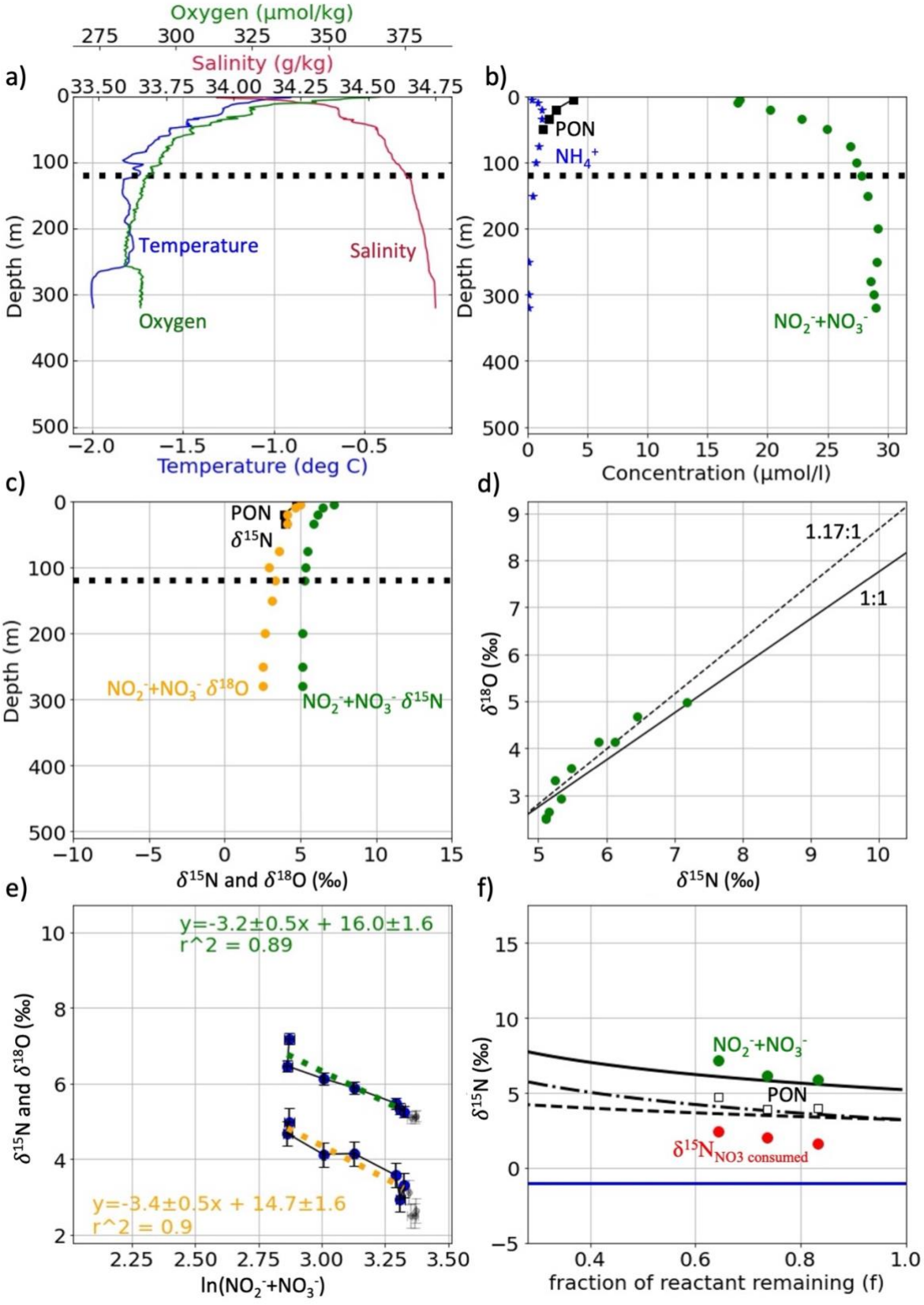
a)
Oxygen (µmol/kg)
Salinity (g/kg)
Depth (m)
Temperature
Salinity
Oxygen
Temperature (deg C)
b)
PON
NH4+
NO2-+NO3-
Depth (m)
Concentration (µmol/l)
c)
PON
δ15N
NO2-+NO3- δ18O
NO2-+NO3- δ15N
Depth (m)
δ15N and δ18O (‰)
d)
1.17:1
1:1
δ18O (‰)
δ15N (‰)
e)
y=-3.2±0.5x + 16.0±1.6
r^2 = 0.89
y=-3.4±0.5x + 14.7±1.6
r^2 = 0.9
δ15N and δ18O (‰)
ln(NO2-+NO3-)
f)
NO2-+NO3-
PON
δ15NNO3 consumed
δ15N (‰)
fraction of reactant remaining (f)

L7

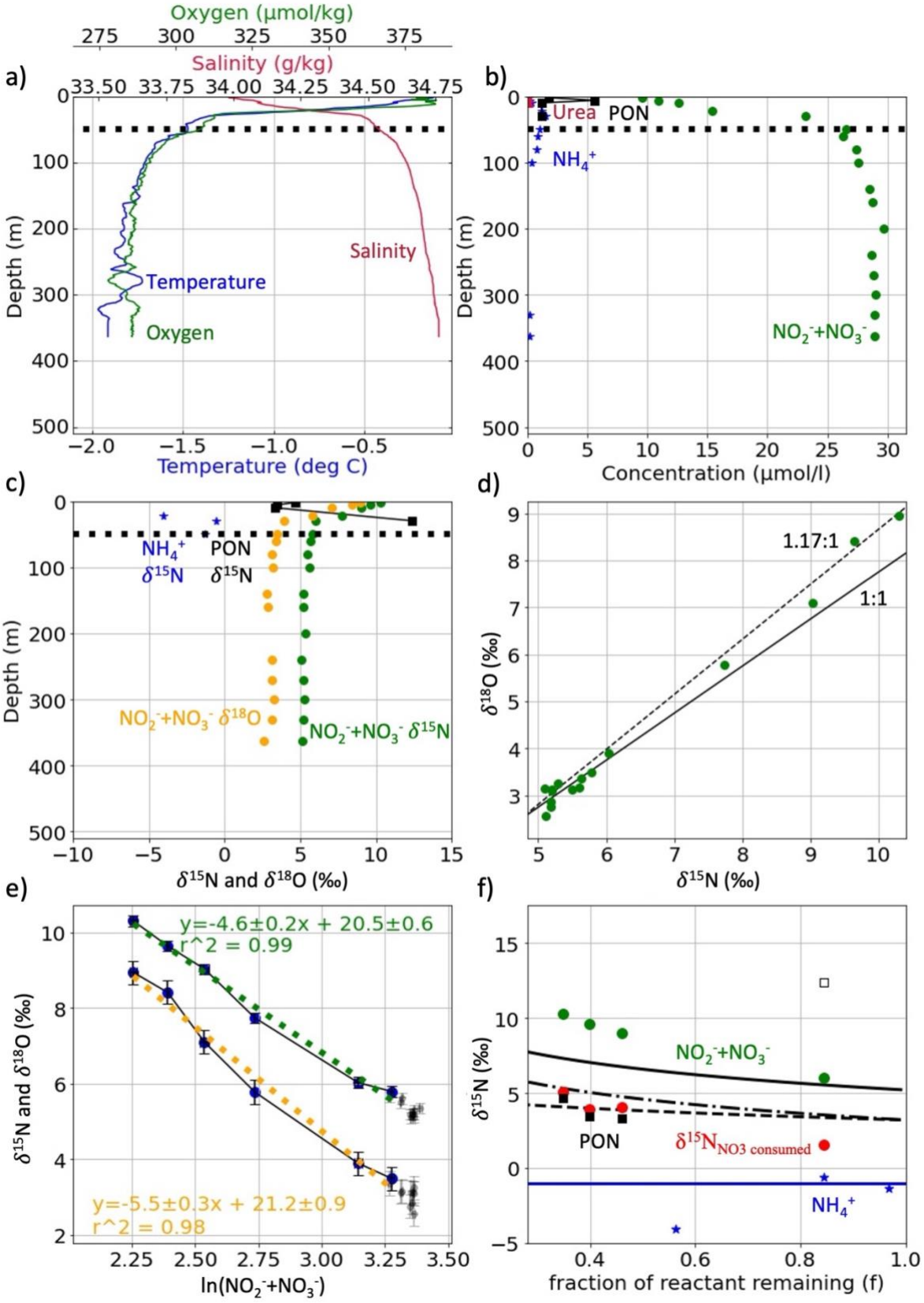
a)
Oxygen (µmol/kg)
275 300 325 350 375
Salinity (g/kg)
33.50 33.75 34.00 34.25 34.50 34.75
Depth (m)
Salinity
Temperature
Oxygen
Temperature (deg C)
b)
Urea
PON
NH4+
NO2-+NO3-
Concentration (µmol/l)
c)
NH4+ δ15N
PON δ15N
NO2-+NO3- δ18O
NO2-+NO3- δ15N
δ15N and δ18O (‰)
d)
1.17:1
1:1
δ18O (‰)
δ15N (‰)
e)
y=-4.6±0.2x + 20.5±0.6
r^2 = 0.99
y=-5.5±0.3x + 21.2±0.9
r^2 = 0.98
δ15N and δ18O (‰)
ln(NO2-+NO3-)
f)
NO2-+NO3-
PON
δ15NNO3 consumed
NH4+
δ15N (‰)
fraction of reactant remaining (f)

L8

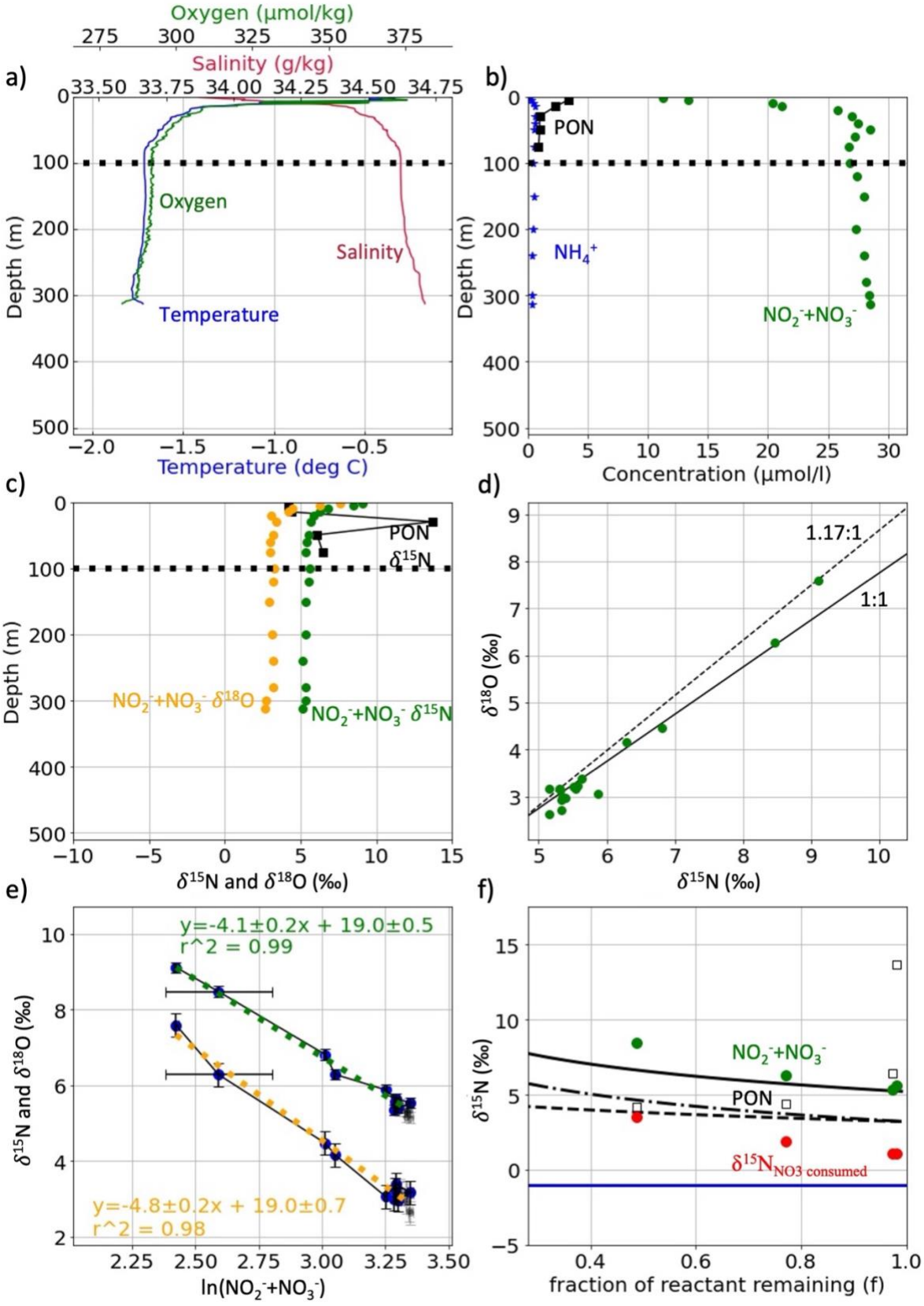
a)
Oxygen (µmol/kg)
Salinity (g/kg)
Depth (m)
Oxygen
Salinity
Temperature
Temperature (deg C)
b)
PON
NH_4^+
$NO_2^-+NO_3^-$
Concentration (µmol/l)
c)
PON $\delta^{15}N$
$NO_2^-+NO_3^-$ $\delta^{18}O$
$NO_2^-+NO_3^-$ $\delta^{15}N$
$\delta^{15}N$ and $\delta^{18}O$ (‰)
d)
1.17:1
1:1
$\delta^{18}O$ (‰)
$\delta^{15}N$ (‰)
e)
y=-4.1±0.2x + 19.0±0.5
r^2 = 0.99
y=-4.8±0.2x + 19.0±0.7
r^2 = 0.98
$\delta^{15}N$ and $\delta^{18}O$ (‰)
$\ln(NO_2^-+NO_3^-)$
f)
$NO_2^-+NO_3^-$
PON
$\delta^{15}N_{NO3\ consumed}$
$\delta^{15}N$ (‰)
fraction of reactant remaining (f)

L9

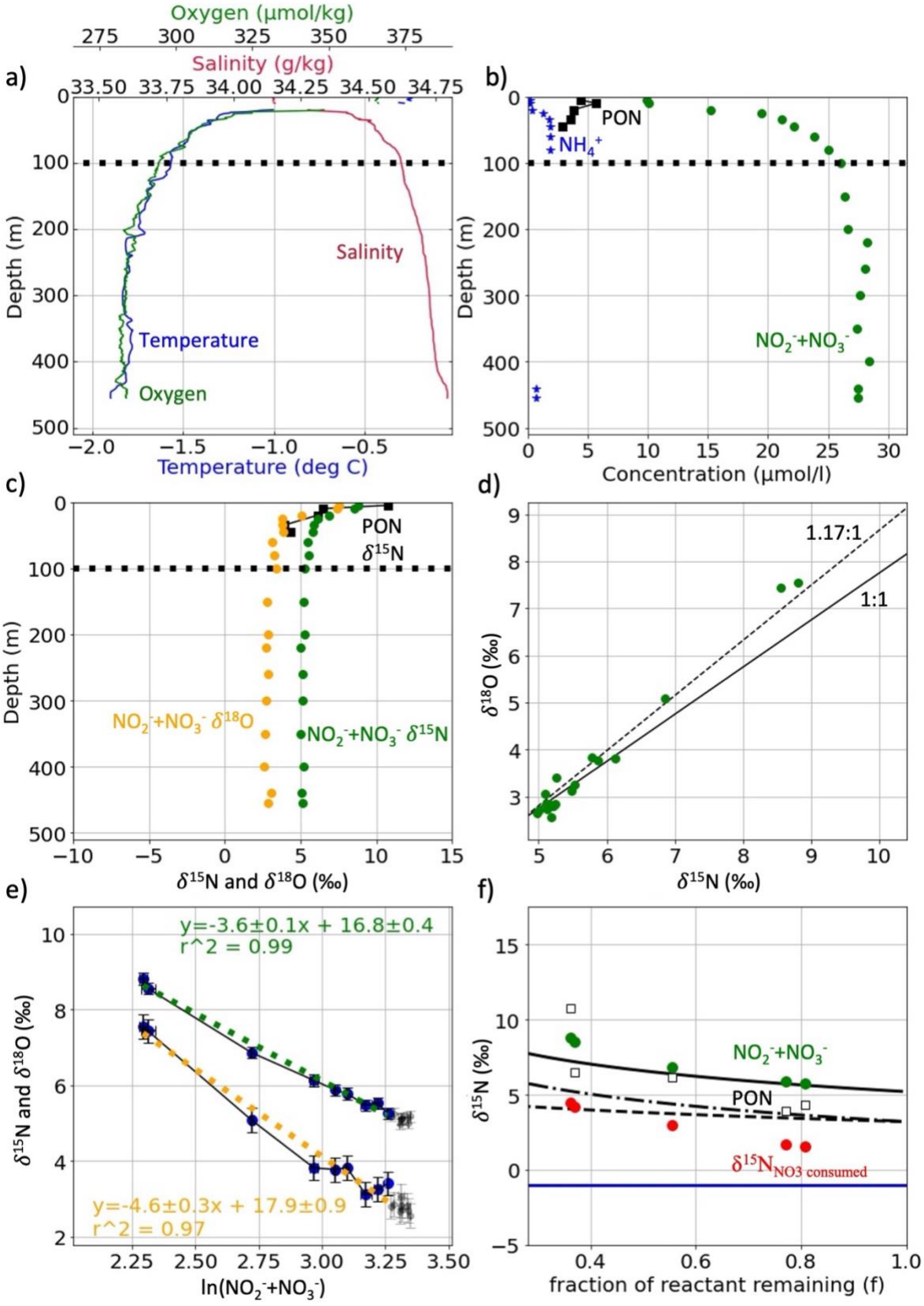
a)
Oxygen (µmol/kg)
275 300 325 350 375
Salinity (g/kg)
33.50 33.75 34.00 34.25 34.50 34.75
Depth (m)
Salinity
Temperature
Oxygen
Temperature (deg C)
b)
PON
NH4+
NO2-+NO3-
Concentration (µmol/l)
c)
PON
δ15N
NO2-+NO3- δ18O
NO2-+NO3- δ15N
δ15N and δ18O (‰)
d)
1.17:1
1:1
δ18O (‰)
δ15N (‰)
e)
y=-3.6±0.1x + 16.8±0.4
r^2 = 0.99
y=-4.6±0.3x + 17.9±0.9
r^2 = 0.97
δ15N and δ18O (‰)
ln(NO2-+NO3-)
f)
NO2-+NO3-
PON
δ15NNO3 consumed
δ15N (‰)
fraction of reactant remaining (f)

L10

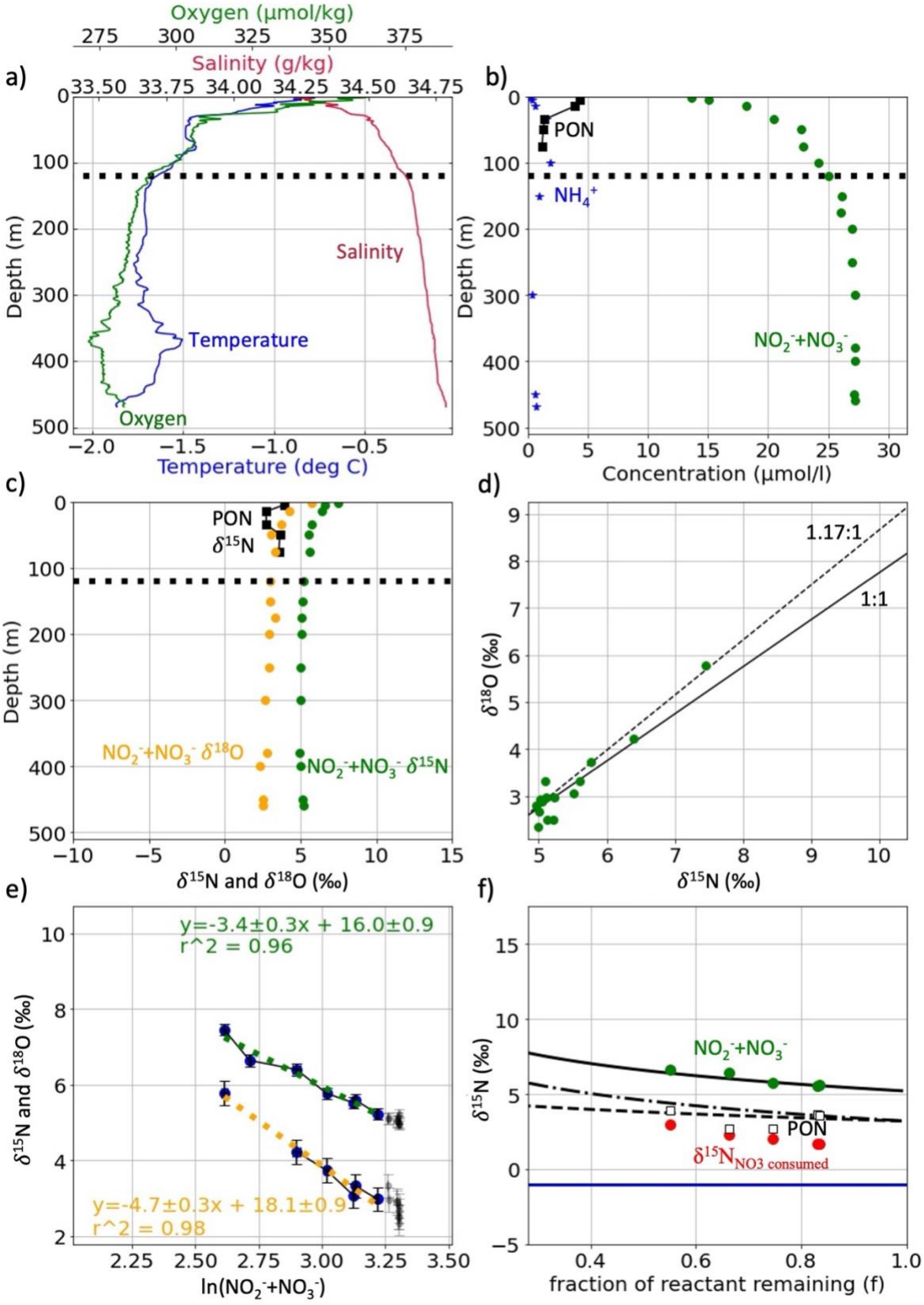
a)
Oxygen (µmol/kg)
275 300 325 350 375
Salinity (g/kg)
33.50 33.75 34.00 34.25 34.50 34.75
Depth (m)
Salinity
Temperature
Oxygen
Temperature (deg C)
b)
PON
NH4+
NO2-+NO3-
Concentration (µmol/l)
c)
PON
δ15N
NO2-+NO3- δ18O
NO2-+NO3- δ15N
δ15N and δ18O (‰)
d)
1.17:1
1:1
δ18O (‰)
δ15N (‰)
e)
y=-3.4±0.3x + 16.0±0.9
r^2 = 0.96
y=-4.7±0.3x + 18.1±0.9
r^2 = 0.98
δ15N and δ18O (‰)
ln(NO2-+NO3-)
f)
NO2-+NO3-
PON
δ15NNO3 consumed
δ15N (‰)
fraction of reactant remaining (f)

L11

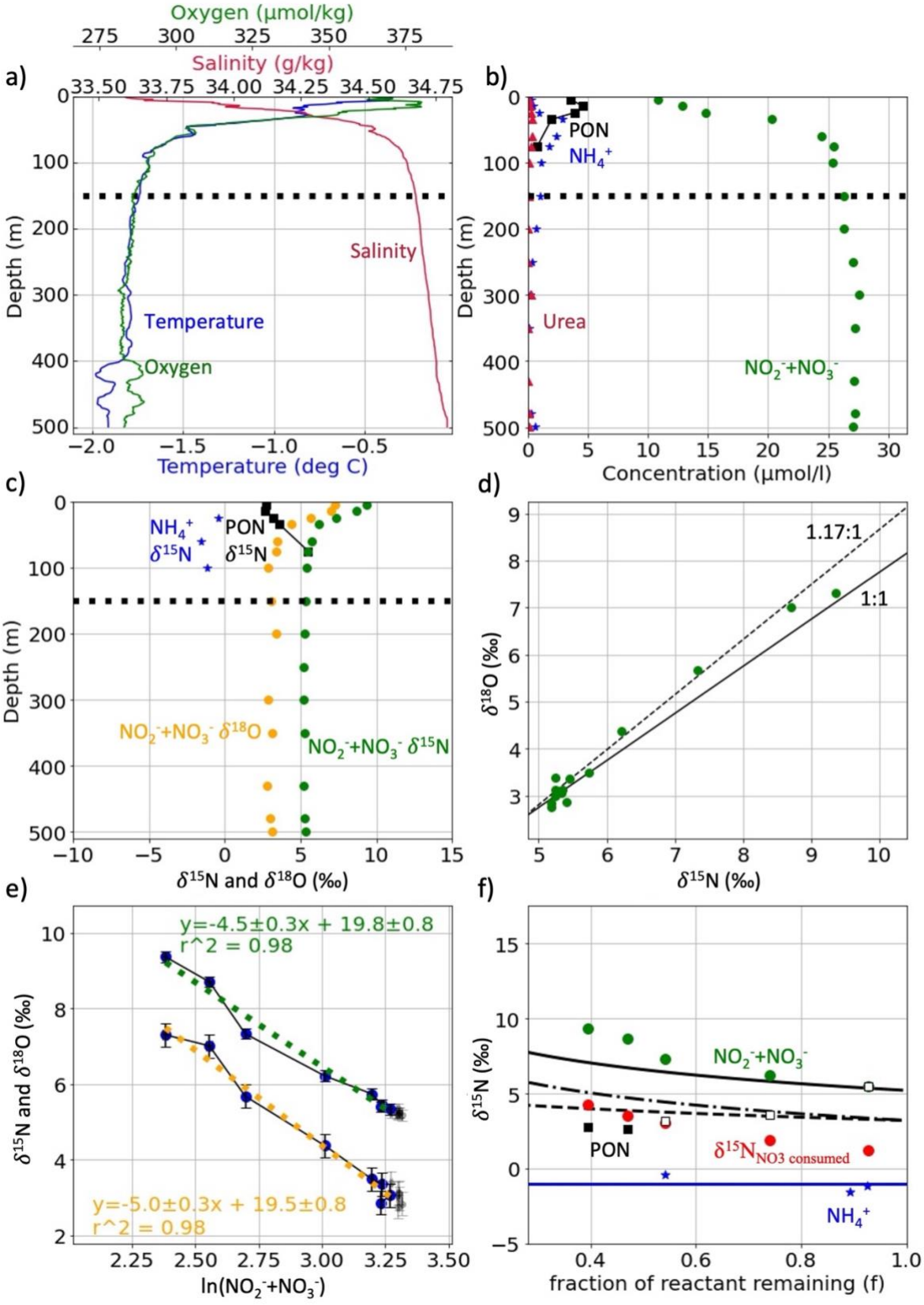
a)
Oxygen (µmol/kg)
275 300 325 350 375
Salinity (g/kg)
33.50 33.75 34.00 34.25 34.50 34.75
Depth (m)
Salinity
Temperature
Oxygen
Temperature (deg C)
b)
PON
NH4+
Urea
NO2-+NO3-
Concentration (µmol/l)
c)
NH4+ δ15N
PON δ15N
NO2-+NO3- δ18O
NO2-+NO3- δ15N
δ15N and δ18O (‰)
d)
1.17:1
1:1
δ18O (‰)
δ15N (‰)
e)
y=-4.5±0.3x + 19.8±0.8
r^2 = 0.98
y=-5.0±0.3x + 19.5±0.8
r^2 = 0.98
δ15N and δ18O (‰)
ln(NO2-+NO3-)
f)
NO2-+NO3-
PON
δ15NNO3 consumed
NH4+
δ15N (‰)
fraction of reactant remaining (f)

L12

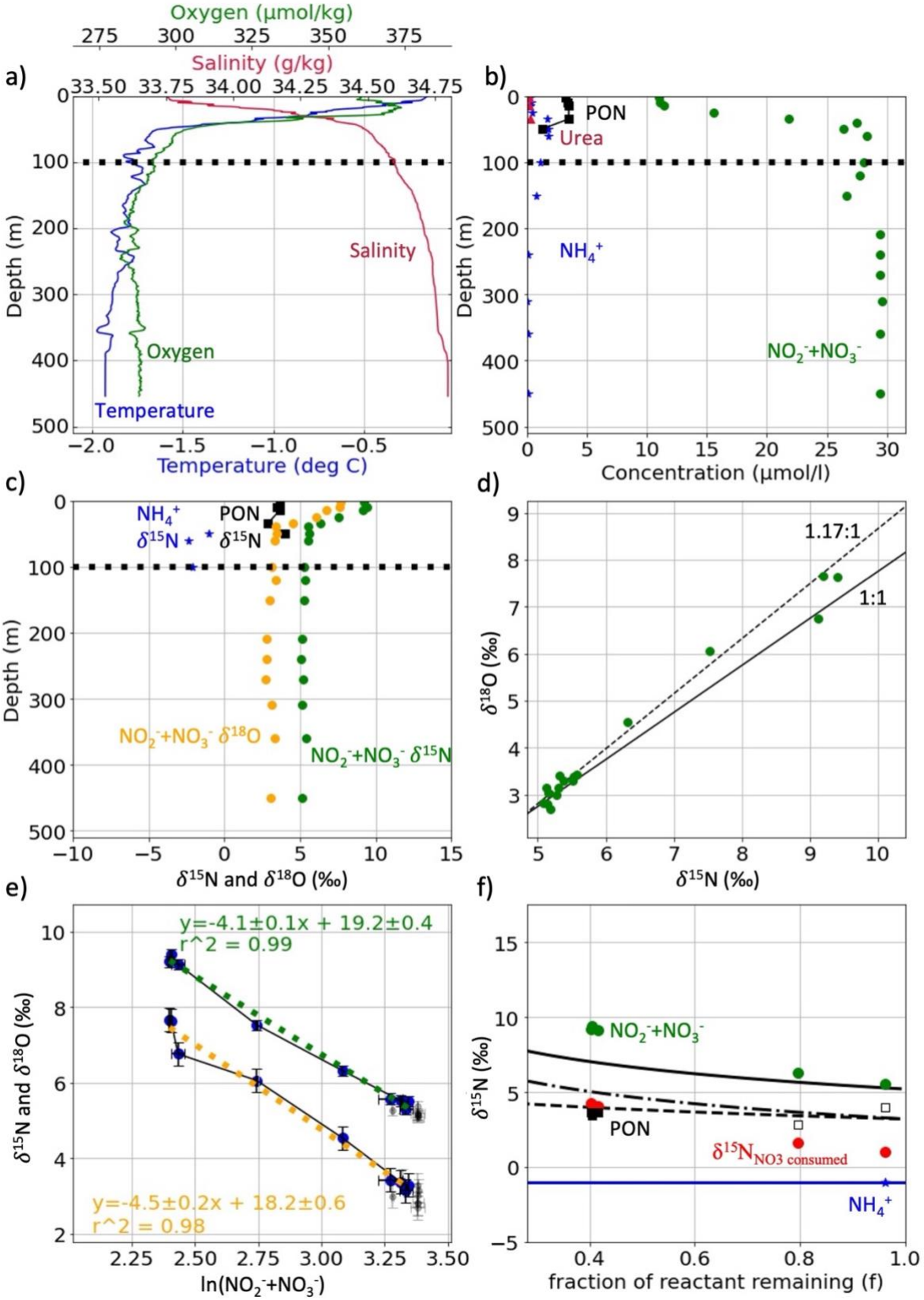
a)
Oxygen (µmol/kg)
Salinity (g/kg)
Depth (m)
Salinity
Oxygen
Temperature
Temperature (deg C)
b)
PON
Urea
NH4+
NO2-+NO3-
Depth (m)
Concentration (µmol/l)
c)
NH4+ δ15N
PON δ15N
NO2-+NO3- δ18O
NO2-+NO3- δ15N
Depth (m)
δ15N and δ18O (‰)
d)
1.17:1
1:1
δ18O (‰)
δ15N (‰)
e)
y=-4.1±0.1x + 19.2±0.4
r^2 = 0.99
y=-4.5±0.2x + 18.2±0.6
r^2 = 0.98
δ15N and δ18O (‰)
ln(NO2-+NO3-)
f)
NO2-+NO3-
PON
δ15NNO3 consumed
NH4+
δ15N (‰)
fraction of reactant remaining (f)

L13

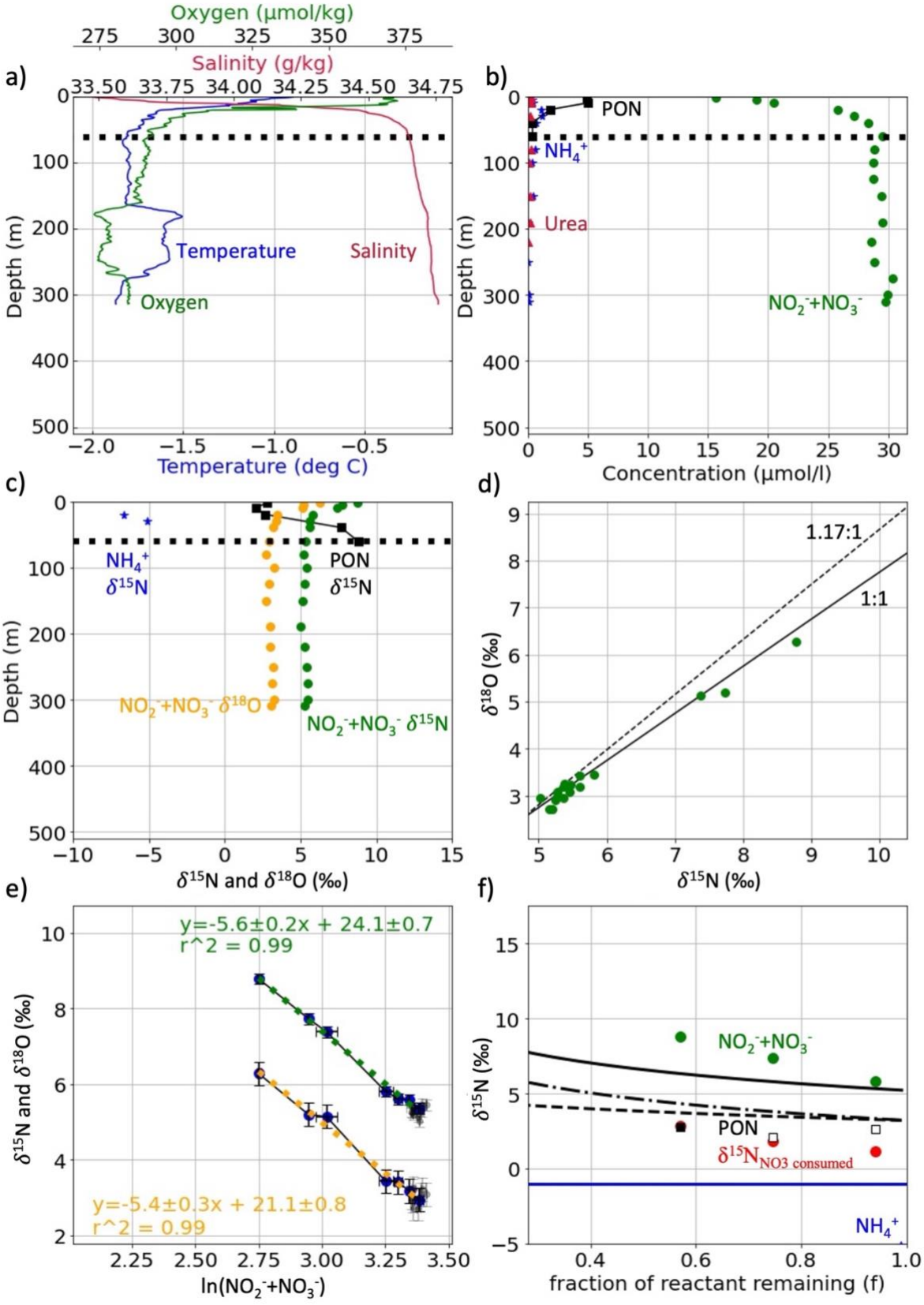
a)
Oxygen (µmol/kg)
275 300 325 350 375
Salinity (g/kg)
33.50 33.75 34.00 34.25 34.50 34.75
Depth (m)
Temperature
Salinity
Oxygen
Temperature (deg C)
b)
PON
NH4+
Urea
NO2-+NO3-
Concentration (µmol/l)
c)
NH4+ δ15N
PON δ15N
NO2-+NO3- δ18O
NO2-+NO3- δ15N
δ15N and δ18O (‰)
d)
1.17:1
1:1
δ18O (‰)
δ15N (‰)
e)
y=-5.6±0.2x + 24.1±0.7
r^2 = 0.99
y=-5.4±0.3x + 21.1±0.8
r^2 = 0.99
δ15N and δ18O (‰)
ln(NO2-+NO3-)
f)
NO2-+NO3-
PON
δ15NNO3 consumed
NH4+
δ15N (‰)
fraction of reactant remaining (f)

L14

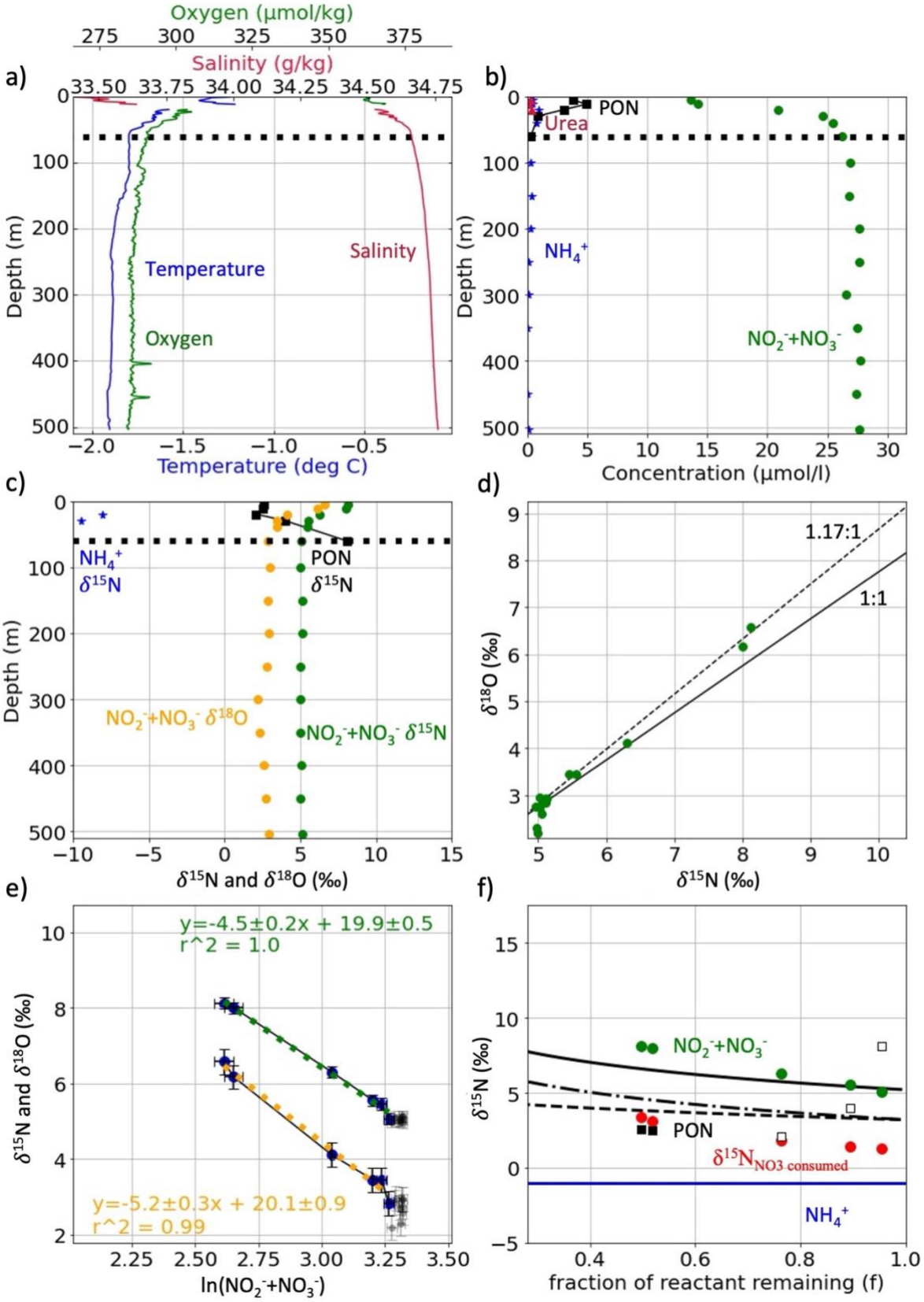
a)
Oxygen (µmol/kg)
275 300 325 350 375
Salinity (g/kg)
33.50 33.75 34.00 34.25 34.50 34.75
Depth (m)
Temperature
Salinity
Oxygen
Temperature (deg C)
b)
PON
Urea
NH_4^+
$NO_2^-+NO_3^-$
Depth (m)
Concentration (µmol/l)
c)
NH_4^+ $\delta^{15}N$
PON $\delta^{15}N$
$NO_2^-+NO_3^-$ $\delta^{18}O$
$NO_2^-+NO_3^-$ $\delta^{15}N$
Depth (m)
$\delta^{15}N$ and $\delta^{18}O$ (‰)
d)
1.17:1
1:1
$\delta^{18}O$ (‰)
$\delta^{15}N$ (‰)
e)
y=-4.5±0.2x + 19.9±0.5
r^2 = 1.0
y=-5.2±0.3x + 20.1±0.9
r^2 = 0.99
$\delta^{15}N$ and $\delta^{18}O$ (‰)
$\ln(NO_2^-+NO_3^-)$
f)
$NO_2^-+NO_3^-$
PON
$\delta^{15}N_{NO3\ consumed}$
NH_4^+
$\delta^{15}N$ (‰)
fraction of reactant remaining (f)

L15

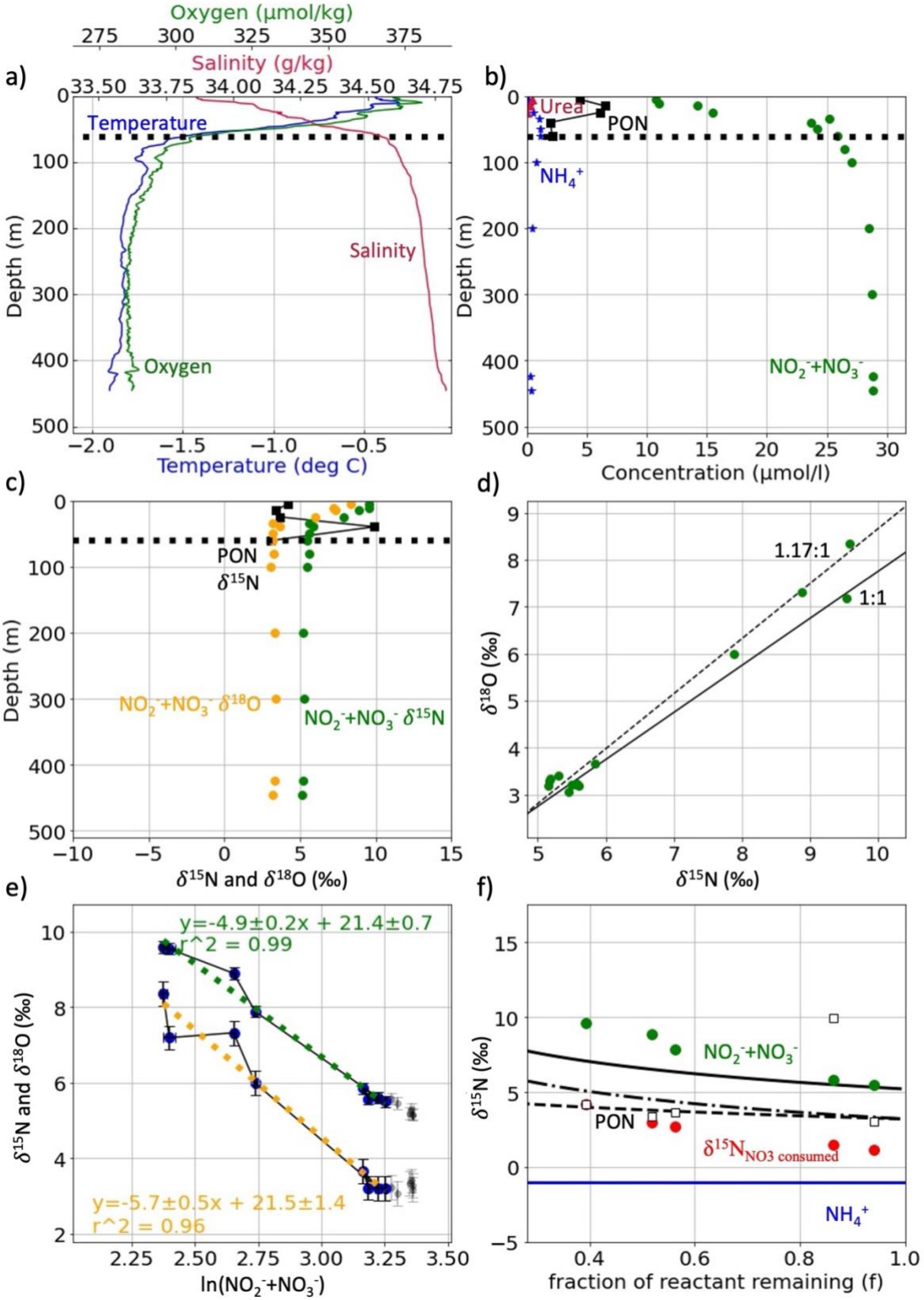
a)
Oxygen (µmol/kg)
275 300 325 350 375
Salinity (g/kg)
33.50 33.75 34.00 34.25 34.50 34.75
Temperature
Salinity
Oxygen
Depth (m)
Temperature (deg C)
b)
Urea
PON
NH4+
NO2-+NO3-
Depth (m)
Concentration (µmol/l)
c)
PON
δ15N
NO2-+NO3- δ18O
NO2-+NO3- δ15N
Depth (m)
δ15N and δ18O (‰)
d)
1.17:1
1:1
δ18O (‰)
δ15N (‰)
e)
y=-4.9±0.2x + 21.4±0.7
r^2 = 0.99
y=-5.7±0.5x + 21.5±1.4
r^2 = 0.96
δ15N and δ18O (‰)
ln(NO2-+NO3-)
f)
NO2-+NO3-
PON
δ15NNO3 consumed
NH4+
δ15N (‰)
fraction of reactant remaining (f)

L16

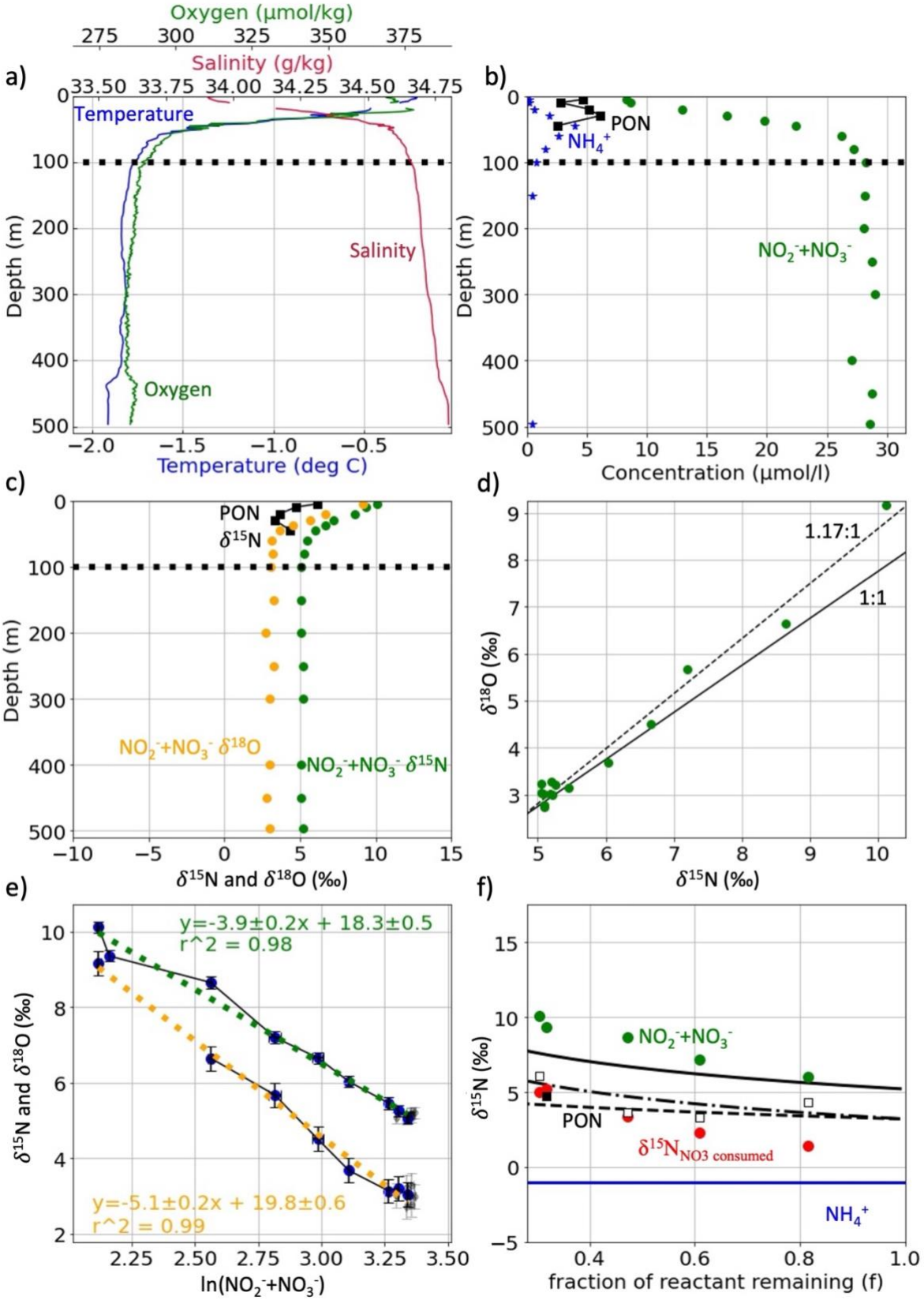
a)
Oxygen (µmol/kg)
275 300 325 350 375
Salinity (g/kg)
33.50 33.75 34.00 34.25 34.50 34.75
Temperature
Salinity
Oxygen
Depth (m)
Temperature (deg C)
b)
PON
NH4+
NO2-+NO3-
Depth (m)
Concentration (µmol/l)
c)
PON
δ15N
NO2-+NO3- δ18O
NO2-+NO3- δ15N
Depth (m)
δ15N and δ18O (‰)
d)
1.17:1
1:1
δ18O (‰)
δ15N (‰)
e)
y=-3.9±0.2x + 18.3±0.5
r^2 = 0.98
y=-5.1±0.2x + 19.8±0.6
r^2 = 0.99
δ15N and δ18O (‰)
ln(NO2-+NO3-)
f)
NO2-+NO3-
PON
δ15NNO3 consumed
NH4+
δ15N (‰)
fraction of reactant remaining (f)

A2: $^{15}\varepsilon_{assim}$ and $^{18}\varepsilon_{assim}$, the impact of mixing, remineralisation and meltwater

A2.1 Mixing

During the mixing of low concentration, high $\delta^{15}N$ and $\delta^{18}O$ $NO_3^-+NO_2^-$ surface waters with upwelled source waters (which have a high $NO_3^-+NO_2^-$ concentration and lower $\delta^{15}N$ and $\delta^{18}O$), the resulting mixture has a $\delta^{15}N$ and $\delta^{18}O$ that is lower than expected for its concentration. This is because the higher concentration, low $\delta^{15}N$ and $\delta^{18}O$ source waters exercise the primary control on the $\delta^{15}N$ and $\delta^{18}O$ of the resulting mixture. The artefactually low $\delta^{15}N$ and $\delta^{18}O$ of the combined $NO_3^-+NO_2^-$ pool will yield an artificially low calculated $^{15}\varepsilon_{assim}$ and $^{18}\varepsilon_{assim}$ (i.e., because the Rayleigh model has been violated; (Sigman et al., 1999)).

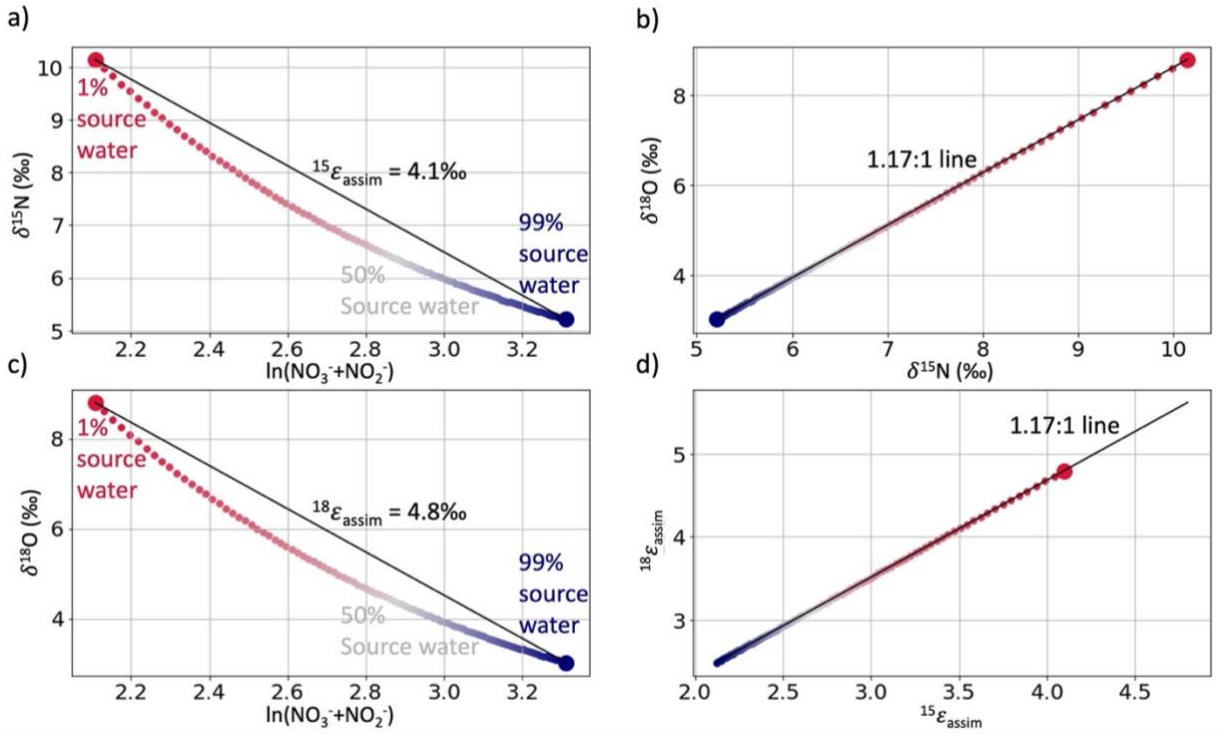

Fig. A2.1.1: Theoretical model illustrating the effects of mixing between source water ($NO_3^-+NO_2^-$ concentration, $\delta^{15}N$, and $\delta^{18}O$ of 27.44 µmol/l, 5.21‰, and 3.02‰ respectively) and water containing partially-assimilated $NO_3^-+NO_2^-$ on the concentration, $\delta^{15}N$, and $\delta^{18}O$ of $NO_3^-+NO_2^-$, and isotope effect derived from the resulting mixture. The assimilated $NO_3^-+NO_2^-$ concentration, $\delta^{15}N$, and $\delta^{18}O$ are calculated by consuming 70% of the source water $NO_3^-+NO_2^-$ (i.e., 30% reactant remaining) with an $^{15}\varepsilon_{assim}$ of 4.1‰ and $^{18}\varepsilon_{assim}$ of 4.8‰ (as theoretically derived in section 4.4.2.3.1 of the main text). During mixing of these waters, the concentration of the resulting mixture is calculated by $[NO_3^-+NO_2^-]_{mix}$= f*$[NO_3^-+NO_2^-]_{source}$ + (1-f)*$[NO_3^-+NO_2^-]_{assimilated}$, while the δX of the resulting mixture is calculated by solving for δX_{mix} in $[NO_3^-+NO_2^-]_{mix}$*δX_{mix} = f*$[NO_3^-+NO_2^-]_{source}$*δX_{source} + (1-f)*$[NO_3^-+NO_2^-]_{assimilated}$*$\delta X_{assimilated}$, where X represents ^{15}N or ^{18}O for changes to $\delta^{15}N$ and $\delta^{18}O$, respectively, and f the fraction of source water in the resulting mixture. In plots (a-c), the source water is represented by the large blue dot, the water containing partially assimilated $NO_3^-+NO_2^-$ by the large red dot, and the result of mixing between the two by the smaller coloured dots, with cooler colours showing a greater contribution of source water. (a) and

(c) show $\delta^{15}N$ versus $\ln(NO_3^-+NO_2^-)$ and $\delta^{18}O$ versus $\ln(NO_3^-+NO_2^-)$, respectively, with the black line representing the assimilation signal with a gradient equal to $-^{15}\varepsilon_{assim}$ and $-^{18}\varepsilon_{assim}$. (c) shows $NO_3^-+NO_2^-$ $\delta^{18}O$ versus $\delta^{15}N$ with the 1.17:1 line plotted in black (see section 4.4.2.3.1of the main text for details). (e) shows $^{18}\varepsilon_{assim}$ versus $^{15}\varepsilon_{assim}$ with the 1.17:1 relationship indicated by the black line. The $^{15}\varepsilon_{assim}$ and $^{18}\varepsilon_{assim}$ of the mixed waters are calculated by performing a regression between the source and mixed water at each degree of mixing. The original assimilation isotope effect used in the theoretical model ($^{15}\varepsilon_{assim}$ = 4.1‰ and $^{18}\varepsilon_{assim}$ = 4.8‰) is represented by the large red dot.

A2.2 remineralisation

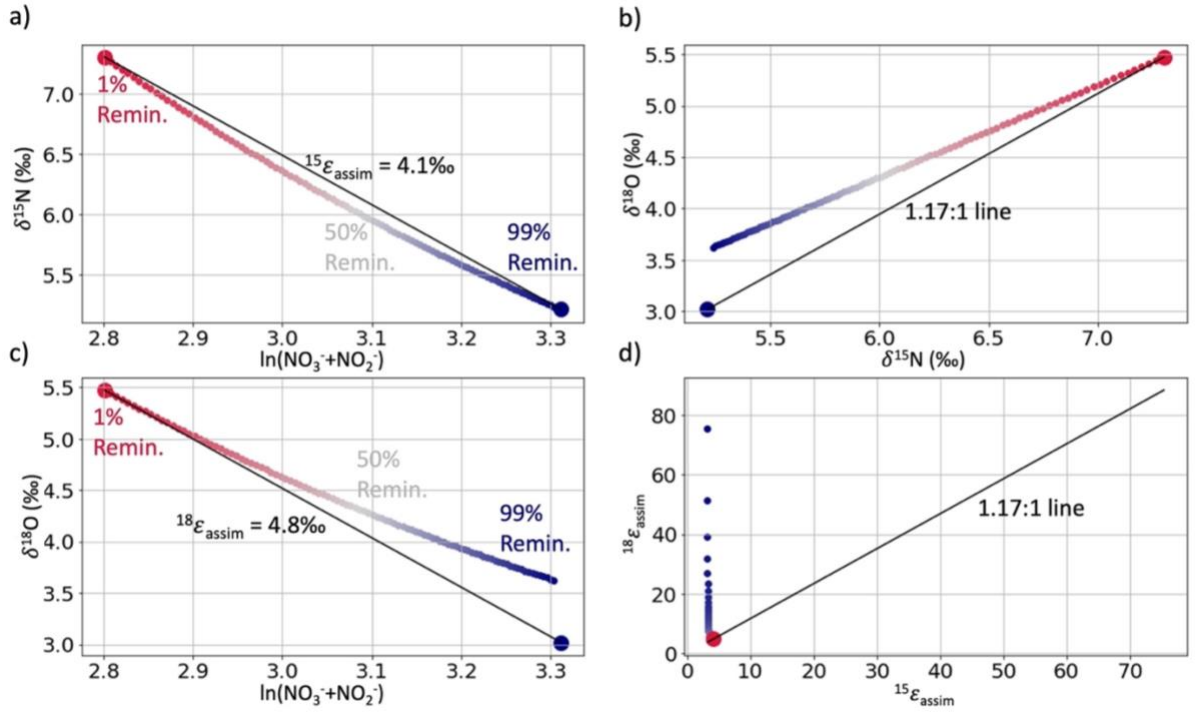

Fig. A2.2.1 Theoretical model illustrating the effect of remineralisation on the $NO_3^-+NO_2^-$ concentration, $\delta^{15}N$, $\delta^{18}O$, and derived isotope effects following partial $NO_3^-+NO_2^-$ assimilation. In plots (a-c), source water ($NO_3^-+NO_2^-$ concentration, $\delta^{15}N$, and $\delta^{18}O$ of 27.44 µmol/l, 5.21‰, and 3.02‰ respectively; represented by the large blue dot) is assimilated with an $^{15}\varepsilon_{assim}$ of 4.1‰ and $^{18}\varepsilon_{assim}$ of 4.8‰, and 40% of the source $NO_3^-+NO_2^-$ is consumed (i.e., 60% reactant remaining) to derive the partially assimilated value (large red dot). The smaller coloured dots represent the effect on the partially assimilated $NO_3^-+NO_2^-$ of differing degrees of remineralisation. (a) shows $\delta^{15}N$ versus $\ln(NO_3^-+NO_2^-)$, with the black line representing the assimilation signal with a gradient equal to $-^{15}\varepsilon_{assim}$. The $\delta^{15}N$ added during remineralisation is set by the accumulated product removed from the $NO_3^-+NO_2^-$ pool during assimilation. (b) shows $\delta^{18}O$ versus $\ln(NO_3^-+NO_2^-)$, with the black line representing the assimilation signal with a gradient equal to $-^{18}\varepsilon_{assim}$. The $\delta^{18}O$ added during remineralisation is set to the $\delta^{18}O$ of seawater + 1.1‰ (i.e., ~-0.3‰ + 1.1‰ = 0.8‰ for the waters adjacent to LCIS) (Boshers et al., 2019; Buchwald et al., 2012; Casciotti et al., 2008; Mirkin et al., 2019; Sigman et al., 2009). (c) shows $\delta^{18}O$ versus $\delta^{15}N$ with the 1.17:1 line plotted in black. (e) shows $^{18}\varepsilon_{assim}$ versus $^{15}\varepsilon_{assim}$ with the 1.17:1 relationship indicated by the black line. The $^{15}\varepsilon_{assim}$ and $^{18}\varepsilon_{assim}$ are calculated by performing a regression between the source and final $NO_3^-+NO_2^-$ at each degree of remineralisation. The isotope effects of assimilation in this theoretical model ($^{15}\varepsilon_{assim}$ = 4.1‰ and $^{18}\varepsilon_{assim}$ = 4.8‰) are represented by the large red dot.

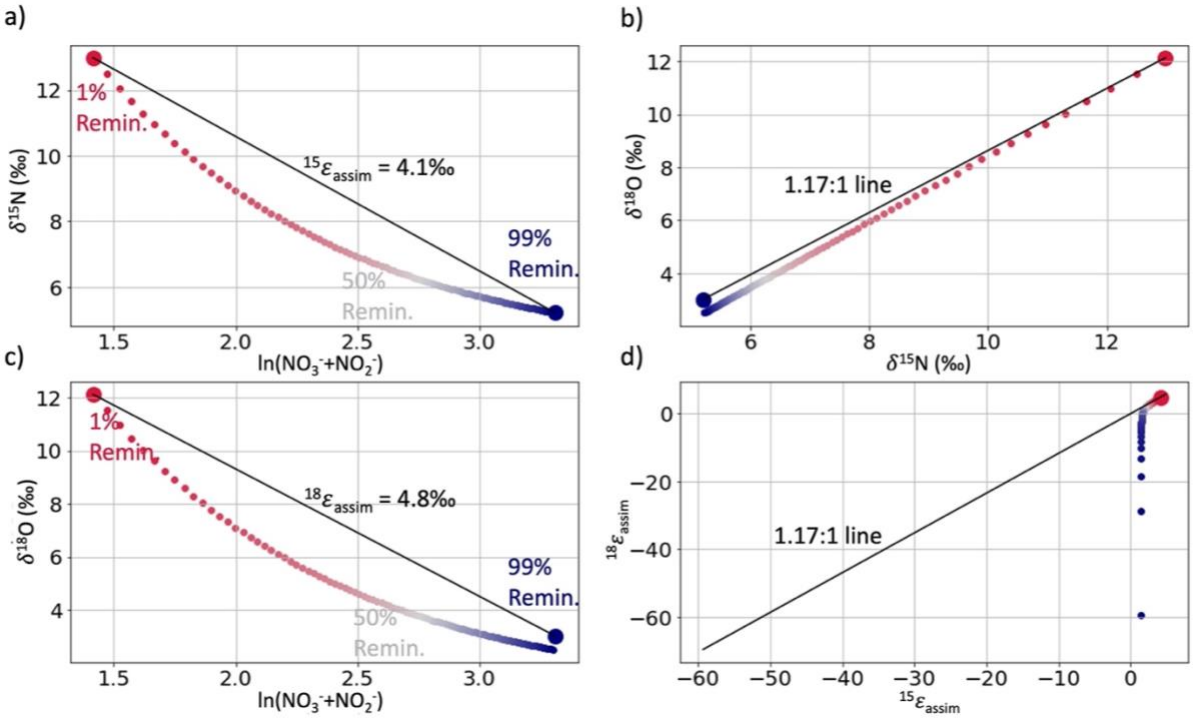

Fig. A2.2.2 Theoretical model illustrating the effect of remineralisation on the NO_3^-+NO_2^- concentration, $\delta^{15}N$, $\delta^{18}O$, and derived isotope effects following near-complete NO_3^-+NO_2^- assimilation. In plots (a-c), source water (NO_3^-+NO_2^- concentration, $\delta^{15}N$, and $\delta^{18}O$ of 27.44 µmol/l, 5.21‰, and 3.02‰ respectively; represented by the large blue dot) is assimilated with an $^{15}\varepsilon_{assim}$ of 4.1‰ and $^{18}\varepsilon_{assim}$ of 4.8‰, and 85% of the source NO_3^-+NO_2^- is consumed (i.e., 15% reactant remaining) to derive the nearly completely assimilated value (large red dot). The smaller coloured dots represent the effect on the nearly completely assimilated NO_3^-+NO_2^- of differing degrees of remineralisation. (a) shows $\delta^{15}N$ versus ln(NO_3^-+NO_2^-), with the black line representing the assimilation signal with a gradient equal to -$^{15}\varepsilon_{assim}$. The $\delta^{15}N$ added during remineralisation is set by the accumulated product removed from the NO_3^-+NO_2^- pool during assimilation. (b) shows $\delta^{18}O$ versus ln(NO_3^-+NO_2^-), with the black line representing the assimilation signal with a gradient equal to -$^{18}\varepsilon_{assim}$. The $\delta^{18}O$ added during remineralisation is set to the $\delta^{18}O$ of seawater + 1.1‰ (i.e., ~-0.3‰ + 1.1‰ = 0.8‰ for the waters adjacent to LCIS) (Boshers et al., 2019; Buchwald et al., 2012; Casciotti et al., 2008; Mirkin et al., 2019; Sigman et al., 2009). (c) shows $\delta^{18}O$ versus $\delta^{15}N$ with the 1.17:1 line plotted in black. (e) shows $^{18}\varepsilon_{assim}$ versus $^{15}\varepsilon_{assim}$ with the 1.17:1 relationship indicated by the black line. The $^{15}\varepsilon_{assim}$ and $^{18}\varepsilon_{assim}$ are calculated by performing a regression between the source and final NO_3^-+NO_2^- at each degree of remineralisation. The isotope effects of assimilation in this theoretical model ($^{15}\varepsilon_{assim}$ = 4.1‰ and $^{18}\varepsilon_{assim}$ = 4.8‰) are represented by the large red dot.

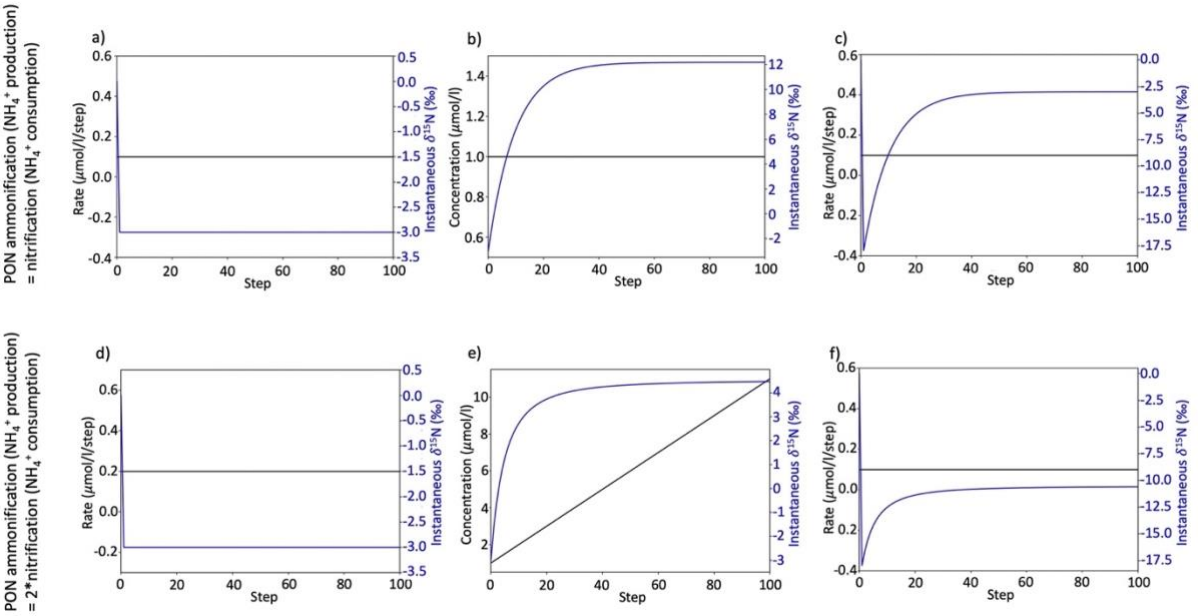

Fig. A2.2.3 Theoretical model illustrating the impact of simultaneous NH_4^+ production (through ammonification) and consumption (through nitrification) on NH_4^+ $\delta^{15}N$ in the case of (a-c) equal rates of ammonification and nitrification and (d-f) where the rate of ammonification is twice that of nitrification. The values shown here are calculated using a forward-stepping model (see A5 below) over 100 steps and initialised with an infinitely large PON pool with a $\delta^{15}N$ of 0‰, a $^{15}\varepsilon_{ammonification}$ of 3‰ (Lehmann et al., 2002; Möbius, 2012), NH_4^+ starting concentration and $\delta^{15}N$ of 1 µmol/l and -1‰, respectively, and a $^{15}\varepsilon_{nitrification}$ of 15‰ (Casciotti et al., 2003). (a) and (d) show ammonification where the black line represents the rate (µmol/l/step) and the blue line the $\delta^{15}N$ of the instantaneous product (i.e., = PON $\delta^{15}N$ - $^{15}\varepsilon_{ammonification}$; ‰). (c) and (f) show nitrification with the black line representing the rate (µmol/l/step) and the blue line the $\delta^{15}N$ of the instantaneous product (i.e., = NH_4^+ $\delta^{15}N$ - $^{15}\varepsilon_{nitrification}$). (b) and (e) show the concentration (black line; µmol/l) and $\delta^{15}N$ (‰) of the NH_4^+ pool (blue line) resulting from the combined influence of ammonification and nitrification, with the NH_4^+ $\delta^{15}N$ levelling off from steps ~60-100. Panels (b) and (e) show that with higher rates of nitrification (b), the NH_4^+ $\delta^{15}N$ levels off at a higher value than at lower rates of nitrification (e), illustrating that increased nitrification drives up the NH_4^+ $\delta^{15}N$.

A2.3 Meltwater input

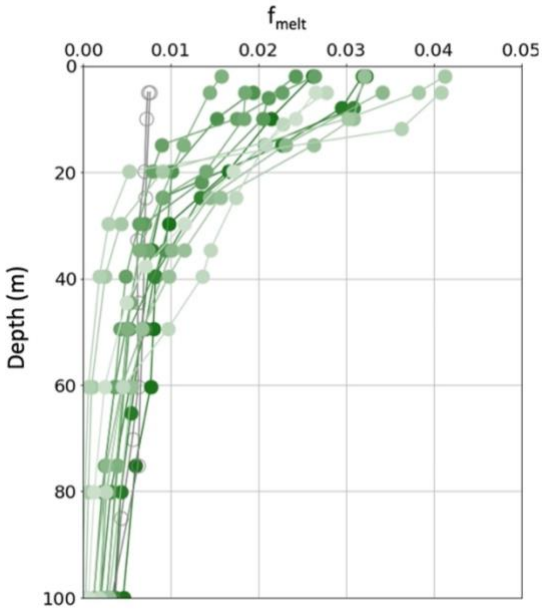

Fig. A2.3.1 Fraction of ice melt (f_{melt}) in the upper 100 m calculated for stations L1-L16. The fraction of ice melt is calculated by solving for f_{melt} in Eq 4.7a with a S_{WW} = 34.68 ± 0.01 g/kg, S_{melt} = 6 g/kg, and $S_{measured}$ equal to the measured salinity at each station and depth. Dot colour represents the station number as in Fig. 4.1.

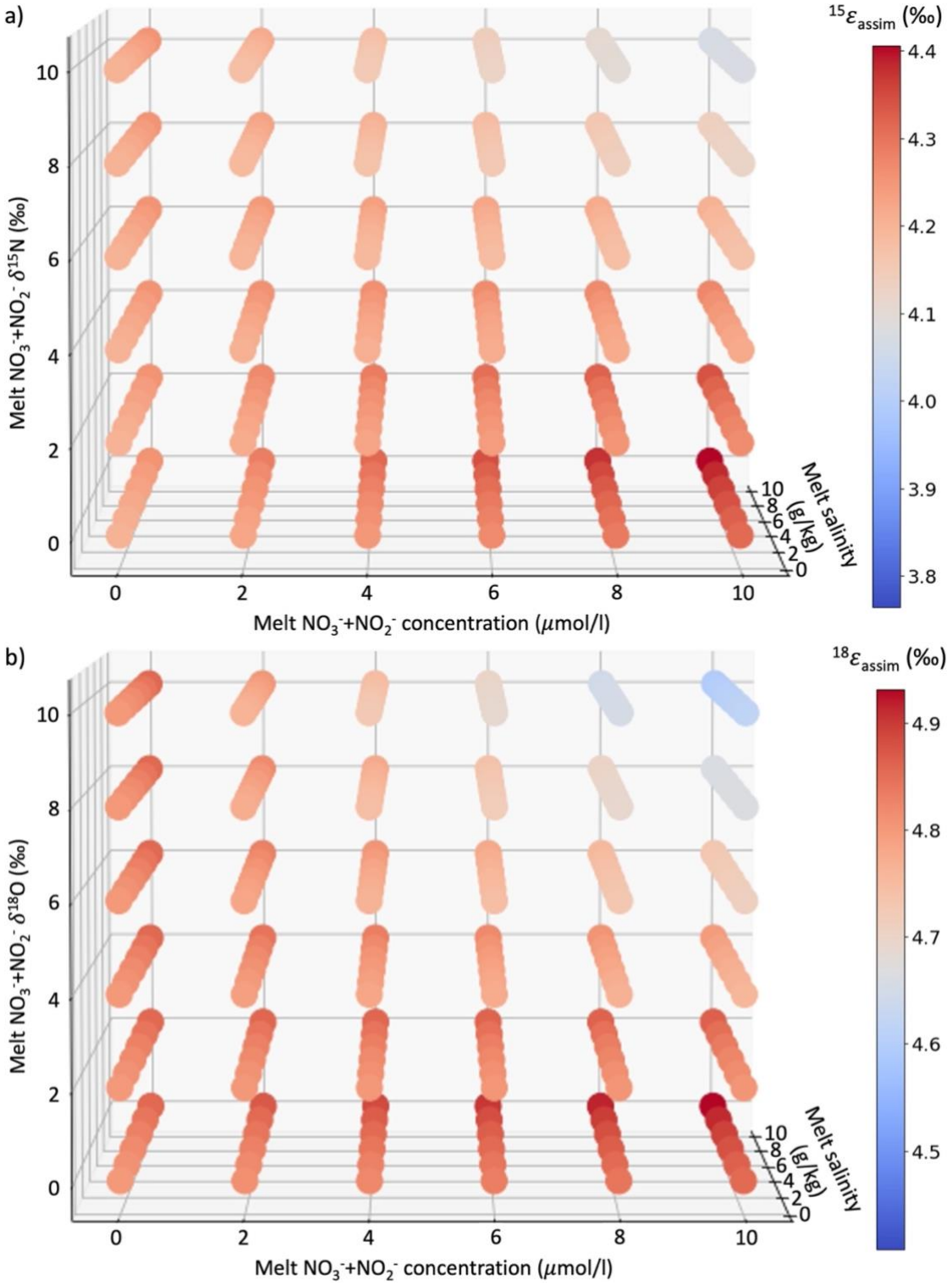

Fig. A2.3.2 Effect of melt removal on (a) $^{15}\varepsilon_{assim}$ and (b) $^{18}\varepsilon_{assim}$ calculated using the melt removed NO_3^-+NO_2^- concentration ($[NO_3^-+NO_2^-]_{melt\ removed}$) and δX ($\delta X_{melt\ removed}$), where X represents (a) ^{15}N for changes to $\delta^{15}N$ and (b) ^{18}O for changes to $\delta^{18}O$. Melt salinity, used to derive the fraction of ice melt (f_{melt}; Eq 4.7a), is varied between 0 and 10 g/kg and plotted on the z-axis. Ice-melt NO_3^-+NO_2^- concentration is varied between 0 and 10 µmol/l (x-axis) and used to solve for $[NO_3^-+NO_2^-]_{melt\ removed}$ in Eq 4.7b. Finally, ice melt NO_3^-+NO_2^- δX is varied between 0 and 10‰ (y-axis), with $\delta X_{melt\ removed}$ calculated from Eq 4.7c. The 3D plot that results is coloured by the derived regionally-averaged (a) $^{15}\varepsilon_{assim}$, with grey denoting the $^{15}\varepsilon_{assim}$ reported in text (4.1 ± 0.7‰), and (b) $^{18}\varepsilon_{assim}$, with grey denoting the $^{18}\varepsilon_{assim}$ reported in text (4.7 ± 0.8‰). Warm colours represent a higher isotope effect and cool colours a lower isotope effect compared to that reported in the text.

A3: f-ratio

A3.1 Deriving $\delta^{15}N_{NO3\ consumed}$ (Eq 4.13)

$$\delta^{15}N_{NO_3^-+NO_2^-\ start\ integrating} = \delta^{15}N^0_{NO_3^-+NO_2^-} - {}^{15}\varepsilon_{assim} \cdot \ln\left(\frac{[NO_3^-+NO_2^-]+[PON]+[NH_4^+]+[urea]}{[NO_3^-+NO_2^-]_o}\right) \quad \text{Eq 4.11}$$

$$\delta^{15}N_{NO3\ consumed} = \delta^{15}N_{NO_3^-+NO_2^-\ start\ integrating} + {}^{15}\varepsilon_{assim}\frac{f\cdot ln\,(f)}{1-(f)} \quad \text{Eq 4.12}$$

where $f = \frac{[NO_3^-+NO_2^-]}{[NO_3^-+NO_2^-]+[PON]+[NH_4^+]+[urea]}$

Substituting Eq 4.11 into Eq 4.12 and simplifying yields:

$$\delta^{15}N_{NO3\ consumed} = \delta^{15}N^0_{NO_3^-+NO_2^-} - {}^{15}\varepsilon_{assim} \cdot \ln\left(\frac{[NO_3^-+NO_2^-]+[PON]+[NH_4^+]+[urea]}{[NO_3^-+NO_2^-]_o}\right) + {}^{15}\varepsilon_{assim} \cdot \frac{\frac{[NO_3^-+NO_2^-]}{[NO_3^-+NO_2^-]+[PON]+[NH_4^+]+[urea]}}{1-\left(\frac{[NO_3^-+NO_2^-]}{[NO_3^-+NO_2^-]+[PON]+[NH_4^+]+[urea]}\right)} \cdot \ln\left(\frac{[NO_3^-+NO_2^-]}{[NO_3^-+NO_2^-]+[PON]+[NH_4^+]+[urea]}\right)$$

$$\delta^{15}N_{NO3\ consumed} = \delta^{15}N^0_{NO_3^-+NO_2^-} - {}^{15}\varepsilon_{assim} \cdot \ln\left(\frac{[NO_3^-+NO_2^-]+[PON]+[NH_4^+]+[urea]}{[NO_3^-+NO_2^-]_o}\right) + {}^{15}\varepsilon_{assim} \cdot \frac{\frac{[NO_3^-+NO_2^-]}{[NO_3^-+NO_2^-]+[PON]+[NH_4^+]+[urea]}}{\frac{[NO_3^-+NO_2^-]+[PON]+[NH_4^+]+[urea]-[NO_3^-+NO_2^-]}{[NO_3^-+NO_2^-]+[PON]+[NH_4^+]+[urea]}} \cdot \ln\left(\frac{[NO_3^-+NO_2^-]}{[NO_3^-+NO_2^-]+[PON]+[NH_4^+]+[urea]}\right)$$

$$\delta^{15}N_{NO3\ consumed} = \delta^{15}N^0_{NO_3^-+NO_2^-} - {}^{15}\varepsilon_{assim} \cdot \ln\left(\frac{[NO_3^-+NO_2^-]+[PON]+[NH_4^+]+[urea]}{[NO_3^-+NO_2^-]_o}\right) + {}^{15}\varepsilon_{assim} \cdot \frac{[NO_3^-+NO_2^-]}{\cancel{[NO_3^-+NO_2^-]+[PON]+[NH_4^+]+[urea]}} \cdot \frac{\cancel{[NO_3^-+NO_2^-]+[PON]+[NH_4^+]+[urea]}}{[PON]+[NH_4^+]+[urea]} \cdot \ln\left(\frac{[NO_3^-+NO_2^-]}{[NO_3^-+NO_2^-]+[PON]+[NH_4^+]+[urea]}\right)$$

$$\delta^{15}N_{NO3\,consumed} = \delta^{15}N^{0}_{NO_3^- + NO_2^-} - {}^{15}\varepsilon_{assim} \cdot \ln\left(\frac{[NO_3^- + NO_2^-] + [PON] + [NH_4^+] + [urea]}{[NO_3^- + NO_2^-]_o}\right) +$$

$${}^{15}\varepsilon_{assim} \cdot \frac{[NO_3^- + NO_2^-]}{[PON] + [NH_4^+] + [urea]} \cdot \ln\left(\frac{[NO_3^- + NO_2^-]}{[NO_3^- + NO_2^-] + [PON] + [NH_4^+] + [urea]}\right)$$

$$\delta^{15}N_{NO3\,consumed} = \delta^{15}N^{0}_{NO_3^- + NO_2^-} + {}^{15}\varepsilon_{assim}\left(\frac{[NO_3^- + NO_2^-]}{[PON] + [NH_4^+] + [urea]} \cdot \right.$$

$$\left. \ln \frac{[NO_3^- + NO_2^-]}{[NO_3^- + NO_2^-] + [PON] + [NH_4^+] + [urea]} - \ln\left(\frac{[NO_3^- + NO_2^-] + [PON] + [NH_4^+] + [urea]}{[NO_3^- + NO_2^-]_o}\right)\right)$$

From log law 2,

$\ln\left(\frac{a}{b}\right) = \ln(a) - \ln(b)$; therefore $-\ln\left(\frac{a}{b}\right) = \ln\left(\frac{b}{a}\right)$

Mechanism: $-\ln\left(\frac{a}{b}\right) = -(\ln(a) - \ln(b)) = \ln(b) - \ln(a) = \ln\left(\frac{b}{a}\right)$

$$\delta^{15}N_{NO3\,consumed} = \delta^{15}N^{0}_{NO_3^- + NO_2^-} + {}^{15}\varepsilon_{assim}\left(\ln\left(\frac{[NO_3^- + NO_2^-]_o}{[NO_3^- + NO_2^-] + [PON] + [NH_4^+] + [urea]}\right) + \right.$$

$$\left.\frac{[NO_3^- + NO_2^-]}{[PON] + [NH_4^+] + [urea]} \cdot \ln\left(\frac{[NO_3^- + NO_2^-]}{[NO_3^- + NO_2^-] + [PON] + [NH_4^+] + [urea]}\right)\right) \qquad \text{Eq 4.13}$$

A3.2 f-ratio selection criteria

The regional f-ratio was derived by averaging the individual f-ratios calculated for each depth at each station if those f-ratios meet three criteria. Firstly, a measured data point was only considered if $\delta^{15}N_{PON} \geq \delta^{15}N_{NH4\ consumed}$, secondly if $\delta^{15}N_{PON} \leq \delta^{15}N_{NO3\ consumed}$, and finally if the calculated f-ratio at that point had a standard deviation <0.25. Twenty-two data points meet these criteria (Fig. 4.6b), with their average providing the mean isotope-derived f-ratio for the waters adjacent to LCIS (as reported in the main text).

The first two criteria are selected to ensure that the calculated f-ratio falls between 0 and 1. A fundamental assumption of Eq 4.2c, which is rearranged to Eq 4.3 and used to derive the f-ratio, is that the PON is formed from the consumption of NH_4^+ and NO_3^-+NO_2^- and therefore has a $\delta^{15}N$ between these two end members. Here, we explore three main clusters where PON

$\delta^{15}N$ falls outside the two end members; (1) at a low degree of nutrient consumption, (2) at a high degree of nutrient consumption where $\delta^{15}N_{PON} > \delta^{15}N_{NO3\ consumed}$, and (3) at a high degree of nutrient consumption where $\delta^{15}N_{PON} < \delta^{15}N_{NH4\ consumed}$.

(1) At a low degree of nutrient consumption (high fraction of reactant remaining), the $\delta^{15}N_{PON}$ is generally high and variable. This variability derives from two sources; firstly, at low degrees of nutrient consumption the $PON_{measured}$ concentration is generally low with a high (but variable) $\delta^{15}N$, likely because it is mainly recalcitrant PON (i.e., $PON_{background}$). This leads to a second source of variability, where to isolate the $PON_{growing}$ signal, we remove $PON_{background}$, which, in the case of low PON concentration data is the primary signal. Thus $PON_{background}$ removal leads to greater variability.

(2) The second scenario outside the two end members occurs where the $\delta^{15}N_{PON}$ is higher than the $\delta^{15}N_{NO3\ consumed}$ at high degrees of nutrient consumption (low fraction of reactant remaining). The PON concentrations of these samples can be high, with a $\delta^{15}N_{PON}$ falling above the Rayleigh instantaneous product in four cases. In another five cases, the $\delta^{15}N_{PON}$ falls between the $\delta^{15}N_{NO3\ consumed}$ and Rayleigh instantaneous product. In both scenarios, the $\delta^{15}N_{PON}$ is higher than expected were NH_4^+ and $NO_3^-+NO_2^-$ assimilation the only processes affecting the PON pool. Removing $PON_{background}$ from $PON_{measured}$ lowers the $\delta^{15}N_{PON}$ signal by removing the low concentration, high $\delta^{15}N$ $PON_{background}$ pool, such that this high $\delta^{15}N_{PON}$ is not an artefact of $PON_{background}$ removal. Instead, NH_4^+ and $NO_3^-+NO_2^-$ assimilation may not be the only processes acting on the PON pool. Were ammonification, which occurs with a $^{15}\varepsilon_{ammonification}$ of 3.0 ± 0.1‰ (Lehmann et al., 2002; Möbius, 2012) also acting on the surface PON pool, it would increase its $\delta^{15}N$. However, it is challenging to quantify the extent of surface ammonification as the NH_4^+ pool is consumed nearly instantaneously after production, so the ambient NH_4^+ concentration cannot be used to quantify the degree of ammonification that has occurred. The only constraint we can place on the system is through our robust knowledge of the N sources supporting PON production in this region, and with the knowledge that if the PON $\delta^{15}N$ cannot be explained by NH_4^+ and $NO_3^-+NO_2^-$ assimilation alone, there may be other processes affecting it. This explanation, however, raises the question of whether all our PON data may have undergone ammonification, at least to some degree, acting to raise the $\delta^{15}N_{PON}$, which would artificially increase the calculated f-ratio. This is not possible to disprove, although is unlikely to have been significant given the near Redfieldian biomass C :

N ratio of 7.4 ± 1.9 (Flynn et al., 2021), indicating active, balanced growth with minimal evidence of ammonification (Hupe & Karstensen, 2000; Körtzinger et al., 2001; Osterroht & Thomas, 2000; Thomas et al., 1999). Furthermore, even if ammonification were occurring in the surface ocean of our study region, the only process that consumes NH_4^+ in these waters is NH_4^+ assimilation (we have shown surface nitrification to be insignificant in our study region; section 4.4.2.3.1). As a result, NH_4^+ produced through ammonification is either accumulating in the surface pool or being reassimilated, with the reincorporation of NH_4^+ into the PON pool largely eliminating the ammonification signal on the $\delta^{15}N_{PON}$. This indicates that $\delta^{15}N_{PON}$ is generally representative of the NH_4^+ and NO_3^-+NO_2^- assimilation signals alone, allowing for the derivation of a reliable f-ratio.

(3) The final case where PON $\delta^{15}N$ falls outside the two end members is relevant to a single data point at a high degree of NO_3^-+NO_2^- consumption that has a $\delta^{15}N$ below the $\delta^{15}N_{NH4\ consumed}$. This is not an artefact of $PON_{background}$ removal as this sample has a relatively high PON concentration and the $\delta^{15}N_{PON\ measured}$ is also low. The only mechanism to produce a $\delta^{15}N_{PON}$ this low is for it to be formed almost entirely through NH_4^+ assimilation with an associated NH_4^+ assimilation isotope effect. This seems unlikely given the available evidence that NH_4^+ assimilation occurs with negligible isotopic fractionation at concentrations relevant to the open ocean (Hoch et al., 1992; Liu et al., 2013; Pennock et al., 1996). A perhaps more likely explanation of this single data point is that it is an outlier with an erroneously low $\delta^{15}N$ and should be ignored.

The final criteria used to select the data over which the f-ratio should be averaged is that the derived f-ratio standard deviation must be <0.25. The f-ratio standard deviation is calculated using a Monte Carlo simulation. A Monte Carlo simulation uses repeated, random sampling from a normal distribution to solve deterministic problems (Mooney, 1997). Using the mean and standard deviation of the known values in Eq 4.3 ($\delta^{15}N_{NH4\ consumed}$, $\delta^{15}N_{NO3\ consumed}$, and $\delta^{15}N_{PON\ growing}$) we derive a normal distribution for each that is then sampled randomly 100 000 times. This random sampling allows us to calculate 100 000 different f-ratios for each data point, with each representing a possible combination given the means and standard deviations of $\delta^{15}N_{NH4\ consumed}$, $\delta^{15}N_{NO3\ consumed}$, and $\delta^{15}N_{PON\ growing}$. The standard deviation across these 100 000 different f-ratios is then taken to derive the standard deviation of the f-ratio at that point. The standard deviation of the regionally averaged f-ratio, as well as that of $\delta^{15}N_{NO3}$

$_{consumed}$ (Eq 4.13) and the Rayleigh equations (Eq 4.4, Eq 4.8b, and Eq 4.9), are similarly calculated in this way.

The criterion that the sample-derived f-ratio must be <0.25 is used to increase the reproducibility of the regional f-ratio average. Instituting this criterion prevents seven data points, all found at a fraction of reactant remaining >0.75, from being included in the regional f-ratio average. The increased f-ratio standard deviation at these points derives from two sources; (1) the Rayleigh instantaneous and accumulated products have a higher standard deviation at higher fractions of reactant remaining (seen in Fig. 4.6a) and (2) at higher fractions of reactant remaining, $\delta^{15}N_{NO3\ consumed}$ and $\delta^{15}N_{NH4\ consumed}$ are more similar (seen in Fig. 4.6a).

(1) The standard deviation of the Rayleigh instantaneous and accumulated product increases at higher fractions of reactant remaining (low degrees of consumption) due, primarily, to the standard deviation associated with the isotope effect. The standard deviations of the source NO_3^-+NO_2^- concentration and $\delta^{15}N$ together result in a consistent standard deviation across the entire Rayleigh reactant, instantaneous, and accumulated product curves, shifting them left and right in the case of concentration, and up and down in the case of $\delta^{15}N$. The impact of the isotope effect standard deviation on the Rayleigh reactant, instantaneous, and accumulated product depends on the fraction of reactant remaining. As the fraction of reactant remaining approaches 1 (no NO_3^-+NO_2^- consumption), the standard deviation associated with the reactant pool is minimal, while the $\delta^{15}N$ of the Rayleigh instantaneous and accumulated product (Eq 4.8b and Eq 4.9) tend to the same value with a large standard deviation. As the fraction of the reactant pool remaining decreases (consumption begins), the standard deviation associated with the Rayleigh reactant pool begins to increase, while that of the Rayleigh instantaneous product decreases to a point and then increases, and the Rayleigh accumulated product standard deviation decreases (Fig. 4.6a, shading). Ultimately, the higher Rayleigh instantaneous and accumulated product standard deviations at higher degrees of reactant remaining increase the standard deviation associated with $\delta^{15}N_{NO3\ consumed}$ for these points, increasing the standard deviation of the calculated f-ratio.

(2) At higher fractions of reactant remaining, the $\delta^{15}N_{NO3\ consumed}$ and $\delta^{15}N_{NH4\ consumed}$ are closer together, meaning that along with the standard deviation of $\delta^{15}N_{NO3\ consumed}$ being larger, the

$\delta^{15}N$ range over which the f-ratio is calculated is smaller, leading to even higher derived f-ratio standard deviations.

The criterion that the f-ratio standard deviation must be <0.25 results in the removal of seven data points with f-ratio standard deviations that are consistently high and vary each time the Monte Carlo simulation is run. Such a high and variable standard deviation indicates that the uncertainties associated with $\delta^{15}N_{NH4\ consumed}$, $\delta^{15}N_{NO3\ consumed}$, and $\delta^{15}N_{PON\ growing}$ for these points overlap too significantly to allow for a reliable f-ratio to be calculated. The standard deviations vary between runs as a result of the Monte Carlo random selection from a normal distribution, with the model sometimes choosing data that yield a greater spread in the calculated f-ratio, and other times a smaller spread, ultimately indicating that the f-ratios derived from these seven data points are not reliable. The standard deviations associated with the f-ratios of the 22 data points over which the regional f-ratio is calculated are consistent between model runs, indicating the f-ratios derived from these data points are robust. If we were to nonetheless include the seven questionable f-ratios in our regional f-ratio average, they would have no meaningful effect on the calculated regional f-ratio, producing a mean value of 0.79 and a standard deviation that constantly varies, ranging from 1.06 to 21.46 after running the Monte Carlo simulation five different times. Using the criteria that the f-ratio at a point must have a standard deviation <0.25 is correct, allowing us to trust the f-ratio for each data point and leading to the production of a consistent regional f-ratio.

Filtering our f-ratios using the three criteria yields 22 reliable data points over which to compute the regional f-ratio (Fig. 4.6b). The average of these 22 data points provides a robust average isotope-derived f-ratio for the waters adjacent to LCIS of 0.81 ± 0.18.

A4: f-ratio sensitivity analysis

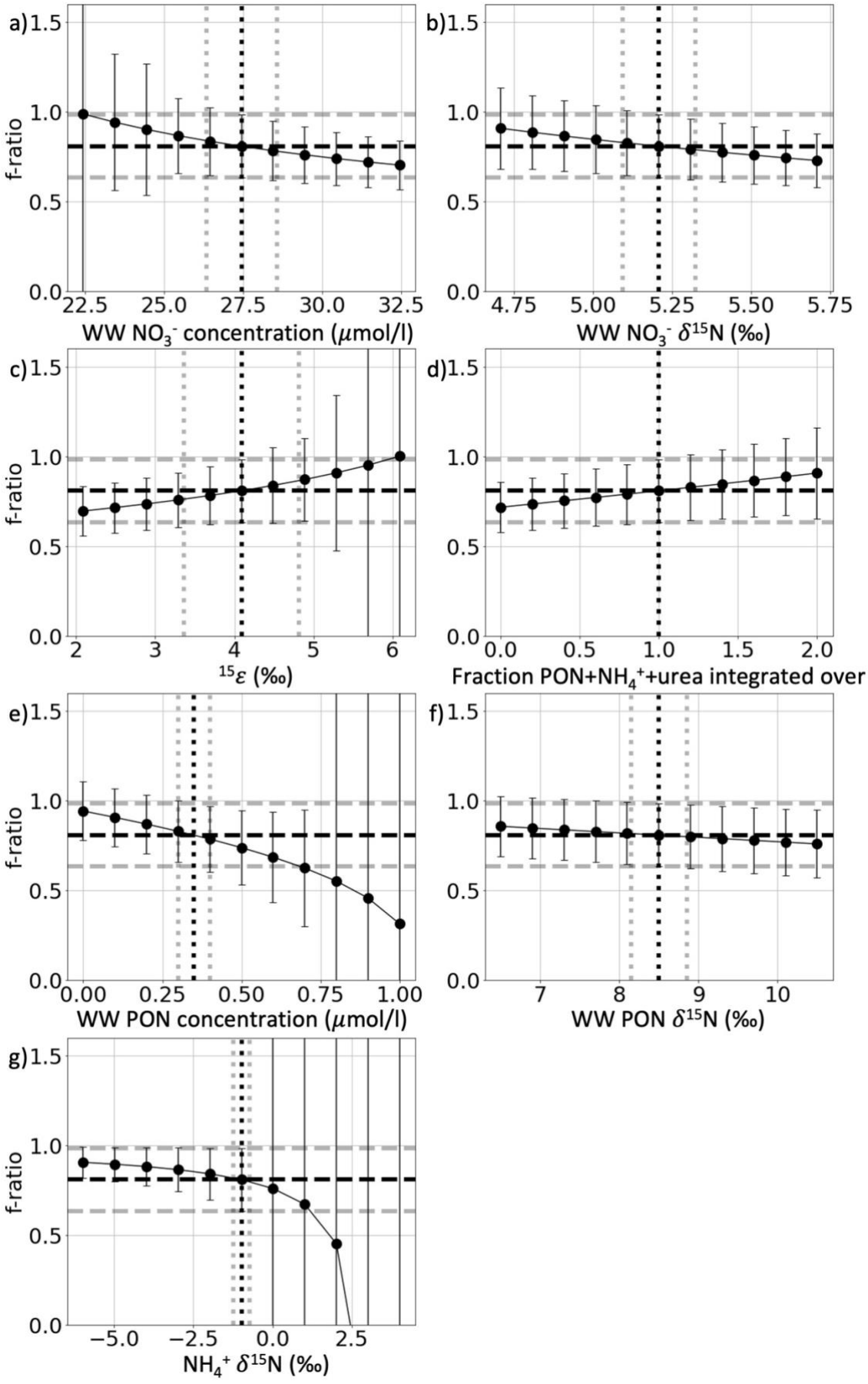

Fig. A4.1 Exploring the sensitivity of the derived f-ratios to variations in a) the source WW $NO_3^-+NO_2^-$ concentration, b) the source WW $NO_3^-+NO_2^-$ $\delta^{15}N$, c) the $NO_3^-+NO_2^-$ N assimilation isotope effect ($^{15}\varepsilon_{assim}$), d) the fraction of the PON + NH_4^+ + urea concentration that is integrated over to derive $\delta^{15}N_{NO3\ consumed}$, e) the source WW PON concentration, f) the source WW PON $\delta^{15}N$, and g) the NH_4^+ $\delta^{15}N$. The horizontal dashed lines represent the average regional f-ratio (black dashed line) ± 1 standard deviation (grey dashed lines) of 0.81 ± 0.18. The vertical dotted lines represent the regional average value of each parameter (black) ± 1 standard deviation (grey). The f-ratios plotted in this figure are calculated over the same 22 data points (the points over which the f-ratio reported in text is calculated). Varying each parameter within a reasonable range (vertical dotted grey lines) yields respective uncertainties in the derived f-ratio that are more than accounted for in the uncertainty associated with our reported f-ratio.

A4.2 Sensitivity analysis results

In all cases, varying the parameters resulted in a consistent impact on the calculated f-ratio, showing either a positive (increased parameter equates to an increased f-ratio) or negative (increased parameter equates to a decreased f-ratio) correlation.

$\delta^{15}N_{NH4\ consumed}$ shows a negative correlation, increasing the f-ratio as $\delta^{15}N_{NH4\ consumed}$ decreases. This is an expected result as the lower the $\delta^{15}N_{NH4\ consumed}$ end member, the further it is from $\delta^{15}N_{PON}$. This greater distance to the end member results in a lower calculated contribution of NH_4^+ consumption to biomass production and thus, a higher f-ratio. The negative correlation indicates that even if the four low NH_4^+ $\delta^{15}N$ values excluded from the $\delta^{15}N_{NH4\ consumed}$ average in section 4.4.2.2 (of the main text) were included, the lower resulting $\delta^{15}N_{NH4\ consumed}$ of -1.8 ± 0.5‰ would lead to a marginally higher calculated f-ratio of 0.83 ± 0.16. Additionally, while all the evidence suggests that NH_4^+ assimilation occurs with a negligible isotope effect at open ocean concentrations (Hoch et al., 1992; Liu et al., 2013), even if it were associated with a small isotope effect, this would lower the $\delta^{15}N_{NH4\ consumed}$ end member, increasing the calculated f-ratio. As such, with regards to $\delta^{15}N_{NH4\ consumed}$, the reported f-ratio errs on the conservative side, potentially underestimating the amount of new production.

We turn now to the first two parameters that influence $\delta^{15}N_{NO3\ consumed}$, the concentration and $\delta^{15}N$ of the source WW $NO_3^-+NO_2^-$, which are both weakly negatively correlated with the derived f-ratio. Artificially increasing the concentration of the source water $NO_3^-+NO_2^-$ moves the Rayleigh reactant, instantaneous and accumulated plots to the right, while artificially increasing the source water $NO_3^-+NO_2^-$ $\delta^{15}N$ moves them vertically upwards in $NO_3^-+NO_2^-$ $\delta^{15}N$ versus fraction of $NO_3^-+NO_2^-$ remaining space (Fig. 4.6a). Both of these actions increase the $\delta^{15}N$ of the Rayleigh reactant, instantaneous product, and accumulated product at a particular degree of consumption, increasing the calculated $\delta^{15}N_{NO3\ consumed}$. The increased

$\delta^{15}N_{NO3\ consumed}$ moves the end member further away from the $\delta^{15}N_{PON}$, leading to a lower calculated f-ratio. Varying the source water $NO_3^-+NO_2^-$ concentration and $\delta^{15}N$ has a relatively weak impact on the calculated f-ratio and is more than accounted for in our reported f-ratio uncertainty.

Varying ${}^{15}\varepsilon_{assim}$ has a positive correlation with the calculated f-ratio, due to the interplay of two impacts of the isotope effect. A higher isotope effect lowers the instantaneous and accumulated Rayleigh product $\delta^{15}N$ at high degrees of reactant remaining, but also causes a steeper, more rapidly increasing Rayleigh reactant, instantaneous product, and accumulated product $\delta^{15}N$ with decreasing fraction of reactant remaining (Fig. A4.3). This means that as ${}^{15}\varepsilon_{assim}$ increases, the calculated $\delta^{15}N_{NO3\ consumed}$ decreases at higher degrees of reactant remaining, while it increases at lower degrees of reactant remaining, with the point of inflection being found at e^{-1} or ~0.368 fraction of reactant remaining (Fig. A4.3). As the data in our region are generally associated with higher degrees of reactant remaining (i.e., lower degrees of $NO_3^-+NO_2^-$ consumption), an increased ${}^{15}\varepsilon_{assim}$ results in, on average, a decrease in $\delta^{15}N_{NO3\ consumed}$, driving this end member closer to $\delta^{15}N_{PON}$ and resulting in an increase in the calculated f-ratio. We derive a mean ${}^{15}\varepsilon_{assim}$ of 4.1 ± 0.7‰ in section 4.4.2.3.1, which is consistent with, though on the slightly lower end of previous summer Southern Ocean estimates (Altabet & Francois, 2001; DiFiore et al., 2006, 2009, 2010; Fripiat et al., 2019; Karsh et al., 2003; Sigman et al., 1999). This indicates that for our region, and the Southern Ocean as a whole, which generally experiences <63.2% $NO_3^-+NO_2^-$ drawdown, a higher ${}^{15}\varepsilon_{assim}$ would yield a higher f-ratio, again indicating that our f-ratio estimate errs on the conservative side.

The final parameter that influences the $\delta^{15}N_{NO3\ consumed}$ end member is the PON + NH_4^+ + urea concentration over which the integrated-instantaneous product is integrated (Eq 4.13). To quantify this effect, we vary the fraction of the PON + NH_4^+ + urea concentration that is integrated over (i.e., (concentration integrated over) = (fraction PON + NH_4^+ + urea integrated over) × (PON + NH_4^+ + urea concentration)). A fraction of 0 equates to integrating over a PON + NH_4^+ + urea concentration of 0, equivalent to the Rayleigh instantaneous product (Eq 4.8b), a fraction of 1 to the concentration of PON + NH_4^+ + urea, and a fraction >1 to more than the concentration of PON + NH_4^+ + urea. Varying this fraction results in a positive correlation with the calculated f-ratio. This is an expected result, for as the concentration integrated over decreases (as it does when moving from a fraction of 1 to 0), the $\delta^{15}N_{NO3\ consumed}$ increases,

moving further from $\delta^{15}N_{PON}$ and decreasing the calculated f-ratio to 0.75 ± 0.17 where the fraction = 0 (which is equivalent to calculating the f-ratio using the Rayleigh instantaneous product; Eq 4.8b). Using the instantaneous product for the $\delta^{15}N_{NO3\ consumed}$ yields the lowest possible f-ratio. As the fraction of the concentration integrated over increases (fraction >1), the f-ratio rises as a result of the increased degree of integration leading to a lowering of $\delta^{15}N_{NO3\ consumed}$, bringing it closer to $\delta^{15}N_{PON}$. By using the integrated-instantaneous $\delta^{15}N_{NO3\ consumed}$ end member, we do not derive the most conservative f-ratio possible, but as shown in the main text (section 4.4.2.3.2), this end member is most appropriate for the study region, allowing for the derivation of a regional f-ratio.

$\delta^{15}N_{PON}$ is influenced by the concentration and $\delta^{15}N$ of the $PON_{background}$ removed from the $\delta^{15}N_{PON\ measured}$ signal. Both the $PON_{background}$ concentration and $\delta^{15}N$ are negatively correlated with the derived f-ratio. For all data points over which the regional f-ratio is calculated, removing the high $\delta^{15}N_{PON\ background}$ signal lowers the $\delta^{15}N_{PON\ measured}$ to isolate the $\delta^{15}N_{PON\ growing}$ ($\delta^{15}N_{PON}$) component of the PON pool, driving $\delta^{15}N_{PON}$ away from the $\delta^{15}N_{NO3\ consumed}$ end member and lowering the derived f-ratio. At lower $\delta^{15}N_{PON\ background}$, the $\delta^{15}N_{PON}$ decreases less, increasing the calculated f-ratio. Artificially decreasing the concentration of $PON_{background}$ increases the $\delta^{15}N_{PON}$ as less $\delta^{15}N_{PON\ background}$ is being removed, driving $\delta^{15}N_{PON}$ closer to the $\delta^{15}N_{NO3\ consumed}$ end member and increasing the calculated f-ratio. If the $PON_{background}$ signal were not removed (i.e., the WW PON concentration = 0 μmol/l), we would derive an f-ratio of 0.88 ± 0.11.

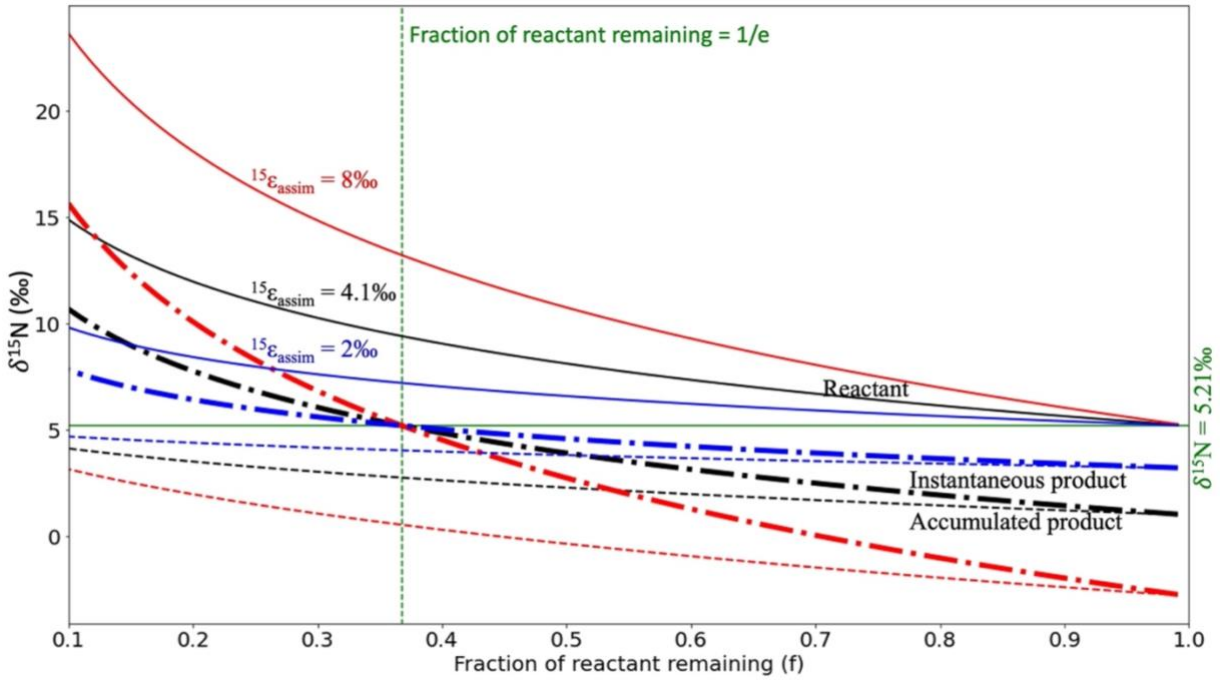

Fig. A4.3 Plot of $\delta^{15}N$ versus the fraction of reactant remaining (f), with the Rayleigh reactant (solid line), instantaneous product (thick dot-dashed line) and accumulated product (dashed line) calculated using a $^{15}\varepsilon_{assim}$ of 4.1‰ (black), 8‰ (red), and 2‰ (blue). In all cases, the source NO_3^-+NO_2^- $\delta^{15}N$ is 5.21‰ (horizontal solid green line). The vertical green dashed line denotes where the fraction of reactant remaining is 1/e (~0.368), representing the point at which the Rayleigh instantaneous products derived using any two values of $^{15}\varepsilon_{assim}$ intersect. This indicates that at a higher $^{15}\varepsilon_{assim}$, the calculated $\delta^{15}N_{NO3\ consumed}$ decreases at fractions of reactant remaining greater than 1/e, while it increases at lower fractions of reactant remaining.

A5: Theoretical N isotope fractionation model

The ocean nitrogen cycle comprises many processes with different isotope effects, as evidenced by Fig. 2.5. In an effort to understand how these processes interact, we created the Ocean Isotope Model™ to simulate simultaneous processes acting on multiple N pools at the same time. The model is constructed on the foundational assumptions of conservation of mass, Rayleigh dynamics, and concentration-weighted mixing. Over short time scales, even in the case where multiple processes act on a single pool, the Rayleigh equations are a good approximation of the instantaneous product due to the short-term closed system nature of these pools. The Rayleigh model is used to calculate the isotopic distribution during the consumption of a pool with a given isotope effect, and is represented by

$$\delta^{15}N_{final} = \delta^{15}N_{initial} - {}^{15}\varepsilon \cdot \ln\left(\frac{[reactant]_{final}}{[reactant]_{initial}}\right)$$

where [reactant] indicates the concentration of the reactant pool. The concentration-weighted isotope mixing equation, represented by

$$\delta^{15}N_{final}[reactant]_{final} = \delta^{15}N_{initial}[reactant]_{initial} + \delta^{15}N_1[reactant]_1 + \delta^{15}N_2[reactant]_2 + \cdots + \delta^{15}N_n[reactant]_n$$

is then used to determine the concentration and δ^{15}N of the reactant pool. The final reactant concentration and δ^{15}N are calculated by taking the initial concentration and δ^{15}N of the reactant pool and adding/subtracting the concentration and δ^{15}N of all the processes that are simultaneously acting on that pool. The use of the Rayleigh equation is appropriate in this case as each step is small, so even if the reactant pool is not a closed system, this will have little impact on the instantaneous calculation and will be accounted for in the next iterative step. The model considers the concentration and δ^{15}N of five ocean N pools, particulate nitrogen (PN; which is equivalent to particulate organic nitrogen (PON) used throughout this thesis), labile dissolved organic nitrogen (DON), ammonium (NH_4^+), nitrite (NO_2^-) and nitrate (NO_3^-). For NO_3^- and NO_2^-, the δ^{18}O is additionally calculated.

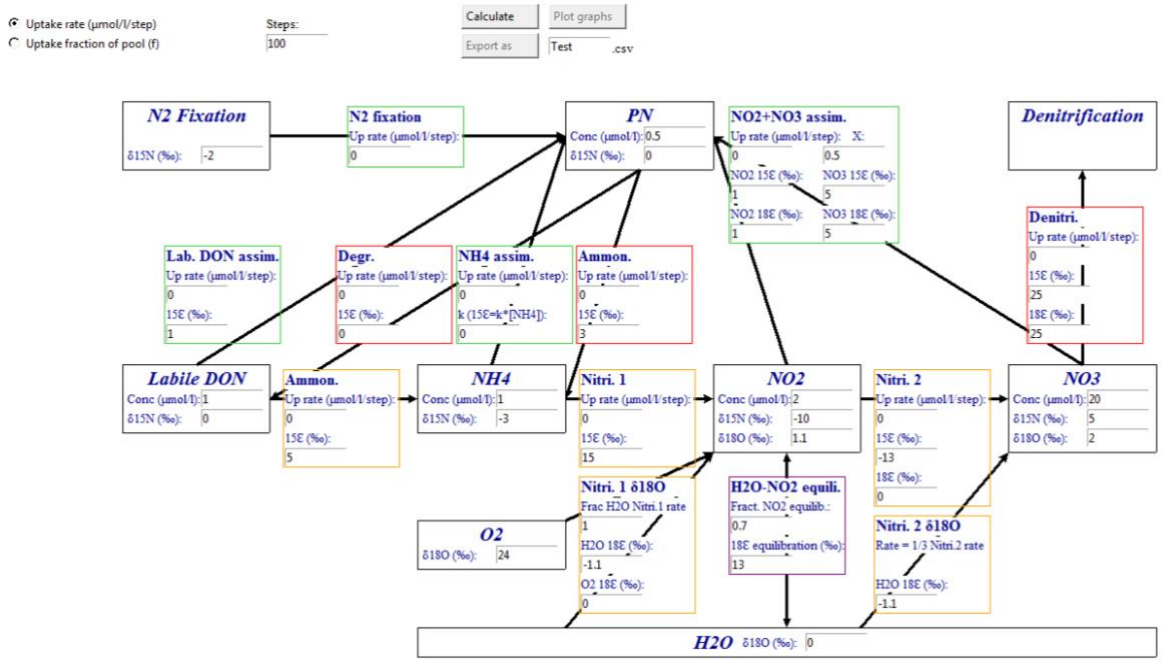

Fig. A5.1: Graphical user interface of the Ocean Isotope Model™. The black boxes represent the N pools (PN, labile DON, NH_4^+, NO_2^-, and NO_3^-) and sources and sinks of N and O (N_2 fixation, denitrification, dissolved O_2, and seawater H_2O). The colourful boxes represent processes acting on the N and O pools, with green boxes representing processes that produce PN (N_2 fixation, labile DON assimilation, NH_4^+ assimilation, and NO_2^-+NO_3^- assimilation), red boxes show processes that consume PN (degradation and ammonification) or remove N from

the system (denitrification), orange boxes represent remineralisation (labile DON ammonification, nitrification 1, and nitrification 2), and the purple box shows the equilibration between the O atoms of NO_2^- and H_2O.

The model is capable of accounting for 11 separate processes acting on the ocean N pools. Each process has an associated rate and isotope effect. The uptake rate can be set in two ways, either as a direct rate (μmol/l/step) or as a fraction of the source pool (f*(concentration of the source pool) = μmol/l/step). The N isotope effects associated with each step is represented by ${}^{15}\varepsilon$, while the O isotope effect is represented by ${}^{18}\varepsilon$. The information relating to each process can be found in the colourful boxes. Each process occurs at a specific rate and with a particular isotope effect, with the rate at each step calculated as follows:

If rate > $([reactant]_{initial})$:

rate = $[reactant]_{initial}$

$([reactant]_{final}) = ([reactant]_{initial}) - rate$

Because the rate is calculated in this way, the source pool is never driven to negative concentrations. One potential complication, however, occurs when a process consumes a pool at a higher rate than that pool is resupplied. This scenario results in the depletion of the pool, setting the consuming process rate to 0. The process adding to the pool is still operating, however, meaning that following the depletion, the pool will increase its concentration. The Ocean Isotope Model™ is designed for use in a steady-state system or in the case where a single pool is being consumed by one or more processes. Analysing the system in a steady state would require that the rates adding N to each pool match the rates coincidentally removing N. In the case of single pool analysis, multiple processes can act on the same pool at different rates, but the pool either cannot be replenished during its consumption or must be replenished at a rate equal to or greater than its consumption. If the model is pushed beyond these constraints, it begins to break down and the results become unreliable.

The processes accounted for in the Ocean Isotope Model™ are:

- N_2 fixation: the production of NH_4^+ from di-nitrogen (N_2) gas, this NH_4^+ is subsequently consumed to form PN.
- NO_2^- and NO_3^- assimilation: the uptake of NO_3^- and NO_2^- to produce PN. If we assume the surface NO_3^- transporters of phytoplankton are incapable of distinguishing between NO_2^- and NO_3^-, it implies that NO_2^- and NO_3^- will be taken up in proportion to their

concentrations. We, however, created an allowance for the transporters to have preferential uptake, reported here as X, which represents the relative preference for NO_2^- over NO_3^-. When X is set to 0.5, it is assumed the phytoplankton have no preference and will therefore consume NO_2^- and NO_3^- at a rate that is dependent on their relative abundance. When X >0.5, NO_2^- is preferentially consumed, while when X <0.5, NO_3^- is preferentially consumed. The rates of NO_2^- and NO_3^- uptake are calculated mathematically as follows:

(NO_2^- uptake rate) = (NO_3^-+NO_2^- uptake rate) * ([NO_2^-] * X) / (([NO_2^-] * X) + ([NO_3^-] * (1 - X))) and (NO_3^- uptake rate) = (NO_3^-+NO_2^- uptake rate) - (NO_2^- uptake rate)

- NH_4^+ assimilation: the uptake of NH_4^+ to produce PN. The isotope effect is proportional to the NH_4^+ concentration ($^{15}\varepsilon$ = k*[NH_4^+], where k can be varied).
- Labile DON assimilation: the uptake of DON to produce PN.
- Degradation: the breakdown of PN to DON.
- Ammonification 1: the breakdown of PN to NH_4^+.
- Ammonification 2: the breakdown of DON to NH_4^+.
- Nitrification 1: the oxidation of NH_4^+ to NO_2^-. This process incorporates one O atom from dissolved O_2 and one from the H_2O pool (Andersson & Hooper, 1983).
- NO_2^- - H_2O equilibration: the process whereby the O atoms of NO_2^- equilibrate with those of seawater with a temperature-dependent isotope effect (Buchwald & Casciotti, 2013). This process is measured as a percentage equilibration rather than a rate. To practically incorporate this process into the model, it has been assumed that the NO_2^- pool has already undergone equilibration to the given percentage. As a result, the NO_2^- added during NH_4^+ to NO_2^- nitrification must be equilibrated prior to being added to the NO_2^- pool. This construction was chosen over a set equilibration rate for simplicity, as to construct it with a set rate would result in a varying percentage of NO_2^- equilibration.
- Nitrification 2: the oxidation of NO_2^- to NO_3^-. This process introduces an O atom from the H_2O pool (Kumar et al., 1983).
- Denitrification: the reduction of NO_3^- to N_2 gas, removing bioavailable N from the system.

The output of the model is comprehensive, giving the concentrations, δ^{15}N, and δ^{18}O (where appropriate) of all the pools as the model progresses. The rates and instantaneous products of each process acting on the various N pools are also recorded and can be displayed. This allows

the true power of the model to be unleashed, in helping to understand the isotope system dynamics when multiple processes act simultaneously on multiple N pools. One example of this might be if NO_3^-, NO_2^- and NH_4^+ assimilation were to occur simultaneously, each with a different isotope effect, to produce PN, which is coincidentally being remineralised to produce new NH_4^+. To determine the impacts that each of these processes will have on one another is impossible without a model.

The Ocean Isotope Model^{TM} should be taken as a helpful theoretical tool to explore the impact of different processes on the isotopic distribution across the ocean N pools and allows for the rapid testing of hypotheses that may explain observational data.

References

Altabet, M. A., & Francois, R. (2001). Nitrogen isotope biogeochemistry of the Antarctic polar frontal zone at 170°W. *Deep-Sea Research Part II: Topical Studies in Oceanography*, *48*(19–20), 4247–4273. https://doi.org/10.1016/S0967-0645(01)00088-1

Andersson, K. K., & Hooper, A. B. (1983). O_2 and H_2O are each the source of one O in NO_2^- produced from NH_3 by Nitrosomonus: ^{15}N-NMR evidence. *FEBS Letters*, *164*(2), 236–240. https://doi.org/10.1016/0014-5793(83)80292-0

Boshers, D. S., Granger, J., Tobias, C. R., Böhlke, J. K., & Smith, R. L. (2019). Constraining the Oxygen Isotopic Composition of Nitrate Produced by Nitrification. *Environmental Science and Technology*, *53*(3), 1206–1216. https://doi.org/10.1021/acs.est.8b03386

Buchwald, C., & Casciotti, K. L. (2013). Isotopic ratios of nitrite as tracers of the sources and age of oceanic nitrite. *Nature Geoscience*, *6*(4), 308–313. https://doi.org/10.1038/ngeo1745

Buchwald, C., Santoro, A. E., McIlvin, M. R., & Casciotti, K. L. (2012). Oxygen isotopic composition of nitrate and nitrite produced by nitrifying cocultures and natural marine assemblages. *Limnology and Oceanography*, *57*(5), 1361–1375. https://doi.org/10.4319/lo.2012.57.5.1361

Casciotti, K. L., Sigman, D. M., & Ward, B. B. (2003). Linking diversity and stable isotope fractionation in ammonia-oxidizing bacteria. *Geomicrobiology Journal*, *20*(4), 335–353. https://doi.org/10.1080/01490450303895

Casciotti, K. L., Trull, T. W., Glover, D. M., & Davies, D. (2008). Constraints on nitrogen cycling at the subtropical North Pacific Station ALOHA from isotopic measurements of nitrate and particulate nitrogen. *Deep-Sea Research Part II: Topical Studies in Oceanography*, *55*(14–15), 1661–1672. https://doi.org/10.1016/j.dsr2.2008.04.017

DiFiore, P. J., Sigman, D. M., & Dunbar, R. B. (2009). Upper ocean nitrogen fluxes in the Polar Antarctic Zone: Constraints from the nitrogen and oxygen isotopes of nitrate. *Geochemistry, Geophysics, Geosystems*, *10*(11). https://doi.org/10.1029/2009GC002468

DiFiore, P. J., Sigman, D. M., Karsh, K. L., Trull, T. W., Dunbar, R. B., & Robinson, R. S. (2010). Poleward decrease in the isotope effect of nitrate assimilation across the Southern Ocean. *Geophysical Research Letters*, *37*(17), 1–5. https://doi.org/10.1029/2010GL044090

DiFiore, P. J., Sigman, D. M., Trull, T. W., Lourey, M. J., Karsh, K., Cane, G., & Ho, R. (2006). Nitrogen isotope constraints on subantarctic biogeochemistry. *Journal of Geophysical Research: Oceans*, *111*(8), 1–19. https://doi.org/10.1029/2005JC003216

Flynn, R. F., Bornman, T. G., Burger, J. M., Smith, S., Spence, K. A. M., & Fawcett, S. E. (2021). Summertime productivity and carbon export potential in the Weddell Sea, with a focus on the waters adjacent to Larsen C Ice Shelf. *Biogeosciences*, *18*(22), 6031–6059. https://doi.org/10.5194/bg-18-6031-2021

Fripiat, F., Martínez-García, A., Fawcett, S. E., Kemeny, P. C., Studer, A. S., Smart, S. M., Rubach, F., Oleynik, S., Sigman, D. M., & Haug, G. H. (2019). The isotope effect of nitrate assimilation in the Antarctic Zone: Improved estimates and paleoceanographic implications. *Geochimica et Cosmochimica Acta*, *247*, 261–279. https://doi.org/10.1016/j.gca.2018.12.003

Hoch, M. P., Fogel, M. L., & Kirchman, D. L. (1992). Isotope fractionation associated with ammonium uptake by a marine bacterium. *Limnology and Oceanography*, *37*(7), 1447–1459. https://doi.org/10.4319/lo.1992.37.7.1447

Hupe, A., & Karstensen, J. (2000). Redfield stoichiometry in Arabian Sea subsurface waters. *Global Biogeochemical Cycles*, *14*(1), 357–372. https://doi.org/10.1029/1999GB900077

Karsh, K. L., Trull, T. W., Lourey, M. J., & Sigman, D. M. (2003). Relationship of nitrogen isotope fractionation to phytoplankton size and iron availability during the Southern Ocean Iron RElease Experiment (SOIREE). *Limnology and Oceanography*, *48*(3), 1058–1068. https://doi.org/10.4319/LO.2003.48.3.1058

Körtzinger, A., Koeve, W., Kähler, P., & Mintrop, L. (2001). C : N ratios in the mixed layer during the productive season in the northeast Atlantic Ocean. *Deep Sea Research Part I: Oceanographic Research Papers*, *48*(3), 661–688. https://doi.org/10.1016/S0967-0637(00)00051-0

Kumar, S., Nicholas, D. J. D., & Williams, E. H. (1983). Definitive ^{15}N NMR evidence that water serves as a source of "O" during nitrite oxidation by *Nitrobacter agilis*. *FEBS Letters*, *152*(1), 71–74. https://doi.org/10.1016/0014-5793(83)80484-0

Lehmann, M. F., Bernasconi, S. M., Barbieri, A., & McKenzie, J. A. (2002). Preservation of organic matter and alteration of its carbon and nitrogen isotope composition during simulated and in situ early sedimentary diagenesis. *Geochimica et Cosmochimica Acta*, *66*(20), 3573–3584. https://doi.org/10.1016/S0016-7037(02)00968-7

Liu, K. K., Kao, S. J., Chiang, K. P., Gong, G. C., Chang, J., Cheng, J. S., & Lan, C. Y. (2013). Concentration dependent nitrogen isotope fractionation during ammonium uptake by phytoplankton under an algal bloom condition in the Danshuei estuary, northern Taiwan. *Marine Chemistry*, *157*, 242–252. https://doi.org/10.1016/J.MARCHEM.2013.10.005

Mirkin, J., Fawcett, S., & West, A. (2019). *Meltwater and circulation characteristics adjacent to Larsen C Ice Shelf: a study of seawater $\delta^{18}O$* [Honours]. The University of Cape Town.

Möbius, J. (2012). Isotope fractionation during nitrogen remineralization (ammonification): Implications for nitrogen isotope biogeochemistry. *Geochimica et Cosmochimica Acta*, *105*, 422–432. https://doi.org/10.1016/j.gca.2012.11.048

Mooney, C. Z. (1997). Monte Carlo Simulation. In *Sage* (116th ed.). Sage. https://books.google.co.za/books?hl=en&lr=&id=xQRgh4z_5acC&oi=fnd&pg=PA5&dq=monte+carlo+simulation&ots=hiMFHRCrPO&sig=sYj9Gdd3ezm_zwAsRs5Hfv8FDyk#v=onepage&q=monte%20carlo%20simulation&f=false

Osterroht, C., & Thomas, H. (2000). New production enhanced by nutrient supply from non-Redfield remineralisation of freshly produced organic material. *Journal of Marine Systems*, *25*(1), 33–46. https://doi.org/10.1016/S0924-7963(00)00007-5

Pennock, J. R., Velinsky, D. J., Ludlam, J. M., Sharp, J. H., & Fogel, M. L. (1996). Isotopic fractionation of ammonium and nitrate during uptake by *Skeletonema costatum*: Implications for $\delta^{15}N$ dynamics under bloom conditions. *Limnology and Oceanography*, *41*(3), 451–459. https://doi.org/10.4319/lo.1996.41.3.0451

Sigman, D. M., Altabet, M. A., McCorkle, D. C., Francois, R., & Fischer, G. (1999). The $\delta^{15}N$ of nitrate in the Southern Ocean: Consumption of nitrate in surface waters. *Global Biogeochemical Cycles*, *13*(4), 1149–1166. https://doi.org/10.1029/1999GB900038

Sigman, D. M., DiFiore, P. J., Hain, M. P., Deutsch, C., Wang, Y., Karl, D. M., Knapp, A. N., Lehmann, M. F., & Pantoja, S. (2009). The dual isotopes of deep nitrate as a constraint on the cycle and budget of oceanic fixed nitrogen. *Deep-Sea Research Part I: Oceanographic Research Papers*, *56*(9), 1419–1439. https://doi.org/10.1016/j.dsr.2009.04.007

Thomas, H., Ittekkot, V., Osterroht, C., & Schneider, B. (1999). Preferential recycling of nutrients—the ocean's way to increase new production and to pass nutrient limitation? *Limnology and Oceanography*, *44*(8), 1999–2004. https://doi.org/10.4319/LO.1999.44.8.1999

Vo, J., Inwood, W., Hayes, J. M., & Kustu, S. (2013). Mechanism for nitrogen isotope fractionation during ammonium assimilation by *Escherichia coli* K12. *Proceedings of the National Academy of Sciences of the United States of America*, *110*(21), 8696–8701. https://doi.org/10.1073/pnas.1216683110

Waser, N. A. D., Harrison, P. J., Nielsen, B., Calvert, S. E., & Turpin, D. H. (1998). Nitrogen isotope fractionation during the uptake and assimilation of nitrate, nitrite, ammonium, and urea by a marine diatom. *Limnology and Oceanography*, *43*(2), 215–224. https://doi.org/10.4319/LO.1998.43.2.0215